

ISMRM

ONE  
COMMUNITY  
FOR CLINICIANS  
AND SCIENTISTS

ISMRM Indian  
CHAPTER  
2025



11<sup>th</sup> Annual Scientific Meeting of  
**ISMRM Indian Chapter**

**CONFERENCE PROCEEDINGS  
BOOKLET**

# President's Message



The Executive Committee and office bearers of **International Society for Magnetic Resonance in Medicine (ISMRM) Indian Chapter** welcome you to the **11<sup>th</sup> Annual Scientific Meeting of the ISMRM Indian Chapter: MR Updates on Acquisition, Recon., Analysis, AI & Beyond** hosted by Indian Institute of Technology, Hyderabad from 27<sup>th</sup> February to 1<sup>st</sup> March 2025.

There are 83 ISMRM (parent body, based out of USA) members from India, which include 44 Full members of ISMRM (active as of February, 2025), 36 Trainee members of ISMRM and 3 Emeritus members of ISMRM from India. There are 19 Full members of ISMRM of Indian Origin (from other countries) who have been attending the Chapter meetings.

The Indian Chapter of ISMRM has grown exponentially over the past few years, and has a current membership strength of 200.

With a meticulously curated scientific program, we are confident that this three-day conference and workshop will offer cutting-edge insights into MR innovation, engaging discussions, and valuable networking opportunities. The Organizing Committee has worked diligently to ensure a stimulating and enriching scientific experience for all attendees.

Complementing the main sessions, various workshops offer hands-on learning in diffusion-weighted imaging, advanced neuro post-processing, AI-driven insights, and Open Recon methods. Led by esteemed academicians and industry experts, these sessions promise to enhance your practical MRI skills.

Stalwarts in the fields of MRI and radiology from the US, Europe, Singapore, and prestigious institutions in India will participate in the conference. We extend our heartfelt gratitude to our sponsors for their generous support, which has played a crucial role in making this event possible and in subsidizing registration fees for students lacking financial support.

We look forward to your active participation, meaningful scientific discussions, and the opportunity to advance MR research together.

**Prof. S. Senthil Kumaran**  
President,  
**All India Institute Of Medical Sciences, Delhi**

# Patron's Message



**Prof. B.S. Murty**  
Director  
**Indian Institute of Technology**  
**Hyderabad**

A warm welcome to all the delegates of the 11th Annual Scientific Meeting of the Indian Chapter of the International Society of Magnetic Resonance in Medicine (ISMRM), hosted by our institution, the Indian Institute of Technology Hyderabad.

It is a privilege to host this gathering of distinguished scientists, clinicians, academicians, industry leaders and students from across India and abroad, fostering collaboration in the field of magnetic resonance imaging (MRI).

At IIT Hyderabad, innovation is at the core of our mission. With a strong emphasis on R&D, industry partnerships, and a thriving startup ecosystem, the institute is committed to driving technological progress. Our dynamic faculty and talented students continuously push the boundaries of knowledge, making significant contributions to science and technology.

Our Department of Biomedical Engineering is engaged in cutting-edge research in biomedical imaging technologies, including MRI. With MR imaging playing an increasingly important role in healthcare today, research in its basic technology, as well as in applied clinical aspects, including AI's role medical imaging, has gained renewed importance for improving healthcare.

As we embark on this three-day journey of insightful discussions and knowledge exchange in this conference, we look forward to strengthening global and local collaborations and shaping the future of MRI research.

Wishing you all a productive and enriching conference!

# Patron's Message

It is my pleasure to extend a warm welcome to all of you to the 11th Annual Scientific Meeting of the ISMRM Indian Chapter, being hosted at IIT Hyderabad.



**Prof. Vinay K. Nandicoori**  
**Director**  
**CSIR - Center for Cellular &**  
**Molecular Biology**

This gathering brings together leading researchers, academicians, and professionals from around the subcontinent and abroad to explore the latest advancements and applications of Magnetic Resonance (MR) across various scientific and medical domains. It provides a unique platform for knowledge exchange, fostering discussions that will shape the future of MR and its transformative impact on healthcare and life sciences. I would like to thank IIT Hyderabad for organizing this significant event, along with all the speakers and participants who have come together to share their expertise.

At CCMB Hyderabad, we strongly believe in the power of interdisciplinary collaboration to drive innovation. MR technology continues to revolutionize biomedical research, clinical diagnostics, and neuroscience, offering deeper insights into complex biological systems. CCMB has always been at the forefront in the development and/or use of novel Magnetic Resonance methods for probing biological systems and processes and this conference is a great way to bring together the research fraternity of this field.

I am confident that this conference will lead to fruitful discussions, new collaborations, and innovative ideas that push the boundaries of MRI research.

Wishing you all a fruitful and inspiring conference!

# Local Organizing Team's message



**Dr. Jaladhar Neelavalli,**  
Convenor  
Dept. of Biomedical  
Engineering  
Indian Institute of Technology  
Hyderabad



**Dr. Anant Bahadur Patel,**  
Co-Convenor  
CSIR – Center for Cellular  
and Molecular Biology



**Dr. Nagarajan Ganapathy,**  
Secretary  
Dept. of Biomedical Engineering  
Indian Institute of Technology  
Hyderabad

On behalf of the local organizing committee at the Indian Institute of Technology (IIT) Hyderabad, we are delighted to invite you to the ISMRM Indian chapter's 11th annual Scientific meeting, taking place from 27th February to 1st March, near the city of Hyderabad.

As magnetic resonance imaging (MRI) enthusiasts, MRI forms the foundation of our research, playing a central role in everything we do. With a comprehensive scientific program focused on the theme of 'MR Updates on Acquisition, Recon., Analysis, AI & Beyond' featuring renowned speakers and workshops for training on various MRI aspects, we look forward to an engaging and inspiring conference.

While you enjoy the conference, please don't forget to explore our campus as well as the city of Hyderabad. IIT Hyderabad is one of India's top science and technology institutes, with a vibrant campus surrounded by serene landscapes. We are most excited to welcome you to our wonderful campus. As most of you have chosen to stay on the campus during the conference, we have made every possible effort to make your stay comfortable.

We thank the Indian chapter of ISMRM for giving us the opportunity to host this event and wish you all a wonderful conference!!!

# Sponsors

## Platinum Sponsor



## Gold Sponsors



GE Healthcare



## Silver Sponsors



## Bronze Sponsor



# A variational autoencoder can reduce the scanning time of arterial spin labeling for cerebral blood flow map generation

Dhanashri Joshi <sup>1</sup>

Amol Gautam <sup>2</sup>

Bhushan Borotikar <sup>1</sup>

1.Symbiosis Centre for Medical Image Analysis, Symbiosis International University, Pune, India,  
2.Department of Radiodiagnosis, Symbiosis University Hospital and Research Centre, Pune, India.

## Introduction

Arterial spin labeling (ASL) is a perfusion magnetic resonance imaging modality that can be used to quantify cerebral blood flow (CBF) in 100gm/ml/min units. ASL provides crucial information about the regional CBF alterations observed in brain disorders such as Alzheimer's disease (AD) [1, 2]. However, in ASL, multiple pairs of control label (CL) images are acquired and averaged to generate a CBF map resulting in poor signal-to-noise ratio (SNR) and higher scanning time [3,4]. Deep learning-based models have recently been proposed for SNR improvement and reduction in scanning time. In this study, we used a variational autoencoder (VAE)-based deep learning framework for CBF map generation from CL image pairs acquired during the ASL sequence. We hypothesized that the use of VAE would enable the generation of a CBF map with a subset of acquired CL pairs and would achieve a similar quality to the CBF map derived from all CL pairs. This will, in turn, reduce the ASL scanning time for the subsequent scans.

## Methods

The study consisted 73 healthy controls (18 male, 55 female) acquired from the AD Neuroimaging Initiative (ADNI) repository (<http://adni.loni.usc.edu/>) including 3D T1 weighted, 2D Pulsed ASL (PASL), and M0 calibration images. The images were acquired on Siemens 3.0T MR scanner with PASL sequence using quantitative imaging of perfusion using a single subtraction II (Q2TIPs) technique [5]. The PASL acquisition parameters were: CL pairs = 52, echo time (TE) = 12ms, repetition time (TR) = 3400ms, inversion time TI1 = 700ms, TI2 = 1900ms, 24 sequential slices with 4mm slice thickness, 1mm slice gap, FOV = 256x256mm, and image matrix = 64x64. ASL image analysis was performed using FSL BASIL toolbox [6,7]. FSL MCFLIRT within BASIL [8] algorithm was applied for motion correction of raw ASL images. CL image pairwise subtraction generated a perfusion-weighted image, which was subsequently used for CBF map computation using the Buxton generic kinetic model [9]. As little temporal variation was observed in CBF during the resting state ASL scan [10], we selected the first 32 CL pairs (60% of total CL pairs) to minimize the scan time while representing the meaningful analysis of CBF maps. CBF maps of CL-52 pairs and CL-32 pairs were computed, extracted as 2D slices of size 128x128. The A Vector Quantized VAE (VQVAE) model was trained for 200 epochs with input as CL-32 CBF map slices and ground truth (GT) as CL-52 CBF map slices using Huber loss function with delta parameter = 1.0, 0.5, and 0.7. Performance of the predicted images was evaluated using validation metrics of SSIM (Structural Similarity Index Measure), MAE (Mean Absolute Error) and MMD

(Maximum Mean Discrepancy).

## Results

The performance of the VQVAE models was evaluated for validation and training loss using Huber loss function for delta values 0.7, 0.5, and 1.0. There was no visible (Figure 1) or quantifiable (Table 1) change in using these three delta values. We examined the CBF value as the mean voxel intensity of the enhanced image and GT image.

## Discussion

This study provides means to significantly reduce the ASL acquisition time without compromising the CBF map quality. In Huber loss, transition point parameter  $\delta$  controls the transition from quadratic to absolute value. We used a sensitivity analysis for  $\delta$  by checking its effect for three values viz. 1.0, 0.5, and 0.7. Table 1 indicated that the HC model with  $\delta=0.7$  provided better results in terms of SSIM (0.99), and the least MAE (0.0014) and MMD (0.064) values, could be used for VQVAE-based CBF map generation using fewer CL pairs. The improvement in the visual quality of enhanced CBF maps can help in detecting subtle abnormalities and improving interpretability. While the model has shown better image enhancement, the quantitative CBF values may not always match with the GT values. This discrepancy may be caused by several factors, such as the non-linear relationship between CBF values and image intensity and the VQVAE model's preference on perceptual enhancement rather than strictly preserving the quantitative measurements.

## Conclusion

The VQVAE model with Huber loss function has shown promising results in terms of SSIM, MAE and MMD to obtain the enhanced CBF maps using only 60% of CL pairs. It will help in the reduction of ASL scanning time and help in interpretability of CBF maps. In future, we plan to train the model on a large dataset with a hybrid loss function for balanced enhancement and quantitative accuracy.

**Table 1:** Train loss, Val loss, MAE, and MMD in ml/100gm/min and SSIM validation metrics.

Model	Train loss	Val loss	SSIM	MAE	MMD
HC delta 1	2.40E-0.5	2.45E-0.5	0.99	0.0015	0.068
HC delta 0.5	2.48E-0.5	2.42E-0.5	0.98	0.0024	0.093
<b>HC delta 0.7</b>	<b>2.58E-0.5</b>	<b>2.39E-0.5</b>	<b>0.99</b>	<b>0.0014</b>	<b>0.064</b>

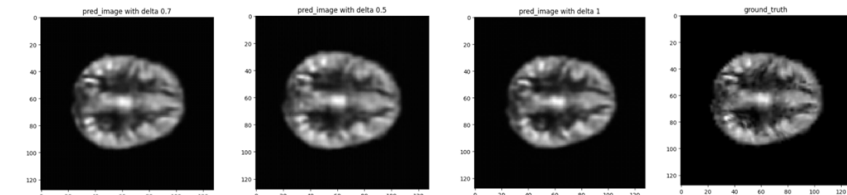


**Figure 1:** The predicted CBF maps obtained from CL-32 pairs with  $\delta = 0.7, 0.5$ , and 1 with the original CL-52 CBF map.

## Reference

- [1] K. Ahmadi, J. B. Pereira, D. Berron, J. Vogel, S. Ingala, O. T. Strandberg, S. Janelidze, F. Barkhof, J. Pfeuffer, L. Knutsson, et al., "Gray matter hypoperfusion is a late pathological event in the course of alzheimer's disease," Journal of Cerebral Blood Flow & Metabolism, vol. 43, no. 4, pp. 565–580, 2023.
- [2] M. Li, T. Zhu, Y. Kang, and S. Qi, "A 3d pseudo-continuous arterial spin labeling study of altered cerebral blood flow correlation networks in mild cognitive impairment and alzheimer's disease," Frontiers in Aging Neuroscience, vol. 16, p. 1345251, 2024.
- [3] K. H. Kim, S. H. Choi, and S.-H. Park, "Improving arterial spin labeling by using deep learning," Radiology, vol. 287, no. 2, pp. 658–666, 2018.
- [4] M. Grade, J. Hernandez Tamames, F. Pizzini, E. Achten, X. Golay, and M. Smits, "A neuroradiologist's guide to arterial spin labeling mri in clinical practice," Neuroradiology, vol. 57, pp. 1181–1202, 2015.
- [5] W.-M. Luh, E. C. Wong, P. A. Bandettini, and J. S. Hyde, "Quipss ii with thin-slice t1 periodic saturation: a method for improving accuracy of quantitative perfusion imaging using pulsed arterial spin labeling," Magnetic Resonance in Medicine: An Official Journal of the International Society for Magnetic Resonance in Medicine, vol. 41, no. 6, pp. 1246–1254, 1999.
- [6] M. A. Chappell, A. R. Groves, B. Whitcher, and M. W. Woolrich, "Variational bayesian inference for a non linear forward model," IEEE Transactions on Signal Processing, vol. 57, no. 1, pp. 223–236, 2008.
- [7] A. R. Groves, M. A. Chappell, and M. W. Woolrich, "Combined spatial and non-spatial prior for inference on mr time-series," Neuroimage, vol. 45, no. 3, pp. 795–809, 2009.
- [8] M. Jenkinson, P. Bannister, M. Brady, and S. Smith, "Improved optimization for the robust and accurate linear registration and motion correction of brain images," Neuroimage, vol. 17, no. 2, pp. 825–841, 2002.
- [9] R. B. Buxton, L. R. Frank, E. C. Wong, B. Siewert, S. Warach, and R. R. Edelman, "A general kinetic model for quantitative perfusion imaging with arterial spin labeling," Magnetic resonance in medicine, vol. 40, no. 3, pp. 383–396, 1998.
- [10] G. G. Brown, C. Clark, and T. T. Liu, "Measurement of cerebral perfusion with arterial spin labeling: Part 2. applications," Journal of the International Neuropsychological Society, vol. 13, no. 3, pp. 526–538, 2007.

# Advanced Neuroimaging and Hybrid Optimization Algorithm with RBFNN for Early Detection of Alzheimer's Disease

Subhabrata Rath\* and Debasish Dutta<sup>#</sup>

Department of BSH, Silicon University- Bhubaneswar, PIN-751024 Odisha, India

<sup>#</sup>Department of Mathematics, National Institute of Technology- Warangal, PIN-506004 Telangana, India

## Introduction

Magnetic Resonance Imaging (MRI) is a critical diagnostic tool in modern medicine, offering detailed images of internal structures without invasive procedures. Ensuring the reliability and accuracy of MRI systems is paramount to maintaining diagnostic confidence. Standardized protocols, such as those outlined by the American College of Radiology (ACR), are utilized to validate MRI systems' performance. The ACR large phantom is a standard tool designed to evaluate critical imaging parameters. This study focuses on the validation of an Indigenous Magnetic Resonance Imaging (IMRI) system, a locally developed MRI system, to benchmark its performance against ACR standards [1]. The ACR phantom tests evaluate various imaging criteria, including geometric accuracy, spatial resolution, slice thickness and position accuracy, image intensity uniformity, percentage signal ghosting, and low-contrast object detectability. These criteria are crucial for ensuring consistent and precise imaging, which directly impacts clinical diagnosis. The IMRI system's validation seeks to establish its readiness for clinical application while identifying potential areas for improvement.

## Methods

The study utilized the ACR large phantom as the test object, following standard ACR guidelines for MRI system validation [2]. The phantom was scanned using the IMRI system under specified conditions, and key slices from T1 and T2-weighted series were analysed. The tests included the following:

**Geometric Accuracy:** Measurements were performed on reference slice 5 of the ACR T1 series to ensure that spatial dimensions in the image matched the known physical dimensions of the phantom.

**High-Contrast Spatial Resolution:** Reference slice 1 from both T1 and T2 series was examined to determine the smallest resolvable structure in both up-down and left-right directions. The measured resolution was compared against the ACR standard of 1.0 mm.

**Slice Thickness Accuracy:** The ramps visible on reference slice 1 of T1 and T2 series were analysed to verify slice thickness accuracy.

**Slice Position Accuracy:** Measurements were taken on slices 1 and 11 of both T1 and T2 series to detect deviations in slice positioning. Deviations greater than 4 mm were considered to adversely affect low-contrast detectability.

**Percentage Signal Ghosting:** Ghosting artifacts were assessed on slice 7 of the T1 series by measuring signal variations at defined regions.

**Low-Contrast Object Detectability:** Slices 8 through 11 of both T1 and T2 series were inspected to identify the visibility of low-contrast objects (spokes). The presence of at least 27 spokes was required to pass this test.

## Results

The IMRI system performed satisfactorily on most tests:

**Geometric Accuracy:** The system passed, with measured dimensions closely matching the physical dimensions of the phantom shown in figure 1.

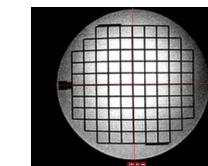


Figure 1. Geometric Accuracy

**High-Contrast Spatial Resolution:** The smallest resolvable structure was 0.9 mm, meeting the ACR standard shown in figure 2.

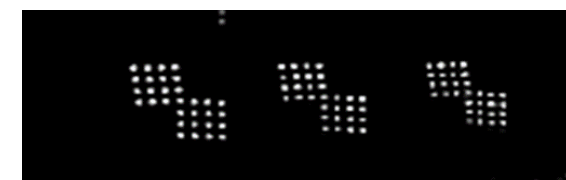


Figure 2. High-Contrast Spatial Resolution

**Slice Thickness & Position Accuracy:** The ramps were clearly visible, confirming accurate slice thickness shown in figure 3a. No measurable differences exceeding 4 mm were observed, indicating correct slice positioning shown in figure 3b.

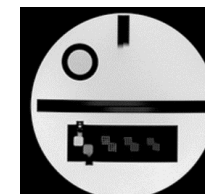


Figure 3a. Slice Thickness

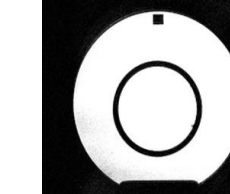


Figure 3b Position Accuracy

fell within acceptable ranges shown in figure 4b .

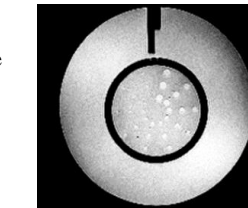


Figure 4a. LCD Detection

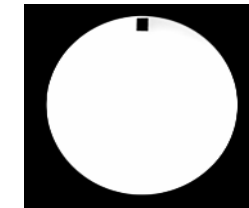


Figure 4b Signal Ghosting

## Discussion

The results highlight the IMRI system's capability to meet most ACR standards, an encouraging outcome for indigenous MRI technology development. Regular validation using the ACR phantom is recommended to monitor performance over time and ensure compliance with diagnostic standards.

## Conclusion

The IMRI system demonstrated satisfactory performance across key imaging parameters such as geometric accuracy, high-contrast spatial resolution, slice thickness and position accuracy, and percentage signal ghosting. These results affirm the system's capability to produce reliable and precise diagnostic images. Overall, the IMRI system shows great promise for clinical application, provided ongoing refinements are implemented to address the identified limitations.

## Reference

- American College of Radiology. "Phantom Test Guidance for MRI Quality Control."
- Kucharczyk, W., Brant-Zawadzki, M., & Nishimura, D. G. (1990). "Clinical MRI: A Practical Approach." Springer.

**Signal Ghosting and Low-Contrast Object Detectability:** This test was passed in T2-weighted images, with 27 spokes visible shown in figure 4a. The calculated ghosting levels

# Accuracy of Indigenous AI tool in detection of Ischemic Neurological Stroke

**Prof. (Dr.) Rajul Rastogi**

Department of Radiodiagnosis, Teerthanker Mahaveer Medical College and Research Center, Moradabad, Uttar Pradesh

## Introduction

Neurological stroke is an acute event associated with significant morbidity if treated beyond the golden period. Ischemic strokes are the commonest and often present in emergency accounting for delay in reporting by expert hands. Hence, the technological advances especially artificial intelligence tools are being developed to suit the needs of the population. Such a tool has been developed indigenously, and we are presenting our initial experience with the same.

## Methods

Twenty-five patients with suspected stroke were reported by a radiologist and by using AI tool with special reference to the presence or absence of infarct, location, arterial territory, diffusion-T2FLAIR

mismatch, hemorrhagic transformation present or absence, and any midline shift. Accuracy of AI tool was compared against the findings made by an expert Radiologist.

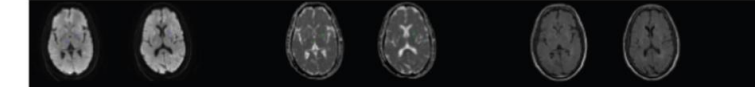
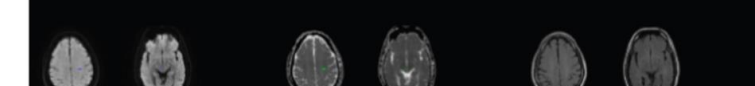
## Results

The AI was 100% accurate in the detection of infarct with more than 95% accuracy in detecting its location. However, moderately high accuracy was noted in detection of the hemorrhagic transformation and midline shift. AI performed poorly in territorial distribution, DWI/T2FLAIR mismatch recognition and detection of midline shift.

## Conclusion

Though the initial results are encouraging as AI could detect all the infarcts suggesting its high utility in emergency setting. However, it needs further

improvement in detection of other parameters which could also help in better management.

REFERRING PHYSICIAN	STUDY DATE	STUDY TIME	ACCESSION NO
<b>Acute Pathologies</b>			
Infarct Present			Yes
Infarct Location (Anat)			RT. and LT. Frontal lobe, RT. Parietal and Temporal lobes, and minor part of Midbrain and Pons.
Infarct Location (Vas)			MCA, ACA, PCA, Bilateral Lenticulostriate artery, and Basilar artery.
Flair mismatch			No
Hemorrhage Present			No
Hemorrhage Type			-
Hemorrhage Location (Anat)			-
Hemorrhage Location (Vas)			-
<b>Acute Ischemic Lesion</b>			
Largest	1.43 ml	Hemorrhage	Edema
Total	1.43 ml	-	-
			
			

# AI-Driven Background Inversion in MR-based Bone Imaging

**Suranjita Ganguly\***

**Yogesh Kannan Mariappan\***

Philips Healthcare, Bangalore, India\* Philips Healthcare, Tokyo, Japan\*\*

**Masami Yoneyama\*\***

**Tejas Shah\***

## Introduction

The FRACTURE sequence in MRI is a gradient-echo-based method with specialized post-processing steps to enhance bone contrast in addition to superior soft-tissue contrast [1-3]. However, the post-processing steps lead to a bright background that complicates downstream processing, necessitating manual adjustments for background inversion. A re-inverted background would enable (a) generation of medical images comparable to those from CT or X-ray; (b) aid for surgery planning in musculoskeletal (MSK) pathologies wherein FRACTURE images, together with MR angiography technique3 REACT and NerveView, are used to create 3D models of the skeleton, blood vessels and nerves; (c) selective removal of background noise leading to cleaner images. However, current approaches like intensity thresholding is not generalizable and require manual effort, especially in FRACTURE images wherein the contrast of bony structures may be like that of the image background. Machine learning (ML)-based models focus on isolating specific ROIs (e.g., tissues, tumors) based on morphology [4-7]. This narrow focus complicates accurate identification of the entire anatomy and distinguishing it from background noise. In this work, we implemented an artificial intelligence (AI)-enabled model, nnUNet, that can identify and selectively remove/invert the background from the FRACTURE images with a minimal training dataset.

## Methods

FRACTURE images acquired from scanning the wrist were used as the dataset for developing the model. To obtain the corresponding masks for each image slice, a GUI was created wherein the following operations could be done on the image: thresholding, dilation, erosion. Following this, the masks were obtained such that each pixel value was identified as the foreground or the background by the labels ‘1’ and ‘0’ respectively. The dataset was then augmented with operations including but not limited to image flip, coarse dropout, rotation, and distortion to populate the dataset. The images were converted into the nnUNet-compatible NIfTI format and normalized. Following this, the data was split into train and test sets. For transfer learning the pre-trained nnUNet model was obtained

and retrained with the 3D full resolution nnUNet architecture. Three-fold cross-validation was employed. The model was trained by iterating over the training data and periodically validating it using the validation set to monitor performance metrics. Hyperparameters were adjusted based on the validation results to improve performance. Finally, the model was tested on a surrogate dataset.

## Results

The trained model was further tested on two augmented datasets. The test accuracy on the augmented data was found to be 99.6%, with 0.994 precision, 0.995 recall and 0.995 F1 score. Fig. 1 (a) shows the FRACTURE data used for testing the model (b) shows the inversion achieved after applying the predicted mask (c) depicts the corresponding confusion matrix for evaluating the model performance.

## Discussion

We showcased the effectiveness of our model on the wrist anatomy, with the key innovation being the full automation of background removal, eliminating the need for any manual intervention. The nnUNet automatically adjusts hyperparameters without requiring explicit monitoring, while also handling training parameters, such as the number of epochs for training. The time required for mask prediction is in the order of just a few seconds, making it highly suitable for real-time deployment. However, this approach needs to be extended to other anatomies and image resolutions beyond our current study.

## Conclusion

The AI-enabled model we developed automates the background inversion process for FRACTURE images. By enabling rapid and efficient background removal, our model can significantly enhance medical imaging workflows such as surgical planning and 3D modeling in musculoskeletal pathologies

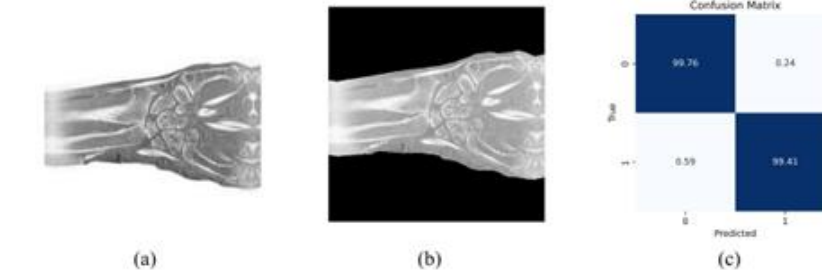


Fig. 1 (a) A 2D slice of a sample FRACTURE image with a bright background (b) The inversion achieved after applying the mask predicted by the trained nnUNet model around the original FRACTURE image (c) The corresponding confusion matrix depicting model performances.

## References

- Johnson B, Alizai H, Dempsey M. Fast field echo resembling a CT using restricted echo-spacing (FRACTURE): a novel MRI technique with superior bone contrast. *Skeletal Radiology*. 2021;50(8):1705-1713. doi:10.1007/s00256-020-03659-7
- Gascho D, Zoelch N, Tappero C, et al. FRACTURE MRI: Optimized 3D multi-echo in-phase sequence for bone damage assessment in craniocerebral gunshot injuries. *Diagnostic and Interventional Imaging*. 2020;101(9):611-615. doi:10.1016/j.dii.2020.02.010
- Ryuna Kurokawa , Hajime Yokota , Takayuki Sada , et al. FRACTURE-Angiography: simultaneous acquisition of bone imaging and angiography. *International Society of Magnetic Resonance in Medicine*. 2024;
- Ma J, He Y, Li F, Han L, You C, Wang B. Segment anything in medical images. *Nature Communications*. 2024;15(1). doi:10.1038/s41467-024-44824-z
- Ge Y, Zhang Q, Sun Y, Shen Y, Wang X. Grayscale medical image segmentation method based on 2D&3D object detection with deep learning. *BMC Medical Imaging*. 2022;22(1):1-14. doi:10.1186/s12880-022-00760-2
- Thylashri S, Yadav UM, Danush Chowdary T. Image segmentation using K- means clustering method for brain tumour detection. *International Journal of Engineering and Technology(UAE)*. 2018;7(2.19 Special issue 19):97-100. doi:10.14419/ijet.v7i2.19.15058
- Zhao Y, Huang Z, Che H, et al. Segmentation of Brain Tissues from MRI Images Using Multitask Fuzzy Clustering Algorithm. *Journal of Healthcare Engineering*. 2023;2023. doi:10.1155/2023/4387134

# Analysis of Tumor Heterogeneity Using DCE-MRI Kinetic Parameters Extracted via Bi-exponential Curve Fitting with TICs

Priyadarshini B<sup>1</sup>Priscilla Dinkar Moyya<sup>2</sup>Myhtili A<sup>3</sup>Anand K R<sup>4</sup>

<sup>1,3</sup> School of Electronics Engineering, Vellore Institute of Technology, Vellore-632014, Tamil Nadu, India, <sup>2</sup> School of Computing Science Engineering and Artificial Intelligence, VIT Bhopal University, Kothrikalan, Madhya Pradesh – 466114, India.

<sup>4</sup> Department of Radiology, Cincinnati Children's Hospital Medical Center, Cincinnati -45229, United States.

## Introduction

To investigate the relationship between temporal intensity parameters derived from Breast Dynamic Contrast-Enhanced Magnetic Resonance Imaging (DCE-MRI) and tumor heterogeneity using a segmented volume. To correlate parameters such as Tau1, Tau2, the maximum intensity (I\_max), and time to peak (TTP) to assess the heterogeneity of the segmented Region of Interest (ROI).

## Methods

A total of 10 patients (QIN breast DCE MRI) were included in this study from TCIA (The Cancer Imaging Archive)[1]. The procedure follows as 1. Select a 4-D image. 2. ROI extraction using energy-based volumetric segmentation by minimax optimization technique [2]. 3. Extraction of Temporal Intensity Curves (TIC) from each voxel. 4. Bi-exponential model fit with TIC and extract parameters like Tau1, Tau2, the maximum intensity (I\_max), and time to peak (TTP). 5. The relationships between the temporal parameters (Tau1, Tau2, I\_max, and TTP) and tumor heterogeneity by correlation analysis.

## Results and Discussion

From Table 1: Low values of Tau1: Indicate that the tumor region has rapid contrast uptake. High values of Tau2: Indicate slower washout, which could be due to slower perfusion. High I\_max values: Suggest high contrast uptake, usually associated with highly vascularized Low I\_max values: Indicate lower contrast enhancement, which could correspond to necrotic. Shorter TTP: Reflects faster arrival and uptake of the contrast agent. Longer TTP: Indicates slower contrast agent uptake.

As reflected in the kinetic parameters, tumor heterogeneity suggests differences in vascular and metabolic activity within the tumor regions. The results highlight the potential of DCE-MRI parameters in assessing tumor aggressiveness and guiding treatment decisions, although further validation in larger cohorts is needed. Further investigation is to explore how DCE-MRI kinetic parameters can be integrated into models for tumor grading and predicting pathological response to treatment.

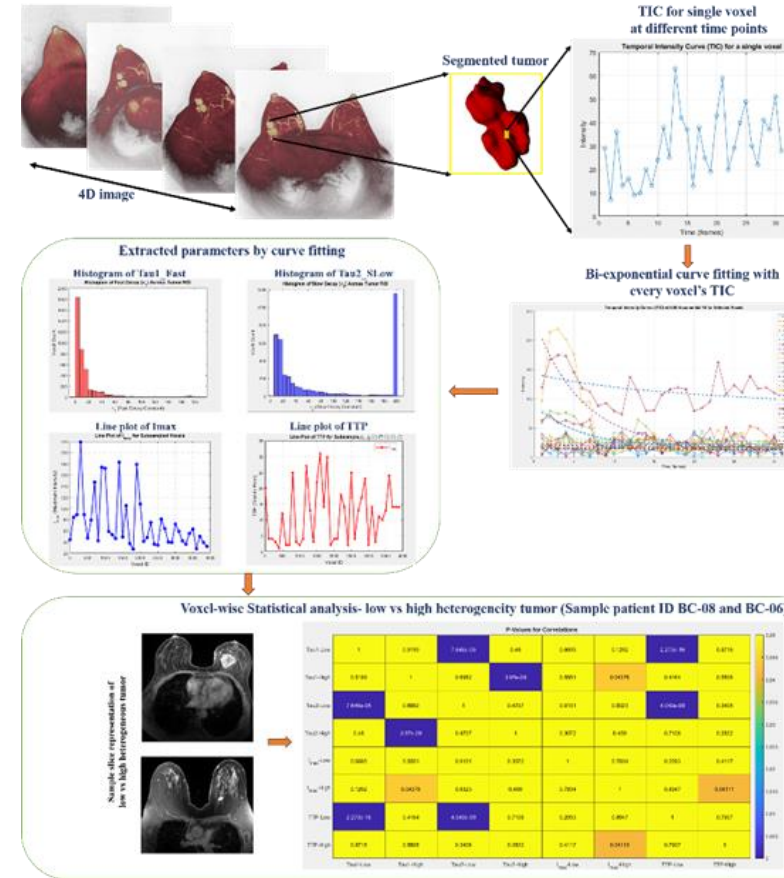


Figure 1: Flow diagram for tumor heterogeneity analysis

Table 1: Average TIC parameters of all patients in the dataset

Patient ID	No.of voxels in ROI	Average Tau1_Fast	Average Tau2_slow	Average Imax	Average TTP
BC-01	12683	0.16591	0.55644	78.667	16.6222
BC-05	2143	7	132.0893	22.423	16.2106
BC-06	738	16.9348	130.5246	59.0353	18.2877
BC-08	47470	0.0317	0.42367	17.4095	16.3519
BC-10	3682	13.3249	108.2205	38.2861	17.9766
BC-12	6130	116.9775	165.5431	138.1806	20.432
BC-13	1058	6.9	105.1303	19.228	15.3122
BC-14	3997	18.4517	109.8145	50.2855	19.5033
BC-15	3410	7.6254	14.0674	126.088	15.5811
BC-16	5147	28.358	108.7356	85.6949	15.7954

## Reference

- [1] Huang, W., Tudorica, A., Chui, S., Kemmer, K., Naik, A., Troxell, M., Oh, K., Roy, N., Afzal, A., & Holtorf, M. (2014). Variations of dynamic contrast-enhanced magnetic resonance imaging in the evaluation of breast cancer therapy response: a multicenter data analysis challenge (QIN Breast DCE-MRI). The Cancer Imaging Archive. <https://doi.org/10.7937/k9/tcia.2014.a2n1ixox>.
- [2] P. Babu, M. Asaithambi and S. Mogappair Suriyakumar, "Automated 3D Tumor Segmentation From Breast DCE-MRI Using Energy-Tuned Minimax Optimization," in IEEE Access, vol. 12, pp. 87532-87544, 2024, doi: 10.1109/ACCESS.2024.3417488.

# Automated Deep Learning Based Cardiac Quantification in Hypertrophic Cardiomyopathy: A Comparative Study with Manual Segmentation and Echocardiography

Shivam Angiras MSc<sup>1</sup>Dr. Deb Kumar Boruah PDCC<sup>1</sup>Prof. Dr. Pranjal Phukan DM<sup>1</sup>Dr. Kalyan Sarma<sup>1</sup>Dr. Prince Das<sup>1</sup>Dr. Rajeev Bharadwaj MD<sup>2</sup>

1. Department of Diagnostic and Interventional Radiology, AIIMS Guwahati

2. Department of Cardiology, AIIMS Guwahati

## Introduction

Hypertrophic cardiomyopathy (HCM), the most common monogenic cardiac disease, affects approximately 1 in 500 individuals [1–4]. MRI plays a crucial role in assessing mitral regurgitation (MR) and myocardial tissue characterization in HCM [5]. LVOT obstruction occurs in ~70% of HCM cases due to septal hypertrophy and pressure gradients, displacing the anterior mitral leaflet (AML) and causing significant SAM-dependent MR [6].

Cardiac MRI surpasses echocardiography in MR quantification and mitral valve evaluation, aiding in surgical planning and clinical management [7, 8]. 2D cine imaging with phase- contrast velocity mapping, quantify MR severity but are time-intensive [9]. Deep learning (DL) accelerates MRI segmentation, reducing manual effort while maintaining accuracy, though challenges persist in cases with asymmetric hypertrophy and complex anatomy [10, 11]. This study examines the equivalence of DL-based segmentation software with manual methods for assessing cardiac parameters in HCM.

## Methods

We analyzed 25 HCM patients (mean age: 51±10 years) undergoing CMR for diagnosis or severity evaluation. CMR was performed using a 3-T scanner (Vida, Siemens) with cine images acquired via a TrueFISP sequence (TR: 2.7 ms, TE: 1.5 ms, flip angle: 60°, temporal resolution: 50 ms). Standard long-axis views and short-axis slices (thickness: 8 mm, gap: 2 mm) were obtained. The Institutional Review Board approved the protocol, and informed consent was obtained.

Cine-CMR images were analyzed using syngo.Via for manual delineation of LV/RV endocardial boundaries, including papillary muscles and trabeculations. LVEF, EDV, and ESV were calculated using Simpson's method. DL-based EF, SV, and EDV were calculated using SuiteHeart software. MR volume was derived using the formula  $MR = LVSV - \text{aortic forward flow}$ . Manual and automated results were compared using paired t-tests, ICC, and Bland-Altman analysis.

## Results

The mean EF measured by DL-based and manual methods was 62.4±8.52% and 61.3±8.54%, respectively, with no significant difference ( $p = 0.077$ ). Agreement was excellent (ICC = 0.89–0.97,  $p < 0.001$ ). Bland-Altman analysis showed good agreement without systematic bias. DL-based software reduced analysis time to 7±3 minutes compared to 30±7 minutes for manual segmentation. MRI provided similar MR grades to echocardiography, differing in 2/19 cases with mild MR.

## Discussion

DL-based software demonstrated high agreement with manual segmentation for assessing cardiac parameters in HCM. While echocardiography is widely used, CMR remains the reference standard for quantifying cardiac metrics. DL algorithms streamline workflows, reduce analysis time, and improve accessibility. Challenges include addressing asymmetric hypertrophy and LVOT gradient measurements. Future work should optimize DL algorithms for HCM-specific challenges and validate findings in multicenter cohorts to enhance clinical application.

## Conclusion

DL-based automated segmentation provides accurate, reliable quantification of cardiac parameters in HCM, reducing analysis time significantly. Current algorithms show promise but require further refinement for complex HCM morphology. Future studies should validate these findings in larger cohorts and explore clinical integration to improve patient outcomes.

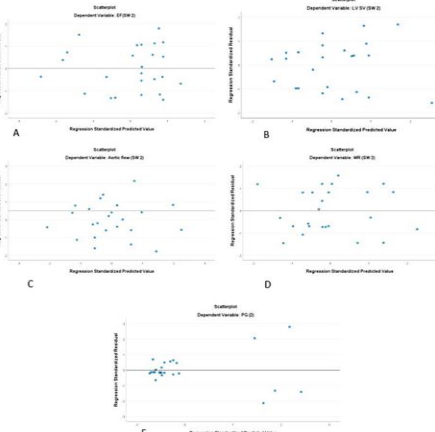


Figure-1) A- EF:  $R = 0.935, R^2 = 0.873, F(1, 23) = 144.69, p < 0.001$ . The regression coefficient for Software 1 was 0.936 ( $p < 0.001$ ), while the intercept was not statistically significant ( $B = 2.8, p = 0.553$ ). B- LVSV:  $R = 0.97, R^2 = 0.944, F(1, 23) = 185.04, p < 0.001$ . The coefficient for Software 1 was 0.984 ( $p = 0.001$ ). C- AF:  $R = 0.91, R^2 = 0.834, p < 0.001$ . The coefficient for Software 1 was 0.9 ( $p = 0.001$ ). D- MR:  $R = 0.97, R^2 = 0.95, p < 0.001$ . The coefficient for Software 1 was 0.9 ( $p = 0.001$ ). E- PG:  $R = 0.99, R^2 = 0.9, p < 0.001$ . The coefficient for Software 1 was 0.9 ( $p = 0.001$ ).

## Reference

- Elliott P, McKenna WJ. Hypertrophic cardiomyopathy. Lancet. (2004) 363:1881–91. doi: 10.1016/S0140-6736(04)16358-7
- Maron BJ, Gardin JM, Flack JM, Gidding SS, Kurosaki TT, Bild DE. Prevalence of hypertrophic cardiomyopathy in a general population of young adults.
- Echocardiographic analysis of 4111 subjects in the CARDIA study. Coronary artery risk development in (young) adults. Circulation. (1995) 92:785–9. doi: 10.1161/01.cir.92.4.785
- Ommen SR, Mital S, Burke MA, Day SM, Deswal A, Elliott P, et al. 2020 AHA/ACC guideline for the diagnosis and treatment of patients with hypertrophic cardiomyopathy: a report of the American College of Cardiology/American Heart Association Joint Committee on Clinical Practice Guidelines. Circulation. (2020) 142:e558–631. doi: 10.1161/CIR.0000000000000937
- Authors/Task Force members, Elliott PM, Anastakis A, Borger MA, Borggreve M, Cecchi F, et al. 2014 ESC Guidelines on diagnosis and management of hypertrophic cardiomyopathy: the task force for the diagnosis and management of hypertrophic cardiomyopathy of the European Society of Cardiology (ESC). Eur Heart J. (2014) 35:2733–79. doi: 10.1093/euroheartj/ehu284
- Ommen SR, Mital S, Burke MA, Day SM, Deswal A, Elliott P, Evanovich LL, Hung J, Joglar JA, Kantor P, Kimmelstiel C, Kittleson M, Link MS, Maron MS, Martinez MW, Miyake CY, Schaff HV, Semsarian C, Sorajja P. 2020 AHA/ACC Guide line for the Diagnosis and Treatment of Patients With Hypertrophic Cardiomyopathy. Circ. (2020; 142: e558-e631
- Anwar MA. Mitral regurgitation in hypertrophic cardiomyopathy: a narrative review of mechanism and current management. Int J Clin Cardiol. (2022) 9:248. doi: 10.23937/2378-2951/1410248
- Ommen SR, Mital S, Burke MA, Day SM, Deswal A, Elliott P, Evanovich LL, Hung J, Joglar JA, Kantor P, Kimmelstiel C, Kittleson M, Link MS, Maron MS, Martinez MW, Miyake CY, Schaff HV, Semsarian C, Sorajja P. 2020 AHA/ACC Guideline for the Diagnosis and Treatment of Patients With Hypertrophic Cardiomyopathy. Circ. (2020; 142: e558-e631
- Gupta AN, Avery R, Soulard G, Allen BD, Collins JD, Choudhury L, Bonow RO, Carr J, Matik M, Elbaz MSM. Direct Mitral Regurgitation Quantification in Hypertrophic Cardiomyopathy Using 4D Flow CMR Jet Tracking: Evaluation in Comparison to Conventional CMR. JCMR. (2021; 23: 138.
- Vermes E, Iacuzio L, Levy F, Bohbot Y, Renard C, Gerber B, Maechoux S, Tribouilloy C. Role of Cardiovascular Magnetic Resonance in Native Valvular Regurgitation: A Comprehensive Review of Protocols, Grading of Severity, and Prediction of Valve Surgery. Front Cardiovasc Med. (2022; 9: 881141.
- Petersen SE, Aung N, Sanghvi MM, et al. Reference ranges for cardiac structure and function using cardiovascular magnetic resonance (CMR) in Caucasians from the UK Biobank population cohort. Journal of Cardiovascular Magnetic Resonance. (2017; 19:1–19. [PubMed: 28081721]
- Hofmann R, Barletta G, Von Bardeleben S, et al. Analysis of left ventricular volumes and function: A multicenter comparison of cardiac magnetic resonance imaging, cine ventriculography, and unenhanced and contrast-enhanced two-dimensional and three-dimensional echocardiography. Journal of the American Society of Echocardiography. (2014; 27:292–301. [PubMed: 24440110]
- Sunesiaputra A, Sanghvi MM, Aung N, et al. Fully-automated left ventricular mass and volume MRI analysis in the UK Biobank population cohort: evaluation of initial results. International Journal of Cardiovascular Imaging. (2018; 34:281–291.

# Automated Diagnosis of Autism Spectrum Disorder using Graph Metrics from Diffusion Tensor Imaging and Machine Learning

Ravi Ratnaik\*

Computational Neuroscience and Biology Lab, School of Biomedical Engineering, Indian Institute of Technology (BHU) Varanasi, Uttar Pradesh, India

Hrithika Usha

Dibyasree Lahkar

Jac Fredo Agastinose Ronickom

## Introduction

Autism Spectrum Disorder (ASD) is a neurodevelopmental condition characterized by challenges in social interaction, communication, and behavior [1]. According to the CDC (2023), the prevalence of ASD has risen to 1 in 36 children. Traditional diagnostic methods, such as Autism Diagnostic Observation Schedule and Autism Diagnostic Interview-Revised, are time-consuming and limited in accuracy. Diffusion Tensor Imaging (DTI), a non-invasive MRI technique, offers promise in diagnosing ASD-related microstructural brain changes and tracking treatment response. DTI-derived metrics, such as Fractional Anisotropy (FA), Axial Diffusivity (AD), Mean Diffusivity (MD), and Radial Diffusivity (RD) have been widely used to characterize microstructural variations [2]. Further, studies have used graph theory to analyze the network of brain regions (nodes) and their structural or functional connections (edges) [3]. However, the graph theory was not explored to study the brain organization and connectivity patterns of ASD using the DTI images. In this study, we used graph metrics and machine learning algorithm to build a diagnostic classification model for ASD.

## Methods

Figure 1 (a) shows the process pipeline of the study. DTI data from the publicly accessible ABIDE II database, including images from 154 individuals with ASD and 129 typically developing (TD) participants, were pre-processed using a standard pipeline [4]. DTI measures such as FA, AD, MD, and RD were computed for 50 regions of interest based on the JHU atlas. A structural correlation graph was constructed using a Pearson correlation-based feature matrix [5]. Graph-theoretical metrics were extracted to characterize the network topology, including Betweenness Centrality, Closeness Centrality, Clustering Coefficient, Degree Centrality, Participation Coefficient, and Strength. This resulted in a total of 300 graph metric features per

participant [3]. Recursive feature elimination with cross-validation was used for feature selection, and the selected features were employed to train the Logistic Regression (LR) machine learning classifier to distinguish ASD from TD participants. Model performance was evaluated using accuracy, sensitivity, specificity, precision, and F1-score.

## Results

The performance of the LR classification model is assessed using different numbers of top features. Figure 1 (b) shows that the accuracy initially improves with an increasing number of features, reaching a peak of 81.61% at 75 features. Beyond this point, the accuracy fluctuates, indicating the potential diminishing marginal utility of additional features, suggesting an optimal feature subset of around 75 for this dataset. The top three features that performed well in classifying ASD and TD participants were Strength of the Cingulum (Cingulate Gyrus) L, Closeness Centrality of the Anterior Corona Radiata L, and Betweenness Centrality of the Genu of the Corpus Callosum.

## Discussion

This study highlights the potential of DTI-based graph-theoretical metrics combined with machine learning classifier to differentiate ASD from TD participants. LR with 75 features shows the highest accuracy of 81.61%, with key brain network features, such as the Strength of the Cingulum and Closeness Centrality of the Anterior Corona Radiata, identified as critical biomarkers for ASD classification.

## Conclusion

DTI and graph theory offer valuable insights into the neurobiological mechanisms of ASD, with machine learning model enhancing diagnostic accuracy. The extracted features show potential for early

detection. Future research can incorporate additional metrics and machine learning classifiers to generalize the diagnostic process further.

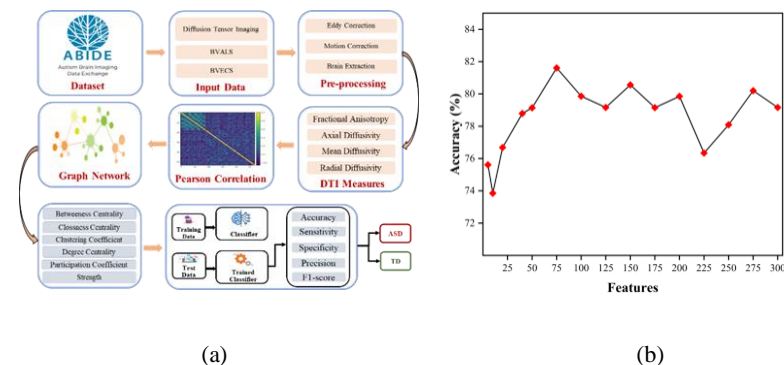


Fig1. (a) Process pipeline of the study and (b) Performance of LR on graph metrics features

## References

- [1] Genovese, Ann, and Merlin G. Butler. "The autism spectrum: behavioral, psychiatric and genetic associations." *Genes* 14.3 (2023): 677.
- [2] Nakagawa, Kai, et al. "Region-based analysis of sensory processing using diffusion tensor imaging." *Plos one* 18.4 (2023): e0284250.
- [3] Sporns, Olaf. "Graph theory methods: applications in brain networks." *Dialogues in clinical neuroscience* 20.2 (2018): 111-121.
- [4] Di Martino, Adriana, et al. "Enhancing studies of the connectome in autism using the autism brain imaging data exchange II." *Scientific data* 4.1 (2017): 1-15.
- [5] Ratnaik, Ravi, et al. "Diagnostic Classification of ASD Improves with Structural Connectivity of DTI and Logistic Regression." *Healthcare Transformation with Informatics and Artificial Intelligence*. IOS Press, 2023. 64-67.

# Automatic Detection of Dura Tail in Meningiomas Using Deep Learning Approach

Kuldeep. Raghuvanshi<sup>1</sup>

Sanskriti Srivastava<sup>1</sup>

Rakesh Kumar Gupta<sup>2</sup>

Anup Singh<sup>1,3</sup>

<sup>1</sup>Centre for Biomedical Engineering, Indian Institute of Technology Delhi, India, <sup>2</sup>Fortis Memorial Research Institute, Gurugram, India, <sup>3</sup>Department of Biomedical Engineering, All India Institute of Medical Sciences, Delhi, India

## Introduction

The most prevalent primary tumors of the central nervous system are meningiomas, which account for 37% [1] of all brain tumors in adults. It is an extra-axial brain tumor that arises from the meninges, which is a protective layer that protects the brain and spinal cord. The meninges consist of three layers: dura mater, arachnoid mater, and pia mater. According to WHO 2021, meningiomas are classified as grades 1,2 and 3. Over 80% of cases are grade I, which are slow-growing and benign tumors that can be effectively treated by surgical resection and radiotherapy. Magnetic resonance imaging is a gold standard for diagnosing and treatment planning of meningiomas.[2]

One of the most common radiologic indicators of meningioma is the "dural tail sign." The dural tail sign occurs due to the thickening and enhancement of the dura, which can be seen from the contrast-enhanced T1 weighted image(T1CE). The reaction of a meningioma tumor depends on the thickening and enhancement of the dura, so it is essential to detect the dura tail sign.[3] The dura tail sign is currently assessed qualitatively, and it is prone to interrater variability. This study aims to evaluate the potential of deep learning for automatically detecting dura tail on MRI images.

## Methods

This study utilizes T1-weighted contrast-enhanced (T1CE) MRI scans of 62 patients with meningioma. Data was collected from a local hospital and publicly available online resources. The ground truth masks were annotated manually using open-source software 3D slicer and then verified by a radiologist. The images were pre-processed to ensure uniformity across all scans by resizing the volumetric data to a fixed dimension of 256, 256, and 128. Additionally, intensity normalization was performed, scaling pixel values to a range of 0-255 to enhance contrast consistency and minimize variations caused by different imaging protocols.

The first stage of the pipeline involves tumor segmentation, where a 2D deep learning-based segmentation network (U-Net) was trained to identify and delineate the tumor region in an MRI slice. The performance of the segmentation network was evaluated using the Dice Similarity Coefficient (DSC), a widely used metric for assessing the overlap between predicted segmentation masks and ground truth annotations. Following segmentation, the second stage focuses on dura tail classification. The predicted tumor masks were multiplied to get the whole tumor volume. A 3D classification model (ResNet-18) was then trained to determine the presence or absence of the dura tail in these reconstructed volumes. 42 datasets are used for training, and 20 are used for testing. The classification model's performance was assessed using test accuracy to measure its effectiveness.

## Results

The segmentation model achieved a Dice Similarity Coefficient (DSC) of 0.82, ensuring reasonably accurate tumor boundary delineation. The dura tail classification model demonstrated 85% test accuracy; out of 20 volumes, it predicted 17 correctly, confirming its effectiveness in detecting the dura tail sign.

## Discussion

This study presents a deep learning framework that integrates tumor segmentation with classification for automated dura tail detection. The segmentation model achieved a high DSC, ensuring reasonably accurate tumor delineation, while the classification model demonstrated a sufficiently high accuracy. This approach minimizes false positives and improves consistency in clinical applications. A small sample size is one of the limitations of this study; results should be validated using a large sample size. Challenges remain, including MRI variability across institutions and ambiguous cases with faint dura tails. Future work should focus on multi-center datasets, multi-

sequence MRI integration, and extending to 3D segmentation for improved accuracy.

## Conclusion

This study presents a deep learning-based framework for automated dura tail detection by integrating tumor segmentation with classification. The proposed approach achieved reasonably accurate results in automatically detecting dura tail signs on MRI images and should be validated on a large, multicentric dataset.

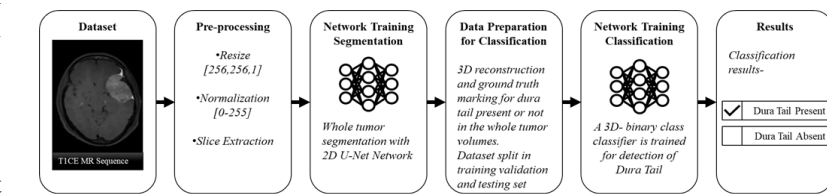


Figure 1 Figure shows a flow diagram of the process followed.

## References

- [1] Y. W. Park et al., "Radiomics and machine learning may accurately predict the grade and histological subtype in meningiomas using conventional and diffusion tensor imaging," Eur Radiol, doi: 10.1007/s00330-018-5830-3.
- [2] Li X, Miao Y, Han L, et al. Meningioma grading using conventional MRI histogram analysis based on 3D tumor measurement. Eur J Radiol. 2019;110:45-53. doi:10.1016/j.ejrad.2018.11.016
- [3] Larson JJ, Tew JM, Wiot G, De Courten-Myers GM. Acta Neurochir (Wien) (1992); 114: 59-63 :Acta. NTcurochirurgica Association of Meningiomas with Dural "Tails"; Surgical Signi cance.; 1992.

# Accelerated Fast-Spin-Echo Simultaneous Multi Slice (SMS) acquisition and DL based Reconstruction with Volume Coil

Nitin Jain

Sudhir Ramanna

Sajith Rajamani

Rajagopalan Sundaresan

Harsh Agarwal

Ramesh Venkatesan

GE HealthCare, Bangalore, India

## Introduction

Scanning obese patients in the non-wide-bore MRI scanner pose challenge in acquiring images with surface coil. Therefore, volume body coil may be preferred for data acquisition, however, in the absence of surface coil, accelerating an MR sequence becomes challenging to lower the scan time. Hadamard encoding based Simultaneous Multi Slices (SMS) has been proposed as an effective technique to achieve considerable reduction in scan time [1]. This technique is different from Multiband SMS where coil sensitivities of multi-channel coils are used for the acceleration [2, 3]. Hadamard based SMS offer inherent additional SNR and lower refocusing pulse SAR and peak B1 requirements it extends slice thickness of the existing refocusing pulse with lower gradient strength.

## Methods

Hadamard SMS uses different RF excitations over various averages to keep scan time similar and achieve multiple slice excitation/separation. Acceleration of factor 2 using SMS (called SMS Factor) is implemented by modulating RF pulse of odd numbered averages by cosine and even numbered averages by sine pulse (with frequency of modulation corresponding to the slice thickness and gap). This result in odd averages as sum and even average as difference of two slices, respectively. There was no need to change the refocusing pulses or decrease flip angles to reduce SAR in this method. The existing hardware RF peak power limits was adhered with no clipping. Additional Fat Saturation, spatial saturation, flow compensation modules are all compatible with the encoding.

Existing slice ordering schemes were adjusted to reduce slice cross

talk effects. Two SMS acquired slices are resolved in image reconstruction by adding and subtracting the odd and even numbered average. It is shown here that the technique blends well with the new DL solutions like ARDL [4].

All acquisitions were performed on a GE HealthCare 1.5T Prime scanner using volume coils. All human subjects were scanned as per study protocol approved by an ethics committee.

## Results

Fig.1 shows axial B/L hip joint T1 weighted DL processed images. Non-SMS image Fig 1(a) is acquired with 2 passes and showed similar image quality as that SMS image Fig 1(b) acquired with single pass and half the scan time (1:28min compared to 3:20min). The TR of 500ms is kept same for both acquisitions. Volunteer was scanned at commercial 1.5T MRI scanner.

## Discussion and Conclusion

Hadamard based SMS has been proven to be quite effective in T1 weighted images acquired using single channel volume coil where parallel imaging based acceleration is not feasible. Since, SMS allow us to complete data acquisition in single pass, the scan time as well as patient motion artifacts get reduced. Deep learning-based reconstruction can help further improvement in image quality in terms of SNR with SMS acquisitions. This version of SMS can also be made compatible with multi-channel FSE acquisition with parallel imaging acceleration that works in tandem with in-plane ARC, Asset or Compressed sensing techniques. The technique is scalable to any SMS integer factor [3].

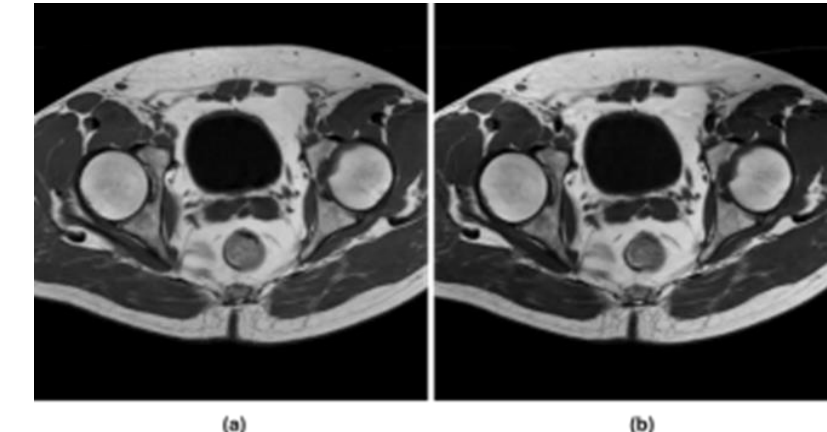


**Figure 1:** DL based Axial T1 weighted image of B/L Hip Joints with TR 500ms (a) no SMS acceleration (3 min 20 sec) b) SMS acceleration (1 min 28 sec)

## References

1. “Simultaneous Multi Slice using Hadamard like encoding with non-Hadamard factors” (2022), #2931, Sudhir Ramanna, et. al, ISMRM Proceedings
2. “Multifrequency Selective rf Pulses for Multislice MR Imaging”, S. Muller, Magn Reson Med 6, 364-371 (1988)
3. “Simultaneous multislice (SMS) imaging techniques”, Markus Barth, Felix Breuer, Peter J. Koopmans, David G. Norris, and Benedikt A. Poser, Magn Reson Med. 2016 Jan; 75(1): 63–81.
4. Lebel RM. Performance characterization of a novel deep learning-based MR image reconstruction pipeline. 2020. arXiv preprint, arXiv:2008.06559.

# Aging Associated White Matter Hyperintensity Increases Caudate and Frontal Horn Distance via Lateral Ventricle Enlargement

Rittika Dutta<sup>1</sup>Ishit Sahoo<sup>1</sup>Archita Khatua<sup>1</sup>Vivek Tiwari<sup>1</sup><sup>1</sup>Indian Institute of Science Education and Research (IISER) Berhampur, India

## Introduction

Changes in brain health with normal aging involve a cascade of brain structure, vascular, and microstructural changes over the period that may have similar or distinct kinetics, order, and magnitude than alterations associated with cognitive impairment. With aging, the brain undergoes structural modifications, including atrophy or shrinkage. Since the caudate nucleus is a part of the brain's circuitry involved in executive functions, memory, and other cognitive abilities, alterations in the size, shape, or distance between the caudate nuclei may potentially impact cognitive behaviors. Simultaneous changes in frontal horn distance are indicative of neurological diseases. Changes in caudate and frontal horn distance may get accelerated in the presence of White Matter Hyperintensity, leading to disrupted communication between brain regions, creating a potential pathway for the transition from normal aging to Mild Cognitive Impairment (MCI) and Alzheimer's Disease (AD). Here, we have investigated the impact of cerebral small vessel disease—specifically, white matter hyperintensity (WMH) load on Caudate and Frontal Horn distance with aging, using brain MRI segmentation and WMH lesion quantification.

## Methods

Brain segmentation was performed on 3D MPAGE and T2-FLAIR images to determine neuroanatomic-volume and White matter hyperintensity (WMH) load in cognitively normal (CN) subjects ( $N=595$ ) from the Alzheimer's Disease Neuroimaging Initiative (ADNI) cohort. Subjects were stratified in 3 age groups: 50-64 years (early), 65-79 years (intermediate), and >80 years (late). Brain region volumes obtained from segmentations were normalized to total intracranial volume (ICV) for each age group using the following equation:

$$V_{\text{norm}} = (V_{\text{estimated}} / V_{\text{ICV}}) \times V_{\text{avg-ICV}}$$

$V_{\text{norm}}$  denotes normalized volume for each age group;  $V_{\text{estimated}}$  is the volume obtained from segmentation, and  $V_{\text{avg-ICV}}$  represents mean ICV. Subjects were further classified into five groups based on WMH load: 0–1 ml, 1–3 ml, 3–5 ml, 5–10 ml, and >10 ml, to explore the impact of WMH on inter-table width (IT), caudate distance (CC), and frontal horn distance (FH), as well as the CC/IT, FH/IT, and FH/CC ratios. Additionally, a mediation model analysis was conducted to examine both the direct and indirect effects of WMH.

## Results

The CC, FH, CC/IT, and FH/IT ratios increase with age in CN subjects, whereas

the FH/CC ratio declines, but IT remains constant (Fig 1B-G). Furthermore, the CN subject showed the enlargement of the lateral ventricle ( $\beta=1.06 \text{ ml/year}$ ,  $p<0.001$ ) with age but caudate volume ( $\beta=0.01 \text{ ml/year}$ ,  $p=0.20$ ) remained constant. However, when WMH load exceeded 3ml, there was a significant increase in CC, CC/IT, and FH/IT ratios and a decrease in FH/CC ratio, with the lateral ventricles mediating alterations in CC ( $\beta=0.011 \text{ ml/year}$ ,  $p<0.01$ ), FH ( $\beta=0.044 \text{ ml/year}$ ,  $p<0.01$ ), CC/IT ( $\beta=0.001 \text{ ml/year}$ ,  $p<0.01$ ), FH/IT ( $\beta=0.001 \text{ ml/year}$ ,  $p<0.01$ ), and FH/CC ( $\beta=-0.009 \text{ ml/year}$ ,  $p<0.01$ ) ratios.

## Discussion

This study explores the relationship between cerebral small vessel disease, brain aging, and white matter hyperintensity (WMH) burden, focusing on the caudate nucleus (CC) and frontal horn (FH) distance. It reveals that age-related WMH growth and ventricular enlargement are progressive, with anatomical alterations observed in cognitively normal (CN) individuals. The caudate distance and frontal horn show significant age-related alterations, indicating neurodegeneration inadvertently leads to ventricular enlargement. However, the caudate volume remains largely constant. WMH load exceeding 3 ml leads to significant alterations in CC, FH, CC/IT, FH/IT, and FH/CC ratios. This suggests that white matter injury may exacerbate age-related structural atrophy. The study highlights the critical role of periventricular white matter integrity in determining the extent of structural changes in older individuals. The findings emphasize the need for further investigation into the underlying mechanisms driving these changes, as well as longitudinal studies incorporating multimodal imaging techniques and cognitive assessments.

## Conclusion

Accumulation of White matter hyperintensity load of more than 3 ml leads to significant changes in Caudate and Frontal horn distance mediated through the enlargement in lateral ventricles. Future research should investigate potential structural indicators—CC/IT, FH/IT, and FH/CC—as predictors of cognitive decline and the onset of mild cognitive impairment (MCI) or Alzheimer's disease (AD).

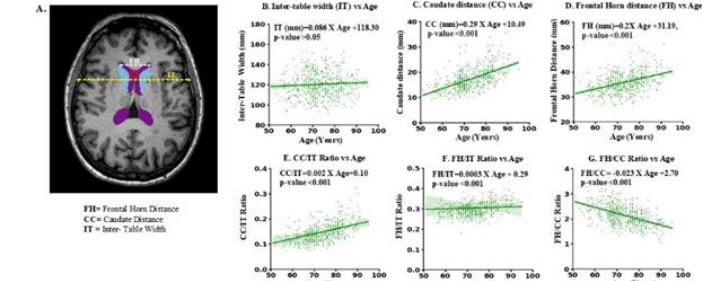


**Figure 1:** (A) Representative T1-weighted axial image of a cognitively normal (CN) brain, illustrating the measurements of frontal horn (FH) distance, caudate (CC) distance, and inner-table (IT) width. (C-G) Linear regression analysis of IT, CC, FH, CC/IT, and FH/IT with age. The analysis was conducted with the age intercept set at 50 years. Statistical significance for the slope and intercept was set at  $p<0.05$ .

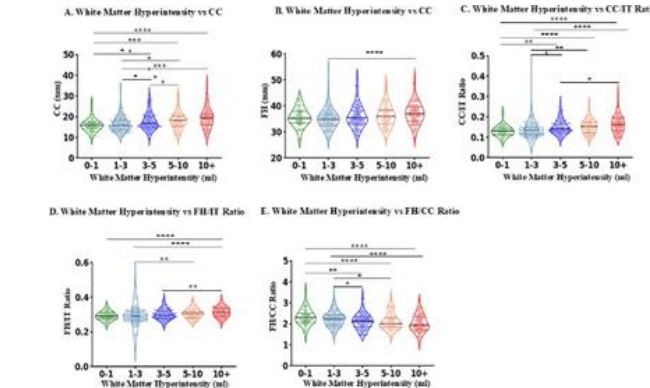


**Figure 2:** Violin plots illustrate the median (solid line) for CC (A), FH (B), CC/IT (C), FH/IT (D), and FH/CC (E) across different White Matter Hyperintensity (WMH) loads. A WMH load exceeding 3 ml is associated with significant changes in neuroanatomic measurements. Statistical differences were analyzed with respect to age. Significance was assessed using Mann-Whitney U tests followed by Bonferroni correction.

## References

- Caçollo A, Dortdivanlioglu B, Rusinek H, Weickenmeier. A multiphysics model to predict periventricular white matter hyperintensity growth during healthy brain aging, *Brain Multiphys*. 2023 May 26:5:100072. doi: 10.1016/j.brain.2023.100072
- Yadav N, Gupta NK, Thakar D, Tiwari V. Magnitude and kinetics of a set of neuroanatomic volume and thickness together with white matter hyperintensity is definitive of cognitive status and brain age, *Translational Psychiatry*, doi: 10.1038/s41398-024-03097-2

# An Artisan Approach to Advanced Head and Neck Imaging

**Dr Hari Kishore Dussa**

Consultant Radiologist; Dr Jwala Srikala Mulugu, Chief Radiologist, Department of Imaging Sciences, Sindhu Hospitals, Hyderabad.

## Introduction

The head and neck constitute a complex anatomical region with some structures sub-millimeter in size. The utilization of a traditional 24-array HN coil presents constraints in obtaining high Signal-to-Noise Ratio (SNR) images, necessitating prolonged scan times for achieving higher resolution imaging, thereby increasing the likelihood of motion artifacts and patient discomfort. 3D ASL imaging was attempted but yielded insufficient perfusion data due to noisy images.

Consequently, the concept of utilizing a surface flex coil, typically employed for body imaging, for the purposes of head and neck imaging was conceived and investigated.

## Methods

An indigenous apparatus was crafted utilizing wood and plastic with a design intended to diminish the distance between the surface coil and the patient's face, preserve adequate ventilation, and attain immobilization. The apparatus was tailored to suspend an 8-ch rectangular phased array small flex coil in an arch configuration anterior to the face, aiming to maximise receiver signal amplitude by

addressing filling factor ( $\eta$ ) and geometry factor ( $g$ ). Imaging experiments so far carried out on 6 healthy volunteers and 3 patients.



## Results

The device helped to obtain thin-slice, high in-plane resolution imaging of the orbits, para-nasal sinuses, oral cavity, and salivary glands within acceptable scan times. Signal-demanding sequences, such as 3D ASL of the tongue, were successfully acquired experimentally.

## Discussion

The optimal utilization of surface array coils for high-resolution imaging of the anterior

head and neck region, without direct face contact, represents a novel approach. Initial results show promising outcomes in terms of patient comfort, immobilization, and high-resolution imaging capabilities that surpass those achieved with the standard 24-channel head and neck coil in comparable scan times.

## Conclusion

This zero-investment coil suspension apparatus enables better images for anatomy and also non-contrast perfusion-weighted imaging of head and neck cancers within reasonable scan times, potentially facilitating comparative analysis of pre- and post-radiation tumor micro-circulation in head and neck malignancies, particularly oral cancers.

# Benchmarking Brain Tumor Segmentation Tools and Insights on Tumor Location in Glioblastoma Survival

**Kavita Kundala, K Venkateswara Raob, Arunabha Majumdar, Neeraj Kumar a,d, Rahul Kumar\***

<sup>a</sup>Department of Biotechnology, Indian Institute of Technology Hyderabad, Kandi, Telangana 502284, India <sup>b</sup>Department of Neurosurgical Oncology, Basavataram Indo American Cancer Hospital & Research Institute, Hyderabad, Telangana 500034, India <sup>c</sup>Department of Mathematics, Indian Institute of Technology Hyderabad, Kandi, Telangana 502284, India <sup>d</sup>Department of Liberal Arts, Indian Institute of Technology Hyderabad, Kandi, Telangana 502284, India

## Introduction

Glioblastoma (GBM) is the most aggressive primary brain tumor, with a median survival of 12–15 months [1]. Invasive molecular characterization is often impractical, making non-invasive imaging, particularly MRI essential for diagnosis and treatment planning [2]. MRI-based tumor segmentation provides critical insights into tumor volume and radiomic features, while understanding location-specific genetic alterations can aid in targeted therapy. This study focuses on two key aspects, identifying the most accurate and robust brain tumor segmentation method and integrating radiomics with genomics to discover non-invasive biomarkers for improved prognosis and treatment strategies.

## Methods

This study benchmarked four CNN-based segmentation models CaPTk, 2DVNet, EnsembleUNets, and ResNet50 using 1,251 GBM subjects from the BraTS 2021 dataset and validated on 611 subjects from the independent UPENN-GBM dataset [3]. Two primary evaluation strategies were employed: direct comparison of segmented tumor regions and radiomic feature analysis using the pyRadiomics library [4]. Model performance was assessed using metrics including Dice Similarity Coefficient (DSC), Hausdorff Distance (HD), Concordance Correlation Coefficient (CCC), Total Deviation Index (TDI), and Root Mean Squared Error (RMSE). The best-performing model was applied to the TCGA-GBM dataset for tumor segmentation. Tumor location-specific survival outcomes were assessed, while genomic and differential expression analyses identified molecular drivers of poor prognosis using R software. Radiomic analysis investigated critical features contributing to survival disparities.

## Results

EnsembleUNets outperformed other methods, achieving a DSC of 0.93 and HD of 18 on the BraTS2021 dataset, with superior radiomic precision confirmed by a CCC of 0.79, TDI of 1.14, and RMSE of 0.53. Validation on the UPENN-GBM dataset further supported these findings, with a DSC of 0.85 and HD of 17.5. Tumor location analysis using the in-house developed tool “tumorVQ” on the TCGA-GBM dataset revealed significantly poorer survival for parietal lobe tumors compared to frontal lobe tumors. Genomic profiling of parietal lobe tumors identified PTEN loss-of-function mutations ( $P < 0.05$ ), FGFR3-TACC3 and EGFR-SEPT14 fusions, and LINC00290 deletions. Differential expression analysis ( $P_{adj} < 0.05$ ) revealed upregulation of PITX2, HOXB13, and DTHD1,

associated with tumor progression, while ALOX15 downregulation was linked to increased relapse risk. Radiomic features, including lower LLL\_GLDMDependanceEntropy (HR = 2.47,  $P = 0.014$ ) and higher HLL\_firstorder\_Mean (HR = 2.90,  $P = 0.025$ ), were strongly associated with poor survival.

## Discussion

This study underscores the importance of accurate tumor segmentation and location-specific analyses in understanding glioblastoma (GBM) heterogeneity and prognosis. EnsembleUNets demonstrated exceptional segmentation performance across BraTS2021 and UPENN-GBM datasets, attributed to its integration of three methods (3D U-Net, 3D MI-U-Net, and 3D+2D MI-U-Net). Its sequential training strategy combines 3D and 2D representations, leveraging multi-modal MR images, BP maps, and probability maps for enhanced accuracy and robustness [5]. Tumor location, radiomic, and genomic analyses revealed the aggressive nature of parietal lobe tumors, driven by PTEN loss-of-function mutations, including missense and frameshift mutations in the PTPc and C2 domains, known to confer resistance to chemotherapeutic drugs. Additional drivers included FGFR3-TACC3 and EGFR-SEPT14 fusions and LINC00290 deletions. Radiomic features, such as lower LLL\_GLDMDependanceEntropy and higher HLL\_firstorder\_Mean, emerged as prognostic imaging markers, while differential expression of PITX2, HOXB13, and DTHD1, and downregulation of ALOX15, highlighted role in activating/altering critical pathways promoting tumor aggressiveness [6]. These findings emphasize integrating radiomic and genomic data to refine prognostic models and enable personalized therapies for GBM.

## Conclusion

EnsembleUNets proved to be the most reliable segmentation model, enabling precise tumor localization and radiomic analysis. Parietal lobe GBM tumors exhibited distinct genomic and radiomic profiles associated with aggressive phenotypes and poor survival outcomes. Key genetic alterations, including PTEN mutations, fusion genes, and LINC00290 deletions, along with critical radiomic features, offer valuable prognostic insights. The integration of imaging biomarkers with genomic data represents a powerful approach for refining GBM prognosis and developing location-specific, personalized therapies. Expanding

radiogenomics datasets and further validating these findings will enhance our understanding of GBM heterogeneity and improve clinical outcomes.

## References:

- [1] M. Duhamel et al., “Spatial analysis of the glioblastoma proteome reveals specific molecular signatures and markers of survival,” *Nat Commun*, vol. 13, no. 1, Dec. 2022, doi: 10.1038/s41467-022-34208-6.
- [2] G. Singh et al., “Radiomics and radiogenomics in gliomas: a contemporary update,” Aug. 31, 2021, Springer Nature. doi: 10.1038/s41416-021-01387-w.
- [3] K. Clark et al., “The Cancer Imaging Archive (TCIA): Maintaining and Operating a Public Information Repository,” *J Digit Imaging*, vol. 26, no. 6, pp. 1045–1057, Dec. 2013, doi: 10.1007/s10278-013-9622-7.
- [4] J. J. M. Van Griethuysen et al., “Computational radiomics system to decode the radiographic phenotype,” *Cancer Res*, vol. 77, no. 21, pp. e104–e107, Nov. 2017, doi: 10.1158/0008-5472.CAN-17-0339.
- [5] K. Kundal, K. V. Rao, A. Majumdar, N. Kumar, and R. Kumar, “Comprehensive benchmarking of CNN-based tumor segmentation methods using multimodal MRI data,” *Comput Biol Med*, vol. 178, p. 108799, Jun. 2024, doi: 10.1016/j.combiomed.2024.108799.
- [6] K. Kundal, N. Kumar, and R. Kumar, “Unravelling the Impact of Tumor Location on Patient Survival in Glioblastoma: A Genomics and Radiomics Approach,” Oct. 04, 2024. doi: 10.1101/2024.10.02.24314823.

# Brain morphological alterations in early-onset and late-onset Parkinson's disease compared to age related healthy controls

Sadhana Kumari<sup>1</sup>Sakshi Arora<sup>1</sup>S Senthil Kumaran<sup>1</sup>Roopa Rajan<sup>2</sup>Achal Kumar Srivastava<sup>2</sup>Departments of NMR<sup>1</sup> and Neurology<sup>2</sup>, All India Institute of Medical Sciences, Ansari Nagar, New Delhi, India

## Introduction

Volume and surface-based atrophy play a significant role in the assessment of progression of Parkinson's disease (PD). Region of interest (ROI)-based structural measures of brain MRI data in early-onset (EOPD) and late-onset (LOPD) provide precise morphological differences between groups.

## Methods

A total of 27 EOPD, 32 young healthy controls (YHC), 28 LOPD, and 27 older healthy controls (OHC) were enrolled for MRI. Regional gray matter volume (GMV), white matter volume (WMV) and surface measures (fractal dimension (FD) and cortical thickness (CT) were assessed using ROI based analysis. Relationship between clinical variables and morphological features were also computed.

## Results

EOPD vs YHC exhibited a reduction in GMV and cortical complexity in frontal, parietal and temporal lobes. In EOPD, a negative correlation of GMV with UPDRS II (in left medial frontal cortex, precuneus and right supplementary motor cortex) were observed (Fig.1 & Table1). These areas showed a significant area under the curve in differentiating EOPD and YHC based on GM volume (Fig.2). FD with UPDRS III in right pericalcarine; GI and UPDRS II in left transverse temporal and pars opercularis; CT with UPDRS III in right superior frontal regions (Table2). Significant results were not seen in LOPD compared to OHC group.

## Discussion

Association of GMV alterations in the left medial frontal cortex, precuneus and the right supplementary motor cortex regions with the UPDRS Part II are closely linked to the severity of motor impairments and impact on daily living activities of EOPD patients.<sup>1,2</sup>

## Conclusion

Study highlights distinct patterns of brain morphometric changes in patients with EOPD. Clinical diagnosis of EOPD may benefit from the use of quantitative morphological estimation with CAT12.

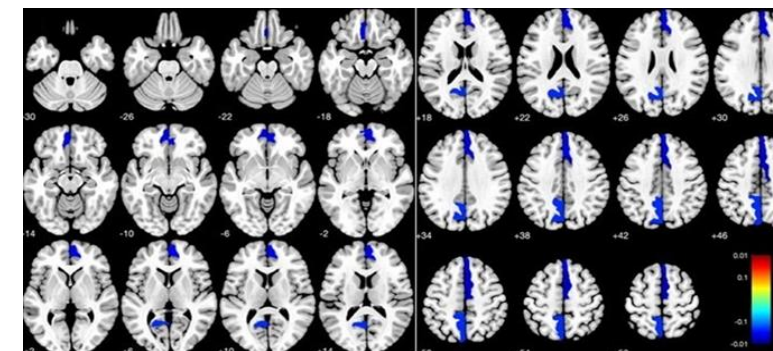


**Figure 1.** Negative correlation between UPDRS II and gray matter volume (GMV) of right supplementary motor cortex, left middle frontal cortex, left precuneus in patients with early onset PD at a significance level of  $p < 0.05$  level of  $p < 0.05$ .

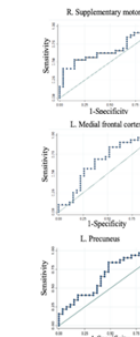


**Figure 2.** ROC curve showing AUC for the mean gray matter volume of right supplementary motor cortex, left medial cortex and left precuneus

**Table 1:** Region of interest (ROI) correlation analysis of gray matter, cortical thickness, gyration index, gyration index and clinical variables in young onset patients with Parkinson's disease (EOPD) and young healthy controls (YHC) using DK-40 atlas.

	Brain Region	Hemisphere	P-value	T-value	Z-value	Clinical Variables
<b>Gray Matter (p&lt;0.05, Holm-Bonferroni corrected)</b>						
Frontal Lobe	Medial Frontal Cortex	Left	0.02	-3.37	-3.01	UPDRS Part II
Parietal	Precuneus	Left	0.04	-2.93	-2.67	UPDRS Part II
Frontal Lobe	Supplementary Motor Cortex	Right	0.02	-4.15	-3.54	UPDRS Part II
<b>Fractal Dimension (p&lt;0.05, Holm-Bonferroni corrected)</b>						
Temporal	Fusiform	Right	0.01	-4.26	-3.62	LEDD
Occipital	Pericalcarine	Right	0.05	-3.55	-3.13	UPDRS Part III
<b>Gyration Index (p&lt;0.05, Holm-Bonferroni corrected)</b>						
Temporal	Transverse Temporal	Left	0.046	-3.38	-3.01	UPDRS Part II
Frontal	Pars Opercularis	Right	0.008	-3.79	-3.31	UPDRS Part II
<b>Cortical Thickness (p&lt;0.05, Holm-Bonferroni corrected)</b>						
Frontal	Superior Frontal	Right	0.03	-2.3	-2.16	UPDRS Part III

## References

- 1.Fioravanti V, Benuzzi F, Codeluppi , et al. MRI correlates of Parkinson's disease progression: A voxel based morphometry study. *Parkinsons Dis.* 2015;378032.
- 2.Radzun A, Deltuva VP, Tamásasukas A, et al. Brain MRI morphometric analysis in Parkinson's disease patients with sleep disturbances. *BMC Neurol.* 2018;18:88.

# Comparative Analysis of U-Net and YOLO Models for Prostate Segmentation using MRI Scans

**Ph. Supriya Devi<sup>1</sup>, Durgesh Kumar Dwivedi<sup>1\*</sup>, Sudhir Kumar Pathak<sup>3</sup>, B. V. Rathish Kumar<sup>2</sup>, Aritrick Chatterjee<sup>7</sup>, Ranjeet Ranjan Jha<sup>4</sup>, Anit Parihar<sup>1</sup>, Apul Goel<sup>5</sup>, Vishwajeet Singh<sup>6</sup>, Sanjoy Sureka<sup>5</sup>, Manoj Kumar<sup>6</sup>, Saurabh Kumar<sup>1</sup>.**

1Department of Radiodiagnosis, King George's Medical University, Lucknow, India, 2Department of Mathematics and Statistics, Indian Institute of Technology, Kanpur, India, 3Learning Research and Development Center, University of Pittsburgh, Pittsburgh, PA, United States, 4Department of Mathematics, Indian Institute of Technology, Patna, India, 5Department of Urology, Sanjay Gandhi Postgraduate Institute of Medical Science, Lucknow, India, 6Department of Urology, King George's Medical University, Lucknow, India, 7Department of Radiology, University of Chicago, Chicago, USA.

## Introduction

Prostate cancer remains a major global health concern, with the U.S. reporting 2 million new cases and 0.61 million deaths, while India recorded 37,948 cases and 18,386 fatalities, ranking among the top ten for incidence in 2024 [3]. Accurate segmentation of the prostate, particularly the peripheral zone (PZ), is crucial for diagnosis and treatment, including radiotherapy.

Manual segmentation is challenging due to the prostate's complex structure and poor MRI contrast, leading to subjectivity, inconsistency, and time consumption. Artificial Intelligence (AI) automates prostate segmentation, ensuring consistency and reproducibility. U-Net, a fully convolutional neural network, excels in pixel-wise accuracy, while YOLO (You Only Look Once) models are optimized for real-time inference. This study compares U-Net and YOLO models for prostate segmentation.

## Methods

This study used publicly available datasets from The Cancer Imaging Archive (TCIA) [1]. Data were pre-processed to match model input requirements. A U-Net model was trained for segmentation, while YOLO versions 8, 9, and 11 were used for instance segmentation with tailored data. Model performance was evaluated using the mean Dice Score, measuring overlap between predictions and ground truth. Inference times were also recorded to assess computational efficiency.

## Results

U-Net achieved the highest segmentation accuracy with a Dice score of 0.8451, capturing fine anatomical details. Among YOLO models, YOLO v11 performed best with a Dice score of 0.8445, closely matching U-Net. YOLO v8 and v9 scored 0.8416 and 0.8434, respectively. Notably, YOLO models had shorter inference times, making them suitable for real-time use. While U-Net generated more precise segmentation masks, YOLO balanced accuracy with speed, benefiting time-sensitive applications.

## Discussion

Our results highlight a trade-off between accuracy and computational

efficiency. U-Net demonstrated superior accuracy for prostate segmentation, achieving a Dice score of 0.8451, making it reliable for detailed anatomical delineation. YOLO models delivered competitive performance with faster inference, particularly YOLO v11, which approached U-Net accuracy while maintaining efficiency. These trade-offs align with prior studies like Kot et al. [2], which emphasized U-Net's accuracy dominance and YOLO's real-time suitability.

Clinically, YOLO models could enhance time-sensitive workflows like intraoperative guidance, while U-Net remains preferable for detailed segmentation. This study uniquely compares multiple YOLO versions with U-Net, providing insights into their strengths and limitations. Future research may explore hybrid models combining U-Net's precision with YOLO's speed for optimized performance.

## Conclusion

AI-driven models like U-Net and YOLO improve prostate segmentation for cancer diagnosis and treatment. U-Net offers higher accuracy, making it ideal for precision tasks, while YOLO's speed suits real-time use. Future work will explore hybrid models to balance accuracy and efficiency, enhancing prostate imaging.

## Acknowledgment:

Dr. D.K. Dwivedi and Prof. B.V. Rathish Kumar express their profound gratitude to the Indian Council of Medical Research (ICMR), New Delhi for their generous funding (Grant No. EM/Dev/IG/27/0337/2023). Furthermore, Prof. B.V. Rathish Kumar (IITK, India) and Dr. S.K. Pathak (Pitt, USA) extend their heartfelt appreciation to SPARC for their funding support (Grant No. SPARC/2019-2020/P1622/SL). Additionally, Dr. D.K. Dwivedi sincerely acknowledges the financial support provided by UPCST (Grant No. CST/D-1381). Dr. D.K. Dwivedi also conveys sincere thanks to the Science and Engineering Research Board (now ANRF), New Delhi for their valuable funding support under Grant No. SUR/2022/001841).

Model	Mean Dice Score	Inference Time
Yolo v8	0.8416	0.0755
Yolo v9	0.8434	0.3984
Yolo v11	0.8445	0.133
Unet	0.8451	0.6883

**Table 1:** Comparison of U-Net and YOLO models in prostate segmentation. U-Net had the highest Dice score (0.8451) but the longest inference time (0.6883s). YOLO models processed faster, with YOLO v8 being the quickest.

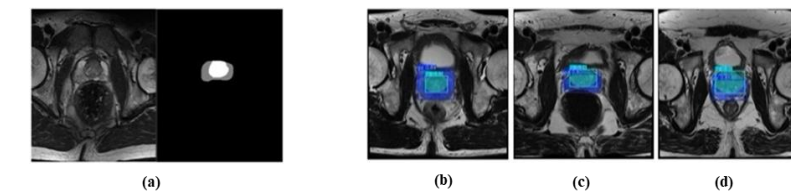


**Figure (a)** shows the U-Net segmentation output with the original MRI image alongside its binary mask. **Figures (b), (c), and (d)** display the outputs of YOLO v8, v9, and v11, respectively, with bounding boxes and predicted regions overlaid on the MRI scans, highlighting their segmentation performance.

## References

1. The Cancer Imaging Archive (TCIA). Available from: <https://www.cancerimagingarchive.net/>
2. Kot E, Les T, Krawczyk-Borysiak Z, Vykhodtsev A, Siwek K. Semantic segmentation of the prostate based on one-fold and joint multimodal medical images using YOLOv4 and u-net. Applied Sciences. 2024 Oct 27;14(21):9814.
3. Siegel RL, Giaquinto AN, Jemal A. Cancer statistics, 2024. CA: a cancer journal for clinicians. 2024 Jan;74(1):12-49.

# Comparison of Pancreatic T1, T2, T2\* & PDFF values between normal, patients with acute, chronic and history of pancreatitis

Monica Gunasingh<sup>1,2</sup>, Nikhil Suryadevara<sup>3</sup>, Suvarna Naidu<sup>3</sup>, Tharani Putta<sup>3</sup>, Sashidhar Kaza<sup>3</sup>, Jithin Sreekumar<sup>1</sup>, and Jaladhar Neelavalli<sup>1</sup>

<sup>1</sup>Biomedical Engineering, Indian Institute of Technology, Hyderabad, India, <sup>2</sup>Philips India Limited, Chennai, India, <sup>3</sup>Department of Radiology, Asian Institute of Gastroenterology, Hyderabad, India

## Introduction

Pancreatitis is an inflammatory condition of the pancreas that can range from mild to severe. Acute pancreatitis (AP) presents as a sudden onset of inflammation, while chronic pancreatitis (CP) is characterized by persistent inflammation. Although CT is the primary imaging modality for evaluating AP, MRI offers significant advantages, including superior soft tissue contrast and the absence of ionizing radiation [1]. The tissue relaxation properties—T1, T2, and T2\* relaxation times—of the pancreatic parenchyma can reveal subtle disease changes that may not be visible to the naked eye [2-5]. Previous studies have examined T1 in combination with proton density fat fraction (PDFF) or T1 and T2 in chronic pancreatitis versus normal subjects. However, these values have not yet been reported in patients with acute pancreatitis. This study aims to compare the T1, T2, T2\*, and PDFF in patients with AP and CP, with both normal subjects and individuals who have recovered from a prior episode of pancreatitis to help identify if multiparametric MRI of pancreas can reveal tissue properties which are not apparent to the naked eye on conventional MRI sequences and can help assess pancreatic health, identify subclinical disease and potentially predict the nature course of illness.

## Materials and Methods

Informed consent was with the approval of the local institutional review board. Data was collected prospectively between September and October 2024, and imaging data from a total of 96 patients were included in the study, out of which 39 (64 % male) had normal appearing pancreas with no prior history of pancreatitis, 18 (67 % male) with history of pancreatitis but with normal appearing pancreas, 16 (81 % male) with acute and 23 (83 % male) with chronic pancreatitis (categorized in accordance with Revised Atlanta Classification and American Pancreatic Association). T1, T2, T2\* and PDFF measurements were performed on patients who underwent a clinically indicated abdominal MRI (Figure 1). Measurements were performed using vendor-provided relaxometric techniques on a Philips 3.0T Elition X system. Figure 2 outlines the seq. parameters. Pancreatic relaxation parameters were measured using ROIs that were placed under the guidance of an experienced body imaging radiologist. Fluid-containing ducts were avoided in the ROIs. The ROIs were placed in three different areas within the pancreas – in the head, body and the tail regions. The mean of the three ROIs was taken to obtain an average value for the pancreas. A one-way ANOVA test followed by a Tukey-Kramer post-hoc test was performed to evaluate the statistical differences between the 4 groups. For instances where the differences between the groups were found to be significant, further statistical evaluation using the same statistical test was performed to see whether the differences came from the head/body/tail of the pancreas.

## Results

The mean and standard deviations of T1, T2, T2\* and PDFF were measured across all groups. T1 values between AP and CP were significantly different from the normal and NPHP groups. There was no statistical difference in T1 of Normal and the NPHP groups. T2 showed statistical differences between the CP and the normal group alone. There was no statistical difference between T2\* values across the groups. In group pairs where T1 and T2 relaxation values showed significant differences, we found that the difference was coming from at least 2 segments of the pancreas (among head, body and tail regions). In PDFF, only the normal group had a significantly different (higher) value compared with the other groups. However, individual regions of the pancreas did not show a significant difference among the same groups in PDFF.

## Discussion and Conclusion

T1, T2, T2\* and PDFF among AP, CP, normals and normals with prior history of pancreatitis was studied. In general, we found that T1 and T2 values are significantly higher among the patient groups (chronic & acute combined) compared to the normal groups (normals & NPHP combined). The higher values may be due to the presence of fibrosis or oedema. Furthermore, T1 (but not T2) values in patients with CP were significantly higher than in AP patients. These observations are in line with previous studies. [7-9] Interestingly, T2\* values did not show any difference among the groups. This may be due to the competing effects of fibrosis (increasing T2\*) and microscopic calcification (decreasing T2\*). Additionally, no significant difference was found between the normal group and the NPHP group, indicating that structural differences that may be resulting from a prior episode of pancreatitis are not detectable with MR.

In conclusion, we find that T1 and T2 values remain the key quantitative MR parameters that can be helpful in identifying subclinical disease.

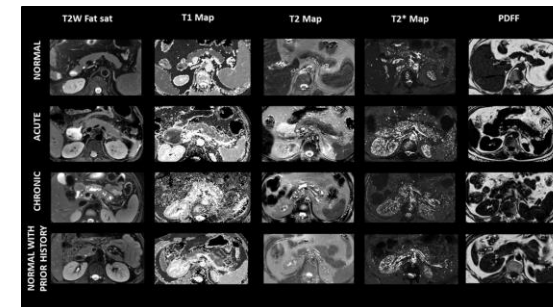


**Figure 1:** representative images of T2 Weighted fat suppression, T1, T2, T2\* and PDFF in a normal subject, a patient with acute pancreatitis, chronic pancreatitis and a normal subject with a prior history of pancreatitis. Note that orientation of the T2FatSat and the quantitative maps is slightly different. All quantitative parametric maps were acquired with the same planning geometry.

Sequence	FOV AP*RL*FH (mm)	Voxel Size AP*RL*FH (mm)	TR (ms)	TE (*no of echoes)	Flip Angle	TSE/TFE factor	/Delta TE (ms)	Slice Thickness (mm)	Slice Gap/Overlap (mm)
T1 relaxation	400*400*18	1.3*1.3*6	3	1.36	20	150 (TFE)	6	0	
T2 relaxation	300*300*15	1.5*1.5*5	1000	9*12	90	9 (TSE)	5	0	
T2* relaxation	350*350*15	1.5*1.5*3	19	1.49*16	25	1.1 (Delta TE)	3	0	
mDixon Quant	300*252*44	1.2*1.2*4	8.6	1.42	3	1.2 (Delta TE)	2	-2	

**FIGURE 2:** Parameters of the relaxation time measurement sequences. FOV - Field of View, TR- Repetition time, TE- Echo time, TFE- Turbo Field Echo, mDixon- Multi-point Dixon. The sequences were cardiac and respiratory gated. The sequence was accelerated using a SENSE factor of 2.5 and oversampling of 120 mm in the phase (Antero-posterior) direction. The T1 relaxation sequence is an inversion recovery (IR) sequence with TFE pre-pulse, an IR delay of 350ms and minimum TI (Inversion Time) delay of 266 ms. The T2 relaxation sequence employs 9 echoes, EPI (Echo Planar Imaging) read-out with an EPI factor of 7.

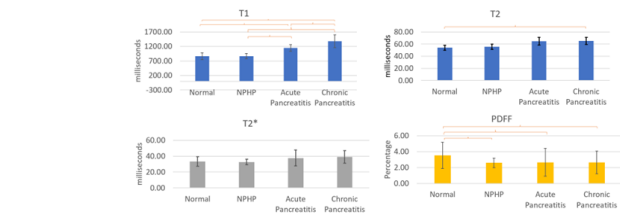


**FIGURE 3:** Bar plot of the mean T1, T2, T2\* and PDFF values of the pancreas in patients with AP, CP, normal subjects and subjects who had prior episode of pancreatitis (NPHP). Statistically significant differences have been observed in the plot.

## References

- Manikkavasakar, S. (2014). Magnetic resonance imaging of pancreatitis: An update. *World Journal of Gastroenterology*, 20(40), 14760. <https://doi.org/10.3748/wjg.v20.i40.14760>
- Milner, F. H., Kepkele, A. L., Dalal, K., Ly, J. N., Kanler, V.-A., & Sica, G. T. (2004). MRI of Pancreatitis and Its Complications: Part 1. Acute Pancreatitis. *American Journal of Roentgenology*, 183(6), 1637–1644. <https://doi.org/10.2214/ajr.183.6.01831637>
- Hill, D. V., & Tirkes, T. (2020). Advanced MR Imaging of the Pancreas. *Magnetic Resonance Imaging Clinics of North America*, 28(3), 353–367. <https://doi.org/10.1016/j.mric.2020.03.003>
- Siddiqui, N., Vendrami, C. L., Chatterjee, A., & Milner, F. H. (2018). Advanced MR Imaging Techniques for Pancreas Imaging. *Magnetic Resonance Imaging Clinics of North America*, 26(3), 323–344. <https://doi.org/10.1016/j.mric.2018.03.002>
- Belleù, A., Canonico, D., & Morana, G. (2024). T1 and T2-mapping in pancreatic MRI: Current evidence and future perspectives. *European Journal of Radiology Open*, 12, 100572. <https://doi.org/10.1016/j.ejro.2024.100572>
- Steinkohl, E., Olesen, S. S., Hansen, T. M., Drewes, A. M., & Jens Brøndum Frøkjær. (2021). T1 relaxation times and MR elastography-derived stiffness: new potential imaging biomarkers for the assessment of chronic pancreatitis. *Abdominal Radiology*, 46(12), 5598–5608. <https://doi.org/10.1007/s0261-021-03276-5>
- Tirkes, T., Lin, C., Fogel, E. L., Sherman, S. S., Wang, Q., & Sandrasegaran, K. (2016). T1 mapping for diagnosis of mild chronic pancreatitis. *Journal of Magnetic Resonance Imaging*, 45(4), 1171–1176. <https://doi.org/10.1002/jmri.25428>
- Violà, N. V., Hilbert, T., Bastiaansen, J. A. M., Knebel, J., Ledoux, J., Stemmer, A., Meuli, R., Kober, T., & Schmidt, S. (2019). Patient respiratory-triggered quantitative T2 mapping in the pancreas. *Journal of Magnetic Resonance Imaging*, 50(2), 410–416. <https://doi.org/10.1002/jmri.26612>

# Characterizing Metabolic Changes in Early-Stage CKD For Improved Diagnosis and Personalized Treatment

**Upasna Gupta<sup>1,2</sup>, Amrita Sahu<sup>1,2</sup>, Dharmendra Singh Bhaduria<sup>3</sup>, Bikash Baishya<sup>1,2</sup>, Neeraj Sinha<sup>1, 2\*</sup>.**

<sup>1</sup>Centre of Biomedical Research, Sanjay Gandhi Post Institute of Medical Sciences Campus, Raebareli Road, Lucknow, Uttar Pradesh, 226014, India. <sup>2</sup>Academy of Scientific and Innovative Research (AcSIR), Ghaziabad- 201002, India

<sup>3</sup>Department of Nephrology and Renal Transplantation, Sanjay Gandhi Postgraduate Institute of Medical Sciences, Lucknow, Uttar Pradesh, 226014, India.

## Introduction

The progressive illness known as chronic kidney disease (CKD) can often be challenging to diagnose in its early stages with conventional diagnostic approaches such as serum creatinine and albumin assessment. Identifying possible biomarkers for early detection and personalized treatment, as well as physiological changes linked to early CKD—an area that hasn't been fully investigated before—is the goal of this study to address this gap.

## Methods

This study presents a metabolomic analysis of 115 human samples using <sup>1</sup>H nuclear magnetic resonance (NMR), which includes 24 healthy controls and 91 patients with early-stage chronic kidney disease (CKD). To identify metabolites that distinguish early-stage CKD, a combination of univariate and multivariate statistical techniques was applied, including the Student T-test, ANOVA, PCA, PLS-DA, and OPLS-DA.

## Results

Myoinositol, pyruvate, creatinine, carnitine, phenylalanine, tyrosine, histidine, 2-hydroxyisobutyrate, and 3-hydroxyisobutyrate were among the eleven different metabolites that shown significant changes ( $p < 0.05$  and  $VIP > 1$ ) within early-stage CKD stages (G1 vs. G2, G2 vs. G3A, and G3A vs. G3B). To assess their diagnostic potential, ROC analysis was performed, revealing an  $AUC > 0.7$  (95% CI). Furthermore, pathway analysis using the KEGG database highlighted significant correlations between specific metabolite patterns and key metabolic pathways, including the metabolism of inositol phosphate, tyrosine, histidine, pyruvate, tryptophan, and phenylalanine, which were found to be relevant in early-stage CKD with statistical significance greater than 0.1.

## Discussion

As the diseases and its related metabolic alterations progress over time, our research is the first to pinpoint a unique metabolomic signature that distinguishes the early stages of chronic kidney disease. Our knowledge of the early stages of metabolic pathway disturbances and the progression of CKD is improved by this research. Changes in these metabolic pathways over time may allow us to identify early signs of deteriorating kidney function and forecast how the disease may develop and allow for earlier therapies to stop or prevent its progression.

## Conclusion

This study highlights potential biomarkers for the early detection of CKD, providing important insights into the biological mechanisms underlying the disease's progression and opening the door to personalized treatment strategies aimed at preventing further kidney damage.

# Comparative analysis of cardiac strain and ejection fraction in dilated and hypertrophic cardiomyopathy patients using MR imaging

Jithin Sreekumar<sup>1</sup>, Monica Gunasingh<sup>1,2</sup>, Rolla Krishna Narayana<sup>3</sup>, Sashidhar Kaza<sup>4</sup>, Jaladhar Neelavalli<sup>1</sup>, and Bhairavi Pramod Reddy<sup>4</sup>

<sup>1</sup>Biomedical Engineering, Indian Institute of Technology, Hyderabad, Hyderabad, India, <sup>2</sup>Philips India Limited, Chennai, India, <sup>3</sup>Philips India Limited, Bangalore, India, Radiology, <sup>4</sup>Asian Institute of Gastroenterology, Hyderabad, India.

## Introduction

Compared to conventional measures like ejection fraction, cardiac based strain measurements have emerged as a sensitive clinical tool in functional assessment of the myocardium [1,2,6]. Echocardiography-based strain evaluation is widely used clinically, yet its accuracy varies with operator expertise, whereas cardiac magnetic resonance imaging (CMR) ensures reliable and operator-independent strain quantification [2,5]. Despite the advantages, cardiac based strain evaluation remains largely unreported in the Indian population. Previous studies have primarily focused on CMR-based strain evaluation to assess myocardial deformation in patients with hypertrophic cardiomyopathy (HCM) [3,4]. The current study aims to evaluate the differences in cardiac strain and its relation to ejection fraction (EF) between patients with Hypertrophic Cardiomyopathy (HCM), Dilated Cardiomyopathy (DCM), and control subjects. Feature tracking (CMR-FT) based algorithm was used for the cardiac strain measurements.

## Methods

We conducted a retrospective study analyzing clinical and imaging data from 224 subjects imaged between 2022 and 2023, including 98 HCM patients (median age 54, IQR 23, 17% women) and 99 DCM patients (median age 53, IQR 19.5, 36% women) and 27 controls (median age 41, IQR 20.5, 15% women). The inclusion criteria for HCM and DCM groups was based on the clinical diagnosis which was arrived at using structural MRI, echocardiography and electrocardiography (ECG) measurements, along with relevant clinical parameters. The control group included patients diagnosed with clinical cardiovascular symptoms but normal structural CMR and EF. All subjects underwent CMR on a 1.5T scanner (Ingenia, Philips). The imaging protocol included steady-state free precession cine images in two long-axis views and continuous short-axis slices covering the entire left ventricle. Strain parameters (Global Radial Strain, Global Circumferential Strain, and Global Longitudinal Strain) were assessed via CMR-FT using vendor supplied software (ISP Ver. 12, Philips). One-way ANOVA with post-hoc analysis was used to evaluate group differences, and linear regression was used for analysing correlations between strain parameters and EF. Table 1 shows the sequence parameters used for the cardiac MR Cine protocol.

## Results

Significant differences were observed in the correlation of different strain measures with ejection fraction across the three patient groups. The R value for GRS, GCS and GLS w.r.t ejection fraction was 0.184, 0.188, 0.13 for HCM patients, 0.57, 0.75, 0.70 for DCM patients and 0.27, 0.17, 0.21 for control subjects respectively (See Figure 1). Using Fischer's z-test, statistically significant differences were observed in the R values for GRS, GCS and GLS, between HCM-DCM and DCM-Control groups, except for the GRS values between DCM and Control group. However, no statistically significant differences were found between the HCM and Control groups. The box plot in Fig. 2 demonstrates the

differences in GRS, GCS, and GLS values between HCM, DCM, and healthy subjects. One-way ANOVA followed by Tukey-Kramer post-hoc analysis indicated that all strain parameters, except for GLS between HCM and DCM patients, showed statistically significant differences ( $p < 0.001$ ).

## Discussion

We evaluated the differences in strain vs. EF relationship between HCM, DCM and control group. We believe this is the first such study in the Indian population. DCM patients showed a stronger correlation with EF, compared to HCM patients and control subjects. This aligns with clinical observations, where an abnormal strain in HCM patients doesn't necessarily correspond to an abnormal EF, suggesting potential compensatory mechanisms that helps in preserving EF. Within the DCM and HCM groups, GCS showed slightly stronger correlation with the EF compared to GLS. This may be due to the significant involvement of the circumferential layer in addition to longitudinal fibers.

## Conclusion

CMR-FT based strain measures could serve as an early indicator for risk stratification, especially in HCM patients.

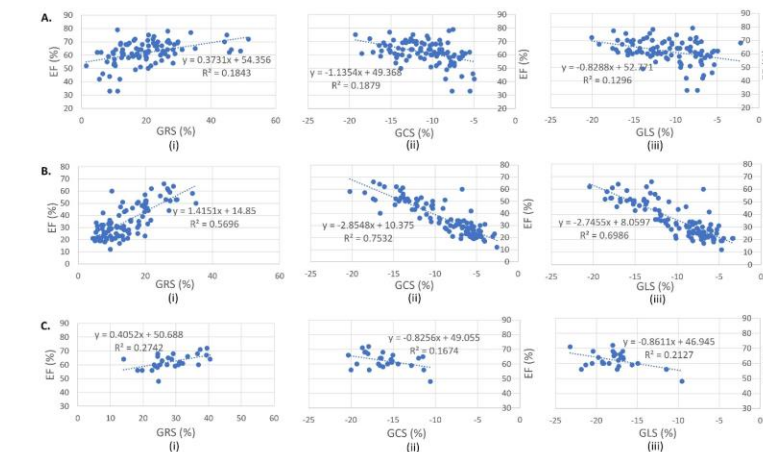


**Figure 1:** Correlation between different strain parameters and the corresponding Ejection Fraction for A. HCM, B. DCM and C. Control subjects. Statistically significant differences in  $R^2$  values for GRS, GCS, and GLS were identified using Fisher's z-test between the HCM-DCM and DCM-Control groups, except for GRS between the DCM and Control groups.

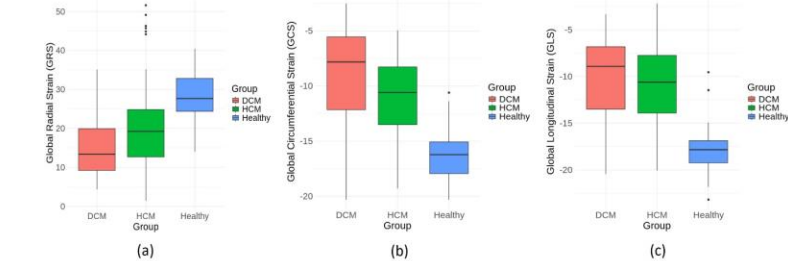


**Figure 2:** The box plots for (a) GRS, (b) GCS and (c) GLS for all HCM, DCM and Control subjects. All the strain values, except for GLS between DCM and HCM, showed significant difference between the groups.

Sequence	FOV (mm)	Voxel Size (mm)	TR (ms)	TE (ms)	Flip Angle	Acq Heart Phases/ Recon Heart Phases	Breath-hold Duration (seconds)	Slice Thickness (mm)
sBTFF_BH_SA	300*300*138 (FH*AP*RL)	1.95*1.94*6 (FH*AP*RL)	3.1	1.54	60	25/39	9	6
sBTFF_BH_2Ch	300*300*40 (FH*RL*AP)	1.8*1.8*8 (FH*RL*AP)	3.1	1.57	60	22/33	9	8
sBTFF_BH_4Ch	300*300*40 (RL*AP*FH)	1.8*1.8*8 (RL*AP*FH)	3.5	1.75	60	24/33	10	8

**Table 1:** Parameters of the cardiac MR Cine protocol- SA- Short Axis, 2Ch- 2 Chamber View, 4Ch- 4 Chamber view, FOV- Field of View, TR- Repetition time, TE- Echo time, SENSE P reduction Factor of 2, oversampling of 110mm.

## References

- Smiseth, O.A., Torp, H., Opdahl, A., Haugaa, K.H. and Urheim, S., 2016. Myocardial strain imaging: how useful is it in clinical decision making? European heart journal, 37(15), pp.1196-1207.
- Rajiah, P.S., Kalisz, C., Broncano, J., Goerne, H., Collins, J.D., François, C.J., Ibrahim, E.S. and Agarwal, P.P., 2022. Myocardial strain evaluation with cardiovascular MRI: physics, principles, and clinical applications. Radiographics, 42(4), pp.968-990.
- Salmanipour, A., Ghaffari Jolfaei, A., Sabet Khadem, N., Rezaeian, N., Chalian, H., Mazloomzadeh, S., Adimi, S. and Asadian, S., 2023. The predictive value of cardiac MRI strain parameters in hypertrophic cardiomyopathy patients with preserved left ventricular ejection fraction and a low fibrosis burden: a retrospective cohort study. Frontiers in Cardiovascular Medicine, 10, p.1246759.
- Pu, C., Fei, J., Lv, S., Wu, Y., He, C., Guo, D., Mabombo, P.U., Chooh, O. and Hu, H., 2021. Global circumferential strain by cardiac magnetic resonance tissue tracking associated with ventricular arrhythmias in hypertrophic cardiomyopathy patients. Frontiers in Cardiovascular Medicine, 8, p.670361.
- Obokata, M., Nagata, Y., Wu, V.C.C., Kado, Y., Kurabayashi, M., Otsuji, Y. and Takeuchi, M., 2016. Direct comparison of cardiac magnetic resonance feature tracking and 2D/3D echocardiography speckle tracking for evaluation of global left ventricular strain. European Heart Journal-Cardiovascular Imaging, 17(5), pp.525-532.
- Brady, B., King, G., Murphy, R.T. and Walsh, D., 2023. Myocardial strain: A clinical review. Irish Journal of Medical Science (1971-), 192(4), pp.1649-1656.

# Comparative Analysis of Existing Deep Learning Models and New Approaches for Brain Tumor Segmentation in MRI Scans

Sankar Narayan Misra<sup>1, 2</sup>, Subhanon Bera<sup>1, 2</sup>, Archith Rajan<sup>3</sup>, Suyash Mohan<sup>3</sup>, Harish Poptani<sup>4</sup>, Sanjeev Chawla<sup>3</sup>, Sourav Bhaduri<sup>1, 2</sup>

<sup>1</sup>Institute for Advancing Intelligence, TCG Centres for Research and Education in Science and Technology, <sup>2</sup>Academy of Scientific and Innovative Research (AcSIR) India, <sup>3</sup>Department of Radiology, University of Pennsylvania, Philadelphia, USA, <sup>4</sup>Centre for Preclinical Imaging, University of Liverpool, Liverpool, UK.

## Introduction

Accurate segmentation of brain tumors from Magnetic Resonance Imaging (MRI) scans is crucial for diagnosis, monitoring disease progression, and formulating treatment strategies. While traditional methods are labor-intensive, advanced deep-learning techniques are being explored for more efficient and precise segmentation. In this study, we compare the performance of five state-of-the-art segmentation models: U-Net, nnU-Net, Attention-U-Net, ELU-Net and U-Net++ [1-7], using the BraTS[8-9] and a private experimental dataset consisting of T2-FLAIR (Fluid-Attenuated Inversion Recovery) and Post-Contrast T1-weighted MRI scans. We further do some fine tuning on the best model by modifying the activation functions and derive two more models. We evaluate the model performances based on Dice and Jaccard scores [10-11], with nnU-Net consistently achieving the highest accuracy among existing models, but our models are able to get better accuracy particularly after transfer-learning on the experimental dataset.

## Methods

The BraTS datasets contain MRI scans (from the year 2019-2021) from 19 institutions stored in NIfTI format. We've used post-contrast T1-weighted (T1PC) and T2-FLAIR modalities for training different UNet models [Table I]. Expert neuro-radiologists validated manual annotations, marking three regions: Necrotic and non-enhancing tumor core, Enhancing tumor region, and Peritumoral edema. A private MRI dataset of 64 glioblastoma (GBM) patients with 2,400 slices was acquired at the University of Pennsylvania under a collaboration with TCG CREST (data sharing ID: RIS76150) using a 3T Tim Trio MR scanner. High-resolution post-contrast T1-MPRAGE and T2-FLAIR images were coregistered to lower-resolution Diffusion Tensor Imaging (DTI) - B0 images, with a resolution of 128x128x35, as part of a continuation of a project focused on quantitative MR imaging, resulting in lower-resolution images being used for segmentation. Using a semi-automated algorithm, lesions were segmented into Contrast-enhancing (ET), Non-enhancing (NCR), and Edema [12]. This is used as a ground truth. Manual skull stripping was necessary as automated tools struggled with the lower-resolution images. We used Adam optimizer with learning rate 0.001, Binary Cross-Entropy as the loss function for 100 epochs. We trained the first model on BraTS dataset with 20,000 slices for training and 4,000 slices for validation, while for transfer learning we considered 2,000 slices for training and 400 slices for validation from the private dataset. We evaluate the model's performance using the Dice score and Jaccard Index [13-16]. We derived two new models PReLU-Net & Weighted ReLU-Net by modifying the activation function of nnU-Net. In PReLU-Net, we replaced the LeakyReLU activation in nnUNet with PReLU. Similarly, in Weighted ReLU-Net, we substituted the LeakyReLU in nnUNet with a weighted sum of PReLU and ReLU. Here the weights are also trainable parameters.

## Results

On the BraTS validation dataset [Fig 1] [Table II], nnU-Net, PReLU-Net & Weighted ReLU-Net achieved the highest performance with a Dice score of 88.95%, 88.96% and 88.91% respectively, followed by AttentionUNet and U-Net++. ELU-Net performed slightly lower, while standard U-Net had the lowest score. When tested on the private dataset [Table II], performance dropped, with Dice scores between 59% and 65%. nnU-Net & Weighted ReLU-Net remained the top performers, followed by U-Net++ and Attention-U-Net. To address the performance drop, transfer-learning was applied in three phases: retraining the last decoder stage, the last two decoder stages, and all decoder stages [Fig 2]. Retraining only the last decoder stage improved Dice scores to 67%-74%, with Weighted ReLU-Net performing best [Table III]. Retraining the last two decoder stages led to a significant boost for nnU-Net, achieving an 82.98% Dice score, with other models also improving. After retraining all decoder stages, most models exceeded 80% Dice score, with Weighted ReLU-Net reaching the highest performance at 85.65%.

## Conclusion

On the BraTS dataset, nnU-Net was the top performer among the existing models, achieving a Dice score of 88.95% and a Jaccard score of 80.43% [Table II]. Attention-U-Net and U-Net++ also performed well, but nnU-Net consistently outperformed them due to its robust self-adaptive framework [17-18]. Observing these strengths of nnUNet architecture, we modified the activation function of nnUNet and derived two new models PReLU-Net & Weighted ReLU-Net to improve the accuracy further. On the private dataset, all models saw a performance drop, with Weighted ReLU-Net and nnUNet leading with a Dice score of 64.60% and 64.07% resp. This variation highlights the challenges of applying models across datasets with different characteristics and emphasizes the importance of domain adaptation strategies. Retraining experiments indicated that performance improvements were most significant when all decoder stages were retrained. Weighted ReLU-Net and Attention-U-Net exhibited notable gains, with Weighted ReLU-Net achieving a Dice score of 85.65% on the private dataset after complete retraining [Table III]. This suggests that using a combination of multiple activation function enhances model generalization and performance across different datasets. A learned combination of activation functions can help maintain stable gradients and improve training efficiency. Using deep-learning models for tumor segmentation aids in accurately determining tumor volume, crucial for assessing post-treatment related changes. Training on BraTS and transfer-learning on private data are necessary due to the lack of publicly available post-treatment MRI datasets. This study has several limitations. First, model performance on the private dataset showed a significant drop compared to the BraTS dataset, suggesting issues with dataset-specific generalization. Second, the small sample size of the private dataset limits the robustness of our findings. The low image resolution used for the private dataset and ground truth ROIs required predictions on these low-resolution images, leading to the manual skull-stripping that may have affected segmentation accuracy. Finally, GPU limitations prevented training with 3D images. Future studies will focus on drawing ROIs on high-resolution images for predictions.

## References

- [1] O. Ronneberger, P. Fischer, and T. Brox, "U-Net: Convolutional Networks for Biomedical Image Segmentation," in Medical Image Computing and Computer-Assisted Intervention—MICCAI 2015: 18th International Conference, Munich, Germany, October 5–9, 2015, Proceedings, Part III, vol. 18, pp. 234–241, Springer International Publishing, 2015.
- [2] S. Oktay, J. Schlemper, L. J. Folgar et al., "Attention-U-Net: Learning Where to Look for the Pancreas," in Medical Image Computing and Computer-Assisted Intervention—MICCAI 2018, vol. 11071, pp. 1–9, Springer, 2018, doi: 10.1007/978-3-030-00934-2\_1.
- [3] F. Isensee, J. Jäger, J. A. Full, S. W. C. W. A. S. G. F. M. K. H. and R. M., "nnU-Net: Self-adapting Framework for U-Net-Based Medical Image Segmentation," in arXiv preprint arXiv:1809.10486, 2020.
- [4] Y. Deng, Y. Hou, J. Yan, and D. Zeng, "ELU-Net: An Efficient and Lightweight U-Net for Medical Image Segmentation," in IEEE Access, vol. 10, pp. 35932–35941, 2022, doi: 10.1109/ACCESS.2022.3163711.
- [5] J. Zhou, R. Yang, L. Yang, Z. Dong, and S. Zhang, "U-Net++: A Nested U-Net Architecture for Medical Image Segmentation," in IEEE Transactions on Medical Imaging, vol. 39, no. 6, pp. 1856–1865, June 2020, doi: 10.1109/TMI.2019.2959601.
- [6] Hatamizadeh, A., Tang, Y., Nath, V., Yang, D., Myronenko, A., Landman, B., Roth, H.R. & Xu, D. Unetr: Transformers for 3d medical image segmentation. In Proceedings of the IEEE/CVF Winter Conference on Applications of Computer Vision 574–584 (2022).
- [7] Liu, H.M., Park, SH. (2022). Extending nn-UNet for Brain Tumor Segmentation. In: Crimi, A., Bakas, S. (eds) Brainlesion: Glioma, Multiple Sclerosis, Stroke and Traumatic Brain Injuries. BrainLes 2021. Lecture Notes in Computer Science, vol 12963. Springer, Cham.
- [8] S. Bakas, H. Akbari, A. Sotiras, M. Bilello, M. Rozyski, J. S. Kirby, et al., "The Multimodal Brain Tumor Image Segmentation Benchmark (BRATS)," IEEE Transactions on Medical Imaging, vol. 34, no. pp. 1993–2024, Oct. 2015, doi: 10.1109/TMI.2014.2377694.
- [9] A. Bakas, M. A. Akbari, A. Sotiras, M. Bilello, J. S. Kirby, M. Rozyski, et al., "Segmentation and Radiomics Analysis of Gliomas: The BRATS Challenges," in Brainlesion: Glioma, Multiple Sclerosis, Stroke and Traumatic Brain Injuries, vol. 11334, pp. 287–297, Springer, 2019.
- [10] Bertels, J. et al. (2019). Optimizing the Dice Score and Jaccard Index for Medical Image Segmentation: Theory and Practice. In: Shen, D., et al. Medical Image Computing and Computer Assisted Intervention – MICCAI 2019. MICCAI 2019. Lecture Notes in Computer Science, vol 11765. Springer, Cham.
- [11] T. Elbelle et al., "Optimization for Medical Image Segmentation: Theory and Practice When Evaluating with Dice Score or Jaccard Index," in IEEE Transactions on Medical Imaging, vol. 39, no. 11, pp. 3679–3690, Nov. 2020
- [12] Wang S, Kim S, Chawla S, Wolf RL, Zhang WG, O'Rourke DM, et al. Differentiation between glioblastomas and solitary brain metastases using diffusion tensor imaging. Neuroimage 2009; 44: 653 - 60. doi: 10.1016/j.neuroimage.2008.09.027
- [13] W. Zhao, K. Li, D. Zhao, Y. Jiang, J. Wu, J. Chen, X. Quan, X. Li, and F. Xue, "Liver segmentation in CT image with no-edge-cutting UNet," in Proc. IEEE 9th Joint Int. Inf. Technol. Artif. Intell. Conf. (ITAIC), Chongqing, China, Dec. 2020, pp. 2315–2318.
- [14] P. Xiaojin, Q. Zhang, H. Zhang, and S. Li, "A fundus retinal vessels segmentation scheme based on the improved deep learning U-Net model," IEEE Access, vol. 7, pp. 126234–126243, 2019.
- [15] V. V. Valindria et al., "Multi-modal Learning from Unpaired Images: Application to Multi-organ Segmentation in CT and MRI," 2018 IEEE Winter Conference on Applications of Computer Vision (WACV) pp. 547–556.
- [16] N. Siddique, S. Paheding, C. P. Elkin, and V. Devabhaktuni, "U-Net and its variants for medical image segmentation: A review of theory and applications", IEEE Access, vol. 9, pp. 82031–82057, 2021.
- [17] X. Huang, S. Belongie, "Arbitrary Style Transfer in Real-Time with Adaptive Instance Normalization", Proceedings of the IEEE International Conference on Computer Vision (ICCV), 2017, pp. 1501–1510
- [18] Guan H, Liu M. Domain Adaptation for Medical Image Analysis: A Survey. IEEE Trans Biomed Eng. 2022 Mar;69(3):1173–1185. doi: 10.1109/TBME.2021.3117407.

Name of the Model	Validation on BraTS Data				Validation on Private Data				Architecture	Training only Last Decoder Stage		Training only Last Two Decoder Layers		Training only All Decoder Layers				
	Validation on BraTS Data		Validation on Private Data		Training only Last Decoder Stage		Training only Last Two Decoder Layers			Training only Last Decoder Stage		Training only Last Two Decoder Layers		Training only All Decoder Layers				
	Dice	Jaccard	Dice	Jaccard	Dice	Jaccard	Dice	Jaccard		Dice	Jaccard	Dice	Jaccard	Dice	Jaccard			
U-Net	85.23%	74.79%	59.84%	43.22%	U-Net	67.10%	50.91%	73.74%	58.84%	82.19%	70.17%	U-Net	67.10%	50.91%	73.74%	58.84%	82.19%	70.17%
nnU-Net	88.95%	80.43%	64.07%	47.62%	nnU-Net	69.86%	54.36%	62.98%	71.19%	84.46%	73.43%	nnU-Net	69.86%	54.36%	62.98%	71.19%	84.46%	73.43%
Attention U-Net	87.29%	77.82%	60.64%	44.04%	Attention U-Net	67.65%	51.58%	79.38%	66.15%	85.06%	74.32%	Attention U-Net	67.65%	51.58%	79.38%	66.15%	85.06%	74.32%
ELU-Net	86.41%	76.49%	59.56%	43.00%	ELU-Net	71.04%	55.47%	71.02%	55.45%	71.02%	55.44%	ELU-Net	71.04%	55.47%	71.02%	55.45%	71.02%	55.44%
U-Net++	87.21%	77.67%	62.13%	45.57%	U-Net++	70.07%	54.38%	77.21%	63.32%	84.37%	73.22%	U-Net++	70.07%	54.38%	77.21%	63.32%	84.37%	73.22%
PReLU-Net	88.96%	80.7%	60.38%	43.61%	PReLU-Net	69.66%	54.20%	82.18%	70.05%	83.03%	71.26%	PReLU-Net	69.66%	54.20%	82.18%	70.05%	83.03%	71.26%
Weighted ReLU-Net	88.91%	80.37%	64.60%	48.20%	Weighted ReLU-Net	74.64%	60.11%	81.26%	68.83%	85.65%	75.15%	Weighted ReLU-Net	74.64%	60.11%	81.26%	68.83%	85.65%	75.15%

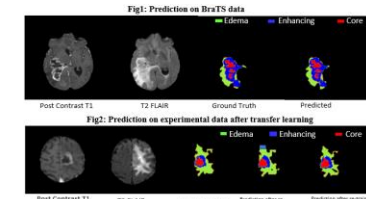


Fig1: Prediction on BraTS data



Fig2: Prediction on experimental data after transfer learning

Table I: Variants of UNet architecture and their corresponding Normalization & Activation Methods		
Name of Architecture	Normalization Method	Activation Function
U-Net	Batch	ReLU
nnU-Net	Instance	Leaky ReLU
Attention U-Net	Batch	ReLU
ELU-Net	Batch	ReLU
U-Net++	Batch	ReLU
PReLU-Net	Instance	PReLU
Weighted ReLU-Net	Instance	Weighted sum of PReLU & ReLU

# Computationally Efficient 3D Patch-Based Super-Resolution for Enhanced Reformatted MRI Visualization

**Siddharth Singh<sup>1</sup>, Durgesh Kumar Dwivedi<sup>\*1</sup>, Ranjeet Ranjan Jha<sup>2</sup>, B V Rathish Kumar<sup>3</sup>, Sudhir Kumar Pathak<sup>4</sup>**

<sup>1</sup>Department of Radiodiagnosis, King George's Medical University, Lucknow, India, <sup>2</sup>Department of Mathematics, Indian Institute of Technology, Patna, India, <sup>3</sup>Department of Mathematics and Statistics, Indian Institute of Technology, Kanpur, India, <sup>4</sup>Learning Research and Development Center, University of Pittsburgh, Pittsburgh, PA, United States\* [durgeshdwivedi@kgmcindia.edu](mailto:durgeshdwivedi@kgmcindia.edu)

## Introduction

Magnetic Resonance Imaging (MRI) is widely used in clinical diagnostics, offering techniques such as Diffusion-Weighted Imaging (DWI) and Diffusion Tensor Imaging (DTI). However, a major limitation is the deterioration of image quality in reformatted 3D visualizations derived from 2D acquisitions. Direct 3D MRI scanning would yield superior results but is often impractical due to extended scan times and patient movement artifacts, especially in less cooperative or pediatric patients [1] [2]. These limitations are especially pronounced in neurological assessments where precise visualization of fine anatomical structures is crucial, and in emergency settings where rapid imaging is essential. Our study aimed to address this challenge by introducing a computationally efficient 3D patch-based super-resolution method that enhances reformatted MRI visualizations without requiring additional scans, improving diagnostic quality while maintaining feasible computational demands. Our method significantly improves diagnostic quality while maintaining feasible computational demands, offering a practical solution for clinical implementation.

## Methods

Data used to prepare this article were obtained from the IXI (Information eXtraction from Images) database (<https://brain-development.org/ixi-dataset/>). The IXI dataset is a collection of nearly 600 MR images from normal, healthy subjects, including T1, T2, PD-weighted, and MRA images, acquired at three different hospitals in London which are widely used as a reference dataset in neuroimaging research. The training was conducted using 3D T2-weighted MRI scans, pre-processed using MRtrix for volume conversion and histogram matching to ensure consistent intensity distributions. Dataset preparation included changes in slice thickness and changes in voxel shapes which were done to match it with the original 2D acquisition parameters. After which MRtrix was used again to reformat the data and get an isotropic volume. A specialized 3D super-resolution system built around a modified U-Net architecture that processes 32×32×32 voxel patches with a 16-voxel stride pattern [3] [4]. The network incorporates custom-designed ConvBlock3D and ResidualBlock3D components with skip connections, optimized for preserving fine anatomical details during the enhancement process as shown in Fig.1. The model training system employs the dual patch validation strategy, which includes aggressive mode (strict quality enforcement) and normal mode (broader coverage), improving robustness across diverse patches. Figure 3 (a) shows the complete pipeline of our research methodology steps. The training was performed on a Windows-based Dell Precision 3640 Tower equipped with Intel Core i7 CPU and Quadro P1000 GPU.

The training process leverages a combined loss function incorporating L1 loss, MSE, and gradient difference loss for edge-based training, optimized using Adam with a carefully tuned learning rate of 5e-5 and adaptive learning rate scheduling which helps us to get a better-reformatted image compared to interpolation method.

## Results

Our optimized U-Net architecture demonstrated significant improvements over standard interpolation techniques, as evaluated over 100 training epochs (Fig.2). Quantitative evaluation showed significant enhancement in image quality metrics, with Peak Signal-to-Noise Ratio (PSNR) improving from 25.48 dB to 29.02 dB and Structural Similarity Index (SSIM) increasing from 0.71 to 0.82, as shown in Fig.3 (b). This patch-based approach proved especially effective in maintaining computational efficiency while preserving anatomical detail across varying structures. The model's robustness was further validated through successful application to novel datasets, confirming its generalization capabilities and practical clinical utility. These results establish a strong foundation for refinements in MRI enhancement techniques.

## Discussion

Current super-resolution approaches for MRI enhancement face several key limitations. Traditional methods either process 2D slices independently, potentially introducing artifacts at slice boundaries or require substantial computational resources for complete volume reconstruction. Our patch-based approach addresses these challenges while introducing some trade-offs that warrant discussion. The primary advantage of our method lies in its computational efficiency, achieved through strategic patch selection and processing. By utilizing 32×32×32 voxel patches with a 16-voxel stride pattern, we balance enhancement quality with processing speed. Our experiments demonstrate that this approach reduces memory requirements by approximately 60% compared to full-volume processing while maintaining high-quality reconstruction. However, we observed minor artifacts at patch boundaries, particularly in regions with high anatomical complexity. Future work should focus on optimizing patch boundary handling and exploring adaptive patch sizing based on anatomical features. Additionally, implementation in clinical workflows will require careful consideration of hardware requirements and integration with existing PACS systems.

## Conclusion

Our study presents a computationally efficient, 3D patch-based super-resolution

framework for enhancing reformatted MRI visualization. Our novel dual-mode patch validation system and custom loss function effectively address the challenges of 3D volume enhancement while maintaining practical computational requirements. The method demonstrates clear advantages over conventional interpolation-based reformatting while maintaining practical computational demands. Its successful generalization to external clinical data highlights its potential for real-world implementation. Future work will focus on broader validation across diverse imaging protocols and integration into clinical diagnostic workflows.

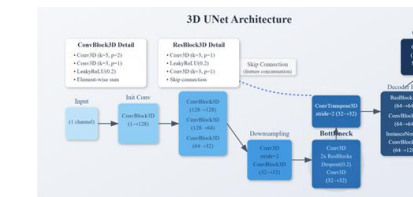


Fig.1 UNet Model Architecture

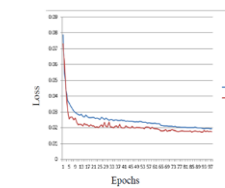


Fig.2 Training and Validation metrics of UNet architecture

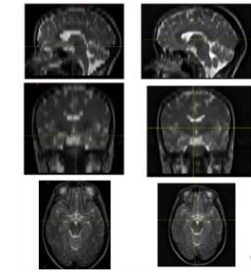


Figure (a) shows the U-Net segmentation output with the original MRI image alongside its binary mask. Figures (b), (c), and (d) display the outputs of YOLO v8, v9, and v11, respectively, with bounding boxes and predicted regions overlaid on the MRI scans, highlighting their segmentation performance.

## References

- Zhao, C., Dewey, B.E., Pham, D.L., Calabresi, P.A., Reich, D.S. and Prince, J.L., 2020. SMORE: a self-supervised anti-aliasing and super-resolution algorithm for MRI using deep learning. *IEEE transactions on medical imaging*, 40(3), pp.805-817.
- Lin, J., Miao, Q., Surawech, C., Raman, S.S., Zhao, K., Wu, H.H. and Sung, K., 2023. High-Resolution 3D MRI With Deep Generative Networks via Novel Slice-Profile Transformation Super-Resolution. *IEEE Access*.
- Kaluvila, A., 2023. Super-resolution of brain MRI via U-Net architecture. *International Journal of Advanced Computer Science and Applications*, 14(5).
- Kaluvila, A., Koonjoo, N., Bhutto, D., Rockenbach, M. and Rosen, M.S., 2022. Synthetic low-field MRI super-resolution via nested U-Net architecture. *arXiv preprint arXiv:2211.15047*.

# Clustering-Based Multiparametric MRI for Differentiation Between True Tumor Progression and Pseudoprogression in Glioblastoma

Sourav Basak<sup>1</sup>, Gabriela W Kostrzanowska<sup>2</sup>, Subhanon Bera<sup>1,3</sup>, Archith Rajan<sup>4</sup>, Sanjeev Chawla<sup>4</sup>, Harish Poptani<sup>2</sup>, Sourav Bhaduri<sup>1,3</sup>

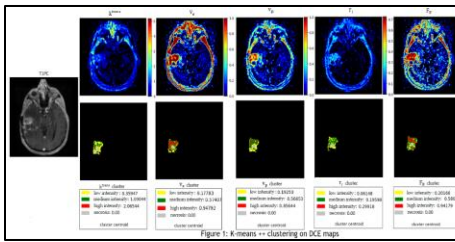
<sup>1</sup>Institute for Advancing Intelligence, TCG Centres for Research and Education in Science and Technology, Kolkata, India,<sup>2</sup>Centre for Preclinical Imaging, University of Liverpool, Liverpool, UK,<sup>3</sup>Academy of Scientific and Innovative Research (AcSIR), Ghaziabad, India,<sup>4</sup>Department of Radiology, Perelman School of Medicine, University of Pennsylvania, Philadelphia, USA.

## Introduction

Glioblastoma (GBM) is a highly aggressive brain tumor with limited survival rates despite extensive treatment [1-3]. Differentiating between trueprogression (TP) and pseudoprogression (PsP) remains a diagnostic challenge, as both appear to be similar on MRI [4,5]. Dynamic contrast-enhanced MRI(DCE-MRI) allows the extraction of pharmacokinetic (PK) parameters, such as Ktrans ,Kep,Ve,Fp and ti to assess tumor vascularity and permeability [6]. We applied a clustering-based approach using a parsimonious PK model selected via Akaike Information Criterion (AIC) [7] to differentiate TP from PsP. Additionally, diffusion tensor imaging (DTI) and dynamic susceptibility contrast (DSC) MRI data were analyzed using the clustering approach [8].

## Methods

This retrospective study included 57 GBM patients (TP: n=38, PsP: n=19) acquired using a 3T Tim Trio MR scanner at the University of Pennsylvania and shared with TCG CREST (data sharing ID: RIS76150). DCE-MRI data was fitted to five PK models (nonlinear Tofts, extended Tofts, Shutter-Speed, 2CXM, and 3S2X models) to generate parametric maps for Ktrans, Kep, Ve, Fp and ti [6]. A parsimonious PK model was chosen based on AIC [9-10]. Clustering using K-means++ [11] was applied to classify pixels into low, medium, and high-intensity regions. Pixels with poor goodness of fit ( $R^2 < 0.2$ ) were defined as necrotic pixels. After clustering, median thresholding [12-13] was performed on the centroids across all datasets to determine high and low clusters globally. Tumors were segmented into enhancing, non-enhancing, and edema regions using the nnU-Net algorithm [14]. Percentage pixels for each cluster was calculated as the ratio of no. of pixels in that cluster and the total no. of pixels in (enhancing + non-enhancing) region. 26 cases (TP: n=13, PsP:n=13) were analyzed for the calculation of mean diffusivity (MD) using DTI and cerebral blood volume (CBV) using DSC imaging, respectively.



## Results

Clustering Analysis (Figs. 1, 2)

Ktrans : TP cases show, higher percentage of high-intensity pixels (0.20) compared to PsP (0.10), with statistically significant p=0.0019, indicating increased perfusion and permeability in TP,while PsP cases have more low-intensity pixels, reflecting reduced perfusion.

Ve: TP cases had higher percentage of high-intensity pixels (0.21) than PsP (0.12), difference was statistically significant. p=0.0048.

Ktrans (Figs. 2 & 3):Enhancing & Non-Enhancing Regions: Mean Ktrans values were significantly different between TP ( $0.13 \text{ min}^{-1}$ ) and PsP ( $0.06 \text{ min}^{-1}$ ), p=0.008, supporting Ktrans as a robust marker

for distinguishing progression types.

Enhancing Region: TP showed higher mean Ktrans ( $0.22 \text{ min}^{-1}$ ) compared to PsP ( $0.10 \text{ min}^{-1}$ ), p=0.048, validating Ktrans role as a differential marker.

Kep (Fig. 3): Enhancing & Non-Enhancing Regions : Mean Kep values differed significantly between TP ( $1.04\text{min}^{-1}$ ) and PsP ( $0.66 \text{ min}^{-1}$ ), p=0.03, indicating potential tissue or vascular changes post-treatment.

Enhancing Region: TP cases exhibit higher mean Kep ( $1.15 \text{ min}^{-1}$ ) than PsP ( $0.64 \text{ min}^{-1}$ ), p=0.008.

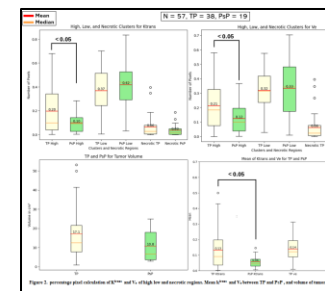
Tumor Volume (calculated after automated nnU-Net segmentation-Fig.2):

Volume: TP cases had larger tumor volumes (mean =  $17.1 \text{ cm}^3$ ) than PsP (mean =  $10.8 \text{ cm}^3$ ), p=0.07, reflecting more aggressive growth in TP.

CBV and DTI (Fig. 4):

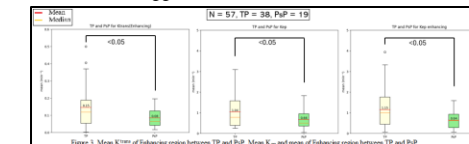
CBV: TP cases showed, higher CBV (mean =  $842.34 \text{ mL}/100\text{g}$ ) than PsP (mean =  $669.00 \text{ mL}/100\text{g}$ ), not statistically significant.

MD: Mean diffusivity (MD) was slightly higher in TP (mean =  $0.00136 \text{ mm}^2/\text{s}$ ) than in PsP (mean =  $0.00124 \text{ mm}^2/\text{s}$ ), without statistical significance.



## Discussion

The results show that both high-intensity clusters of Ktrans and Ve differ significantly between TP and PsP, with mean Ktrans values significantly higher in TP than in PsP highlighting increased vascular permeability and perfusion as key markers of true progression There was also a statistically significant difference in mean Kep between TP and PsP , further indicating treatment response. Tumor volume was larger in TP, consistent with its more aggressive nature.



Our clustering-based analysis of Multiparametric-MRI demonstrates that high-intensity clusters of Ktrans, Ve, mean Ktrans and mean Kep are statistically significant parameters for differentiating TP from PsP. Tumor volume difference between TP and PsP was near significant (p=0.07), suggesting that TP is associated with more severe tumor profile. These findings support using DCE-MRI and clustering techniques as non-invasive tools for distinguishing TP from PsP. Future studies should validate these results with larger datasets and integrate more comprehensive multimodal imaging data.

## Conclusion

## References

- Schaff, Lauren R., and Ingo K. Mellinghoff. "Glioblastoma and other primary brain malignancies in adults: a review." *Jama* 329, no. 7 (2023): 574-587.
- Hanif, Farina, Kanza Muzafer, Kahlashan Perveen, Saima Mehnood Malhi, and Shabana Usman Simjee. "Glioblastoma multiforme: a review of its epidemiology and pathogenesis through clinical presentation and treatment." *Asian pacific journal of cancer prevention* 18, no. 1 (2017): 3-9.
- Fernandes, Catarina, Andreia Costa, Ligia Osório, Rita Costa Lago, Paulo Linhares, Bruno Carvalho, and Cláudia Caero. "Current standards of care in glioblastoma therapy." *Exon Publications* (2017): 197-241.
- Fekete, B., K. Werkenius, M. Tisell, A. Pividic, A. Smits, A. S. Jakola, and B. Rydenhag. "What predicts survival in glioblastoma? A population-based study of changes in clinical management and outcome." *Frontiers in surgery* 10 (2023): 124936.
- Young, Jacob S., Nadeem Al-Adli, Katie Scotford, Soonmei Cha, and Mitchel S. Berger. "Pseudoprogression versus true progression in glioblastoma what neurosurgeons need to know." *Journal of neurosurgery* 139, no. 3 (2023): 748-759.
- Bhaduri, Sourav, Clémentine Lesbats, Jack Sharkey, Claire Louise Kelly, Soham Mukherjee, Arthur Taylor, Edward J. Delikatny, Sungheon G. Kim, and Harish Poptani. "Assessing tumor haemodynamic heterogeneity and response to choline kinase inhibition using clustered dynamic contrast enhanced mr parameters in rodent models of glioblastoma." *Cancers* 14, no. 5 (2022): 1223.
- Cavanaugh, James Stephens. 2020. "Bootstrap Cross-Validation Improves Model Selection in Pharmacometrics." *Statistics in Biopharmaceutical Research* 14 (2): 168-203. doi:10.1080/19466315.2020.1828159.
- Wang, S., M. Martinez-Lage, Y. Sakai, S. Chawla, S. G. Kim, M. Alonso-Basanta, R. A. Lustig et al. "Differentiating tumor progression from pseudoprogression in patients with glioblastomas using diffusion tensor imaging and dynamic susceptibility contrast MRI." *American Journal of Neuroradiology* 37, no. 1 (2016): 28-36.
- Fusco, Roberta, Mario Sansone, Silvio Maffei, Nicola Raino, and Antonella Petrillo. "Dynamic contrast-enhanced MRI in breast cancer: A comparison between distributed and compartmental tracer kinetic models." *Journal of Biomedical Graphics and Computing* 2, no. 2 (2012): 23.
- Akaike, Hirotugu. "A new look at the statistical model identification." *IEEE transactions on automatic control* 19, no. 6 (1974): 716-723.
- Arunkumar, N., Mazin Abd Mohammed, Mohd Khanapi Abd Ghani, Dheyaa Ahmed Ibrahim, Enas Abdulhay, Gustavo Ramirez-Gonzalez, and Victor Hugo C. de Albuquerque. "K-means clustering and neural network for object detecting and identifying abnormality of brain tumor." *Soft Computing* 23 (2019): 9083-9096.
- Wiharto W, Suryani E. The Comparison of Clustering Algorithms K-Means and Fuzzy C-Means for Segmentation Retinal Blood Vessels. *Acta Inform Med*. 2020 Mar;28(1):42-47. doi: 10.5455/aim.2020.28.42-47. PMID: 3210514; PMCID: PMC708533.
- Pander, T., 2022. A new approach to adaptive threshold based method for QRS detection with fuzzy clustering. *Biocybernetics and Biomedical Engineering*, 42(1), pp.404-425.
- Isensee, Fabian, Paul F. Jäger, Peter M. Full, Philipp Vollmuth, and Klaus H. Maier-Hein. "nnU-Net for brain tumor segmentation." In *Brainlesion:Glioma, Multiple Sclerosis, Stroke and Traumatic Brain Injuries: 6th International Workshop, BrainLes 2020, Held in Conjunction with MICCAI 2020, Lima, Peru, October 4, 2020, Revised Selected Papers, Part II* 6, pp. 118-132. Springer International Publishing, 2021.

# Cortical Morphometric Differences Between Young-Onset and Late-Onset Parkinson's Disease: A Deformation-Based Approach.

S Senthil Kumaran<sup>1</sup>, Priyanka Bhat<sup>1</sup>, Pankaj<sup>1</sup>, Sadhna Kumari<sup>1</sup>, Vinay Goyal<sup>2</sup>, Achal K Srivastava<sup>3</sup>, Roopa Rajan<sup>3</sup>, Divya M R<sup>3</sup>.

<sup>1</sup>- Department of NMR, All India Institute of Medical Sciences, New Delhi, India-110029 <sup>2</sup>- Department of Neurology, Neurosciences Institute, Medanta, The Medicity- 122001.

<sup>3</sup>- Department of Neurology, Centre for Neuroscience, All India Institute of Medical Sciences, New Delhi, India-110029

## Introduction

Parkinson's Disease (PD), a progressive neurodegenerative disorder, is typified by dopaminergic neuron loss in the substantia nigra. Although PD affects ~1% of people over 60 years of age; around 10% of cases present as Young-Onset Parkinson's Disease (YoPD), where symptoms begin before 50 years and exhibit different clinical progression compared to typical PD. Neuroimaging [voxel-based morphometry (VBM), surface-based morphometry (SBM), and tractography] has been used to unveil structural brain alterations in PD and YoPD, with a particular emphasis on early stages and disease progress<sup>1</sup>. Deformation-based morphometry (DBM) is an effective modality in detecting subtle morphological changes<sup>2-4</sup>, but widespread clinical usage in PD has been limited. This study aims to use DBM and SBM to develop insights into morphometric patterns in clinically stable PD and YoPD.

## Methods

53 PD (27 YoPD with onset <50 years and 26 PD with onset >50 years), all with Hoehn & Yahr (H&Y) stage up to 3 and right-sided symptom onset, were recruited from the Movement Disorders clinic. PD were screened based on UKPD Brain Bank criteria, with exclusions for neuropsychiatric comorbidities and contraindications to MRI. Clinical assessments included the Unified Parkinson's Disease Rating Scale (UPDRS), Parkinson's Disease Questionnaire-39 (PDQ-39), and Purdue Peg Board (PPB) tests, with all evaluations conducted in the "ON" state. 15 healthy volunteers were recruited from local population. 3D T1-weighted scans were acquired on a 3T scanner (Achieva 3T) using TR/TE: 8/4 ms, flip angle=8°, 1mm slices, FOV=232 mm with a 32-channel head coil.

For cortical volume and thickness estimation, cortical surface reconstruction data were preprocessed with FreeSurfer<sup>5</sup>, including skull-stripping, segmentation of gray matter (GM), white matter (WM), and cerebrospinal fluid, and cortical surface generation using mri\_watershed and bias field correction. Cortical thickness was measured from pial to white matter surfaces, smoothed at 10 mm FWHM. DBM analysis, conducted with the Computational Anatomy Toolbox (CAT12) in SPM12<sup>3,6,7</sup>, involved preprocessing to resample, bias-correct, and affine-register images to SPM's unified segmentation protocol, including skull stripping, brain parcellation, and tissue classification. Local morphological changes were assessed with Jacobian determinant maps.

Statistical comparisons between groups (HC vs. PD, PD vs. YoPD, etc.) were made using general linear models with False Discovery Rate (FDR) correction for multiple comparisons, at  $p<0.05$ .

## Results

Healthy controls (HC, n=15, age=40.78 ± 7.58 years), PD (age=65.42 ± 5.73), and YoPD (age=51.29 ± 4.36) groups highlighted differential structural changes by disease duration. Both PD and YoPD groups were further stratified by disease duration into PD<5 (age=63.23 ± 5.04), PD>5 (age=67.62 ± 5.72), YoPD<5 (age=49.26 ± 3.08), and YoPD>5 (age=53.83 ±

4.51) groups. Clinically the PD and YoPD were stable and no differences were observed in scores across groups.

**Thickness Analysis:** Significant cortical thinning was observed in PD [bilateral superior temporal gyrus, precuneus, middle temporal region, left lingual gyrus, pars orbitalis, and inferior parietal lobule]; PDless [left- precuneus, superior frontal gyrus, and supramarginal gyrus, and right- inferior parietal lobule, precuneus, pars triangularis, and precentral region]; YoPD [left- lingual and superior frontal gyri, and the right pericalcarine region]; YoPD less [left cuneus and right superior parietal region].

**Volume Analysis:** Significant decrease in GM volume was observed in PD [left inferior parietal lobe, lateral orbitofrontal gyrus, supramarginal gyrus, precentral gyrus, lingual region, and middle temporal region and right- lateral occipital region, superior frontal gyrus, and pars triangularis]; PDless [left- inferior parietal, pars orbitalis, lingual, supramarginal, superior frontal, and inferior temporal regions; and right- pars-opercularis, inferior temporal region, inferior parietal lobe, superior frontal gyrus, supramarginal gyrus and lateral orbitofrontal regions.]; YoPD [left- left lateral occipital region]; YoPD less [left- lingual, caudal middle frontal regions and right- inferior parietal, cuneus, pars-opercularis regions].

**DBM Analysis:** DBM detected significant atrophy in PD [in left subgyral region within temporal lobe, postcentral gyrus, superior frontal gyrus, superior parietal lobule and right- superior frontal gyrus, cuneus, inferior parietal lobule; bilateral cerebellar decline]; PDless [left insula, anterior cingulate, decline, superior temporal gyrus and right thalamus, insula]; YoPD [left precuneus, superior frontal gyrus, postcentral gyrus, decline and right thalamus (medial dorsal nucleus), postcentral gyrus]; YoPD less [left cingulate gyrus, cerebellum (culmen and tonsil) and right inferior frontal gyrus].

## Discussion

DBM revealed subtle atrophic changes in subcortical and cerebellar regions in addition to cortical regions as compared to volumetric analyses. In spite of similar clinical status across groups, the study iterated on the potential of DBM as an imaging biomarker in PD-associated neurodegeneration.

## Conclusion

DBM provides critical insights into the structural alterations associated with PD and YoPD.

## References:

- Borghammer, P. et al. A deformation-based morphometry study of patients with early-stage Parkinson's disease. *Eur J Neurol* 17, 314–320 (2010).
- Gaser, C. Structural MRI: Morphometry. 399–409 (2016) doi:10.1007/978-3-642-35923-1\_21.

3.Gaser, C., Nenadic, I., Buchsbaum, B. R., Hazlett, E. A. & Buchsbaum, M. S. Deformation-Based Morphometry and Its Relation to Conventional Volumetry of Brain Lateral Ventricle in MRI. *Neuroimage* 13, 1140–1145 (2001).

4.Ashburner, J. & Friston, K. J. Voxel-based morphometry--the methods. *Neuroimage* 11, 805–821 (2000).

5.Fischl, B. & Dale, A. M. Measuring the thickness of the human cerebral cortex from magnetic resonance images. *Proc Natl Acad Sci U S A* 97, 11050–11055 (2000).

6.Dahnke, R., Yotter, R. A. & Gaser, C. Cortical thickness and central surface estimation. *Neuroimage* 65, 336–348 (2013). 7. Yotter, R. A., Dahnke, R., Thompson, P. M. & Gaser, C. Topological correction of brain surface meshes using spherical harmonics. *Hum Brain Mapp* 32, 1109–1124 (2011).

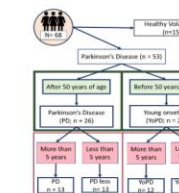


Figure 1. Study Flow Chart.

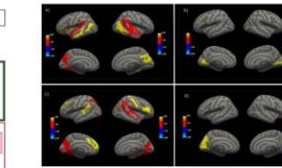


Figure 2- Cortical thickness A] Healthy vs PD; B] Healthy vs PDless; C] Healthy vs YoPD and d] Healthy vs YoPDless. (PFDR < 0.05)

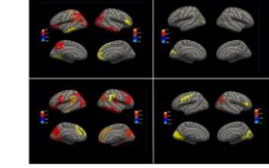


Figure 3- Volume changes- A] Healthy vs PD; B] Healthy vs PDless; C] Healthy vs YoPD and d] Healthy vs YoPDless. (PFDR < 0.05)

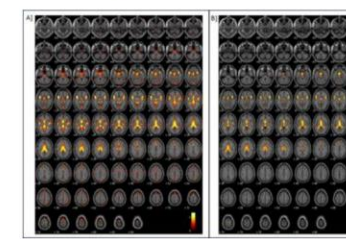


Figure 4 – DBM in PD- A] Healthy vs PD; B] Healthy vs PDless. (P<sub>corr</sub> < 0.05)

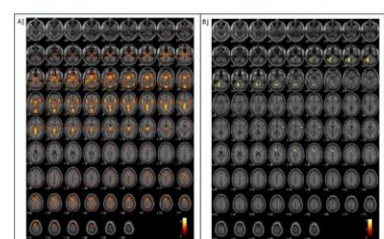


Figure 5- DBM in YoPD- A] Healthy vs YoPD and d] Healthy vs YoPDless. (PFDR < 0.05)

# Clinically interpretable 3D CNN for glioma classification using diffusion tensor imaging of normal-appearing white matter

Sreejith Vidyadharan<sup>1</sup>, BVVSN Prabhakar Rao<sup>1</sup>, P. Yogeeshwari<sup>2</sup>, C. Kesavadas<sup>3</sup>, Venkateswaran Rajagopalan<sup>1\*</sup>

<sup>1,1\*</sup>Department of Electrical and Electronics Engineering, Birla Institute of Technology and Science Pilani, Hyderabad Campus, Hyderabad, 500078, India <sup>2</sup>Department of Pharmacy, Birla Institute of Technology and Science Pilani, Hyderabad Campus, Hyderabad, 500078, India <sup>3</sup>Department of Imaging Sciences and Interventional Radiology, Sree Chitra Tirunal Institute for Medical Sciences and Technology, Trivandrum, 695011, India

## Introduction

Glioma is the most common type of brain tumor, classified into low-grade glioma (LGG) and high-grade glioma (HGG). While biopsy is the standard method for glioma classification, it is invasive and prone to complications. Magnetic resonance imaging (MRI) derived features are frequently used for non-invasive glioma classification. Glioma primarily spreads/diffuses via white matter (WM) pathways to the surrounding brain regions. This leads to compromised WM structural integrity which cannot be assessed in conventional MRI sequences. Such an assessment of the tumor pathophysiological effects on the WM structural integrity can be obtained using diffusion tensor imaging (DTI). Previous studies have shown that glioma is not merely a local phenomenon but also a global phenomenon because glioma invades surrounding brain tissues often compromising its WM structural integrity. However, existing DTI-based deep learning studies have primarily considered glioma as a local phenomenon, training convolutional neural networks (CNNs) exclusively on tumor-region images. Moreover, these studies lack clinical interpretability in their trained deep-learning models. In this study, we address these gaps by using DTI MRI volume (i.e., a 3D image) of the normal-appearing WM (NAWM, i.e., the non-tumorous region/WM excluding the whole tumor region) to train a 3D CNN model for classifying LGG and HGG patients. We hypothesize that the trained 3D CNN model will capture differential diffuse patterns from the NAWM region between LGG and HGG patients, enabling high classification accuracy, sensitivity, and specificity. Additionally, we have integrated occlusion sensitivity analysis (OSA), a model interpretability method into this deep learning framework which will highlight the regions primarily focused by the 3D CNN model for decision-making (whether LGG or HGG). These regions will also reveal the potential WM damage in the surrounding brain tissues beyond tumor boundaries which may be differentially affected in the LGG and HGG patients due to tumor pathophysiology.

## Methods

Routine clinical (i.e., low-resolution images as opposed to high-resolution research scans) DTI MRI volumes from 86 patients (39 LGG, 47 HGG) were acquired from Sree Chitra Tirunal Institute for Medical Sciences and Technology, Trivandrum. These DTI MRI volumes were processed to obtain fractional anisotropy (FA), axial diffusivity (AD), radial diffusivity (RD), and mean diffusivity (MD) images of the NAWM region for each patient. A 3D CNN model was trained using individual DTI maps of the NAWM region from 76 patients and was evaluated based on the model's accuracy, sensitivity, and specificity. OSA was performed on the remaining 10 patients (5 LGG, 5 HGG)

using the DTI map for which the 3D CNN model achieved more than 90 % accuracy. The heatmap obtained from the OSA will reveal the regions primarily focused on by the 3D CNN for glioma classification. Fig. 1 shows the overview of the methodology.

## Results

Our clinically interpretable 3D CNN model achieved 92% accuracy with FA and 90% with MD images of the NAWM region. OSA revealed that the 3D CNN model primarily focused on the regions surrounding the tumor boundaries where the extent of these regions was more widespread in HGG when compared to LGG as shown in Fig. 2.

## Discussion

This study examined the global impact of glioma on the NAWM region and its role in glioma classification. The 3D CNN model achieved superior accuracy, sensitivity, and specificity when trained with FA and MD images of NAWM. These findings highlight the sensitivity of FA and MD metrics in capturing tumor-induced subtle WM changes in the surrounding brain regions beyond tumor boundaries. Moreover, OSA revealed extensive WM damage in HGG that extended beyond tumor boundaries, often reaching the contralateral hemisphere. In contrast, LGG showed more localized WM alterations near tumor boundaries as shown in Fig. 2.

## Conclusion

This study underscores the potential of NAWM analysis for glioma classification while providing clinically interpretable insights into the differential impact of tumor-induced WM alterations in LGG and HGG patients. The integration of DTI-based NAWM analysis with 3D CNN enables accurate, non-invasive glioma classification while incorporating OSA into the framework will provide clinically interpretable results for the clinicians. Additionally, as this method does not rely on handcrafted features, it can be seamlessly integrated into clinical workflows, enhancing diagnostic precision and supporting personalized treatment strategies.

## Keywords

LGG, HGG, MRI, diffusion tensor imaging, brain, 3D CNN, occlusion sensitivity, white matter

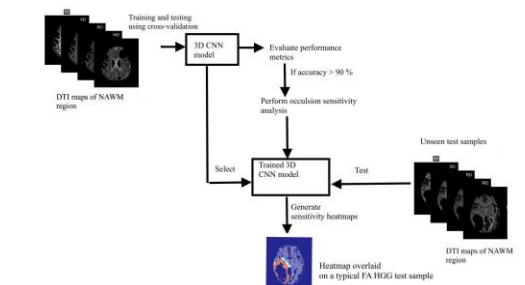


Fig. 1. Overview of the proposed methodology

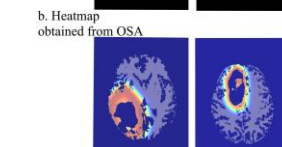
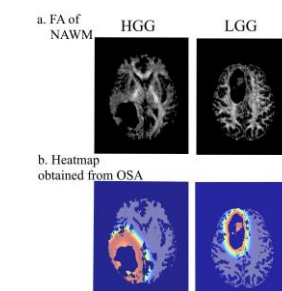


Fig. 2. OSA heatmap comparison between a typical LGG and HGG patient

# Characterizing heart shape and its distribution among patients across geographies

## Introduction

One of the main hurdles for widespread clinical adaptation of Cardiac MRI (CMR) is its complex planning which requires considerable technologist's expertise, and double-oblique planning for imaging the clinically relevant cardiac planes. Hence automated or semi-automated planning is a critical clinical need for CMR examinations. As the development of the AI models for automatic cardiac MRI planning[1] accelerate, one of the key questions that needs addressed is the generalizability of these AI models, which are typically trained with data obtained from specific regions.

In this regard, our goal is to define heart shape descriptors that can be measured and characterized across different geographies. Major aspects that affect the planning of the heart are its shape, size, and the orientation of the heart chambers. In this study, we have considered Atrio Ventricular angle ([2], angle made between the long axis of the atrium and the ventricle) measured in vertical and horizontal long axis of the heart and investigated how these angles vary across populations from three different geographies.

## Methods

All data were obtained with informed consent of the patients undergoing clinically indicated Cardiac MR exams. A standardized 3D survey [3] data with a breath-hold duration of 12 – 15s was obtained with a resolution of 3mm X 3mm X 3mm. Multiple landmarks like the ventricular apex, atrioventricular grooves, mitral valve center etc. were manually annotated on standard cardiac imaging planes such as L2Chamber (L2CH) and 4 chamber (4CH) views by an MRI technologist with more than 5 years' of experience. The long axis of the atrium, and the ventricles were drawn as shown in the figure 1. The angulation between these long axis lines were meticulously measured, providing us with 3 main shape descriptors of the heart shape, labeled here as – L2, L4 and R4. The distribution of these 3 shape descriptors obtained across 3 different geographies (India, USA and Netherlands) were analyzed with one-way ANOVA.

## Results

A total of 575 patients underwent the study and the distribution of the subjects across the 3 geographies are shown in Table 1.

The spread of the Atrio ventricular angulations with the L2CH and 4CH views (i.e., L2, L4, R4) obtained from these different geographies are shown in the figure 2. One way ANOVA results indicate that there is no statistically significant difference in the distribution of these shape descriptors between the sites examined.

Geography	# of patients
India	512
Netherlands	21
USA	42

## DISCUSSION

: We measured atrio ventricular angulations in 2 planes, as the shape descriptors of the heart to characterize the spread of heartshapes across populations. To the best of our knowledge, this is the first such study. We found that the distribution of heart-shapes is not different across different geographies, suggesting that automatic cardiac MR planning models trained on data obtained from specific regions are generalizable and hence applicable across different geographies. One of the key limitations of this study is that the number of patient data available from the different geographies are different. We believe that this may partially explain the variations seen. Another limitation is that we have not yet included heart size differences governed by the body-mass-index of the patient in this study. However, it can be noted the heart shapes typically play more important role than the size in AI based feature segmentations.

## Conclusion

The data obtained in this initial study suggests that the heart shapes, as described by the atrio ventricular angulations, follow similar distribution across the geographies. This indicates that automatic or semi-automatic models used for CMR planning can generalize. Further studies with more patients, specific models and additional regions are needed.

## References:

- Kuusisto JK et al., Revisiting left atrial volumetry by magnetic resonance imaging: the role of atrial shape and 3D angle between left ventricular and left atrial axis. BMC Med Imaging. 2021, 21(1):167.
- Vineeth V et al., Quantitative differences in the heart habitus between breath-hold and free-breathing states, measured using a 3D survey in cardiac patients. Proceedings of ISMRM 2024, 4559.
- Sharma S et al., Instance Segmentation Based approach for Robust automatic 3D Multi-View Planning for Cardiac MRI. Proceedings of ISMRM 2024, 1667.

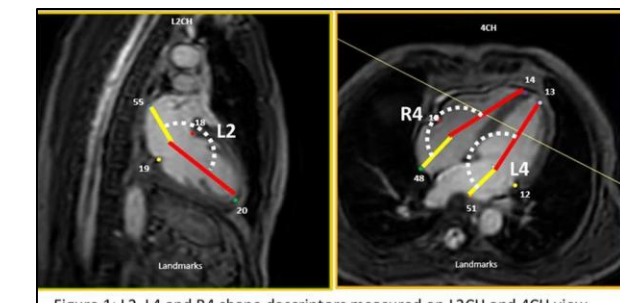


Figure 1: L2, L4 and R4 shape descriptors measured on L2CH and 4CH view.

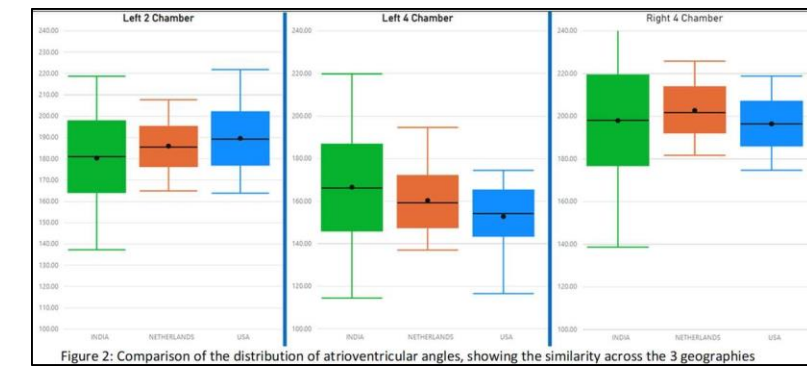


Figure 2: Comparison of the distribution of atrioventricular angles, showing the similarity across the 3 geographies

## CNN-based 3T to 7T dMRI Reconstruction: A Trapezoidal Rule Approach

B.V. Rathish Kumar<sup>1</sup>, Ranjeet Ranjan Jha<sup>2</sup>, S.K. Pathak<sup>3</sup>, Arnav. B.<sup>4</sup>, Aditya Nigam<sup>4</sup>

<sup>1</sup>IIT Kanpur, <sup>2</sup>IIT Patna, <sup>3</sup>University of Pittsburgh and <sup>4</sup> IIT Mandi

### Introduction

Diffusion MRI (dMRI) is a non-invasive technique used to study the brain's white matter, crucial for diagnosing mental diseases and surgical planning. Higher magnetic field strengths, such as 7T, enhance the resolution and clarity of fiber tract imaging but are expensive. This study introduces a novel CNN-based method to simulate 7T dMRI from 3T data, enabling cost-effective alternatives. The proposed model transforms 3T data into high-resolution 7T data and reconstructs multi-shell, multi-tissue fiber orientation distributions (MSMT fODFs) from single-shell data.

### Methods

We present TRGANet, a CNN-based architecture that uses a Trapezoidal Rule (TR) for ODE solver optimization and a Graph Attention Layer. The network is trained to perform two tasks: transforming 3T to 7T spherical harmonics coefficients (SHC) and reconstructing 7T MSMT fODFs from 3T single-shell data. The model is optimized with L1 and total variation losses. Validation was carried out using the Human Connectome Project (HCP) dataset.

### Results

Our model demonstrated strong performance in transforming 3T data into 7T SHC and MSMT fODFs. The evaluation metrics, such as %RMSE and SHC coefficients, showed improvements over existing methods, particularly in terms of sharper and more anatomically accurate results. The reconstructed images and fiber tracts reflected higher clarity and precision compared to previous approaches.

### Discussion

The CNN-based framework, enhanced by the Trapezoidal Rule and graph attention mechanism, provides an effective solution for simulating high-resolution 7T dMRI from standard 3T data. By learning the complex relationship between lower and higher field strength data, our method offers an innovative approach to improving dMRI quality without requiring expensive 7T equipment. The use of ODE solver-based learning also significantly enhances model accuracy and robustness.

### Conclusion

The proposed TRGANet model successfully transforms 3T dMRI data into high-

quality 7T images, demonstrating its potential as a cost-effective alternative for clinical and research applications. The combination of the Trapezoidal Rule and graph attention in our framework provides a promising approach to enhance dMRI image quality, making it a viable solution for advancing neuroimaging without the need for 7T scanners.

### References:

1. AlexanderD.C. et al. Image quality transfer and application in dMRI, Neuroimage, 2017
2. BeisteinerR. et al. Clinical fMRI: evidence for a 7T benefit over 3T, Neuroimage, 2011
3. QinY. et al. Super-resolved q-space deep learning with uncertainty quantification, Med. Image Anal. (2021)

# Deciphering Cognitive and Neuro-Metabolic Dysfunctions in Alzheimer's Disease Progression: Evidence from the 5xFAD Model

Chaynita Dashora<sup>1,2</sup>

Anant Bahadur Pate<sup>1,2</sup>

<sup>1</sup>CSIR-Centre for Cellular and Molecular Biology, Habsiguda, Hyderabad, India; <sup>2</sup>Academy of Scientific and Innovative Research, Ghaziabad, India  
Email: chaynita.dashora@ccmb.res.in

## Introduction

Alzheimer's Disease (AD) is a chronic neurodegenerative disorder characterized by amyloid-beta (A $\beta$ ) plaque accumulation, and neurofibrillary tangles leading to a progressive cognitive decline [1]. The 5xFAD mouse model, which harbors mutations in APP and PSEN1 genes, recapitulates the aggressive pathophysiology of familial AD [2]. This study quantitatively evaluated age-dependent alterations in amyloid pathology, and brain energy metabolism in 5xFAD mice with the progress of AD. **Methods**  
Biomarkers related to brain energy metabolism, antioxidants, and neuroinflammatory cytokines are expected to be dysregulated in response to the severity and duration of hypoxia [3]. Blood samples from neonates are collected at 1-, 6-, and 48-hours post-birth from multiple hospitals across different regions of Odisha, followed by plasma isolation for metabolic profiling using a 700 MHz NMR spectrometer. Volumetric segmentation of infant brain MRI images was performed using the IFS and iBITS pipelines to analyze volumetric differences between HIE and healthy neonatal brains.

## Methods

5xFAD male mice of age 3, 6, and 12 months were used in the study. Cognitive performance was assessed using the Morris Water Maze test [3]. A $\beta$  levels were measured in the cerebral cortex and hippocampus using Enzyme Linked Immuno Sorbent Assay (ELISA) and immunohistochemistry (IHC) [4]. For metabolic measurement, mice were anesthetized using urethane (1.5 mg/kg, intraperitoneal), and infused with [1,6-<sup>13</sup>C]<sub>2</sub>glucose or [2-<sup>13</sup>C]acetate through the lateral tail vein [5]. The brain metabolism was arrested using a focused beam microwave irradiation (3 kW, 1.2 s) at a predefined time. The concentration and <sup>13</sup>C labeling of metabolites were measured in <sup>1</sup>H-[<sup>13</sup>C]-NMR spectra of extracts recorded at 600 MHz Bruker Avance III NMR spectrometer [6]. The cerebral metabolic rate of glucose oxidation (CMR<sub>Glc(ox)</sub>) in glutamatergic and GABAergic neurons and cerebral metabolic rate of acetate oxidation (CMR<sub>Ace(ox)</sub>) was calculated in the cerebral cortex and hippocampus regions [7]. The statistical significance was evaluated by Student's t-test using GraphPad Prism 8.0. All data are presented as Mean $\pm$ SD.

## Results

5xFAD mice exhibited significant ( $p<0.01$ ) memory impairment, with increased escape latency observed at 6 months ( $56.7\text{s}\pm23.8\text{ s}$ , n=) compared to age-matched

wild-type (WT) controls ( $29.5\text{s}\pm18.3\text{ s}$ ) which worsened further at 12 months ( $71.5\text{s}\pm21.2\text{ s}$  vs  $36.1\text{s}\pm13.2\text{ s}$ ) (Fig.1). Soluble A $\beta_{42}$  and A $\beta_{40}$ , and amyloid plaque burden were observed as early as 3 months in 5xFAD mice and increased significantly ( $p<0.01$ ) with the progress of age. Representative <sup>1</sup>H-[<sup>13</sup>C]-NMR spectrum from the cerebral cortex of 5xFAD mice is shown in Fig 1. The concentrations of different <sup>13</sup>C labeled metabolites like Glu<sub>C4</sub> ( $p<0.03$ ), GABA<sub>C2</sub> ( $p<0.05$ ), and Asp<sub>C3</sub> ( $p<0.03$ ) reduced significantly in the cerebral cortex and hippocampus of 5xFAD mice at 3 months with further progressive declines up to 12 months. There was a significant reduction in the CMR<sub>Glc(ox)</sub> in glutamatergic and GABAergic neurons in both brain regions in 5xFAD mice at all ages when compared with age matched WT mice. The reduction in glucose oxidation rates was more pronounced in 12 months, with glutamatergic and GABAergic neurons showing a decline of 27% ( $p=0.009$ ) and 33% ( $p=0.005$ ), respectively, in the cerebral cortex and 37% ( $p=0.004$ ) and 39% ( $p=0.001$ ), respectively, in the hippocampus. In contrast, the CMR<sub>Ace(ox)</sub> was significantly increased in the cerebral cortex ( $p=0.011$ ) and hippocampus ( $p=0.011$ ) of 12-month-old 5xFAD mice compared to WT mice, indicating enhanced glial activity and neuroinflammatory processes.

## Discussion

This study reveals significant age-dependent alterations in cognitive functions and neurometabolic activity in the 5xFAD mouse model of AD. The marked decrease in <sup>13</sup>C-labeled metabolites in 5xFAD mice starting at 3 months and continuing till 12 months highlights early disruptions in excitatory and inhibitory neurotransmission. Moreover, the reduced glucose oxidation in glutamatergic and GABAergic neurons suggests that compromised energy production may be a key factor contributing to the synaptic dysfunction observed in AD. The progressive deficits in neurometabolism correlate with the A $\beta$ -levels and cognitive decline observed in the 5xFAD mice, reinforcing that metabolic dysregulation plays a central role in AD pathophysiology. Additionally, the observed increases in acetate metabolism at later stages point to glial activation and neuroinflammation, which have been implicated in the progression of AD.

## Conclusion

This study demonstrates that the early deficits in energy metabolism contribute to cognitive decline, while later-stage neuroinflammation, reflected in increased acetate metabolism, further exacerbates disease progression. Together, these results suggest that targeting neuronal metabolism, and its interplay with glial

cells may offer novel therapeutic avenues for early intervention in AD.

## Acknowledgement

This study demonstrates that the early deficits in energy metabolism contribute to cognitive decline, while later-stage neuroinflammation, reflected in increased acetate metabolism, further exacerbates disease progression. Together, these results suggest that targeting neuronal metabolism, and its interplay with glial cells may offer novel therapeutic avenues for early intervention in AD.

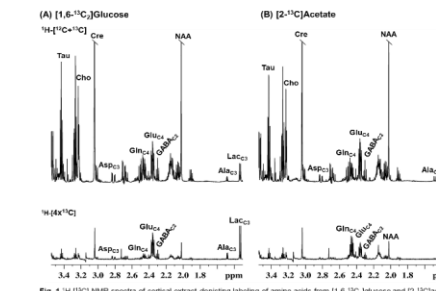


Fig. 1 <sup>1</sup>H-[<sup>13</sup>C]-NMR spectra of cortical extract depicting labeling of amino acids from [1,6-<sup>13</sup>C]glucose and [2-<sup>13</sup>C]acetate.

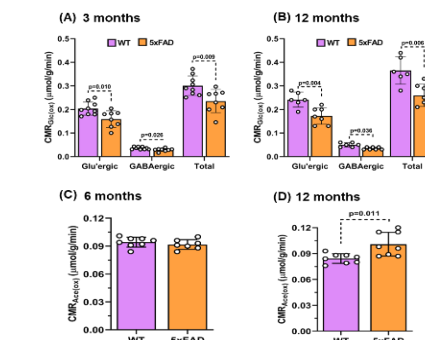


Fig 2. Cerebral metabolic rate of glucose oxidation (A,B) and acetate oxidation (C,D) in the cerebral cortex of 5xFAD and WT mice.

## Reference

- [1] CM Karch et al (2014) *Neuron*, 83(1):11. [2] H Oakley et al (2006) *J Neurosci*, 26(40):10129. [3] AB Patel et al (2018) *J Cereb Blood Flow Metab*, 38(7):1213. [4] AA Epstein et al (2013) *J Neuroimmune Pharmacol*, 8(5):1224. [5] V Tiwari et al (2013) *J Cereb Blood Flow Metab*, 33(10):1523. [6] RA de Graaf et al (2003) *Magn Reson Med*, 49(1):37. [7] PK Mishra et al (2018) *J Neurochem*, 146(6):722.

# Differentiating a primary CNS lesion from a metastatic brain lesion: A radiomics study

## Introduction

To build a machine learning based model to identify tumor type, based on the tumor's ones( necrosis, edema and tumor enhancing area) using quantitative radiomic feature using a contrast enhancing t1-weighted MRI image data set.

## Methods

We used a pre-operative CEMRI dataset from patients with proven primary tumor ( $n = 27$ ) and metastatic tumor ( $n = 22$ ) to calculate radiomic features on the preprocessed and segmented tumor masks, followed by an optimal feature selection and multiclass classification. On both unimodal and multimodal feature sets, the performance of three classifiers was evaluated, and the most discriminative radiomic characteristics involved in the categorization of primary and metastatic subtypes depending on the zone were obtained.

## Results

Multimodal characteristics outperformed unimodal features in differentiating edema of the primary tumor from other zones, with an accuracy of 55 percent on test data and over 84 percent on cross validation, as well as an overall specificity of over 57 percent. Among the unimodal feature sets, those obtained from Zone-1 (necrosis) performed exceptionally well in identifying all three tumor Zones. with a test data accuracy of 77 percent and a cross validation accuracy of over 84 percent, and an overall specificity of

over 77 percent.

## Conclusion

This study shows how a radiomics-based Contrast-Enhanced MRI can reliably distinguish between primary and metastatic tumor zones that appear identical otherwise.

## Keywords

radiomics, IDH-wild-type, IDH1 negative, classification, GBM, multiple lesions, solitary lesions, Metastatic tumor, glioblastoma multiforme, MRI

## Diffusion Tensor Imaging in Pediatric Kidney Transplants.

Suraj D. Serai, Hansel J. Otero, Tatiana Morales, Tricia Bhatti, Bernarda Viteri

### Introduction

We aim to determine the feasibility of MR diffusion tensor imaging (DTI) at 3T on pediatric kidney transplant recipients, compare transplanted kidneys quantitative diffusion values to otherwise healthy control kidneys, and correlate DTI values with allograft histopathology and function.

### Methods

In this NIH-funded prospective study, Imaging Modalities of Pediatric Assessments of Kidney Transplants (IMPAKT), pediatric kidney transplant recipients (referred for clinical allograft biopsies) and healthy controls underwent MRI to obtain DTI-derived metrics (fractional anisotropy [FA] and track length) of the kidney cortex from February 2020 to October 2023 in a single pediatric center. DTI was performed with 2 b-values and 20 noncollinear directions. DTI-derived metrics were compared between the transplant recipients (with and without rejection and/or chronic damage), and healthy controls using two-sample t-test or Wilcoxon rank-sum test.

### Results

Fifteen kidney transplant recipients (4F/11M, median age 16 years, IQR 13-18 years) and 30 control kidneys from 15 healthy controls (9F/6M, median age 15 years, IQR 12-22 years) were evaluated. With our imaging protocol, DTI was feasible on kidney allografts and healthy controls. A statistically significant difference in FA values was observed between allografts (median [IQR]: 0.25 [0.25-0.28]) and

controls (0.28 [0.27-0.33], p value = 0.003). A difference was also observed for track length between allografts (mean:  $19.36 \pm 5.21$ ) and controls ( $12.80 \pm 3.34$ , p-value < 0.001). There were no differences in FA or track length between allografts with and without rejection, and/or with chronic damage index score of 2+ vs. those with a score < 2.

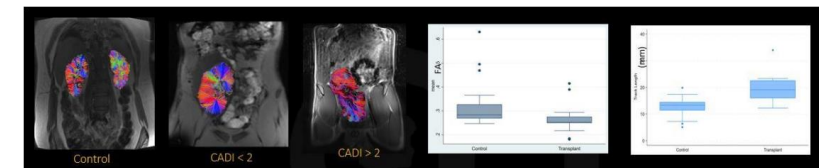
### Discussion

: In this pilot of the IMPAKT study we determined that prospective MR imaging performed prior to clinical biopsies among pediatric kidney transplant recipients is feasible with a success rate of 100% of high-quality images obtained for analysis in 15 kidney transplant recipients, recruitment remains ongoing. When comparing DTI parameters between pediatric kidney allografts (median donor aged 31 years) and healthy controls (median age 15 (IQR,12:22), we found a significant difference in the FA values, with lower values in kidney allografts ( $0.26 \pm 0.06$ ) than in control kidneys ( $0.32 \pm 0.09$ ). Our findings suggest that kidney allografts result in loss of coherent normal orientations resulting in multidirectional water diffusion and, hence, relatively low FA values. For MR-DTI of the kidney to be used for clinical decision making, the technique needs to be consistent and diffusion metrics need to be reliably obtained. In our study, DTI metrics (track length, ADC and FA) were obtained from kidneys on every subject and significant differences in track length and FA were observed between native and transplanted kidneys. The superimposed DTI fiber tractography over clinical MR images allows clinicians to

have a better understanding of the additional information provided using DTI which cannot be obtained with conventional MR images. Our study had limitations, mainly those of the relatively small sample size and the unequal gender distribution. However, our main objective was to test feasibility pilot of DTI on patients with kidney transplant and even with a relatively small sample size, we were able to show some statistically significant differences. Next, the underlying pathologic conditions that led to impaired kidney function were heterogeneous. Thus, the potential for DTI to differentiate between pathologic conditions (e.g., acute rejection, acute tubular necrosis) cannot be derived from our results.

### Conclusion

Our study proved clinical feasibility of DTI in pediatric kidney transplants. DTI of the kidney cortex shows significantly different FA values between transplanted and control kidneys. These results demonstrate the feasibility of DTI-metrics in pediatric kidney allografts and healthy controls.



## Does Resting fMRI have the potential of EEG to pick up epilepsy network: An exploratory methodology study

### Introduction

Comparative Analysis of Automatics and Semi-Automatic of Artifacts Identification and removal to identify epilepsy network using RS-fMRI Studies.

### Methods

128 epilepsy patients with MTS, Multiple foci, FCD, tumor, and gliosis, etc. underwent rs-fMRI study. Their rs-fMRI data were analyzed with the ICA analysis in FMRIB's Software Library (FSL). Different biological networks and non-biological networks and other artifactual networks were studied using ICA analysis and identification was done using two different methodologies, one is the Automated ICA cleaning approach using FMRIB's ICA based X noisefier (FIX) and another one is Semi-automatic approach called visual correlation method developed in house.

### Results

ICA was generated from all the RS-fMRI images and labelling was done using FSL-FIX and semi-automatic approach and accuracy of both approaches was correlated . After observing the result of the approach, the semiautomatic correlation approach is a more accurate and efficient method for the identification and removal of artifacts than the automatic approach (FSL-FIX).

### Conclusion

Automated ICA-based cleaning approach, FIX is using machine learning for identifying the artifacts and removal of them, but the semi-automatic approach or correlation method identifies artifacts based on correlation. This study concludes that the correlation-based method is more accurate than the automated ICA-based cleaning approach to identify epilepsy networks as the

automatic classifier was identifying it as noise and certain large scale networks were also misclassified as noise in a pathological condition such as epilepsy

# Deep Learning-Based Framework for Automated Stroke Detection Using DWI and ADC MRI Sequences

Ankit Kandpal<sup>1</sup>, Rakesh Kumar Gupta<sup>2</sup>, Anup Singh<sup>1,3,4</sup>

<sup>1</sup>Centre for Biomedical Engineering, Indian Institute of Technology Delhi, New Delhi; <sup>2</sup>Department of Radiology, Fortis Memorial Research Institute, Gurugram;

<sup>3</sup>Department of Biomedical Engineering, All India Institute of Medical Sciences Delhi, New Delhi; <sup>4</sup>Yardi School of Artificial Intelligence, Indian Institute of Technology Delhi, New Delhi

## Introduction

Stroke involves a rapid decline in brain function caused by a disruption in blood supply to the brain. Ischemic strokes account for nearly 85% of all stroke cases [1]. Diffusion-weighted-imaging (DWI) is widely used to identify the ischemic core region. DWI images with high b-value (e.g.,  $b=1000 \text{ s/mm}^2$ ) and apparent-diffusion-coefficient (ADC) maps have been used to identify and differentiate various tissue regions within the stroke-affected area. There is a need for fast and automated method which can assist radiologists in achieving objective assessment of stroke, including identification of potential stroke affected slices. The current study aims to develop a fully automated framework for identification of the stroke affected slices using DWI and ADC maps.

## Methods

MRI data from Ischemic Stroke Lesion Segmentation 2022 (ISLES22) challenge was used for the current study [2]. The dataset consisted of MRI data of 151 patients with previously diagnosed or suspected stroke along with labelled masks of stroke lesion. MRI acquisition sequences included FLAIR and DWI ( $b = 1000 \text{ s/mm}^2$ ) images and ADC maps. All the images provided in the ISLES22 challenge were already preprocessed. The dataset was split into training, validation, and testing sets in the ratio of 70:10:20. The image data was divided into three groups: DWI images (group-1), ADC images (group-2), and the combination of DWI and ADC (group-3). Images for group-3 were generated by having DWI in one channel and ADC in another channel of the same image.

For stroke detection, three classification networks MobileNet-v2, Inception-v3, and Xception were employed as the base models. On-the-fly affine data augmentation were carried out to reduce model overfitting. To evaluate the overall performance of the classifier's accuracy, precision, and recall were computed. All networks were re-trained on our dataset for 50 epochs using Adam optimizer with an initial learning rate 0.0001. The learning rate dropped by 0.1 every five epochs. The batch size and L2-regularization were set at 4 and 0.00001, respectively.

## Results

The results of stroke detection corresponding to different image sequences are presented in Table 1. For DWI, Inception-v3 achieves the highest accuracy (0.95), precision (0.95), and recall (0.79) on validation data, while Xception achieves the highest precision (0.96) and recall (0.78) on the test set. For ADC,

Inception-v3 performs best overall, particularly on recall with a test recall of 0.38. Combining DWI and ADC image sequence improves performance across all metrics, with Inception-v3 achieving the best accuracy (0.96) and recall (0.80) on the validation set and the highest test precision (0.96). Notably, all networks exhibit poor recall on ADC maps. Xception provides a good balance between accuracy and recall but has lower precision compared to the other models.

## Discussion

The current study evaluated the performance of a DL framework for stroke identification on DWI and ADC maps. The findings highlight that integrating the two image sequences improves classification accuracy. DWI and ADC images provide information on the tissue microstructure and are highly sensitive to diffusion of the water molecules, which helps identify the ischemic core. This is a preliminary study which needs to be further validated on large data from multi-centers.

**Conclusion:** The current study suggests that a deep learning framework trained on the combination of DWI and ADC images can identify the stroke affected image slices with a mean classification accuracy of 0.92.

## Reference

- [1] C. Zerna, G. Thomalla, B. C. V Campbell, J. Rha, and M. D. Hill, "Series Stroke 1 Current practice and future directions in the diagnosis and acute treatment of ischaemic stroke," *The Lancet*, vol. 392, no. 10154, pp. 1247–1256, 2018, doi: 10.1016/S0140-6736(18)31874-9.
- [2] C. W. Cereda et al., "A benchmarking tool to evaluate computer tomography perfusion infarct core predictions against a DWI standard," *Journal of Cerebral Blood Flow and Metabolism*, vol. 36, no. 10, pp. 1780–1789, Oct. 2016, doi: 10.1177/0271678X15610586.

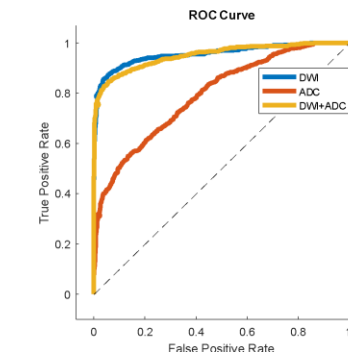


Figure 1 Receiver Operating Characteristic (ROC) curves for DWI (in blue), ADC (in orange), and DWI+ADC (in yellow) image sequences for the test dataset.

Networks	Dataset	DWI			ADC			DWI+ADC		
		ACC	PR	RE	ACC	PR	RE	ACC	PR	RE
MobileNet-v2	Validation	0.94	0.87	0.71	0.86	0.71	0.15	0.94	0.96	0.65
	Test	0.90	0.93	0.71	0.77	0.90	0.22	0.90	0.96	0.68
Inception-v3	Validation	0.95	0.95	0.75	0.86	0.71	0.21	<b>0.96</b>	<b>0.92</b>	<b>0.80</b>
	Test	0.93	0.96	0.79	0.79	0.88	0.31	<b>0.92</b>	<b>0.96</b>	<b>0.76</b>
Xception	Validation	0.94	0.84	0.78	0.86	0.60	0.26	0.95	0.88	0.78
	Test	0.93	0.96	0.78	0.80	0.83	0.38	0.93	0.94	0.78

Table 1 Performance Comparison of MobileNet-v2, Inception-v3, and Xception on DWI, ADC, and Combined DWI+ADC Modalities Using Validation and Test Datasets

# Design, Development and Performance Evaluation of Ultra Flexible Multi-Channel Surface Receive Coil for 1.5T MRI System

Sanket Gothankar, Bhaskara Naik, Arvind Sharma, Mahadev Dipnaik, Tejashree Jadhav, Rahul Roy Chowdhury, Tapas Bhuiya, Rajesh Harsh

Scientist, Medical System Division, SAMEER, Mumbai, India

## INTRODUCTION

MRI (magnetic resonance imaging) is a non-invasive diagnostic technique used in medical diagnosis to create detailed images of the body parts. The design and performance of radiofrequency coils, particularly surface receive coils, have a considerable impact on the quality of MRI pictures [1]. A 4-channel ultra-flexible surface receiving coil designed for a 1.5T MRI system was developed and evaluated. The coil is engineered to fit uneven anatomical surfaces, resulting in maximum signal sensitivity. The selection of flexible materials and a properly planned coil layout allows for great flexibility while maintaining RF performance. The coil's performance was evaluated by imaging a phantom and wrapping it around it. The results highlight the potential for enhanced signal reception and adaptability in clinical and research applications, particularly when imaging anatomically complicated areas. [2].

## METHODS

A 4-channel flexible surface receiving coil was developed using a 0.254 mm thick FR-4 substrate since it is cost-effective and widely available. To achieve optimal signal reception, each coil channel's impedance was optimized to  $50\ \Omega$ . The coil was tuned to 63.87 MHz, the Larmor frequency for a 1.5T MRI system, using a Vector Network Analyzer and a decoupled probe. Active detuning was tested with an external DC bias voltage, and the S21 parameter was monitored; the results are reported in table 1. The coil's performance was assessed by comparing it to a single-channel loop coil and axial slices were acquired using a single-channel coil and a four-channel flexible coil. The Signal-to-Noise Ratio (SNR) was measured using software created by the CDAC, Trivandrum as part of the iMRI project.

## RESULT

The performance evaluation demonstrated a significant improvement in SNR when using the 4-channel flexible coil compared to the single-channel loop coil. Table 2 presents a summary of the SNR results.

Channel	Tune-S21 (dB)	Active Detune- S21 (dB)	Difference (dB)
CH1	-22.29	-55.28	32.99
CH2	-21.48	-50.85	29.37
CH3	-21.40	-53.47	32.07
CH4	-21.54	-55.27	33.73

Coil Type	SNR (Mean)	SNR (NEMA)
Single-Channel loop Coil (Rigid)	21.5083	36.069
4-Channel Ultra- Flexible Surface Receive Coil	28.8929	92.0515

## CONCLUSION

In SNR studies, the 4-channel ultra-flexible surface receive coil performed much better than the single-channel loop coil, confirming its improved performance for 1.5T MRI systems. Its versatility and use of a cost-effective FR-4 substrate make it a viable option for high-quality imaging in anatomically difficult areas.

## DISCUSSION

The higher SNR demonstrates the benefits of multi-channel and anatomically adaptable designs. The FR-4 substrate ensured cost effectiveness and mechanical adaptability, while precise tuning and detuning resulted in adequate channel decoupling and impedance matching. Future research could look into higher channel counts and testing on human phantoms to broaden its clinical relevance. This coil is a significant step forward in improving MRI imaging quality and adaptability.



Figure 1. Left: MRI scan setup with single-channel surface receive loop coil (rigid) for phantom imaging; Right: developed ultra-flexible 4-channel receive coil wrapped around phantom



Figure 2. SNR measurement with a single-channel loop coil: axial slice of a phantom



Figure 3. SNR measurement with 4-channel flexible surface receive coil: axial slice of a phantom

## Reference

- [1] B. D. Collick et al., "Rapid development of application-specific flexible MRI receive coils," *Phys. Med. Biol.*, vol. 65, no. 19, p. 19NT01, Sep. 2020, doi: 10.1088/1361-6560/abaffb.
- [2] P. B. Roemer et al., "The NMR phased array," *Magn. Reson. Med.*, vol. 16, no. 2, pp. 192-225, Nov. 1990, doi: 10.1002/mrm.1910160203.

# Designing an electromagnetic field generator for intraoperative real time tracking in image guided interventions

Varun Nair<sup>1</sup>, Devasenathipathy Kandasamy<sup>2</sup>, Amit Mehndiratta<sup>1,3</sup>

<sup>1</sup>Centre for Biomedical Engineering, Indian Institute of Technology Delhi, New Delhi, India, <sup>2</sup> Department of Radio Diagnosis, All India Institute of Medical Sciences, New Delhi, India, <sup>3</sup>Department of Biomedical Engineering, All India Institute of Medical Sciences, New Delhi, India.

## Introduction

Magnetic resonance imaging (MRI) provides superior soft tissue contrast which is beneficial in detecting lesions in the brain, spinal cord, liver, and musculoskeletal system. This advantage makes MRI a valuable tool for image-guided interventions, such as biopsies, ablations, and catheter-based procedures [1]. These procedures require high precision and dexterity due to their minimally invasive nature. The development of such skills requires intricate training, that maybe difficult to achieve in standard clinical teaching settings due to ethical considerations and resource constraints [2]. Simulation-based training has the potential to overcome these concerns with real time intraoperative tracking and navigation of surgical instruments [3]. Among the various real time tracking techniques, electromagnetic (EM) sensor-based tracking stands out for its high spatial accuracy, and ability to function without a direct line of sight, making it particularly well-suited for minimally invasive procedures [4]. This study aims to design and simulate an EM field generator circuit for real-time instrument tracking, that can be integrated in a simulator for training in image-guided interventions.

## Methods

The electronics design was adapted from an open-source framework, incorporating modifications to improve functionality and ensure system compatibility. A key aspect was the planar field generator, consisting of eight independent coils, each with its dedicated circuitry. The circuit for each coil included three main components: a signal generator, a current amplifier, and a field generator coil. The signal generator was assembled on a perforated board using a Teensy 4.0 microcontroller and an AD9833 function generator. This setup produced the desired waveform via serial port communication, and the voltage magnitude of the generated signal was measured. The current amplifier circuit was designed using KiCAD 8.0 and featured a three-stage amplification. It included a TL081 op-amp, an LM7171 high-speed op-amp, and an LMH6321 current booster, providing the necessary drive capability (as shown in Figure 1). SPICE simulation of the circuit was performed to calculate the expected current output based on the measured voltage. This ensured optimal performance before hardware implementation. The field generator coil was designed as square planar windings on a PCB, following specifications derived from an open-source framework. The windings consisted of 25 turns: 13 on one side and 12 on the other. Each turn had a 0.5 mm width, with 0.25 mm spacing. The outermost turn

measured 7 cm in length. To evaluate the coil's effectiveness, the magnetic field vectors were computed at equally spaced grid points using the Biot-Savart law and filament current model, based on the simulated current output. The vectors were plotted via a MATLAB simulation to generate a 3D magnetic field map.

## Results

The output of the first two amplification stages was visualized and quantified using the PicoScope 2205A. The Teensy microcontroller controlled eight function generators, each operating with a frequency step size of 2 kHz. The signal generator produced an RMS voltage of 620 mV and an RMS current of 63  $\mu$ A. The current amplifier circuit boosted the output current to 230 mA, while the voltage was regulated to approximately 5 V. Magnetic field intensity plots obtained from a single coil revealed a trapezoidal distribution, with the field strength being highest near the coil and gradually decreasing with distance. At a distance of 1 cm from the coil, the field intensity measured 25 Gauss, whereas at 10 cm, it dropped to less than 2 Gauss. The 3D field map visualization provided insights into the spatial distribution of the magnetic field (as shown in figure 2).

## Discussion and Conclusion

The designed EM field generator is successfully able to generate a magnetic field suitable for tracking applications. The square coils were chosen as magnetic field sources due to their ability to simplify PCB layout and fabrication. Implementing the coils on a PCB allows precise positioning of each track, enabling accurate prediction of the generated magnetic fields with analytical methods. The voltage induced in the receiver coil due to generated field can be demodulated and scaled to determine the magnetic flux contribution from each coil. Once the flux has been calculated, the position and orientation can be estimated using an iterative nonlinear least squares algorithm. Once the tracking module has been fully integrated, it can be used to train radiologists in performing MRI, ultrasonography (USG), or computed tomography (CT) guided interventions via simulation-based training. As a training simulator, such a system would enable precise virtual positioning and orientation of the needle within the imaging environment, allowing the trainee to visualize the trajectory of the needle and improve their hand-eye coordination. Beyond training applications, the module can also facilitate real time tracking of intervention instruments, especially in USG guided interventions. While their application in MRI systems is limited because of the constraints of EM tracking, such modules can be an asset in MRI/USG fusion

imaging based interventions where the EM tracking can provide accurate guidance of the needle to the lesions that are visible only via MRI, but the procedure needs to be performed under USG guidance [6].

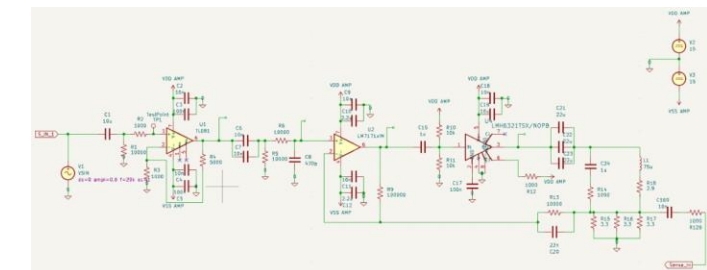


Figure 1 Circuit diagram designed in KiCAD 8.0

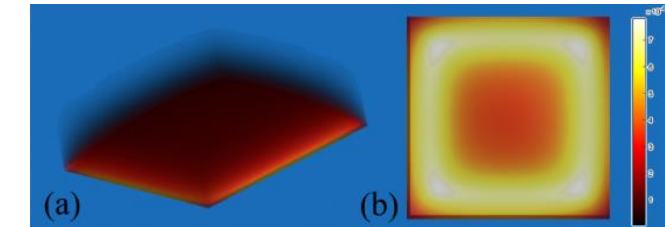


Figure 2 Spatial variation of the simulated magnetic field strength at 0 to 10 cm above the coil (a), and at exactly 1 cm above the coil (b)

## Reference

- [1] S. M. Thompson et al., "Body Interventional MRI for diagnostic and Interventional radiologists: current practice and future prospects," *Radiographics*, vol. 41, no. 6, pp. 1785–1801, Oct. 2021, doi: 10.1148/rug.2021210040.
- [2] H. Jamil et al., "Interventional radiology in low- and middle-income countries," *Annals of Medicine and Surgery*, vol. 77, Apr. 2022, doi: 10.1016/j.amsu.2022.103594.
- [3] I. Mandal and U. Ojha, "Training in Interventional Radiology: A Simulation-Based Approach," *Journal of Medical Education and Curricular Development*, vol. 7, Jan. 2020, doi: 10.1177/2382120520912744.
- [4] A. Ramadani, M. Bui, T. Wendler, H. Schunkert, P. Ewert, and N. Navab, "A survey of catheter tracking concepts and methodologies," *Medical Image Analysis*, vol. 82, p. 102584, Aug. 2022, doi: 10.1016/j.media.2022.102584.
- [5] H. A. Jaeger et al., "Anser EMT: the first open-source electromagnetic tracking platform for image-guided interventions," *International Journal of Computer Assisted Radiology and Surgery*, vol. 12, no. 6, pp. 1059–1067, Mar. 2017, doi: 10.1007/s11548-017-1568-7.
- [6] P. Fletcher et al., "Vector Prostate Biopsy: A novel Magnetic Resonance Imaging/Ultrasound image fusion transperineal biopsy technique using electromagnetic needle tracking under local anaesthesia," *European Urology*, vol. 83, no. 3, pp. 249–256, Jan. 2023, doi: 10.1016/j.euro.2022.12.007.

# Diffusion Tensor Imaging and Arterial Spin labeled Imaging in Traumatic Brain Injury

**Ekta Dixit<sup>1</sup>, Sudhir Kumar Pathak<sup>2</sup>, B. V. Rathish Kumar<sup>3</sup>, Ranjeet Ranjan Jha<sup>4</sup>, Maninder Singh<sup>1</sup>, Hirak Doshi<sup>1</sup>, Siddharth Singh<sup>1</sup>, Abhishek Singh<sup>5</sup>, Anit Parihar<sup>1</sup>, Chhitij Srivastava<sup>5</sup>, Bal Krishna Ojha<sup>5</sup>, Anil Chandra<sup>5</sup>, and Durgesh Kumar Dwivedi<sup>1</sup>**

<sup>1</sup>Department of Radiodiagnosis, King George's Medical University, Lucknow, India, <sup>2</sup>Learning Research and Development Center, University of Pittsburgh, Pittsburgh, PA, United States, <sup>3</sup>Department of Mathematics and Statistics, Indian Institute of Technology, Kanpur, India,

<sup>4</sup>Department of Mathematics, Indian Institute of Technology, Patna, India, <sup>5</sup>Department of Neurosurgery, King George's Medical University, Lucknow, India

## Introduction

Traumatic Brain Injury (TBI) caused by external forces, leading to structural and functional damage in the brain. Diffusion Tensor Imaging (DTI) is an advanced MRI technique that measures the diffusion of water molecules within brain tissue. It provides critical insights into white matter integrity using metrics such as: Apparent Diffusion Coefficient (ADC), Fractional Anisotropy (FA) and Radial Diffusivity [1]. ASL parameters include: Time to Peak (TTP), Mean Transit Time (MTT), and Cerebral Blood Volume (CBV) [2]. DTI detects microstructural damage (axonal injury, demyelination) caused by TBI, while ASL assesses perfusion deficits (reduced blood flow and vascular dysfunction). DTI and ASL analysis helped in early TBI diagnosis, prognosis, and treatment monitoring. This integrated approach enhances clinical understanding of TBI severity, progression, and recovery.

## Methods

Image Acquisition was performed with Philips 3T MRI Scanner. DTI image acquisition protocol: Gradient Directions: 30–64 directions, b-values: 0 and 1000s/mm<sup>2</sup>, Voxel Size: 2 mm<sup>3</sup> isotropic, Slice Thickness: 2 mm with no gap, Repetition Time (TR): ~8000–10000 ms, Echo Time (TE): ~90–100 ms. Philips MRI viewer used to draw Region of Interests (ROIs) in DWI, DTI, and ASL images to obtain ADC, FA, RD, TTP, MTT, and CBV values. T1-weighted and T2-weighted images were seen for accurate anatomical localization of Injury. We manually drawn 3 ROIs in Injury region and 3 ROIs in normal area and obtained mean values of ADC, FA, RD, and values of TTP, MTT, CBV from each ROI.

## Results

The ROIs (green circles) in ADC map (fig.1A) and CBV map (fig.2B). ADC, FA, and RD, reveals differences between TBI and control regions (fig.1D). The mean ADC values were higher in TBI regions compared to control regions ( $1.9 \pm 0.7$  vs  $1.5 \pm 0.5$  ( $10^{-3}$ mm<sup>2</sup>/sec)), mean FA values were lower in TBI regions ( $0.7 \pm 0.2$  vs  $0.9 \pm 0.3$ ) and mean RD values were elevated in TBI regions ( $1.6 \pm 0.6$  vs  $1 \pm 0.3$ ). Further, ASL parameters TTP, and CBV were elevated in TBI regions ( $602 \pm 335$  vs  $434 \pm 291$ ), while MTT showed slight increment. Fig.2A shows mean ADC, FA, RD values TBI and control regions for each patient. The ADC and RD are elevated in injury regions in all the patients. On the other hand, the FA is reduced in injury regions in all the patients. The TTP is elevated in injury regions in 7 out of 10 patients. The CBV shows elevated levels in injury region in half of the patients. MTT shows elevated levels in injury regions of 6 patients.

## Discussion

ADC and RD exhibit a strong positive correlation, indicating that an increase in extracellular diffusion is associated with structural disruption in injury regions. FA is negatively correlated with both ADC and RD, giving idea that reduced anisotropy is linked to increased isotropic diffusion in damaged tissues. In the injury group, the ADC and RD are both high, suggesting that injury severity directly affects diffusion properties. Elevated CBV levels suggests increased blood volume in injury and low MTT suggest slow blood flow rate in both injury and control regions. These findings suggests a relation between diffusion and perfusion metrics in characterizing white matter integrity loss in TBI patients.

## Conclusion

The analysis of diffusion and perfusion MRI parameters highlights significant differences between injury and control regions in TBI patients. ADC, FA, RD provides insights into white matter integrity, while ASL derived parameters (TTP, MTT, CBV) reveal cerebral perfusion deficits. The correlations observed between these parameters further strengthen the interdependence of these imaging biomarkers. These findings support the use of multi-parametric MRI in TBI assessment, aiding in early diagnosis, prognosis, and treatment planning.

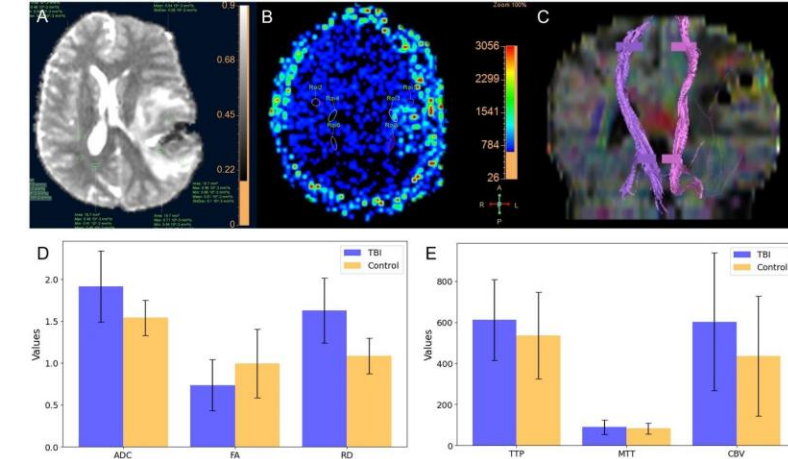


Figure 1 Showing ROIs in (A) ADC map (B) ASL CBV map. (C) DTI (D) plot showing mean ADC ( $10^{-3}$ mm<sup>2</sup>/sec), FA, RD values in TBI or injury and control regions. (E) plot showing mean TTP, MTT, CBV values in TBI or injury and control regions.

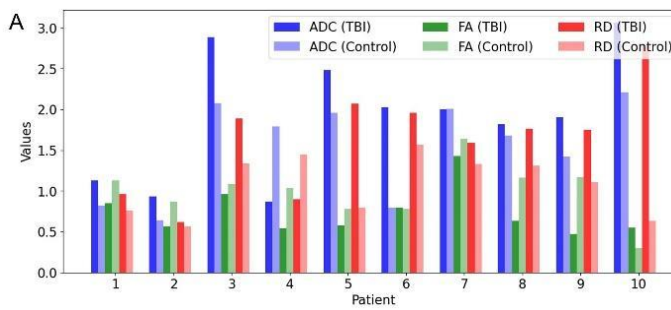


Figure 2 (A) plot showing ADC ( $10^{-3}$ mm<sup>2</sup>/sec), FA, and RD values in injury and control regions of each patient.

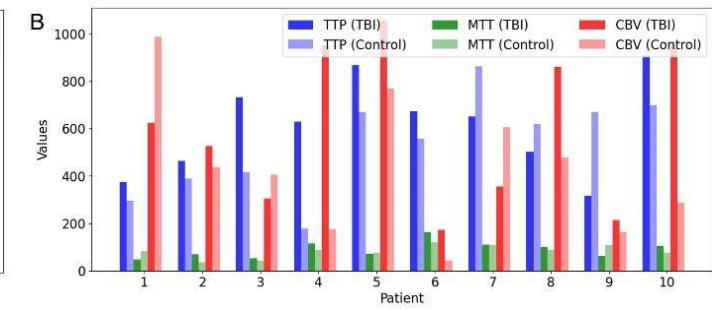


Figure 2 (B) plot showing TTP, MTT, and CBV values in injury and control regions of each patient.

## Acknowledgements

Dr. D.K. Dwivedi expresses sincere gratitude to CST (Grant No. CST/D-1381). Dr. D.K. Dwivedi and Prof. B.V. Rathish Kumar extend their sincere thanks to the funding agencies for their support: the Indian Council of Medical Research, New Delhi (ICMR, Grant No. EM/Dev/IG/27/0337/2023). Furthermore, Prof. B.V. Rathish Kumar (IITK, India) and Dr. S.K. Pathak (Pitt, USA) express their heartfelt appreciation to SPARC for their support (Grant No. SPARC/2019-2020/P1622/SL).

## Additional

Additionally, Dr. D.K. Dwivedi conveys sincere gratitude to the Science and Engineering Research Board (now ANRF), New Delhi (SERB, Grant No. SUR/2022/001841).

## Reference

- [1] [1] E.A. Wilde, S. R. McCauley, J. V. Hunter, E. D. Bigler, Z. Chu, Z. J. Wang, G. R. Hanten et al., Neurology 70, no. 12 (2008): 948-955.
- [2] P. Sasitom, J. Ramalho, and M. Castillo., World journal of radiology 2, no. 10 (2010): 384.

# Do brain volumes of obese and non-obese Indian middle-aged men differ? - a first look

Sneha Majumder<sup>1</sup>, Kavitha Menon<sup>2</sup>, Amol Gautam<sup>3</sup>, Bhushan Borotikar<sup>1</sup>

<sup>1</sup>Symbiosis Centre for Medical Image Analysis, Symbiosis International (Deemed University), Pune, India <sup>2</sup>Symbiosis School of Culinary Arts and Nutritional Sciences, Symbiosis International (Deemed University), Pune, India

<sup>3</sup>Department of Radiodiagnosis, Symbiosis University Hospital and Research Centre, Symbiosis International (Deemed University), Pune, India

## Introduction

India is said to have one of the fastest-growing obesity rates in the world. Obesity is not only a risk factor for other metabolic diseases but also is a threat to cerebral complications [1]. It has been reported earlier that obesity is associated with alterations in brain volumes in the Western population [2]. However, obesity as a disease has a pathophysiological dependence on the accretion of fat, and Indian ethnicity is more vulnerable to fat accumulation and abdominal obesity [3]. Among Indian men, obesity has increased to 22.9% from 9.3% within a span of 15 years [4], whereas there have been fewer attempts to understand the impact of obesity on the brains of Indian men. This study aims to evaluate the volumetric changes in the brain due to obesity among Indian middle-aged men in urban settings.

## Methods

A case-control study was designed with a sample size of n=23 (obese = 11). The volunteers meeting the inclusion criteria were categorized into obese and non-obese cohorts based on waist circumference, as per the international criteria of the World Health Organization. Cohorts were formed after scrutinizing for MRI contraindications and disease history. The anthropometric measurements such as body mass index (BMI), waist circumference (WC), waist to hip ratio (WHR) were recorded along with body composition analysis by bioelectrical impedance analysis (BIA). The volunteers were scanned for a T1-weighted brain MRI in a 3T MRI scanner (Philips Healthcare, Ingenia 3.0 T) with the turbo field echo (TFE) sequence and the parameters: TE = 3.0ms, TR = 6.4ms, FOV = 210mm x 210mm x 180mm, voxel size = 1mm x 1mm x 1.2 mm, matrix = 210 x 210, slices = 150, gap = 0mm, slice thickness = 1.2mm and flip angle = 8degrees. The images were converted to NIfTI format from DICOM by MRIcron (RRID:SCR002403), pre-processed, and analyzed in FSL (FMRIB software library). The skull stripping was done by FSL-BET tool. Next, to generate the partial volume estimation (PVE) maps of white matter, grey matter (Figure 1, 2), and cerebrospinal fluid, and volume estimation of each segmented class, the FSL-FAST tool was used. To normalize the volumes with skull size, the SIENAX tool was applied. FSL-FIRST was used to segment (Figure 3) and calculate the volume of the left hippocampus. The statistical analyses were carried out in SPSS ver. 22 (IBM Corp, NY, USA). Independent T-Test was applied to compare the means of the volumetric parameters of obese and non-obese cohorts.

## Results

The mean BMI and WC in the obese group were  $30.14 \pm 3.98 \text{ kg/m}^2$  and  $99.89 \pm 5.28 \text{ cm}$ , respectively (Table 1). The obese group had shown a significant

decrease in peripheral grey matter volume ( $p=0.014$ ), total grey matter volume ( $p=0.020$ ) and total brain volume ( $p=0.027$ ). The significant differences were observed after normalizing the volumes with the skull size by SIENAX package (Table 2).

## Discussion

This study reports significant reduction in brain volumes in obese individuals with no other morbidities. These findings corroborate well with earlier findings in the Western population, indicating the risks of developing the cerebral consequences of obesity [5], [6]. Reduced grey matter volume is associated to cognitive decline and neurodegenerative diseases like Alzheimer's Disease and Parkinson's disease [7]. Reduction in total brain volume is a classical depiction of brain atrophy [8]. The brain function and cognition is severely impacted in presence of brain atrophy [9]. The left hippocampus showed no significant difference among the cohorts as reported in earlier literature [10], [11]. This may indicate the limitation of small sample size of the current study.

## Conclusion

This is the first study in India that delved in understanding the complications in the brain due to obesity among middle aged Indian men. Even after considering the limitation of small sample size of this study, the grey matter volumes (total and peripheral) and total brain volume were significantly low in obese group. This reinforces the gravity of obesity as a disease beyond the established metabolic complications. Early intervention to manage obesity may help in ceasing the detrimental cerebral consequences.

Parameters	mean±SD	
	Obese (n=11)	Non-obese (n=12)
Age (years)	47.36±4.8	45.75±4.3
Weight (Kg)	85.44±9.3	66.38±6.8
BMI ( $\text{kg}/\text{m}^2$ )	30.14±3.98	23.24±2.2
Waist circumference (cm)	99.89±5.28	83.09±4.8
Waist to hip ratio	0.96±0.03	0.83±0.4
Fat percentage	29.80±3.71	21.72±2.6

Parameters (tools)	mean±SD ( $\text{cm}^3$ )		p-value <sup>#</sup>
	Obese (n=11)	Non-obese (n=12)	
Grey matter volume (FSL-FAST)	581.60±42.37	577.09±41.86	0.800
White matter volume (FSL-FAST)	517.65±15.64	513.59±10.95	0.834
Total brain volume (FSL-FAST)	1099.26±92.08	1090.68±76.73	0.812
Peripheral grey matter volume (SIENAX)	537.60±22.62	563.26±23.33	0.014*
Total grey matter volume (SIENAX)	631.31±22.19	655.25±23.59	0.020*
Total white matter volume (SIENAX)	651.52±24.37	662.40±14.69	0.218
Total brain volume (SIENAX)	1282.84±39.79	1317.66±27.61	0.027*
Volume of left hippocampus (FSL-FIRST)	3.14±0.56	2.97±0.20	0.351



Figure 1 PVE map of grey matter segmented by FSL-FAST



Figure 2: PVE map of white matter segmented by FSL-FAST

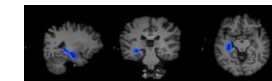


Figure 3: Segmentation of left hippocampus by FSL-FIRST  
Reference

- [1] M. Venkata Rao, R. Nagarathna, V. Majumdar, S. S. Patil, S. Rathi, and H. Nagendra, "Prevalence of Obesity in India and Its Neurological Implications: A Multifactor Analysis of a Nationwide Cross-Sectional Study," *Ann. Neurosci.*, vol. 27, no. 3-4, pp. 153–161, Jul. 2020, doi: 10.1177/097275312097465.
- [2] H. Tanaka, D. D. Gorlay, M. Dekhtyar, and A. P. Haley, "Cognition, Brain Structure, and Brain Function in Individuals with Obesity and Related Disorders," *Curr. Obes. Rep.*, vol. 9, no. 4, pp. 544–549, Dec. 2020, doi: 10.1007/s13679-020-00412-y.
- [3] G. Danaei et al., "National, regional, and global trends in fasting plasma glucose and diabetes prevalence since 1980: systematic analysis of health examination surveys and epidemiological studies with 370 country-years and 2.7 million participants," *The Lancet*, vol. 378, no. 9785, pp. 31–40, Jul. 2011, doi: 10.1016/S0140-6736(11)60679-X.
- [4] G. Singh, R. Agrawal, N. Tripathi, and A. Verma, "Overweight and obesity, the clock ticking in India? A secondary analysis of trends of prevalence, patterns, and predictors from 2005 to 2020 using the National Family Health Survey," *Int. J. Noncommunicable Dis.*, vol. 8, no. 1, p. 31, Mar. 2023, doi: 10.4103/jncd.jncd\_58\_22.
- [5] J. Mazon, A. Haas de Mello, G. Ferreira, and G. Rezin, "The impact of obesity on neurodegenerative diseases," *Life Sci.*, vol. 182, Jun. 2017, doi: 10.1016/j.lfs.2017.06.002.
- [6] A. Neto, A. Fernandes, and A. Barateiro, "The complex relationship between obesity and neurodegenerative diseases: an updated review," *Front. Cell. Neurosci.*, vol. 17, Nov. 2023, doi: 10.3389/fcell.2023.1294420.
- [7] J. P. Kueck, J. K. Morris, and J. A. Stanford, "Current Perspectives: Obesity and Neurodegeneration - Links and Risks," *Degener. Neurol. Neuromuscul. Dis.*, vol. 13, pp. 111–129, Dec. 2023, doi: 10.2147/DNN.D388579.
- [8] R. Sungura, C. Onyambu, E. Mpolyia, E. Souli, and J.-M. Vianney, "The extended scope of neuroimaging and prospects in brain atrophy mitigation: A systematic review," *Interdiscip. Neurosci.*, vol. 23, p. 100875, Mar. 2021, doi: 10.1016/j.inat.2020.100875.
- [9] V. A. Cardenes et al., "Brain atrophy associated with baseline and longitudinal measures of cognition," *Neurobiol. Aging*, vol. 32, no. 4, pp. 572–580, Apr. 2011, doi: 10.1016/j.neurobiolaging.2009.04.01.
- [10] A. Ambikairajah, H. Tabatabaei-Jafari, E. Walsh, M. Horberger, and N. Cherbuin, "Longitudinal Changes in Fat Mass and the Hippocampus," *Obesity*, vol. 28, no. 7, pp. 1263–1269, 2020, doi: 10.1002/oby.22819.
- [11] N. Cherbuin, K. Sargent-Cox, M. Fraser, P. Sachdev, and K. J. Anstey, "Being overweight is associated with hippocampal atrophy: the PATH Through Life Study," *Int. J. Obes.*, vol. 39, no. 10, pp. 1509–1514, Oct. 2015, doi: 10.1038/ijo.2015.106.

# Detecting Alzheimer's disease with Efficient ViTs

Shanawaj S Madarkar, Madhumitha V, Sunayna Padhye, Konda Reddy Mopuri

{ai23mtech13003@iith.ac.in, ai23resch11004@iith.ac.in, ai23mtech12002@iith.ac.in, krmopuri@ai.iith.ac.in}

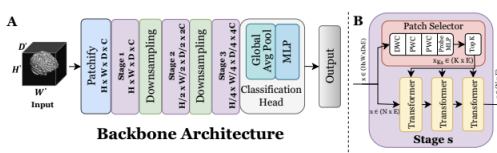
Department of Artificial Intelligence, Indian Institute of Technology, Hyderabad, India

## Introduction

Classifying Alzheimer's disease using high-dimensional 3D structural MRI (sMRI) scans is a challenging task due to the data-intensive nature and complexity of the models required. This work addresses this challenge by proposing a Vision Transformer (ViT)-based architecture that leverages the high inductive bias of CNNs as a guiding module for transformers. Additionally, we introduce efficient strategies to mitigate the quadratic complexity of transformers.

## Methods

### A. Architecture



We propose a multi-stage, multi-scale ViT backbone with hierarchical downsampling using 3D CNNs across three stages for multi-resolution feature extraction. To mitigate the quadratic complexity of transformers, each stage incorporates a patch selector module using factorized convolutions, retaining only the top-k informative patches (S1:1500, S2:1000, S3:150) for Key and Value generation, reducing computational cost. Attention with top-k patches is computed as:

$$\text{Attn}(Q, K, V) = \text{Softmax} \left( \frac{QK^T}{\sqrt{d}} \right) V \quad (1)$$

where,  $Q=xW_Q$ ,  $K=x_{K_x}W_K$ ,  $V=x_{K_x}W_V$ ,  $x \in \mathbb{R}^{N \times E}$ ,  $x_{K_x} \in \mathbb{R}^{K_x \times E}$  and  $W_Q, W_K, W_V \in \mathbb{R}^{E \times E}$ . A classification head with Global Average Pool aggregates spatial features for final classification. Fig 1 describes this architecture in detail.

## B. Experiments

The architecture was trained and evaluated on three datasets: ADNI, OASIS, and AIBL. From ADNI, we collected 3802 scans including Alzheimer's Disease (AD), Mild Cognitive Impairment (MCI), and Cognitively Normal (CN) subjects, along with 1261 scans from OASIS and 1097 scans from AIBL. For ADNI, both binary (AD vs. CN) and multi-class (AD vs. MCI vs. CN) classification tasks were performed, while only binary classification was conducted for OASIS and AIBL to ensure robust evaluation across diverse datasets and tasks. We employed an 80:20 train-test split for binary classification and a 70:10:20 train-validation-test split for multi-class classification.

## Results

Table I shows 2-way results of our proposed model against SOTA and baseline model, which randomly picks top-k patches without a patch selector module for all 3 datasets. Table II shows results of 3-way classification on ADNI dataset.

## Conclusion

This work introduces a novel framework for efficient 3D MRI scan processing, demonstrating robust performance and generalizability across three Alzheimer's disease datasets. The proposed model outperforms state-of-the-art methods by at

least  $\sim 3\%$  accuracy while maintaining a lower parameter cost of  $\sim 3.5M$ , ensuring computational efficiency.

TABLE I  
PERFORMANCE COMPARISON WITH SOTA AND BASELINE ON ADNI,  
OASIS, AND AIBL DATASETS FOR 2-WAY CLASSIFICATION (AD-CN)

Dataset	ADNI		OASIS		AIBL		# Params (M)
	Acc. (%)	AUC (%)	Acc. (%)	AUC (%)	Acc. (%)	AUC (%)	
3DResNet152 [1]	87.65	86.92	70.77	70.49	77.59	61.95	117.54 M
3D ViT [2]	80.24	81.35	67.69	67.13	73.56	76.60	33.87 M
M3T [3]	90.05	88.78	80.47	81.67	82.35	80.26	29.12 M
LongFormer [4]	93.43	93.30	82.35	82.86	85.77	84.47	$\sim 35M$
Random K	$96.75 \pm 1.18$	$98.67 \pm 0.06$	$97.83 \pm 0.40$	$99.81 \pm 0.32$	$90.73 \pm 1.23$	$91.20 \pm 1.52$	<b>3.24 M</b>
Top K	$97.09 \pm 1.25$	$98.68 \pm 0.20$	$97.63 \pm 0.62$	$99.82 \pm 0.24$	$91.09 \pm 1.59$	$91.60 \pm 0.99$	<b>3.47 M</b>

TABLE II  
PERFORMANCE COMPARISON WITH BASELINE MODEL (RANDOM K) FOR  
3-WAY CLASSIFICATION ON ADNI DATASET

Model	Acc. (%)	Prec. (%)	Recall (%)	F1 (%)	Loss
Random K	$94.57 \pm 0.65$	$94.67 \pm 0.45$	$93.14 \pm 0.57$	$93.8 \pm 0.52$	$0.28 \pm 0.02$
Top K	$94.45 \pm 0.48$	$94.85 \pm 0.62$	$92.88 \pm 0.51$	$93.78 \pm 0.54$	$0.26 \pm 0.04$

## Reference

- [1] K. He, X. Zhang, S. Ren, and J. Sun, "Deep Residual Learning for Image Recognition," in Proceedings of the IEEE Conference on Computer Vision and Pattern Recognition, 2016, pp. 770–778.
- [2] A. Dosovitskiy, L. Beyer, A. Kolesnikov, D. Weissenborn, X. Zhai, T. Unterthiner, M. Dehghani, M. Minderer, G. Heigold, S. Gelly et al., "An image is worth 16x16 words: Transformers for image recognition at scale," in ICLR, 2020.
- [3] J. Jang and D. Hwang, "M3t: Three-dimensional medical image classifier using multi-plane and multi-slice transformer," in Proceedings of the IEEE/CVF Conference on Computer Vision and Pattern Recognition, 2022, pp. 20718–20729.
- [4] I. Beltagy, M. E. Peters, and A. Cohan, "Longformer: The long-document transformer," arXiv preprint arXiv:2004.05150, 2020.

# Development of anatomically adaptive RF coils for 1.5 T MRI Application

Aravind Prajapati<sup>1</sup>, Mr. Bhaskara Naik S<sup>1</sup>, Mr. Rajesh Harsh<sup>1</sup>, Mr. Tapas K. Bhuiya<sup>1</sup>, Dr. Ashwin Ganesh Kothari<sup>2</sup>

<sup>1</sup>Medical System Department, Society for Applied Microwave Electronics Engineering and Research Mumbai, India, <sup>2</sup>Dept. of Electronics and Communication, Visvesvaraya National Institute of Technology Nagpur, India

## Introduction

Magnetic Resonance Imaging (MRI) stands as a formidable imaging technique, hinging on arrays of detector coils to capture faint RF signals. However, the presence of parasitic coupling among array elements undermines the performance of the imaging system, introducing significant complexity into the array design process. This research not only highlights a notable reduction in surface current through the adoption of a tailored high impedance coil structure but also demonstrates the enhanced adaptability and expandability inherent in this innovative design. Moreover, it underscores improvements in signal-to-noise ratio, quality factor, field of view, and specific absorption rate.

## Methods

### Low Impedance detector:

A low impedance coil refers to a coil or winding in an electrical circuit with a relatively small impedance( $10\Omega$ ). Low-impedance coils (LICs) excel in efficiently capturing electromagnetic fields (EMF) while facilitating the flow of current. Consequently, this current generates a secondary radiofrequency field that neighboring elements can detect. The low impedance coils were fabricated as loops measuring 6 mm in width and almost 5 inch in diameter. On each loop, a single capacitor was consisting of a ( $C_L$ ) 20 pF capacitor along with a variable capacitor placed on top for tuning purposes. Additionally, an ( $C_m$ ) 8 pF fixed capacitor and a ( $L_m$ ) 778 nH inductor were utilized for matching at the port. These coils were subsequently connected to low-input impedance preamplifiers. This concept is depicted in Figure 1(a).

### High impedance detector:

In our pursuit to eradicate resonant inductive coupling among elements, we embarked on crafting a novel element design. This design enables the measurement of electromagnetic fields (EMF) without permitting current flow or the inadvertent induction of signals into neighboring elements. Our work introduces an alternative method for constructing a high-impedance coil (HIC), enabling tuning to various frequencies using a standard  $50\ \Omega$  coaxial cable while maintaining a high Q-factor. This method involves integrating a lumped capacitor ( $C_t$ ) into the gap within the outer conductor of the coaxial cable, as illustrated in Figure 1(b).

## Results

For exploring tuning variability concerning coil geometry, the reflection coefficients of both the HIC and LIC were examined. As shown in Figure 2(a),2(b),2(c), the HIC's reflection coefficient at 63.87 MHz ranged from -20.74, -16.79, -14.07 dB when arranged as a circle, 8×13 ellipse, and 6×15 ellipse, respectively. Conversely, the LIC, offering more flexibility, exhibited reflection coefficients of -16.58, -6.39, and -2.9 dB under the same configurations.

## Discussion

Recent advancements in MRI detector arrays have shifted towards utilizing high impedance coils instead of low impedance coils. These high impedance coils offer improved flexibility and signal sensitivity, enabling parallel signal acquisition. Constructed from flexible coaxial cables, these coils are tuned to the desired frequency by adjusting parameters such as coil length, dielectric properties of the coaxial cable insulator, and the ratio of inner conductor to outer conductor radii. However, achieving this tuning dependency can be challenging, especially in MRI scanning where coil size is typically predetermined based on the shape and size of the object to be imaged. Various methods have been proposed to tune the coils while keeping the coil length constant, such as the use of multi-gap-multi-turn techniques. However, these methods often compromise mechanical flexibility. In this study, we present a novel approach to fabricate high impedance coils that allows for tuning at the desired frequency while maintaining a high Q-factor and SNR. This is accomplished by introducing a lumped capacitor ( $C_t$ ) in the gap of the outer conductor of the coaxial cable, as depicted in Fig. 1(b).

## Conclusion

The high-impedance detector-array exemplifies a breakthrough in MRI technology, offering adaptive, wearable imaging capabilities. By eliminating signal coupling and enhancing flexibility, the detector enables detailed imaging of soft-tissue biomechanics during natural movements. This innovation not only improves imaging quality but also expands MRI's applications, promising advancements in medical diagnostics and research on joint and tissue dynamics.

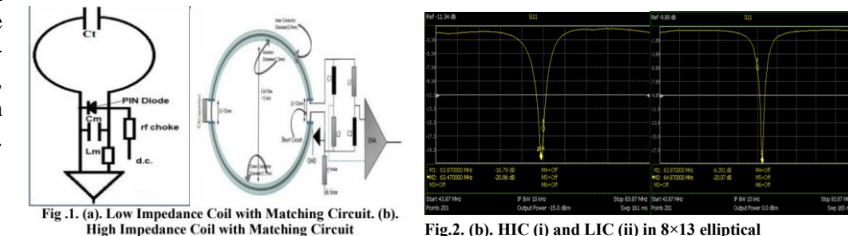


Fig.1. (a). Low Impedance Coil with Matching Circuit. (b). High Impedance Coil with Matching Circuit

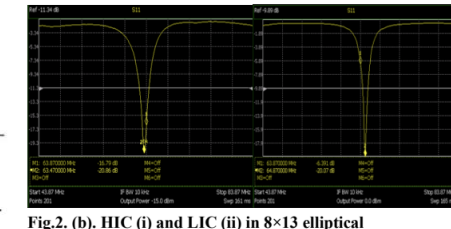


Fig.2. (b). HIC (i) and LIC (ii) in 8x13 elliptical

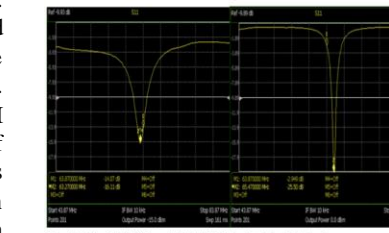


Fig.2. (c). HIC (i) and LIC (ii) in 6x15 elliptical

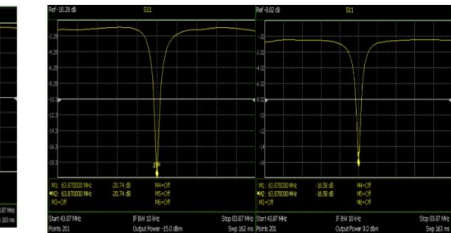


Fig.3. (a). HIC (i) and LIC (ii) in Circular (~12.5)

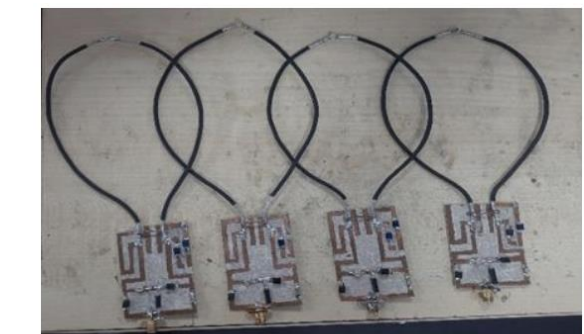


Fig.3. Fabricated of 4 channels HIC

# Early Biomarkers of Birth Asphyxia-Induced HIE: A Novel NMR, Neuroimaging, and AI-Based Approach for Precise Diagnosis

Ashish Panigrahi<sup>1</sup>Rittika Dutta<sup>1</sup>Vivek Tiwari<sup>1</sup>

<sup>1</sup> Indian Institute of Science Education and Research, Berhampur, India  
Email: ashishprd30@iiserbpr.ac.in, vivekt@iiserbpr.ac.in

## Introduction

Hypoxic-Ischemic Encephalopathy (HIE) is a severe neonatal condition resulting from oxygen deprivation during birth, often leading to long-term neurological impairments. Globally, HIE affects approximately 2% of live births, with a higher incidence in developing countries [1]. In India, Odisha reports one of the highest neonatal mortality rates, with 32 deaths per 1,000 live births, of which 29.09% are attributed to moderate to severe perinatal asphyxia [2]. Early detection and timely intervention are crucial in mitigating the risk of irreversible neurological damage. However, no definitive quantitative early clinical marker currently exists to reliably determine whether a neonate has developed HIE. Diagnosis typically becomes apparent only at the first developmental milestone, around six months of age [3]. This study proposes a novel approach integrating 'Neuroimaging and Blood-Based Metabolomics' with AI models for highly precise determination of HIE within six hours of Birth.

## Methods

Biomarkers related to brain energy metabolism, antioxidants, and neuroinflammatory cytokines are expected to be dysregulated in response to the severity and duration of hypoxia [3]. Blood samples from neonates are collected at 1-, 6-, and 48-hours post-birth from multiple hospitals across different regions of Odisha, followed by plasma isolation for metabolic profiling using a 700 MHz NMR spectrometer. Volumetric segmentation of infant brain MRI images was performed using the IFS and iBITS pipelines to analyze volumetric differences between HIE and healthy neonatal brains.

## Results

Preliminary plasma NMR analysis revealed significantly elevated concentrations of lactate (3.8-fold), glutamine (1.2-fold), and creatine phosphate (1.7-fold) in neonates diagnosed with birth asphyxia compared to non-HIE subjects over time. In parallel, neuroimaging segmentation showed substantial structural changes, including a 10% enlargement of ventricles and a 7.7% cortex thinning in HIE-affected neonates. These findings indicate clear differences in metabolite concentrations and brain structure between HIE and non-HIE subjects.

## Discussion

Elevated levels of lactate, glutamine, and creatine phosphate in the plasma of birth asphyxiated neonates indicate significant disruptions in brain energy metabolism due to hypoxic-ischemic injury, reflecting a shift to anaerobic glycolysis and compensatory mechanisms for cellular energy balance. Concurrent neuroimaging analysis revealed notable structural abnormalities, including

ventricular enlargement and cortical thinning, suggesting neuronal loss and cerebral atrophy. These findings highlight the potential of metabolite and imaging biomarkers for early HIE detection. Integrating these markers with AI-driven models could enhance diagnostic accuracy, enabling timely interventions and improving neurodevelopmental outcomes in affected neonates.

## Conclusion

This study introduces a novel approach combining blood-based metabolomics, neuroimaging metrics, and AI-driven analysis for the early detection of HIE in neonates. By enabling timely interventions like Therapeutic Hypothermia (TH), this framework has the potential to revolutionize HIE diagnosis and improve neonatal outcomes, particularly in high-risk regions like Odisha.

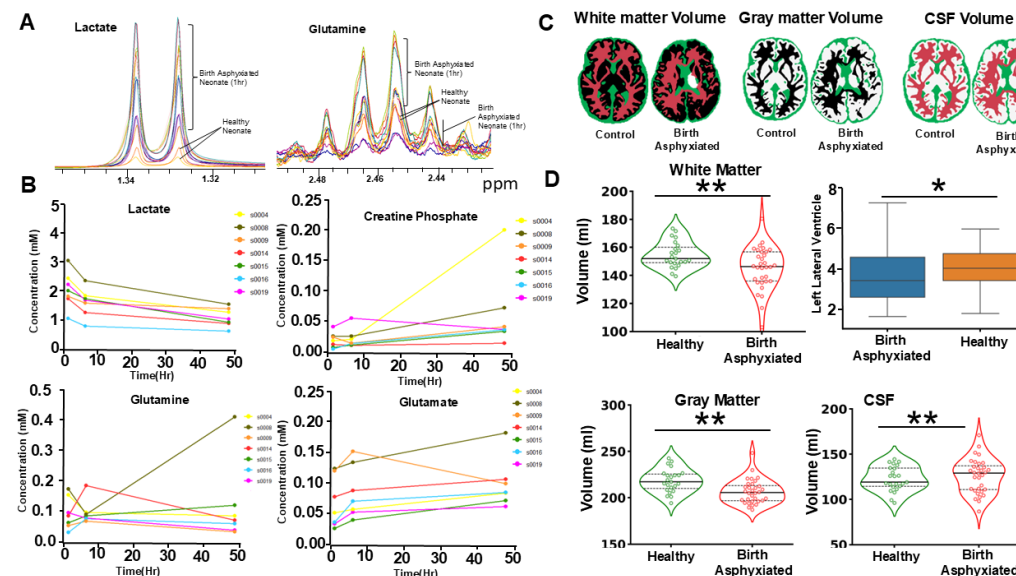


**Figure 1: Metabolomics and Neuroimaging Alterations in Birth Asphyxiated Neonates.** (A) Representative plasma NMR spectra highlighting significantly elevated levels of lactate and glutamine in birth-asphyxiated neonates compared to healthy controls. (B) Longitudinal quantification of plasma metabolites, including lactate, glutamine, and creatine phosphate, measured at 1, 6, and 48 hours post-birth, showing progressive metabolic dysregulation in HIE subjects. (C) Neuroimaging segmentation illustrating white matter, gray matter, and cerebrospinal fluid (CSF) volume differences between normal and HIE neonates. (D) Violin plots and box plots depicting significant reductions in white matter (WM) and gray matter (GM) volumes and increased CSF volume in HIE-affected neonates (\*p < 0.05, \*\*p < 0.01).

## Reference

- [1] M. AlMuqbil, J. Alanazi, N. Alsaif, D. Baarmah, W. Altwaijri, A. Alrumayyan, et al., "Clinical Characteristics and Risk Factors of Neonatal Hypoxic-Ischaemic Encephalopathy and Its Associated Neurodevelopmental Outcomes During the First Two Years of Life: A Retrospective Study in Saudi Arabia," *Int J Gen Med*, vol. 16, pp. 525-536, 2023.
- [2] D. C. N. Dr. Meena Somi, Dr. Bijaya K. Padhi, Dr. Neetika Ashwani, "Patterns of Morbidity among Newborns Admitted In SNCUs of Odisha, India," *International Journal of Health Sciences & Research*, vol. 8, September 2018.
- [3] M. J. Debuf, K. Carkeet, and F. Piersigilli, "A Metabolic Approach in Search of Neurobiomarkers of Perinatal Asphyxia: A Review of the Current Literature," *Front Pediatr*, vol. 9, p. 674585, 2021.

# Echo Shifted PD-FSE Knee MR Image Transformation Into Water, Fat and Field Inhomogeneity Images at 0.5T

Harsh Kumar Agarwal<sup>1</sup>Hongxu Yang<sup>2</sup>Uday Patil<sup>1,3</sup>Lehel Ferenczi<sup>2</sup>Avinash Gopal<sup>2</sup>Ramesh Venkatesan<sup>1</sup>

1. GE HealthCare, Bangalore, India, 2. GE HealthCare, The Netherlands, 3. Manipal Hospitals, Bangalore, India

## Introduction

MR Imaging of knee is an important non-invasive tool for the evaluation of disorders such as meniscal, ligamentous, soft-tissue, bone and bone-marrow injuries and abnormalities[1]. PD-fat-sat is an essential contrast of knee MRI. Fat-saturation can be challenging at low field strength as water and fat are resonating in proximity of each other (74Hz at 0.5T) requiring longer CHESS RF pulse and sensitivity to B0 field-inhomogeneity[2]. Dixon based fat separation/suppression techniques are robust to B0 field-inhomogeneity, however they are associated with 2- or 3-fold increase in scan time[3]. An AI-based method is proposed in this abstract which decomposes a single FSE MRI image with shifted echo time into water, fat and field-inhomogeneity MR images.

## Methods

**Shifted echo-time MRI:** Complex-phase difference between water and fat signal evolves since excitation. In FSE-MRI refocusing RF pulse reverses the phase evolution leading to water and fat signal alignment at echo times. Like Dixon MRI, shifted echo time images are acquired to spread water and fat signals in the complex value plane. The fraction of water/fat signal in knee MRI is typically fixed over a tissue so the fat fraction image has abrupt changes across the tissue interfaces. In the presence of pathology, such as over bone, a rapidly varying fat fraction is observed. The presence of field-inhomogeneity in FSE image acquisition typically manifests as smoothly varying phase across the image. Therefore, shifted echo time MRI has information about water, fat and field inhomogeneity.

**AI based water-fat-inhomogeneity separation:** Single-shifted echo-time MRI was processed through UNet without downsampling but with dilated convolution [5,6]. Pyramid pooling module [7,8] is used to aggregate the information at the different dilated scales. Learning is constrained by deep image prior [9] based on image generation physics,  $I = W + F e^{j\theta}$ . Where  $\theta$  is the known phase difference between the water-peak and the most prominent fat signal peak based on the shifted echo time value and field strength.  $I$  is the shifted echo-time image,  $W$ ,  $F$  are water, fat, and field-inhomogeneity map images, respectively. Retrospectively, shifted echo-time images for any arbitrary  $\theta$  is generated using same equation. The corresponding loss function for training the AI model is,

$$\text{Loss} = \sum [(W - \hat{W})^2 + (F - \hat{F})^2 + (Fm - \hat{Fm})^2 + (I - (W + F e^{j\theta}) e^{jFm})^2]$$

**In-vivo Datasets:** Patients for knee MR Imaging at a commercial 1.5T scanner at the diagnostic center were given the option to participate in the IRB-approved study at 0.5T research MRI scanner. 40 consecutive patients participated in this study were considered. Proton density fTED [4,10] was acquired in all three planes (sagittal, coronal, and axial) with FOV=18cm, Matrix Size:320x224, TR/TE=1674/28.1, rBW=22.7kHz, slice-thickness/spacing=5mm/1.5mm in 4:15minutes. Each fTED dataset consists of two pairs of (in-phase and out-phase) shifted echo-time images. Water, fat, and field-inhomogeneity are estimated for each pair of images and used for AI model training and testing purposes.

AI model is trained for a range of echo time shifts (leading to  $\theta \neq 0$ ). Quantitative performance (SSIM and PSNR) metrics of the model for estimating water and fat images are shown in Figure 1. The performance of the model increases rapidly with an increase in  $\theta$  and then plateaus. Shifted echo-time image is important as a water image from non-shifted echo-time (in-phase) image looks similar to ground truth but is missing the bone pathology as shown in Figure 2. Further, qualitative assessment of the AI model of a patient with subtle bone edema is shown in Figure 3. Edema was visible in  $\theta \geq 30^\circ$ . Figure 4 shows that the input to the AI model at  $\theta = 30^\circ$  looks similar to the in-phase MRI image. Therefore, prospective acquired MRI images with  $\theta = 30^\circ$  can provide also provide in-phase contrast without AI processing.

Review of the fTED-generated water MRI images and AI-generated water images with input MRI images of  $\theta = 0^\circ$ ,  $30^\circ$  and  $190^\circ$  was done over 10 patients not used for training by an experienced radiologist with over 30 years of experience in reading MRI images shows that AI images generated with shifted echo ( $\theta = 30^\circ$  and  $180^\circ$ ) had all the pathologies present in the ground truth fTED image.

## Conclusion

AI-based method is shown to estimate water, fat, and field inhomogeneity images from single shifted echo-time knee FSE PDw MRI. The proposed method is able to exploit the information encoded in complex value and expected spatial variation to generate realistic MRI images with all the pathologies over 10 patients in the radiologist's review. The proposed method can reduce the data acquisition times of the fat-suppressed/separated MRI images. Further work is required to understand the performance in the presence of metal implants, other anatomies, and other MRI contrasts.

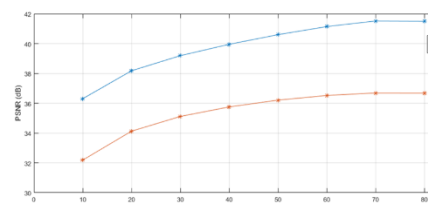
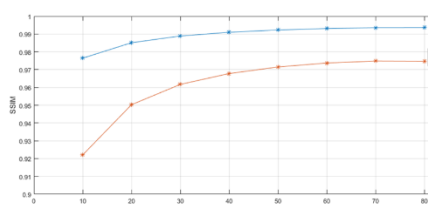


Figure-1 SSIM and PSNR for different echo time shifting leading to different phase between water and primary fat signal peak.

## Results

Shifted echo-time image is important as a water image from non-shifted echo-time (in-phase) image looks similar to ground truth but is missing the bone pathology as shown in Figure 2. Further, qualitative assessment of the AI model of a patient with subtle bone edema is shown in Figure 3. Edema was visible in  $\theta \geq 30^\circ$ . Figure 4 shows that the input to the AI model at  $\theta = 30^\circ$  looks similar to the in-phase MRI image. Therefore, prospective acquired MRI images with  $\theta = 30^\circ$  can provide also provide in-phase contrast without AI processing.

Review of the fTED-generated water MRI images and AI-generated water images with input MRI images of  $\theta = 0^\circ$ ,  $30^\circ$  and  $190^\circ$  was done over 10 patients not used for training by an experienced radiologist with over 30 years of experience in reading MRI images shows that AI images generated with shifted echo ( $\theta = 30^\circ$  and  $180^\circ$ ) had all the pathologies present in the ground truth fTED image.

## Conclusion

AI-based method is shown to estimate water, fat, and field inhomogeneity images from single shifted echo-time knee FSE PDw MRI. The proposed method is able to exploit the information encoded in complex value and expected spatial variation to generate realistic MRI images with all the pathologies over 10 patients in the radiologist's review. The proposed method can reduce the data acquisition times of the fat-suppressed/separated MRI images. Further work is required to understand the performance in the presence of metal implants, other anatomies, and other MRI contrasts.

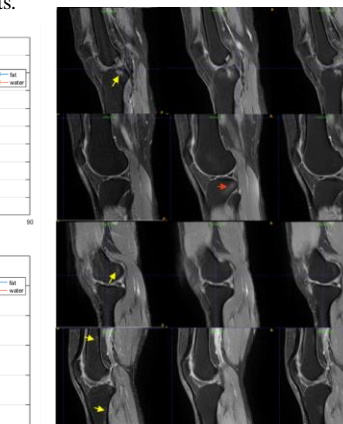


Figure-2 Water Image obtained from fTED and proposed AI method with in-phase ( $\theta=0$ ) and out-phase ( $\theta=180$ ) images. The bone edema pathology marked by yellow arrow in ground truth image.

## Reference

- [1] ACR-SPR-SSR Practice parameter for the performance and interpretation of MRI of the Knee. Res 6-2015.
- [2] Brown et al., Magnetic Resonance Imaging: Physical Principles and Sequence Design, 2014.
- [3] Hu et al., 2012. ISMRM workshop on fat-water separation: insights, applications and progress in MRI. MRM, 68(2)
- [4] Ma et al. Fast spin-echo triple-echo dixon (fTED) technique for efficient T2-weighted water and fat imaging. MRM. 2007 Jul;58(1).
- [5] Philip et al., Image-to-image translation with conditional adversarial networks." CVPR, 2017.
- [6] Zhixin et al., Iterative prompt learning for unsupervised backlit image enhancement., CVF, pp. 8094-8103. 2023.
- [7] Yu, F. Multi-scale context aggregation by dilated convolutions. arXiv:151.07122 (2015).
- [8] Kaiming et al. PAMI, 37, no. 9 (2015): 1904-1916.
- [9] Dmitry et al. Deep image prior.CVPR, pp. 9446-9454. 2018.
- [10] Rajamani et al., Fast spin-echo triple-echo dixon (fTED) for fat suppression at 0.5T in the presence on knee implant. ISMRM 2024: 0485

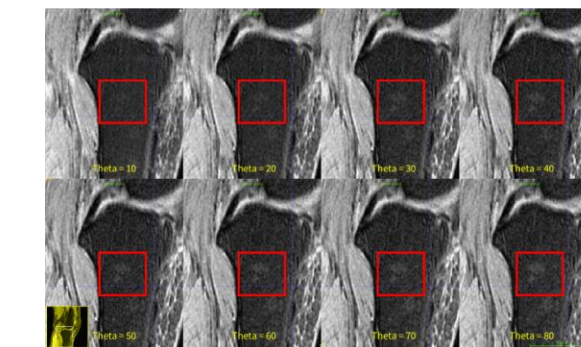


Figure-3 Qualitative assessment of impact of  $\theta$  on estimating in the subtle bone edema in the bone. Red box is drawn over the edema



Figure-4 fat suppressed MRI at 1.5T and fTED generated water MRI at 0.5T and AI generated water MRI at 0.5T with  $\theta=30$  as input. The simulated MRI images for  $\theta=30$  and acquired in-phase ( $\theta=0$ ) and out-phase ( $\theta=180$ ). Pathology is marked by yellow arrows.

# Enhanced Multi-shell Diffusion MRI Estimation Using V-NET with Multi-Scale Attention

Hirak Doshi<sup>1</sup>

B V Rathish Kumar<sup>1</sup>

Sudhir Pathak<sup>2</sup>

Durgesh K Dwivedi<sup>3</sup>

<sup>1</sup> Department of Mathematics and Statistics, IIT Kanpur, <sup>2</sup> Learning Research and Development Centre, University of Pittsburgh, USA,  
<sup>3</sup>Department of Radiodiagnosis, King George's Medical University, Lucknow

## Introduction

Diffusion MRI (dMRI) enables the non-invasive investigation of tissue microstructure by measuring water molecule diffusion within biological tissues. Multi-shell dMRI estimation extends traditional single-shell acquisition by sampling diffusion signals at multiple b-values allowing for more accurate modeling of complex tissue structures. While high-angular resolution diffusion imaging (HARDI) improves tissue characterization, it requires extensive sampling, leading to prolonged scan times, limiting clinical feasibility. One of the key advantages of multi-shell dMRI estimation is its ability to reduce acquisition time while preserving important microstructural information. To address this, deep learning-based reconstruction methods have been proposed. In this direction, Jha et al [1] introduced MSR-NET, a deep learning model designed to reconstruct dMRI volumes at  $b = 2000 \text{ s/mm}^2$  from data acquired at  $b = 1000 \text{ s/mm}^2$ . MSR-NET utilizes the spherical harmonic space using an encoder-decoder architecture with attention and feature modules. Similarly, Dugan et al. [2] proposed a 3D U-NET-based model that estimates high b-value (2000 and 3000  $\text{s/mm}^2$ ) dMRI volumes from low b-value ( $1000 \text{ s/mm}^2$ ) data. The aim of this study is to present a deep learning-based reconstruction method for multi-shell dMRI estimation using a V-NET architecture enhanced with a Multi-Scale Attention Module (MSA).

## Methods

Our method incorporates a V-NET architecture with a MSA to enhance feature extraction for multi-shell diffusion MRI (dMRI) estimation. This architecture builds upon V-NET by incorporating dense connections, multi-scale receptive fields, and spatial-channel attention mechanisms to improve learning. The MSA module employs three parallel convolutional branches with different dilation rates (1, 2 and 4) to capture features at multiple receptive fields. Additionally, channel attention is applied through global average and max pooling. A spatial attention mechanism further refines the feature representation by using a  $7 \times 7$  convolution over pooled feature maps. To further improve feature extraction, the model employs DenseBlocks which consist of three convolutional layers where each layer concatenates previous outputs to promote feature reuse and improve gradient flow. In the V-NET, the encoder path consists of four downsampling levels, where each level includes a convolutional layer followed by a DenseBlock. The deepest layer or bottleneck contains a DenseBlock with the highest number of channels to extract high-level semantic features. In the decoder path, transposed convolutions are used for upsampling, followed by another DenseBlock at each stage. Skip connections from the encoder are concatenated with the decoder features after adaptive resizing to ensure spatial alignment.

## Results

The predicted  $b=2000 \text{ s/mm}^2$  volume from the single-shell data based on preliminary training and validation process is shown in Fig 1. The plot highlighting the convergence of the training and validation loss is shown in Fig 2.

## Discussion

Our model was trained and validated on HCP preprocessed data. A total of 19 subjects were selected of which 16 subjects were used for training and 3 subjects were used for validation. The model was trained with an initial learning rate of 0.001 and a batch size of 16. A weighted loss function combining mean squared error and L1 loss was used. The results shown in this study are based on preliminary findings and the training process. While our model demonstrates a reliable performance on HCP data, the model can be further improved by incorporating spherical harmonics, learning the nonlinear mapping between the spherical harmonics coefficients between  $b1000$  and  $b2000$  levels which is a planned future work..

## Conclusion

We introduced a V-NET-based deep learning approach incorporating MSA for improved multi-shell dMRI estimation. Our model effectively captures both local and global diffusion features through multi-scale receptive fields, spatial-channel attention and dense connectivity. Preliminary results demonstrate promising reconstruction accuracy paving the way for future enhancements using spherical harmonics.

## References

1. R R Jha, A Nigam, A Bhavsar, S K Pathak, W Schneider, BVR Kumar, Multi-Shell D-MRI Reconstruction via Residual Learning utilizing Encoder-Decoder Network with Attention (MSR-Net), 42nd Annual International Conference of the IEEE Engineering in Medicine Biology Society, EMBC, 2020.
2. R Dugan, O Carmichael, Multi-shell dMRI Estimation from Single-Shell, Data via Deep Learning, LNCS 14312, pp. 14–22, 2023.

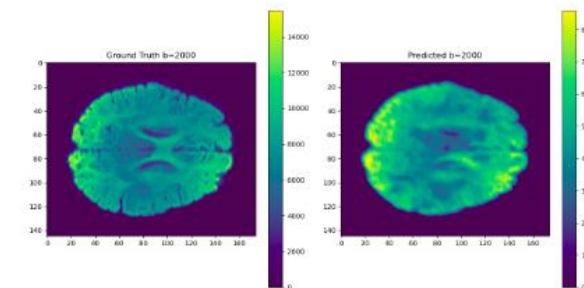


Fig. 1 Ground-truth and predicted volume

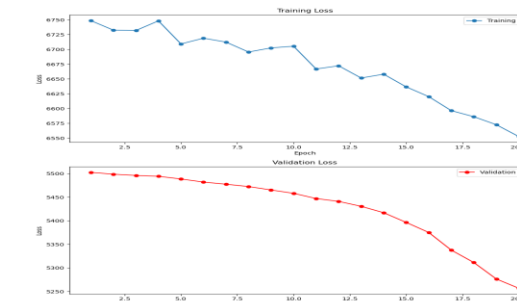


Fig. 2 Training and validation loss.

## Acknowledgements

Prof. B.V. Rathish Kumar and Dr. D.K. Dwivedi express their profound gratitude to the Indian Council of Medical Research (ICMR), New Delhi for their generous funding (Grant No. EM/Dev/IG/27/0337/2023). Furthermore, Prof. B.V. Rathish Kumar (IITK, India) and Dr. S.K. Pathak (Pitt, USA) extend their heartfelt appreciation to SPARC for their funding support (Grant No. SPARC/2019-2020/P1622/SL). Additionally, Dr. D.K. Dwivedi sincerely acknowledges the financial support provided by UPCST (Grant No. CST/D-1381). Dr. D.K. Dwivedi also conveys sincere thanks to the Science and Engineering Research Board (now ANRF), New Delhi for their valuable funding support under Grant No. SUR/2022/001841).

# Evaluating Hybrid Multidimensional MRI for Clinically Significant Prostate Cancer Detection: An Indian Perspective

**Ph. Supriya Devi<sup>1</sup>, Aritrick Chatterjee<sup>7</sup>, Sanjoy Sureka<sup>5</sup>, Arpan Yadav<sup>5</sup>, B.V. Rathish Kumar<sup>2</sup>, Sudhir Kumar Pathak<sup>3</sup>, Ranjeet Ranjan Jha<sup>4</sup>, Anit Parihar<sup>1</sup>, Saurabh Kumar<sup>1</sup>, Apul Goel<sup>6</sup>, Manoj Kumar<sup>6</sup>, Durgesh Kumar Dwivedi<sup>1\*</sup>**

<sup>1</sup>Department of Radiodiagnosis, King George's Medical University, Lucknow, India, <sup>2</sup>Department of Mathematics and Statistics, Indian Institute of Technology, Kanpur, India, <sup>3</sup>Learning Research and Development Center, University of Pittsburgh, Pittsburgh, PA, United States, <sup>4</sup>Department of Mathematics, Indian Institute of Technology, Patna, India, <sup>5</sup>Department of Urology, Sanjay Gandhi Postgraduate Institute of Medical Science, Lucknow, India, <sup>6</sup>Department of Urology, King George's Medical University, Lucknow, India, <sup>7</sup>Department of Radiology, University of Chicago, Chicago, USA.

## Introduction

Prostate cancer (PCa) is a leading malignancy in men globally, with rising incidence in India. Early detection and accurate characterization are crucial. While multiparametric MRI (mpMRI) is the standard for PCa detection and staging, it has limitations, including a 76% negative predictive value for clinically significant tumors (Grade Group  $\geq 2$ ) [1], poor tissue differentiation, and inter-observer variability. Hybrid Multidimensional MRI (HM-MRI) integrates ADC and T2 mapping to generate tissue maps. Unlike mpMRI, which relies on subjective interpretation, HM-MRI directly measures tissue microstructure, avoiding contrast agents and improving diagnostic accuracy. This is the first Indian study evaluating HM-MRI's relevance for PCa detection.

## Methods

After institutional ethical clearance, HM-MRI and mpMRI scans were acquired for four patients using a 3T MRI (Philips Ingenia ElitionX). The HM-MRI protocol included echo times (47, 75, 100 ms) and b-values (0, 750, 1500 s/mm<sup>2</sup>), enabling simultaneous ADC and T2 measurement per voxel. This generated a 3x3 multidimensional datasets, facilitating tissue composition mapping of epithelium, stroma, and lumen fractions. Two radiologists segmented tumors per PIRADS v2.1 criteria. Tissue composition maps were computed using an in-house MATLAB script (MathWorks). Biopsy reports were analyzed to validate correlations between tissue composition and histopathology findings.

## Results

Our preliminary work shows HM-MRI identified significant changes in tissue composition, with a marked increase in epithelial volume and reduction in lumen space in areas suspicious for PCa. Compared to mpMRI, HM-MRI demonstrated improved visualization of tissue microstructure and diagnostic accuracy of 100%. Tissue composition analysis revealed a mean epithelium volume fraction of 31.55% in cancerous ROIs compared to 16.90% in benign regions. These findings suggest HM-MRI captures subtle tissue alterations that may be missed by conventional techniques, supporting its use as a reliable imaging modality for prostate cancer detection.

## Discussion

Our study showed that HM-MRI enhances tissue characterization by quantifying epithelial volume and lumen fraction, key indicators of PCa aggressiveness. Increased epithelial volume and reduced lumen space, distinct malignancy markers, were better defined with HM-MRI than mpMRI, demonstrating superior characterization for detecting clinically significant PCa. This is the first evaluation of HM-MRI for prostate cancer detection in India, addressing mpMRI's limitations in detecting subtle tissue changes. HM-MRI aligns with global studies, such as Lee et al. [1], showing its ability to quantify tissue composition and improve diagnostic accuracy. Chatterjee et al. [2] validated its correlation with histology. However, the small sample size necessitates further validation in larger

S. No.	Patient			ADC_epi	ADC_lumen	ADC_stroma	V_epi	V_lumen	V_stroma
1	Pca-010	Cancer	Avg	0.3763	2.9515	1.4809	0.1698	0.4259	0.4042
		Benign	Avg	0.3	2.8985	0.802	0.0328	0.1931	0.7741
		Cancer	Std Deviation	0.155	0.1083	0.4166	0.1391	0.2782	0.2113
2	Pca-005	Benign	Std Deviation	0	0.1428	0.1399	0.0313	0.05	0.0317
		Cancer	Avg	0.3638	2.8994	1.4425	0.149	0.3891	0.4619
		Benign	Avg	0.4325	2.8178	1.2263	0.0077	0.2934	0.6989
3	Pca-003	Cancer	Std Deviation	0.1446	0.1412	0.4365	0.1079	0.3094	0.3167
		Benign	Std Deviation	0.184	0.1362	0.513	0.0195	0.255	0.254
		Cancer	Avg	0.3667	2.9336	0.7	0.5345	0.5059	-0.0404
4	Pca-001	Benign	Avg	0.3182	2.7945	1.6446	0.4168	0.5191	0.0641
		Cancer	Std Deviation	0.1633	0.121	0	0.238	0.3468	0.1234
		Benign	Std Deviation	0.0519	0.1425	0.1753	0.0789	0.1593	0.0979
		Cancer	Avg	0.3	0.9991	0.9991	0.4087	0.7291	-0.1378
		Benign	Avg	0.3002	1.3444	1.3444	0.2186	0.6768	0.1046
		Cancer	Std Deviation	0	0.4546	0.4546	0.2695	0.3202	0.3202
		Benign	Std Deviation	0.0008	0.4952	0.4952	0.1559	0.3121	0.3075

**Table 1** This table presents the ADC values and corresponding fractional volumes of epithelium, lumen, and stroma tissues within the regions of interest (ROIs) for cancerous and benign areas of the prostate gland in four patients.

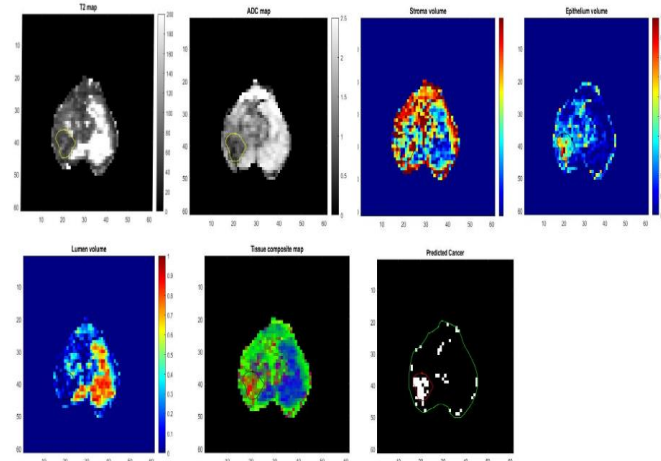


**Fig. 1** Images from a 64-year-old male (PSA 12.4 ng/mL) with Gleason 4+3 prostate cancer. The set includes ADC, T2, tissue composition, and predicted cancer maps. The red ROI marks cancer, the green ROI indicates benign tissue. HM-MRI estimated cancer as stroma 38.91%, epithelium 14.9%, lumen 46.19%, and benign tissue as stroma 29.34%, epithelium 0.77%, lumen 69.89%. Gleason 4+3 cancer showed increased epithelium with reduced stroma and lumen, accurately detected by HM-MRI.

## References

- Lee Y, Chatterjee A, Fütterer JJ, et al. Hybrid Multidimensional Prostate MRI: A Quantitative Step in the Right Direction. *Radiology*. 2022;303(2):285-287. doi:10.1148/radiol.221452.
- Chatterjee A, Oto A, Walker A, et al. Validation of Prostate Tissue Composition by Using Hybrid Multidimensional MRI: Correlation with Histologic Findings. *Radiology*. 2022;303(2):288-294. doi:10.1148/radiol.2021212051.

## Acknowledgments

Dr. D.K. Dwivedi and Prof. B.V. Rathish Kumar express their profound gratitude to the Indian Council of Medical Research (ICMR), New Delhi for their generous funding (Grant No. EM/Dev/IG/27/0337/2023). Furthermore, Prof. B.V. Rathish Kumar (IITK, India) and Dr. S.K. Pathak (Pitt, USA) extend their heartfelt appreciation to SPARC for their funding support (Grant No. SPARC/2019-2020/P1622/SL). Additionally, Dr. D.K. Dwivedi sincerely acknowledges the financial support provided by UPCST (Grant No. CST/D-1381). Dr. D.K. Dwivedi also conveys sincere thanks to the Science and Engineering Research Board (now ANRF), New Delhi for their valuable funding support under Grant No. SUR/2022/001841).

# Evaluating the Role of Artificial Intelligence in Identifying Ventriculomegaly of Clinical Significance

**Prof. (Dr.) Rajul Rastogi,**

Department of Radiodiagnosis, Teerthanker Mahaveer Medical College and Research Center, Moradabad, Uttar Pradesh

## Introduction

Ventriculomegaly can occur due to variety of causes including hydrocephalus. However, the relationship between ventriculomegaly and raised intraventricular pressure is non-linear. The management is however, guided by changes in optic nerve disk. Routinely, linear indices like Evan's index is used to assess ventriculomegaly. Recent literature suggests that ventricular volume is more sensitive in predicting optic nerve disk changes. Hence, we conducted the pilot study to assess the relationship of Artificial Intelligence Based Ventricular Volume and Changes in Optic Nerve disk in patients with Ventriculomegaly.

## Methods

Thirty patients with ventriculomegaly based on Evan's index in MRI brain performed on 1.5T MR scanner underwent Artificial Intelligence Based Ventricular Volume Assessment followed by Optic Nerve Disk Examination. Thirty age & sex matched controls also underwent MRI brain and AI based ventricular volume assessment.

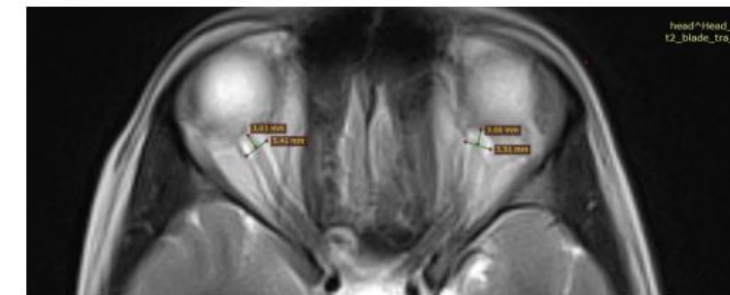
## Results

Only 16 out of 30 patients with ventriculomegaly based on Evan's index had true ventricular volume increase compared to controls as per AI based tool. Fourteen out of sixteen patients with increased ventricular volume on AI based assessment revealed changes in Optic Nerve Disk.

## Conclusion

Artificial Intelligence based Ventricular Volume Assessment on Brain MRI is superior to linear dimensions with better prediction of increase intraventricular pressure. It allows identification of patients with true hydrocephalus with high degree of accuracy, thus allowing early intervention in true cases and obviates apprehension & unnecessary procedure in false positive cases detected by linear ventricular dimensions.

Hydrocephalus Assessment (No. of Subjects)	ONSD	
	Present	Absent
Evans Index	Present	7
	Absent	12



Characteristic	Percentage (%)
Sensitivity	36.8
Specificity	0
PPV	87.5
NPV	0
Accuracy	35

# Evaluating Tumor Consistency in TSH-Secreting Pituitary Macroadenoma: A Case Study Using In-Vivo and In-Vitro MR Elastography

Shivani Tripathi<sup>2</sup>, S Senthil Kumaran<sup>1</sup>, Priyanka Bhat<sup>1</sup>, Umesh Gautam<sup>3</sup>, Sitikantha Roy<sup>3</sup>, Ashish Suri<sup>2</sup>, Ajay Garg<sup>4</sup>, Roger C Grimm<sup>5</sup>, Richard L Ehman<sup>5</sup>, Sandeep Ganji<sup>6</sup>, Yogesh Kannan Mariappan<sup>7</sup>, Hemlata Jehangir<sup>8</sup>

1 Department of Nuclear Magnetic Resonance, All India Institute of Medical Sciences, New Delhi, India (110029) 2 Department of Neurosurgery, All India Institute of Medical Sciences, New Delhi, India (110029) 3- Dept of Applied Mechanics, Indian Institute of Technology, Delhi, Hauz Khas, New Delhi (110016) 4 Department of Neuroradiology, All India Institute of Medical Sciences, New Delhi, India (110029) 5 Department of Radiology, Mayo Clinic, 200 First St SW, Rochester, MN 55905 6 Philips, Cambridge, MA, United States, Department of Radiology, Mayo Clinic, Rochester, MN, United States 7 Philips Innovation campus, Bangalore, India – 560016 8 Department of Neuropathology, All India Institute of Medical Sciences, New Delhi, India (110029)

## Introduction

Thyroid-stimulating hormone-secreting pituitary adenomas (TSHomas) are rare, accounting for less than 1% of all pituitary adenomas<sup>1,2</sup>. Although routine MRI sequences are used to determine the tumor consistency that could aid efficient tumor resection; MR elastography (MRE) has been shown to have improved efficacy in predicting tumor consistency and aid preoperative preparation<sup>3</sup>. Given the rarity of TSHomas, there have been lack of MRE studies. We report a case of pituitary adenoma wherein in-vivo MRE as well as in-vitro MRE (post-surgical specimen) were performed.

## Methods

A female (16 years) presented with delayed primary amenorrhea with increased frequency of micturition. The subject was a part of study approved by the Institute Ethics Committee (IEC-842/07.08.2020). A contrast enhanced MRI revealed a T2/FLAIR iso-intense enhancing mass lesion ( $37 \times 30 \times 31$  mm) with extension into bilateral cavernous sinuses and partially encasing bilateral cavernous ICA. Inferiorly the lesion was eroding the sellar floor and extending into sphenoid sinus. Lesion was diagnosed as a pituitary adenoma and endoscopic trans-nasal trans-sphenoidal (TNTS) procedure was planned. Prior to TNTS, MRE was acquired on a 3T MR scanner (Ingenia 3.0 T, Philips Healthcare, The Netherlands) using a 32-channel head coil. Investigations and procedures were done after written informed consent from the subject. The MRE sequence was acquired with 48 slices in axial orientation (TR 4800ms), with a frequency of 60Hz applied using a specially designed driver for brain (provided by author RE) and a Resoundant system (Mayo Clinics). Data processing was done using a customized image processing pipeline. The storage modulus ( $G'$ ) and loss modulus ( $G''$ ) were estimated from the images (Figure 1). Post-surgical tumor sample was used for in-vitro estimations (completed at physiological body temperature ( $37^\circ\text{C}$ ) within 1 hour of excision). The samples were carefully prepared using a scalpel blade to create a near-to-flat surface for testing. Experimental procedure- Nanoindentation testing was performed to characterize the viscoelastic properties of tumor tissues using the iNano nanoindenter (KLA Corporation, CA, USA). The specimens were placed in a sample holder tray with the help of a washer to prevent specimen movement during the experiments. The sample holder tray was filled with normal saline solution at  $37^\circ\text{C}$  to maintain the physiological body environment. All the experiments were performed using a flat-ended cylindrical indenter of  $100\text{ }\mu\text{m}$  diameter. The cylindrical flat punch tip keeps the contact area consistent throughout the indentation. An oscillating force of  $20\text{ }\mu\text{N}$  at  $10\text{ Hz}$  frequency was applied to the indenter, and oscillating displacement and phase difference were recorded. Poisson's ratio of tumor tissue was considered to be 0.5 throughout the analysis. Calculation of viscoelastic properties- The viscoelastic properties of brain tissues are expressed in terms of storage (quantifying the elastic response of the tissues) and loss modulus (quantifying the viscous response of the tissues) (Figure 2).

## Results

MRE brain tumor revealed stiffness, storage and loss moduli as  $1330.30 \pm 57.4\text{ Pa}$ ,

$1226.1 \pm 124\text{ Pa}$ ,  $163.4 \pm 386.5\text{ Pa}$  respectively (Table 1). In-vitro indentation at 15 different locations were performed on the sample and averaged the viscoelastic properties. The storage and loss moduli were  $2056.1 \pm 197.7\text{ Pa}$  and  $508.9 \pm 233.9\text{ Pa}$ , respectively. The values represent respective mean  $\pm$  standard deviations.

## Discussion

TSHomas are rare pituitary tumors, and our report offers a unique perspective on their characterization using MRE and in-vitro estimations. With the rarity of TSHomas limiting the availability of studies, MRE here provides an innovative method to assess tumor consistency, which could be vital for preoperative planning. It has emerged as an effective technique, offering quantitative measures of viscoelastic properties that can inform surgical strategies and possibly enhance outcomes. In this case, both in-vivo and in-vitro MRE measurements were conducted, providing a comprehensive view of the tumor's viscoelastic properties. The high storage modulus obtained in the in-vitro setting indicates a substantial elastic response, while the loss modulus reflects the viscous properties of the tissue. The tumor exhibited a notable degree of stiffness and elasticity, aligning with findings from prior studies of pituitary tumors where more rigid tissues were often challenging to resect<sup>4</sup>.

## Conclusion

This report underscores the utility of MRE in assessing the viscoelastic properties of pituitary adenomas, with both in-vivo and in-vitro methods.

## Reference

- Carides, M. D., Mehta, R., Louw, J. & Mohamed, F. A challenging case of a pituitary macroadenoma and toxic thyroid adenoma with inappropriate TSH secretion. *Endocrinol Diabetes Metab Case Rep* 2024, (2024).
- Yap, Y. W., Ball, S. & Qureshi, Z. Emergence of a latent TSHoma pituitary macroadenoma on a background of primary autoimmune hypothyroidism. *Endocrinol Diabetes Metab Case Rep* 2018, 18–0083 (2018).
- Cohen-Cohen, S. et al. Predicting pituitary adenoma consistency with preoperative magnetic resonance elastography. *J Neurosurg* 136, 1356–1363 (2021).
- Sakai, N. et al. Shear Stiffness of 4 Common Intracranial Tumors Measured Using MR Elastography: Comparison with Intraoperative Consistency Grading. *American Journal of Neuroradiology* 37, 1851–1859 (2016).

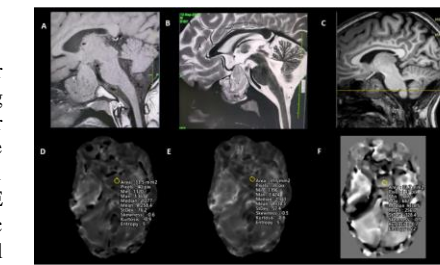


**Figure 1:** Representative image of imaging sequences in the subject- A] T 1 weighted, B] T 2 weighted, C] Stiffness in Tumor region, D] Storage modulus Tumor region, E] loss modulus in right Tumor region, F] Slice selection planning

Regions	Stiffness (Pa)	Stiffness $\pm$ SD	Storage modulus (Pa)	Storage modulus $\pm$ SD	Loss modulus	Loss modulus $\pm$ SD
Tumor region	13330.3	57.4	1226.1	124	163.4	386.5
Frontal pole(R)	2247.22	199.94	1850.77	156.55	1323.05	45.37
Frontal pole(L)	2549	315.89	2112.16	105.49	1419.11	134.51
Temporal(R)	2536.08	121.87	2571.17	63.12	754.16	39.31
Temporal (L)	2286.58	74.17	1602.61	60.33	1191.39	133.56
Cerebellum(R)	1537.67	44.32	1727.44	90.57	1332.66	70.58
Cerebellum(L)	1771	85.92	1498.66	34.63	1251.94	54.54

**Table 1:** MRE parameters (stiffness; storage modulus and loss modulus in pascals) in tumor region and other non-affected brain regions.

$$G' = \frac{K_0(1-\nu)}{2d} \quad (1)$$

$$G'' = \frac{D_{\text{so}}\nu(1-\nu)}{2d} \quad (2)$$

where,  $K_0$  is the sample stiffness,  $D_{\text{so}}$  is the sample damping,  $\nu$  is the Poisson's ratio of the tumor tissues, and  $d$  is the punch diameter.

$$K_0 = \left[ \frac{F_0}{x_0} \cos \phi \right]_{\text{in-contact}} - \left[ \frac{F_0}{x_0} \cos \phi \right]_{\text{out-of-contact}} \quad (3)$$

$$D_{\text{so}} = \left[ \frac{F_0}{x_0} \sin \phi \right]_{\text{in-contact}} - \left[ \frac{F_0}{x_0} \sin \phi \right]_{\text{out-of-contact}} \quad (4)$$

where,  $F_0$ ,  $x_0$  are the amplitudes of force and displacement oscillations, respectively and  $\phi$  is the phase difference between them.

**Figure 2:** Formuale used for estimating Storage modulus ( $G'$ ) and Loss modulus ( $G''$ ) in vitro.

# Exploring Tanning-Induced Molecular Changes in Leather Using MRI

G. Mothi Prasad<sup>1</sup>

Santhosh Nedunchezhiyan<sup>2</sup>

G. C. Jayakumar<sup>2</sup>

Nitin P. Lobo<sup>1</sup>

1 CATTERS (NMR), CSIR-Central Leather Research Institute, Chennai-600020, India

2 Biochemistry & Biotechnology Laboratory, CSIR-Central Leather Research Institute, Chennai-600020, India

## Introduction

Leather processing involves multiple stages that rely on different performance chemicals, with water serving as the primary medium for transport. These processes lead to significant chemical interactions in animal skin and hide [1]. Tanning, a critical step in leather processing, stabilizes collagen fibers by cross-linking them, making the material durable and resistant to decomposition. While MRI has proven effective in revealing water behavior and molecular interactions in both clinical and material science contexts [2], its potential in studying leather processing remains underexplored. In this study, samples were analyzed from various stages of leather processing before and during vegetable tanning to investigate molecular and structural changes using MRI modalities. By mapping T1 and T2 relaxation times and apparent diffusion coefficients (ADC), we gained valuable insights into water mobility and structural rigidity at different processing stages. The study demonstrates the potential of MRI as a tool for understanding tanning mechanisms and the molecular transformations that influence leather properties throughout the processing stages.

## Methods

MRI was performed on a 400 MHz Bruker AV-III HD WB spectrometer with a MicWB40 probe and MICRO2.5 gradients. Leather samples were analyzed at various stages, including untreated skin, pickled pelt stages, and 30% Wattle Myrob-treated tanned samples. T1, T2, and ADC were measured using MSME and DWI sequences. Parametric maps depicted spatial relaxation and diffusion variations, aiding molecular and structural analysis of tanning effects.

## Results

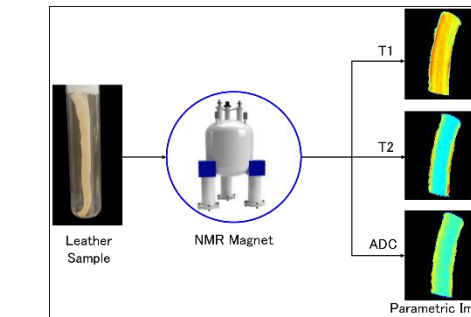
The MRI analysis provided key insights into the molecular and structural changes across the leather processing stages. T1, T2, and ADC revealed distinct trends across the samples. T1 values decreased from ~1168 (after fleshing) to ~626 ms (pickled pelt) and ~594 (30% Wattle Myrob-treated), indicating reduced water mobility and increased molecular rigidity. T2 initially increased from ~15.0 to 17.3 ms (pickled pelt), suggesting increased water interaction with the matrix during the pickling stage but dropped to 10.1 ms post-tanning, indicating reduced water dynamics and enhanced structural rigidity after tanning. Similarly, ADC values rose slightly from  $9.6 \times 10^{-4}$  mm<sup>2</sup>/s in the flesh stage to  $10.3 \times 10^{-4}$  mm<sup>2</sup>/s in the pickled pelt stage but dropped to  $9.9 \times 10^{-4}$  mm<sup>2</sup>/s after tanning. This reflects increased water diffusion during pickling, followed by restricted mobility due to tanning-induced matrix consolidation.

## Discussion

The progressive reduction in T1 relaxation times reflects increased molecular rigidity as water mobility decreases through the processing and tanning stages. This trend aligns with the known effects of tanning agents in cross-linking collagen fibers, which reduce free water and enhance structural integrity [3]. The non-linear behavior of T2 relaxation times highlights the dynamic interactions between water and the leather matrix. The initial increase in T2 during the pickled pelt stage suggests transient hydration effects, while the subsequent reduction after tanning indicates tighter molecular packing and restricted water dynamics [4]. The slight rise in ADC during the pickled pelt stage aligns with increased water diffusion due to the loosening of the matrix, which facilitates greater water movement. The subsequent decline after tanning reflects the densification of the leather matrix, restricting diffusion. Compared to existing studies in clinical and material sciences, where MRI has been used to probe water interactions and tissue structures, this study extends the application to leather science. Few studies have explored tanning processes at the molecular level, making this work a valuable contribution to the field [5].

## Conclusion

This study highlights the utility of MRI as a powerful tool to investigate molecular and structural changes during leather processing. Key findings include the reduction in T1 and ADC values, indicating increased rigidity and restricted water mobility, and the non-linear behavior of T2, which highlights hydration effects during pickling and matrix densification after tanning. These insights provide a deeper understanding of the tanning process, particularly the effects of Wattle Myrob in enhancing leather stability. By integrating relaxation and diffusion mapping, this research offers a comprehensive approach to studying water dynamics and structural transitions, providing insights that can optimize leather processing methods in a non-destructive way.



## References

- [1] K. J. Sreeram and L. A. Zugno, Eds., *Emerging Trends in Leather Science and Technology*. Singapore: Springer Nature, 2024.
- [2] P. T. Callaghan, *Principles of Nuclear Magnetic Resonance Microscopy*. Oxford: Oxford University Press, 1993.
- [3] B. Madhan, N. N. Fathima, J. R. Rao, V. Subramanian, B. U. Nair, and T. Ramasami, "Hydration in matrix stabilization of collagen fibers: Relevance to mechanistic insight into tanning," *J. Am. Leather Chem. Assoc.*, vol. 98, p. 263–272, 2003.
- [4] N. N. Fathima, M. Baias, B. Blumich, and T. Ramasami, "Structure and dynamics of water in native and tanned collagen fibers: Effect of crosslinking," *Int. J. Biol. Macromol.*, vol. 47, no. 5, pp. 590–596, Dec. 2010, doi: 10.1016/J.IJBIOMAC.2010.08.003.
- [5] L. Zhu, E. Del Federico, A. J. Ilott, T. Klokernes, C. Kehlet, and A. Jerschow, "MRI and Unilateral NMR Study of Reindeer Skin Tanning Processes," *Anal. Chem.*, vol. 87, no. 7, pp. 3820–3825, Apr. 2015, doi: 10.1021/ac504474e.

# Feasibility of free breathing cine cardiac magnetic resonance and prevalence of adverse prognosticators in patients with hypertrophic cardiomyopathy.

**Dr. Rengarajan Rajagopal<sup>1</sup>, Dr. Arun Bazal<sup>1</sup>, Dr. Surender Deora<sup>2</sup>**

<sup>1</sup>.Department of Diagnostic and Interventional Radiology, All India Institute of Medical Sciences, Jodhpur

<sup>2</sup>.Department of Cardiology, All India Institute of Medical Sciences, Jodhpur

## Introduction

Hypertrophic cardiomyopathy (HCM) is a common cardiomyopathy presenting with various clinical symptoms ranging from arrhythmias, heart failure, and sudden cardiac death. Contemporary evaluation of patients with suspected HCM includes cardiac MRI. Free breathing cine cardiac MRI sequences, currently under research, provide superior patient comfort. Newer techniques like multiparametric mapping help in tissue characterisation. We performed a study to assess patient comfort during FB- cine-CMR and to describe the spectrum of adverse imaging findings in patients with suspected HCM.

## Methods

This is a prospective study in a tertiary cardiac care centre in North west India which included patients with clinical suspicion of HCM (n=26) with an age range of 37 to 55 years. Cardiac MRI was performed using FB-cine sequences along with multiparametric mapping. A prior cohort of patients who underwent CMR using conventional breath hold sequences was used for comparison of patient discomfort.

## Results

No patient reported any discomfort during the examination (as compared to 24% of patients reporting discomfort with conventional breath-hold sequences – past data from our institute). The maximum left ventricular thickness ranges

from 22 mm to 29 mm. Adverse prognostic imaging features like left ventricular wall thickness > 30 mm was seen in 4 patients, LVOTO was seen in 11 patients while 9 patients had LGE involving > 15% of myocardium. None of the patients had LV apical aneurysm at time of scan. Two patients showed evidence of myocardial edema.

## Conclusion

Free breathing cine CMR offers superior patient comfort as compared to conventional breath hold sequences. Adverse imaging markers are commonly seen in CMR in Indian patients with suspected HCM.

# Gradient non-linearity corrections for Indigenous MRI

**Rahul Roy Chowdhury**

**Mahadev Kashinath Dipnaik**

**Tejasree Jadhav**

**Dharmesh Verma**

**Rajesh Harsh**

(Scientist, Medical System Division, SAMEER, Mumbai, India)

## Introduction

Phase Encoding (PE) gradients are critical for spatial encoding in MRI systems, ensuring accurate representation of k-space data. However, non-linear increments in PE gradient areas often lead to redundant k-space coverage and inconsistencies, resulting in ghosting artifacts and phase distortions in the phase encoding direction. These artifacts significantly degrade image quality and hinder diagnostic accuracy [1]. This study identifies and addresses the root cause of these non-linearities in PE gradient increments. A computational analysis of spectrometer waveform data revealed irregularities in amplitude transitions and gradient areas. Corrective measures were implemented by ensuring consistent, linear current increments for PE gradients. The trapezoidal rule was applied for area calculations, and Power Spectral Density (PSD) analysis validated the results. The proposed solution demonstrated significant improvements in MRI image quality, with a substantial reduction in ghosting artifacts (Figure 1). Corrected images showed consistent and linear PE gradient increments compared to non-linear mappings (Figure 2). This achievement represents a significant advancement in improving the fidelity of phase-encoded MRI imaging and demonstrates the potential for enhancing image quality across various MRI applications.

## Methods

The waveform data was extracted from the gradient amplifier output captured at the oscilloscope, with the time and amplitude values separated. This data was sampled across 256 phase encodes, with each phase encode representing a discrete point in time. Signal processing involved identifying rise and fall points by detecting amplitude thresholds. Missing points, caused by variations in the signal, were interpolated by evaluating the largest amplitude differences between adjacent samples, assuming the missed points fell along these transitions. The area under the curve of the waveform was calculated using the trapezoidal rule, which approximates the integral of the signal by summing areas of trapezoids between adjacent points, providing an estimate of the total energy over the scan duration. Flat regions of the waveform were identified based on a noise threshold, and these regions were averaged to calculate the mean flat amplitude, representing the steady-state behaviour of the signal. Additionally, the Power Spectral Density (PSD) of the signal was calculated to quantify the distribution of power across various frequency components. The PSD analysis provided further validation of the flat amplitude measurements, ensuring that no high-frequency noise or distortions affected the steady regions of the signal [2]. Finally, after identifying any irregularities such as missed points or amplitude variations, corrections were

applied to the waveform. The correction was performed at the transmitter hardware architecture by incorporating a fine-tuning mechanism in phase calculation with floating-point hardware support for improved accuracy till 6 decimal points. The corrected waveform was then validated by comparing the original and adjusted areas under the curve, ensuring that the adjustments did not introduce significant errors or deviations from the expected behaviour.

## Results

Non-linear PE gradients showed redundant k-space coverage. Corrected gradients exhibited consistent and linear area increments.

The improvement was quantified by the Root Mean Square Error between the actual phase area and the phase area defined by the PSD. The RMSE reduced from 0.5625 to 0.1059 after correction, denoting a significant improvement of 81.17% in the accuracy of the phase area.

## Discussion

The observed ghosting artifacts in MRI images were traced to inconsistencies in the spatial encoding caused by non-linear increments in phase encode (PE) gradient areas. These irregularities lead to redundant or identical k-space coverage at certain PE steps, contributing to artifacts in the phase encoding direction. Addressing this issue required analyzing waveform data and introducing corrections to linearize the increment of PE gradient areas.

## Conclusion

The inconsistency in the total area in the phase encode gradients, as evidenced by non-linear increment of area at every PE step is rectified and corrected. As a result, the increment in area of the current phase encode gradients is more consistent compared to previous case. The effect is observed in scanned images as a visible reduction in ghosting artifacts along the phase encode direction.

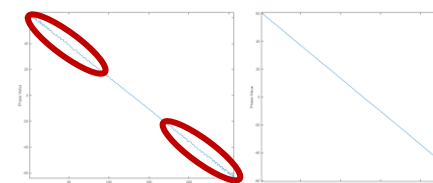


Figure 1. PE Gradient Area Plot without Gradient correction (Left)  
PE Gradient Area Plot with Gradient correction (Right)

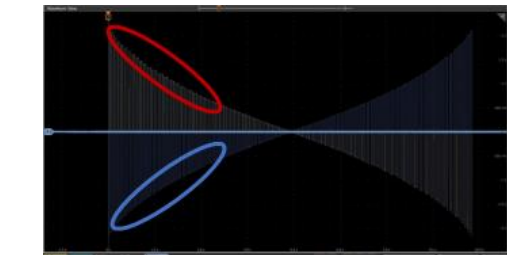


Figure 2. Comparison between two Phase Encode Gradients  
(Gray - Non-linear Gradient Mapping; Blue - Linear Gradient Mapping)



Figure 3. Corrected images demonstrated a significant reduction in ghosting artifacts Quantitative improvements in phase encoding fidelity were achieved

## Reference

1. Feinberg, D. A., & Setsompop, K. (2013). "Ultra-fast MRI using controlled aliasing." *Journal of Magnetic Resonance*, 229, 90-100.
2. Pruessmann, K. P., Weiger, M., Borst, P., & Boesiger, P. (2001). "Advances in sensitivity encoding with arbitrary k-space trajectories." *Magnetic Resonance in Medicine*, 46(4), 638-651.

# Global and regional rsfMRI Connectivity Analysis Using Graph Theory in Pre and Post Embolization Intracranial Dural Fistulas

**Bejoy Thomas**

(Dept. of Imaging Sciences and Interventional Radiology, Sree Chitra Tirunal Institute for Medical Sciences and Technology, Kerala, India, 695011)

**Jithin Sivan Sulaja**

**Smitha K Achuthan**

**Santhosh Kumar Kannath**

## Introduction

Intracranial arteriovenous fistula (DAVF) is a neurovascular disorder caused by abnormal connections between arteries and veins in the brain, leading to disrupted cerebral blood flow. It manifests through a spectrum of neurological and non-neurological symptoms, including headaches, seizures, cognitive impairments, cranial bruits, and psychiatric symptoms [1-3]. Despite its clinical significance, the mechanisms underlying DAVF-induced brain dysfunction remain poorly understood. Recent advancements in functional neuroimaging, particularly resting-state functional MRI (rsfMRI), have allowed researchers to investigate functional connectivity alterations in brain networks. Graph-theoretical analysis, quantifies topological properties. These metrics provide valuable insights into disruptions in brain network organization caused by DAVF [4,5]. This study employs rsfMRI and graph-theoretical approaches to analyze global and local functional connectivity in DAVF patients, comparing them with healthy controls. It also evaluates post-treatment changes at one month and one year after embolization.

## Methods

This study prospectively included 50 patients with DAVF and 50 age-matched healthy controls (HC). rsfMRI and structural images were acquired using a 3.0 T GE Discovery MR750W scanner. Functional connectivity matrices were constructed using the Dosenbach atlas, which parcellates the brain into 160 regions of interest (ROIs) fig (1). Graph-theoretical analysis was performed using the GRETNA toolbox to compute global and nodal network metrics, including assortativity, synchronization, hierarchy, degree centrality, clustering coefficient, nodal efficiency, and shortest path length. Metrics were evaluated across sparsity thresholds (0.05–0.5) to ensure robust connectivity analysis.

## Results

Pre-embolization DAVF patients exhibited significant disruptions in global and nodal network properties compared to HC. Global network metrics revealed heightened synchronization and reduced hierarchy,

indicating excessive connectivity and impaired network organization. Reduced global efficiency and higher clustering coefficients further reflected disrupted information processing. Aggressive DAVF cases (Cognard type 2B and above) demonstrated more pronounced alterations. At the nodal level, pre-embolization patients showed decreased clustering coefficient and nodal efficiency, particularly in regions associated with the default mode network (DMN) and visual cortex, correlating with clinical symptoms such as cognitive dysfunction and visual disturbances. Elevated betweenness centrality and shortest path length in key hubs like the posterior cingulate cortex and occipital lobe indicated compensatory reorganization but compromised global efficiency. Post-embolization, partial normalization of network properties was observed. At one month, clustering coefficient and nodal efficiency showed improvement, while betweenness centrality and shortest path length remained elevated. By the one-year follow-up, further recovery was noted, particularly in the DMN and visual regions. However, residual disruptions in global and nodal metrics indicated the chronic impact of DAVF on brain connectivity.

## Discussion

The study demonstrates significant disruptions in brain network connectivity in DAVF patients, particularly in the DMN and visual cortex, which correlate with cognitive and visual impairments. Post-embolization, partial recovery of functional connectivity was observed, though residual disruptions highlight the chronic impact of DAVF. These findings underscore the potential of graph-theoretical metrics and rsfMRI as valuable tools for assessing treatment efficacy and guiding targeted therapeutic strategies.

## Conclusion

This study highlights the significant alterations in brain network connectivity caused by DAVF and the potential for partial recovery following embolization. Graph-theoretical metrics demonstrated the potential as a non-invasive biomarker for assessing disease severity,

therapeutic efficacy, and recovery trajectory. The findings emphasize the importance of early and targeted interventions aimed at restoring disrupted connectivity in critical regions, particularly the DMN and visual cortex. Future research integrating multimodal imaging and longitudinal analyses could further elucidate the pathophysiology of DAVF and improve personalized diagnosis and treatment strategies. This study underscores the promise of network-based approaches for advancing clinical care in DAVF patients.

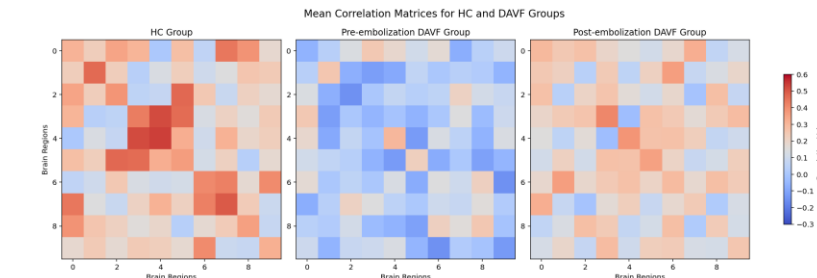


**Figure 1.** Displaying the mean correlation matrices for the HC, pre-embolization DAVF, and post-embolization DAVF groups. Each matrix highlights the connectivity patterns between various brain regions, with distinct differences in correlation values and distributions across the three groups.

## Reference

- [1] Cognard C, et al. Intracranial dural arteriovenous fistulas: clinical and angiographic correlation with a revised classification of venous drainage. *Radiology*. 1995;194(3):671-680. DOI: 10.1148/radiology.194.3.7862961.
- [2] van Dijk JM, TerBrugge KG, Willinsky RA, Wallace MC. Clinical course of cranial dural arteriovenous fistulas with long-term persistent cortical venous reflux. *Stroke*. 2002;33(5):1233-1236. DOI: 10.1161/01.STR.0000014757.27414.CD.
- [3] Gandhi D, Chen J, Pearl M, Huang J, Gemmete JJ, Kathuria S. Intracranial dural arteriovenous fistulas: classification, imaging findings, and treatment. *AJNR Am J Neuroradiol*. 2012;33(6):1007-1013. DOI: 10.3174/ajnr.A2667.
- [4] Bullmore E, Sporns O. Complex brain networks: graph theoretical analysis of structural and functional systems. *Nat Rev Neurosci*. 2009;10(3):186-198. DOI: 10.1038/nrn2575.
- [5] Fornito A, Zalesky A, Bullmore ET. Network scaling effects in graph analytic studies of human resting-state fMRI data. *Front Syst Neurosci*. 2010;4:22. DOI: 10.3389/fnsys.2010.00022.

# Glymphatic Function and Cognitive Improvement in Opioid Dependence: A DTI-ALPS Index Study on Buprenorphine Treatment.

Nisha Chauhan<sup>1</sup>Anju Dhawan<sup>2</sup>Biswadip Chatterjee<sup>2</sup>Siddharth Sarkar<sup>2</sup>S Senthil Kumaran<sup>1</sup><sup>1</sup>Department of Nuclear Magnetic Resonance, AIIMS, New Delhi, India<sup>2</sup>National Drug Dependence Treatment Centre (NDDTC), AIIMS, New Delhi, India

## Introduction

The glymphatic system is crucial for clearing metabolic waste from the brain, and its dysfunction is associated with neurotoxicity and cognitive decline. Chronic opioid dependence disrupts brain clearance pathways, leading to cognitive deficits and neural damage. While buprenorphine is an established treatment for opioid dependence, its effects on glymphatic function remain underexplored. This study employs the DTI-ALPS (Along-the-Perivascular Space) index, to evaluate glymphatic function in opioid-dependent patients at baseline and after three months of buprenorphine treatment. Healthy controls are included to determine whether treatment restores glymphatic function to normative levels and its association with cognitive recovery.

## Methods

13 healthy controls (HC) and 13 opioid-dependent patients were recruited from NDDTC. Patients underwent buprenorphine maintenance treatment (BMT) and were assessed at baseline (2–5 days post-initiation) and follow-up (3 months). All were right-handed and provided informed consent.

**Cognitive Tests:** At both the time points MOCA and Stroop Color Word Test (SCWT) were administered for measuring global cognition and executive functioning.

**Diffusion Tensor Imaging:** MRI was performed on a 3T Philips Ingenia scanner at AIIMS using a spin-echo EPI sequence (TR 1000 ms, TE 83 ms, 64 directions, 2.3 mm slices, b-value 1000 s/mm<sup>2</sup>).

**DTI ALPS Index Analysis:** The DTI-ALPS index quantifies water diffusivity along perivascular spaces in the corona radiata relative to diffusion perpendicular to fiber tracts. DTI data were pre-processed in FSL (motion correction, eddy current correction, skull stripping), and FA maps were generated. Spherical ROIs were placed on white matter tract such as superior longitudinal fasciculus and superior corona radiata in MNI152 space (Fig1).

**Statistical Analysis:** Paired t-tests compared DTI-ALPS index and cognitive scores at baseline and follow-up. Independent t-tests compared HC vs. patients. Spearman correlation analysed associations between ALPS index changes and SCWT/MOCA scores. Analyses were performed in SPSS v26 ( $p < 0.05$ ).

## Results

The DTI-ALPS index was significantly lower in opioid-dependent patients at baseline ( $1.20 \pm 0.07$ ) vs. healthy controls ( $1.36 \pm 0.05$ ;  $p < 0.001$ ) but improved after 3 months of BMT ( $1.34 \pm 0.06$ ;  $p < 0.001$ ), aligning with healthy controls. MOCA scores, initially lower in patients ( $25.80 \pm 2.35$  vs.  $27.63 \pm 1.06$ ;  $p = 0.017$ ), improved at follow-up ( $27.70 \pm 1.42$ ;  $p = 0.888$ ). SCWT scores improved from baseline ( $75.90 \pm 31.61$  s) to follow-up ( $66.80 \pm 27.70$  s;  $p = 0.012$ ), though initially lower than controls ( $65.20 \pm 8.10$  s;  $p = 0.150$ ). Digit Span

scores were lower at baseline ( $9.0 \pm 1.1$  vs.  $12.1 \pm 1.2$ ;  $p < 0.001$ ) but improved at follow-up ( $11.1 \pm 1$ ;  $p < 0.001$ ), nearing control levels ( $p = 0.310$ ). ALPS index changes correlated positively with SCWT ( $R^2 = 0.623$ ) and MOCA ( $R^2 = 0.533$ ) (Figure 2, Table 1).

## Discussion

Baseline ALPS index deficits support evidence that chronic opioid use disrupts brain clearance, contributing to neuroinflammation. After three months of BMT, ALPS index recovery to control levels suggests glymphatic function improvement, potentially due to buprenorphine's neuroprotective effects. Cognitive gains in MOCA and SCWT align with glymphatic recovery, supporting the link between improved clearance and reduced neurotoxicity.

## Conclusion

BMT significantly improves glymphatic function, as reflected by the DTI-ALPS index, and enhances cognitive performance in opioid-dependent patients. The recovery of glymphatic function to levels comparable to healthy controls highlights buprenorphine's potential in mitigating opioid-induced neurotoxicity.

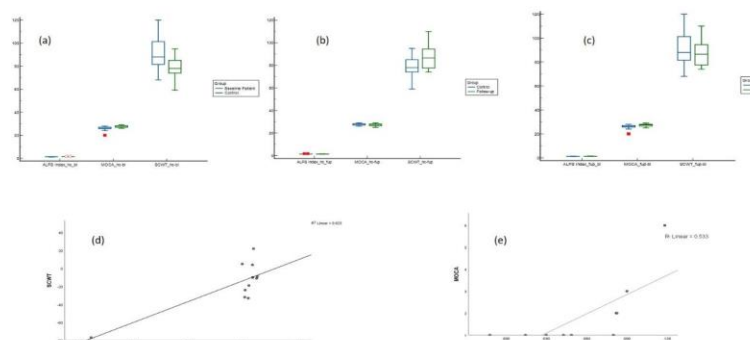


Figure 2. (a-c) Box plots of DTI-ALPS index and cognitive scores (SCWT, MOCA) across groups. (d) ALPS index change positively correlates with SCWT. (e) ALPS index correlates with MOCA.

Table 1: Comparison of DTI-ALPS Index and Cognitive Scores (MOCA and SCWT) between Healthy Controls, Baseline and Follow-Up Patients. Statistical significance is reported for comparisons between group: Healthy Controls vs. Baseline; Healthy Controls vs. Follow-Up; and Baseline vs. Follow-Up.

Variables	Healthy Control (HC) (n=13)	Baseline (BL) (n=13)	Follow-up (FUP) (n=12)	p-Value: HC vs BL	p-Value: HC vs FUP	p-Value: BL vs FUP
Age (years)	$28.62 \pm 5.10$	$28.31 \pm 4.88$	-	0.877	-	-
Drug Duration (years)	-	$8.14 \pm 3.96$	-	-	-	-
Daily Buprenorphine Dose (mg)	-	$14.2 \pm 2.74$	-	-	-	-
ALPS Index Right	$1.44 \pm 0.14$	$1.33 \pm 0.11$	$1.359 \pm 0.110$	0.042*	0.153	0.045*
ALPS Index Left	$1.44 \pm 0.13$	$1.30 \pm 0.13$	$1.347 \pm 0.118$	0.012*	0.090	0.008*
ALPS Index	$1.44 \pm 0.12$	$1.31 \pm 0.11$	$1.353 \pm 0.950$	0.011*	0.072	0.039*
MOCA	$27.85 \pm 1.06$	$25.77 \pm 2.05$	$27.33 \pm 1.241$	0.007*	0.102	0.042*
SCWT	$79.62 \pm 10.49$	$91.77 \pm 17.69$	$87.08 \pm 11.405$	0.011*	0.226	0.024*

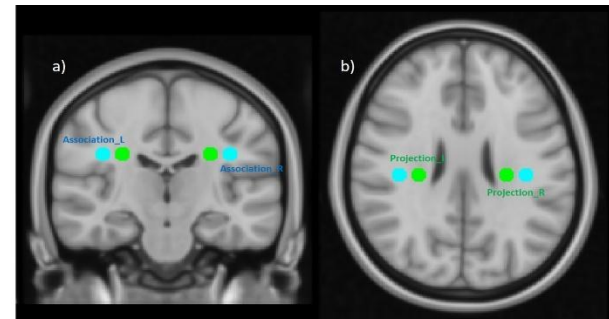


Fig 1: Representative brain MRI showing ROI placement for DTI-ALPS index calculation. (a) Coronal view of association fiber ROIs (Association\_L, Association\_R). (b) Axial view of projection fiber ROIs (Projection\_L, Projection\_R).

# Geometry Matters: Tumor Geometry wrapped in Artificial Intelligence is Discriminative of Brain Metastases and Glioma

Neha Yadav<sup>1</sup>, Jayshaan Baibhav<sup>1</sup> and Vivek Tiwari<sup>1</sup>

<sup>1</sup> Indian Institute of Science Education and Research (IISER) Berhampur, India

## Introduction

: Noninvasive discrimination of Brain-Metastases (Brain-Mets) arising from extracranial cancer and spreading to the brain versus Gliomas, based on radiographic findings is often inconclusive and is only confirmed upon invasive biopsies. The overall geometry of tumors and its subcomponents; enhancing, non-enhancing, necrosis, and edema, are highly complex and irregular. Therefore, non-Euclidean measures such as Fractality and Lacunarity can be employed to measure the geometric complexity in the tumor subcomponents. Advanced imaging techniques, together with AI-based quantitative platforms are required for non-invasive and immediate delineation of Brain-Mets from low-grade and high-grade-Gliomas (LGG and HGG).

## Methods

The study consisted of glioma (N=159, LGG and HGG) and Brain-Mets (N=200) subjects obtained from TCIA [1- 4] (The Cancer Imaging Archive). Preoperative T1w, T2w, T2-FLAIR, and T1-Gd MRI images were used for segmenting tumor subcomponents: enhancing, non-enhancing plus necrosis and edema. We quantified the 3D-Fractal Dimension (FD3D) and lacunarity (Lac3D) measures of each tumor subcomponent using an in-house developed pipeline [5-6] and further integrated the FD3D and Lac3D measures in ML-model to develop a quantitative highly precise platform discriminative of ‘Brain-Metastases’ from ‘Gliomas’ Fig. 1. Model performance was evaluated for each tumor subcomponent (and their combinations) using accuracy, sensitivity, specificity, and normalized confusion matrices.

## Results

The FD3D and Lac3D of the tumor subcomponents were not significantly distinct between Brain-Mets (arising from Breast Cancer, Lung Cancer, Melanoma, Gastrointestinal Cancer, and Renal

Cancer). Measurement of the FD3D of nonenhancing and edema subcomponents revealed significantly higher fractal dimension in the gliomas compared to Brain-Mets. Measurement of the Lac3D of the non-enhancing subcomponent revealed significantly lower lacunarity in the gliomas compared to Brain-Mets, whereas the edema subcomponent showed no differences. The combination of FD3D of nonenhancing and edema was able to discriminate Brain-Mets and glioma with 88% accuracy.

## Discussion

Brain-Mets exhibited lower fractality in the non-enhancing and edema subcomponents compared to LGG and HGG, with FD3D of the enhancing subcomponent, being intermediate between LGG and HGG. This suggests that a smoother geometry of non-enhancing and edema subcomponents together with irregular enhancing subcomponents is a typical feature of Brain-Mets compared to Gliomas (LGG and HGG). Here, we establish that Brain-Mets have distinct geometry from gliomas, and these geometric metrics are robust, sensitive, and specific features that can discriminate Brain-Mets. Within Brain-Mets, a subset of subjects with FD3D values lower than the threshold for the edema component has poor survival indicative of the prognostic relevance of geometric measures.

## Conclusion

These findings suggest that tumor subcomponent geometry matters and is discriminative of Glioma and Brain-Mets. Thus, bypassing the need of immediate biopsies for discrimination of Brain-Mets from Glioma

## References

- Clark K, Vendt B, Smith K, Freymann J, Kirby J, Koppel P, Moore S, Phillips S, Maffitt D, Pringle M, Tarbox L, Prior F. The Cancer Imaging Archive (TCIA): Maintaining and Operating a Public Information Repository, Journal of Digital Imaging, Volume 26, Number 6, December, 2013, pp 1045-1057. DOI: 10.1007/s10278-013-9622-7

2. Bakas S, Akbari H, Sotiras A, Bilello M, Rozycski M, Kirby J, Freymann J, Farahani K, Davatzikos C. (2017) Segmentation Labels and Radiomic Features for the Pre-operative Scans of the TCGA-LGG collection [Data Set]. The Cancer Imaging Archive. DOI: 10.7937/K9/TCIA.2017.GJQ7R0EF

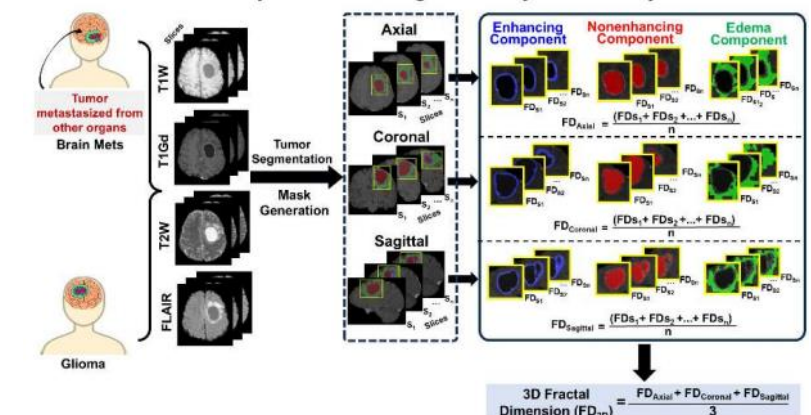
3. Bakas S, Akbari H, Sotiras A, Bilello M, Rozycski M, Kirby J, Freymann J, Farahani K, Davatzikos C. (2017). Segmentation Labels for the Pre-operative Scans of the TCGA-GBM collection [Data set]. The Cancer Imaging Archive. DOI:10.7937/K9/TCIA.2017.KLXWJJ1Q

4. Ramakrishnan D, Jekel L, Chadha S, Janas A, Moy H, Maleki N, Sala M, Kaur M, Petersen G C, Merkaj S, von Reppert M, Baid U, Bakas S, Kirsch C, Davis M, Bousabarah K, Holler W, Lin M, Westerhoff M, Aneja S, Memon F, Aboian M (2023). A Large Open Access Dataset of Brain Metastasis 3D Segmentations on MRI with Clinical and Imaging Feature Information (Version 1) [dataset]. The Cancer Imaging Archive. DOI: https://doi.org/10.7937/6be1-r748

5. Kroell N, (2021). imea: A Python package for extracting 2D and 3D shape measurements from images. Journal of Open Source Software, 6(60), 3091, <https://doi.org/10.21105/joss.03091>

6. Yadav N, Mohanty A, V A, Tiwari V. Fractal dimension and lacunarity measures of glioma subcomponents are discriminative of the grade of gliomas and IDH status. NMR Biomed. 2024 Oct 5:e5272. doi: 10.1002/nbm.5272. PMID: 3936775

Fig.1: Segmentation and Mask generation of Tumor subcomponents from preoperative MRI of Brain Mets and Glioma subjects For Calculating 3D Fractality and Lacunarity.



## Low-Field MRI in Musculoskeletal and Implant Imaging

Manish Saini<sup>1</sup>, Devasenathipathy Kandasamy<sup>1</sup>, Shivanand Gamanagatti<sup>1</sup>, Ankur Goyal<sup>1</sup>, Puneet Misra<sup>4</sup>, Rakesh Kumar<sup>4</sup>, Harshal Salve<sup>4</sup>, Yatin Sharma<sup>2</sup>, Benjamin Schmitt<sup>3</sup>, Vikas Gulani<sup>5</sup>,

<sup>1</sup>Department of Radiodiagnosis and interventional radiology, All India institute of medical science, New Delhi, India. <sup>2</sup>Raju Sharma<sup>1</sup> Siemens Healthineers, Gurugram, India. <sup>3</sup>Siemens Healthineers, Sydney, Australia. <sup>4</sup>Centre of community medicine, All India institute of Medical Sciences <sup>5</sup>Department of Radiology, Michigan institute for Imaging technology and translation (MIITT), Ann Arbor, MI, United states.

### Introduction

High-field MRI (1.5T/3.0T) is commonly used in routine orthopedics imaging due to its higher soft tissue resolution and better signal-to-noise ratio. However, low-field MRI (<1T) is gaining recognition due to recent advancements in image acquisition and reconstruction and reduced susceptibility artifacts, leading to better soft tissue visualization adjacent to bones and implants. Low-field MRI also has the advantage of being cost-effective.

### Methods

150 Patients with suspected spine, joint pathologies, and tendon/ligament injuries, including those with metallic implants, were imaged on a 0.5 T MRI scanner (Magnetom Free.star, Siemens Healthineers, Erlangen, Germany) installed in a container in the Comprehensive Rural Healthcare Services Project (CRHSP) facility in Ballabgarh. Images were assessed for image quality, identification of pathology, and implant status.

### Results

Low-field MRI showed significantly reduced metal-related susceptibility artifact with improved soft tissue/osseous visualization in the periprosthetic region Fig01. The VRT images generated from MRI data were of high quality Fig02, providing a 3D perspective in the visualization of data. Diagnosis of joint pathologies, partial/complete tendon tears, soft tissue injuries, bone marrow edema, and degenerative changes of the spine could be made with confidence.

### Discussion

Low-field MRI is a valuable modality, and it can be an alternative

for patients with metallic implants and those requiring serial imaging, where CT is the current modality of choice. It has the potential to overcome the extensive implant-induced artifacts that are seen in any standard high-field scanners. It also has the advantage of low cost and easy accessibility in areas with limited resources.

### Conclusion

Low-field MRI can be an important tool in orthopedic and implant imaging. It offers artifact reduction, improved periprosthetic visualization, and adequate diagnostic capability.



**Fig 01:** Image A & B are morphological T1 images showing reduced metal-related susceptibility artifact with improved soft tissue/osseous visualization. C is CT like bone imaging with multi-echo gradient technique. D showing 3D VRT with prosthesis marked with white arrow.



**Fig 02:** Showing 3D VRT for foot.

# Mathematical Modelling for Gadolinium-Free Contrast Imaging: Advancing Radiological Assessment of Gliomas

**Barsa Rani Dey<sup>1</sup>, Neha Yadav<sup>1</sup>, Bejoy Thomas<sup>2</sup>, Vivek Tiwari<sup>1</sup>**

<sup>1</sup> Department of Biological Sciences, IISER Berhampur <sup>2</sup> Sree Chitra Tirunal Institute for Medical Sciences and Technology, Trivandrum

## Introduction

Gadolinium (Gd), a paramagnetic contrast agent commonly utilized in Magnetic Resonance Imaging (MRI) to delineate regions with broken blood brain barrier of Glioma, has raised significant concerns due to the accumulation of Gd deposits in brain tissues [1-3]. This study aims to develop pipelines to eliminate the need for Gadolinium by leveraging conventional, non-invasive pre-operative MRI sequences: T1-weighted (T1w), T2-weighted (T2w), and T2-Fluid Attenuated Inversion Recovery (T2-FLAIR) as shown in Figure 1 to generate an MRI modality analogous to the post-Gd-T1w sequence.

## Methods

Using pre-operative MRI modalities (T1w, T2w, and T2-FLAIR, Post-Gd-T1w) from The Cancer Genome Atlas (TCGA) cohort of LowGrade Glioma (N=65) and High-Grade Glioma (N=101) subjects [4, 5], two strategies were developed. The first approach employs a Mathematical Modelling Method, where optimized mathematical operations, such as addition and subtraction maps applied to pre-contrast MRI modalities (T1w, T2w, and T2-FLAIR), to generate images resembling post-Gd-T1w sequences as shown in Figure 2. For further validation, MRI data from glioma subjects provided by the Sree Chitra Tirunal Institute of Medical Sciences and Technology (SCTIMST) were utilized to assess the robustness and generalizability of these methods. The second approach leverages a Deep Learning Framework based on a 3D conditional generative adversarial network (cGAN) architecture [6]. This model utilizes pre-contrast MRI modalities as input, comprising 240×240×155 mm<sup>3</sup> for each modality for all the subjects, to predict images analogous to the post-Gd-T1w modality

## Results

Quantitative analysis of the images generated using the proposed mathematical approach demonstrated high similarity to post-Gd T1w imaging in TCGA cohorts as well as in medical data received from Sree Chitra Tirunal Institute of Medical Sciences, Trivandrum, achieving an overall similarity of 80%. The evaluation metrics included a Structural

Similarity Index (SSIM) of 85% ± 5 and a Peak Signal-to-Noise Ratio (PSNR) of 82% ± 5%. Additionally, the Mean Squared Error (MSE) was calculated at 0.02 ± 0.03, highlighting the accuracy and reliability of the image synthesis process.

## Discussion

This study highlights the potential of utilizing various non-invasive MRI modalities to synthesize Gadolinium-enhanced T1-weighted (post-Gd-T1w) images, providing a safer and non-invasive alternative for glioma tumour detection. By leveraging pre-operative MRI modalities through mathematical modelling and deep learning techniques, the proposed methodologies address concerns related to Gadolinium accumulation in brain tissues. The mathematical modelling approach achieved an 80% overall similarity to post-Gd-T1w images, with satisfactory SSIM and PSNR metrics. While this method is computationally efficient and non-predictive, its performance may vary with imaging sequence variability and tumour characteristics. Further optimization and validation on larger datasets are essential to enhance its applicability for glioma detection and diagnosis.

## Conclusion

This study highlights the potential of utilizing various non-invasive MRI modalities to synthesize Gadolinium-enhanced T1-weighted

(post-Gd-T1w) images, providing a safer and non-invasive alternative for glioma tumour detection. By leveraging pre-operative MRI modalities through mathematical modelling and deep learning techniques, the proposed methodologies address concerns related to Gadolinium accumulation in brain tissues. The mathematical modelling approach achieved an 80% overall similarity to post-Gd-T1w images, with satisfactory SSIM and PSNR metrics. While this method is computationally efficient and non-predictive, its performance may vary with imaging sequence variability and tumour characteristics. Further optimization and validation on larger datasets are essential to enhance its applicability for glioma detection and diagnosis.

## References

- [1] Kanda, T., Fukusato, T., Matsuda, M., Toyoda, K., Oba, H., Kotoku, J., Haruyama, T., Kitajima, K., & Funii, S. "Gadolinium-based Contrast Agent Accumulates in the Brain Even in Subjects without Severe Renal Dysfunction: Evaluation of Autopsy Brain Specimens with Inductively Coupled Plasma Mass Spectrometry". *Radiology*, 276(1), 228–232, 2015.
- [2] Yang, Q., Li, N., Zhao, Z. et al. "MRI Cross-Modality Image-to-Image Translation". *Sci Rep* 10, 3753, 2020.
- [3] Layne, K. A., Dargan, P. I., Archer, J. R. H., & Wood, D. M. Gadolinium deposition and the potential for toxicological sequelae - A literature review of issues surrounding gadolinium-based contrast agents. *British journal of clinical pharmacology*, 84(11), 2522–2534, 2018.
- [4] Scarpace, L., Mikkelsen, T., Cha, S., Rao, S., Tekchandani, S., Gutman, D., Saltz, J. H., Erickson, B. J., Pedano, N., Flanders, A. E., Barnholtz-Sloan, J., Ostrom, Q., Barborak, D., & Pierce, L. J. (2016). The Cancer Genome Atlas Glioblastoma Multiforme Collection (TCGA-GBM) (Version 5) [Data set]. The Cancer Imaging Archive.
- [5] Pedano, N., Flanders, A. E., Scarpace, L., Mikkelsen, T., Eschbacher, J. M., Hermes, B., Sisneros, V., Barnholtz-Sloan, J., & Ostrom, Q. (2016). The Cancer Genome Atlas Low Grade Glioma Collection (TCGA-LGG) (Version 3) [Data set]. The Cancer Imaging Archive.
- [6] Gauthier, Jon. "Conditional generative adversarial nets for convolutional face generation." Class project for Stanford CS231N: convolutional neural networks for visual recognition, Winter semester 2014.5 (2014): 2.

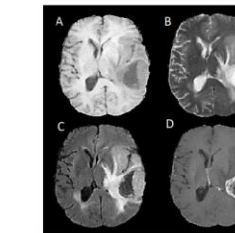


Figure 1: Conventional MRI modalities used for detection of Glioma and generation of tumor mask. A) T1-weighted, B) T2-weighted, C) T2-FLAIR, and D) Post-Contrast T1-weighted.

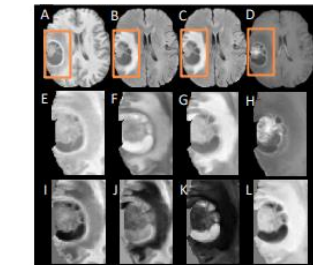


Figure 2: (A) T1-weighted, (B) T2-weighted, (C) T2-FLAIR, and (D) Post-Contrast T1-weighted images, along with their corresponding isolated tumor regions in (E), (F), (G), and (H), respectively, for each modality. Images (I-L) illustrate outputs generated by applying basic mathematical operations on pre-contrast MRI modalities: (I) Subtraction of T1-weighted from T2-weighted, (J) Subtraction of T2-FLAIR from T1-weighted, (K) Subtraction of T2-FLAIR from T2-weighted, and (L) Subtraction of T2-weighted from T2-FLAIR.

## Mid-Field Hadamard Encoded Simultaneous Multi Slice PROPELLER MRI

**Sudhir Ramanna<sup>1</sup>, Nitin Jain<sup>1</sup>, Sajith Rajamani<sup>1</sup>, Arjun Narula<sup>2</sup>, Harsh Agarwal<sup>1</sup>, Ramesh Venkatesan<sup>1</sup>**

<sup>1</sup> GE HealthCare, Bangalore, India, <sup>2</sup> Narula Diagnostic Center, Haryana, India

### Introduction

PROPELLER MRI acquired data over rectangular strips, called blades, rotated about k-space origin. It has shown to be robust to motion artifacts<sup>1</sup>. Variable sampling pattern of PROPELLER data acquisition makes it SNR efficient compared to cartesian data acquisition. Low and Mid-Field MRI have lower SNR requiring longer scan times making them susceptible to motion artifacts. Therefore, PROPELLER MRI can provide motion robust SNR efficient data acquisition at low and mid field MRI.

Significant T1 reduction is present at low and mid-field MRI systems when compared to widely used 1.5T and 3.0T field strengths. Therefore, shorter TR with efficient slice packing can provide similar contrast at low and mid field strengths. SMS acceleration technique can reduce the effective number of slices to be encoded in a given TR. Multiband techniques<sup>2,3</sup> uses coil sensitivities and Hadamard encoding uses multiaverage scans<sup>4</sup> to resolve the simultaneously excited slices. Hadamard encoded SMS can exploit multi averaging at low/mid field MRI.

Compared to multiband, Hadamard encoded SMS excite neighbouring slices, therefore cost efficient lower peak B1 RF amplifier can be utilized at low/mid-field MRI systems. In this abstract we have presented Hadamard encoded SMS propeller MRI tailored for low and mid field MRI systems.

### Methods

This cross-sectional, single-center study included 41 patients with chronic constipation who underwent MR defecography. Anorectal Manometry (ARM) and balloon expulsion tests were conducted prior to MR imaging. MR defecography findings were correlated with anal and rectal pressures to classify PFD types based on The London Classification. The study also evaluated structural anomalies in cases with normal ARM results.

### Results

Human subject was scanned research a 0.5T scanner using multi-channel coils as per IRB approved protocol with informed consent. Proposed method consists of optimization in acquisition and reconstruction. Acquisition: Adjacent slices are simultaneously excited. Instead of increasing the strength of the refocusing RF pulse, slice gradient are adjusted to enable simultaneous refocusing of slices without need for high peak B1 RF amplifier. Averaging in PROPELLER is typically done with increased number of blades. Instead, same blade angles are acquired multiple time to acquire all sets of Hadamard encoding for each blade angle. Imaging prepulses such as, fat saturation, spatial saturation and flow compensation modules were updated to enable their application over adjacent slices. Reconstruction: Each blade angle has complete set of Hadamard encoded data, therefore simultaneous excited slices are

resolved by linear combination as first step of the image reconstruction. This enabled application of other fast imaging techniques for PROPELLER MRI such as parallel imaging and compressed sensing to further reduce the scan time. AI based image enhancement methods<sup>5</sup> can also be applied with the proposed method since slices are resolved at the first step of the image reconstruction pipeline.

### Discussion

16 slice T2w PROPELLER MRI is acquired using proposed SMS method with SMS acceleration factor 2. Thereby reducing the need of TR from 6900msec to 3500msec and more efficient slice packing in one acquisition. The reduction in scan time is used to increase NEX from 1 to 2 therefore boosting the SNR of the images while maintaining the scan time. Figure 1 shows the reconstructed slices with adjacent slices that are simultaneously excited are placed together. Figure 2 shows the similar slice for T2w and STIR PDw MRI showing the compatibility of the proposed technique with the prepulses, namely inversion prepulse to suppress the fat. Application of inversion prepulse is technically challenging with non-Hadamard multiband acquisition. Further, proposed technique is not dependent on coil sensitivities and g-factor of multi-channel coils enabling its application with single channel coils such as single channel transmit/receive head coil. The neighbouring slices are similar to each other and therefore higher acceleration can be achieved in the compressed sensing based fast imaging. CONCLUSION Hadamard encoded PROPELLER SMS is proposed for low field MRI scanner to achieve increased slice coverage, reduced scan time or increased SNR. Proposed method does not need higher peak B1 RF amplifier specifications, does not need pulse stretching or VERSE[6], does not raise SAR significantly requiring lower refocusing flip angles, compatible with prepulses such as inversion recovery and compatible with existing fast imaging techniques such as parallel imaging, partial Fourier and compressed sensing. Further evaluation on other contrasts, anatomies and field strength is warranted.

### Conclusion

MR Defecography correlates with the London classification of different types of PFD on anal manometry. In addition, it rules out structural anomalies in patients with normal ARM.

### References

- Pipe, J. G. Motion correction with PROPELLER MRI: application to head motion and free-breathing cardiac imaging. MRM, 1999;42(5), 963-969.
- Müller, S. Multifrequency selective RF pulses for multislice MR imaging. MRM, 1988; 6(3), 364-371.
- Barth, M., Breuer, F., Koopmans, P. J., Norris, D. G., et al. Simultaneous multislice (SMS) imaging

techniques. MRM, 2016;75(1), 63-81.

- Ramanna, S., Agarwal, H., Sundaresan, R., Rajamani, S., et. al. Simultaneous Multi Slice using Hadamard like encoding with non-Hadamard factors. Proceedings of ISMRM 2022:2931
- Lebel RM. Performance characterization of a novel deep learning-based MR image reconstruction pipeline. 2020. arXiv:2008.06559.
- Hargreaves, B. A., Cunningham, C. H., Nishimura, D. G., & Conolly, S. M. Variable-rate selective excitation for rapid MRI sequences. MRM, 2004, 52(3), 590-597.

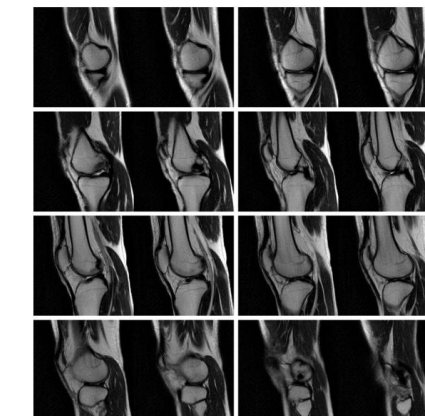


Figure 1: T2w MRI acquired using proposed Hadamard encoded PROPELLER MRI. Adjacent slices are excited together are shown together.

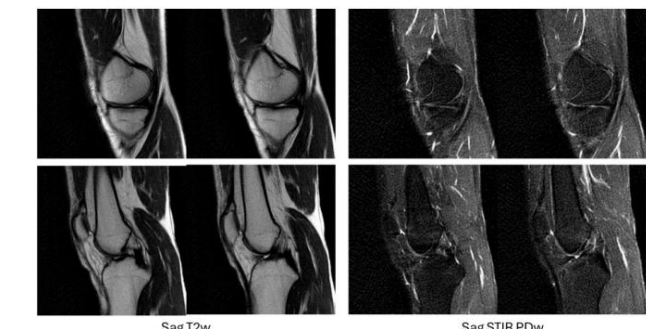


Figure 2: Sag T2w MRI and corresponding Sag STIR PDw MRI acquired using proposed Hadamard encoded PROPELLER MRI. Adjacent slices are excited together are shown together.

# Normative Brain Morphometry and Brain Age Prediction in the Indian Population Using GAMLSS and Ensemble Models

A. Aman<sup>1</sup>, K. S. Jadhav<sup>2</sup>, B. Aggarwal<sup>1</sup>

<sup>1</sup>Max Super Speciality Hospital, Saket, New Delhi, India    <sup>2</sup> Indian Institute Technology Bombay, Mumbai, India

## Introduction

Normative modeling is crucial for understanding brain morphometric variations across the lifespan. While extensive normative studies exist for Western populations, research focused on the Indian population remains limited. This study establishes age-related percentile curves for brain volumetric and cortical thickness features using GAMLSS on clinical-grade gadolinium-enhanced T1w MRI scans, a standard imaging protocol in routine hospital settings. This approach ensures immediate clinical applicability while addressing the critical need for population-specific normative data.

## Methods

We analyzed retrospective data from 1,541 healthy individuals (aged 13-77 years; 52% female) collected across eight different Max hospitals using gadolinium-enhanced T1w MRI. Data preprocessing included intracranial volume normalization and outlier removal using Local Outlier Factor method. GAMLSS was employed to model age-related changes and generate percentile curves. A stacked ensemble model, stratified by age groups, was developed for brain age prediction to account for non-linear aging trajectories. Model performance was evaluated through explained variance, mean absolute error (MAE), and residual diagnostics, with comparisons to existing non-Indian normative datasets.

## Results

The normative model effectively captured lifespan trajectories of brain morphometry in the Indian cohort, revealing distinct aging patterns compared to Western datasets, particularly in subcortical volumes and cortical thinning rates, illustrated in Fig. 1 and Fig. 2. The stacked ensemble approach demonstrated robust performance across age ranges, with strongest predictions in younger groups (MAE = 1.44 years, SD = 0.21 for ages 10-19) and reliable performance in middle-age (MAE = 2.51-2.74 years) and older groups (MAE = 2.17-2.36 years), illustrated in Fig. 3. Feature importance analysis revealed age-specific patterns, with para-hippocampal regions showing consistent significance across age groups and ventricle-related features becoming increasingly important in older ages.

## Discussion

This study presents the first normative brain morphometry model for an Indian cohort using clinical-grade gadolinium-enhanced T1w MRI. Our approach demonstrates superior adaptability to non-linear changes compared to previous methods like Bayesian regression and MFPR. The use of routine clinical MRI

protocols enhances the model's immediate applicability in hospital settings, potentially facilitating early detection of neurodegenerative disorders.

## Conclusion

We present a comprehensive normative model of brain morphometry specifically tailored to the Indian population, demonstrating strong predictive capabilities across age groups. This work establishes a foundation for population-specific brain aging assessment in clinical settings, with significant implications for detecting neurodegenerative conditions.

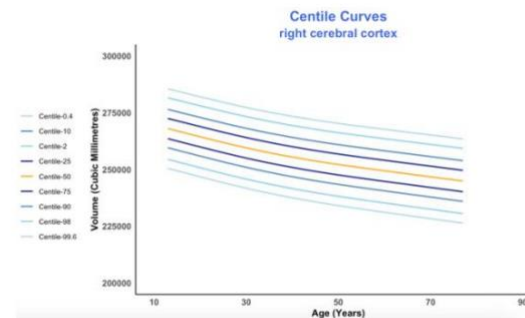


Fig.1 – Centile curves showing age-related changes in right cerebral cortex volume across different percentiles (97.5th, 90th, 75th, 25th, and 10th) from ages 10 to 80 years.

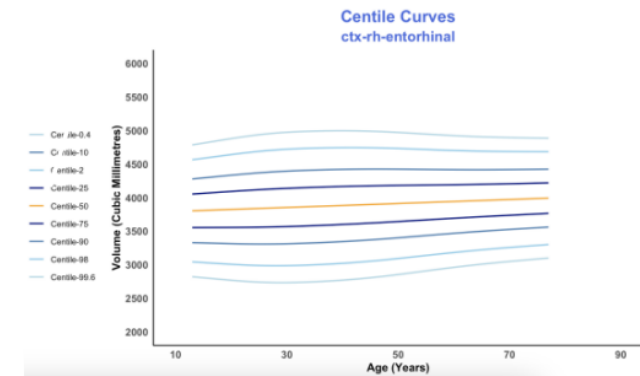


Fig.2 – Centile curves showing age-related changes in cortical thickness for right Entorhinal cortex across different percentiles (97.5th, 90th, 75th, 25th, and 10th) from ages 10 to 80 years.

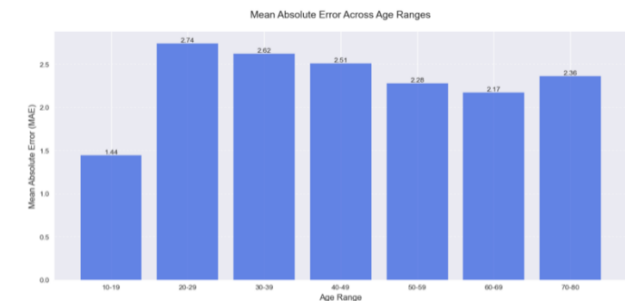


Fig.3 – Mean Absolute Error (MAE) in years for brain age prediction across different age ranges, showing lowest error of 1.44 years in the 10-19 age group and varying between 2.17-2.74 years for other age groups.

# Silent Strokes: A Quantitative Investigation on How Small Vessel Disease Rewires the Aging Brain

Niraj K Gupta, Neha Yadav, Ananya Praharaj, Vivek Tiwari

Indian Institute of Science Education and Research (IISER) Berhampur

## Introduction

While investigating the brain structural-health with aging, the T2-FLAIR MRI scans revealed that a substantial subset of subjects even within the cognitively normal (CN) group (~50% of the subjects in the age group of 50–64 age group, and ~85% in the age group >65 years) presented with significant load of cerebral small vessel disease (CSVD). The CSVD load with aging is observed as Periventricular White Matter Hyperintensities (PVWMH) and Deep White Matter Hyperintensities (DWMH), accumulation of which may disrupt brain health. This study examines whether PVWMH and DWMH have distinct thresholds and kinetics that lead to deficits in cognitive domains, compromise in fiber integrity and neuroanatomical volumetry and alterations in resting-state functional connectivity.

## Methods

A kNN-based approach quantified PVWMH and DWMH volume from T2-FLAIR, while T1w images were segmented to quantify 174 neuroanatomical volume, and thickness parameters across NACC (N=389) and ADNI (N=382) cohorts. Seed- based network-analysis of Default Mode Network (DMN)-regions (PCC, mPFC, LP, PHC) was conducted on EPI rs-fMRI scans followed by preprocessing. Fractional Anisotropy (FA) measurements were analyzed to understand axonal fiber integrity. CN subjects were stratified into WMH quartiles: PVWMH (Q1:  $\leq 0.93$  ml, Q4:  $>6.12$  ml), and DWMH (Q1:  $\leq 0.92$  ml, Q4:  $>2.75$  ml). Cognitive domains assessed included global cognition, memory, language, attention, and executive function. Age-adjusted structural parameters and cognitive scores were compared across WMH quartiles. Mediation analysis examined WMH effects on cognition via neuroanatomical changes, and piecewise fitting identified WMH inflection points with age.

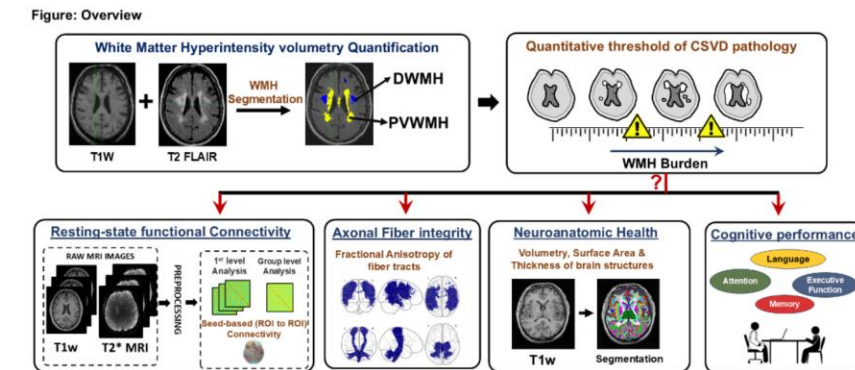
## Results

The progression kinetics of WMH volumes show an exponential increase with age, with PVWMH escalating nearly twice as fast as DWMH,

particularly after 61 years. Cognitive function remained intact at total WMH volumes  $\leq 4.1$  ml and PVWMH  $\leq 2.3$  ml. As PVWMH surpasses a load  $>2.3$  ml (Q3), distinct cognitive impairments are evident in attention (DST-F: -12.4%, p=0.002; and DST-B: -17.2%, p=0.002), executive-function (TMT-A: -21.3%, p=0.015; & TMT-B:-29.9%, p=0.03), and semantic memory (animal-naming: -12%, p=0.004), relative to no WMH group (Q1), upon adjusting for age. Meanwhile, DWMH  $>2.75$ ml (Q4) led to impairment in attention domain (DST-F: -10.5%; DST-B: -16.6%). Significant volumetric atrophy of various brain structures, along with reduced FA in corpus callosum, SLF, SFOF, cingulate and internal capsule was observed for subjects with PVWMH  $>2.3$ ml. No neurovolumetric changes were observed across DWMH quartiles. A mediation model indicated that PVWMH contributed to deficits in executive functions (TMT-B) via atrophy in set of brain structures: precentral gyrus (64%), accumbens (39%), paracentral gyrus (32%), RMFG (31%), and lingual gyrus (30%). Additionally, aging brains with CSVD burden present with reduced DMN connectivity in the Anterior-Posterior as well as within Posterior regions even in early age group.

## Discussion

Small vessel infarcts accelerate structural, cognitive and functional disruptions beyond typical aging-associated change. This study identifies a critical threshold of PVWMH ( $>2$  mL) beyond which cognitive deficit in executive function and semantic memory is observed, which is mediated via atrophy in a set of neuroanatomic structures. These changes are exacerbated by disruptions in commissural and association fiber integrity, alongside diminished connectivity within Default Mode Network.



# Prediction of IDH Mutation in Grade 4 Gliomas Utilizing DCE-MRI with a Machine Learning Based Classifier

Satyajit Maurya<sup>1</sup>, Virendra Kumar Yadav<sup>1</sup>, Rakesh Kumar Gupta<sup>2</sup>, Anup Singh<sup>1,3,4</sup>

<sup>1</sup>Centre for Biomedical Engineering, Indian Institute of Technology Delhi, India; <sup>2</sup>Fortis Memorial Research Institute, Gurugram, India; <sup>3</sup>Department of Biomedical Engineering, All India Institute of Medical Sciences, Delhi, India; <sup>4</sup>Yardi School of Artificial Intelligence (ScAI), Indian Institute of Technology Delhi, India

## Introduction

Glioblastoma (GB) represents one of the most aggressive primary brain tumors, characterized by poor prognosis making its treatment particularly challenging [1]. The discovery of isocitrate dehydrogenase (IDH1/2) mutations in gliomas by Parsons et al. has revolutionized our understanding of glioma biology, as these mutations significantly influence patient outcomes [2]. IDH, a small protein involved in crucial cellular processes including mitochondrial oxidative phosphorylation and glutamine metabolism is mutated in around 7% of grade 4 gliomas. The median overall survival for IDH-mutant grade 4 astrocytoma (IDHm) is 27–31 months while for IDH-wildtype GB (IDHw) it is 15–18 months [2]. Traditional methods for detecting the IDH mutation status rely on invasive procedures; there is a growing need for non-invasive techniques especially for tumors in regions where biopsies carry significant risks. Advanced MRI techniques have emerged as promising tools in this direction. Previous studies have utilized diverse qualitative and quantitative imaging parameters to evaluate IDH mutational status [3]. IDHw shows elevated CBV values compared to IDHm as highlighted in some studies [4].

In this study, we investigated a machine learning-based approach using quantitative DCE-MRI perfusion features to determine the IDH mutation. DCE-MRI parameters may be differentially expressed in IDHm and IDHw tumors, reflecting tumor microenvironment and angiogenesis. The trained model aims to provide a clinically valuable tool for improved diagnosis and treatment planning.

## Methods

The dataset for this study comprised pre-operative, contrast-enhanced MRI scans from 92 grade 4 glioma subjects. The data included 15 subjects with histopathologically confirmed IDHm and 77 with IDHw. Imaging was performed using a 3T whole-body MR scanner (Ingenia, Philips Healthcare, Best, The Netherlands) with a 16-channel receive-only coil. The MRI protocol involved acquiring a tri-planar localizer, conventional MR images, data for T1 mapping, and DCE-MRI. Quantitative parameters were computed for the enhancing tumor sub-component using the piecewise linear (PL) model, hemodynamic parameters were calculated using the first-pass analysis of concentration-time (C(t)) curves, and Extended Tofts Model (ETM) was employed to estimate kinetic parameters [5].

To identify the most important features for distinguishing between IDHm and IDHw gliomas, a random forest-based machine learning classifier was trained on a set of quantitative MRI parameters. A recursive feature elimination technique optimized the model performance. Given the class imbalance in the dataset, Synthetic Minority Over-sampling Technique (SMOTE) was utilized to generate synthetic samples of the minority class [6].

## Results

Feature elimination method identified seven key quantitative DCE-MRI parameters that included the slopes of the second (Slope-1) and third line (Slope-2) segments derived from the piecewise linear (PL) model fit of the concentration-time curve; hemodynamic parameters cerebral blood volume (CBV) and cerebral blood flow (CBF) calculated using first-pass analysis of the concentration time curves; and kinetic parameters that included extracellular space volume (Ve), fraction of plasma volume (Vp), and the volume transfer

constant (Ktrans).

The random forest classifier, trained on these seven features, demonstrated robust performance across multiple evaluation metrics. The model achieved a five-fold cross-validation score of 0.866, an F1 score of 0.913, and an area under the ROC curve (AUC) of 0.96. Figure 2 shows the confusion matrix of the predictions on the test set.

## Discussion

DCE-MRI-derived parameters could serve as reliable non-invasive IDH mutation status assessment biomarkers. In our analysis, Ktrans was the most important feature followed by Vp, Slope-2, CBV, Ve, CBF, and Slope-1 in descending order of importance.

The temporal parameters (Slope-1 and Slope-2) suggest the significantly differing timing of contrast agent dynamics between mutant and wild-type tumors. Hemodynamic parameters, CBV and CBF demonstrate their usefulness as indicators of tumor microvasculature correlating well with known tumor biology [5]. This increased vascularity and blood supply is associated with more aggressive tumor growth and proliferation, which aligns with the poorer prognosis typically seen in IDHw [7]. An increased Ktrans value demonstrates increased vessel permeability (representing the leaky nature of the vasculature) associated with the aggressive angiogenic behavior of IDHw tumors. The importance of Vp is emphasized by an increased vascular density. Lastly, among the kinetic parameters, the lower importance of Ve suggests that tumor vascular characteristics (as captured by Ktrans, Vp, CBV, and CBF) may play a stronger role in distinguishing these tumor subtypes. The robust performance of the random forest classifier indicates the effectiveness of these selected DCE-MRI parameters for non-invasive tumor characterization.

## Conclusion

Our findings suggest that this approach could potentially reduce the need for invasive biopsies, particularly in cases where the location of the tumor makes surgical sampling risky. However, the study's retrospective nature and the relatively small sample size warrants further validation in larger, prospective cohorts. Additionally, standardization of DCE-MRI acquisition and analysis protocols across institutions would be necessary for broader clinical implementation.

## Reference

- [1] A. Sengupta, A. K. Ramanan, R. K. Gupta, S. Agarwal, and A. Singh, "Glioma grading using a machine-learning framework based on optimized features obtained from T1 perfusion MRI and volumes of tumor components," *J. Magn. Reson. Imaging*, vol. 50, no. 4, pp. 1295–1306, 2019.
- [2] H. Yan et al., "IDH1 and IDH2 mutations in gliomas," *N. Engl. J. Med.*, vol. 360, no. 8, pp. 765–773, 2009.
- [3] M. Perrech et al., "Qualitative and quantitative analysis of IDH1 mutation in progressive gliomas by allele-specific qPCR and western blot analysis," *Technol. Cancer Res. Treat.*, vol. 18, p. 1533033819828396, 2019.
- [4] L. Siakallis, C.-C. Toprceanu, J. Panovska-Griffiths, and S. Bisdes, "The role of DSC MR perfusion in predicting IDH mutation and 1p19q codeletion status in gliomas: meta-analysis and technical considerations," *Neuroradiology*, vol. 65, no. 7, pp. 1111–1126, 2023.
- [5] A. Sengupta et al., "On differentiation between vasogenic edema and non-enhancing tumor in high-grade glioma patients using a support vector machine classifier based upon pre and post-surgery MRI images," *Eur. J. Radiol.*, vol. 106, pp. 199–208, 2018.
- [6] N. V. Chawla, K. B. Bowyer, L. O. Hall, and W. P. Kegelmeyer, "SMOTE: synthetic minority over-sampling technique," *J. Artif. Intell. Res.*, vol. 16, pp. 321–357, 2002.
- [7] J. Huang, J. Yu, L. Tu, N. Huang, H. Li, and Y. Luo, "Isocitrate dehydrogenase mutations in glioma: from basic discovery to therapeutics development," *Front. Oncol.*, vol. 9, p. 506, 2019.

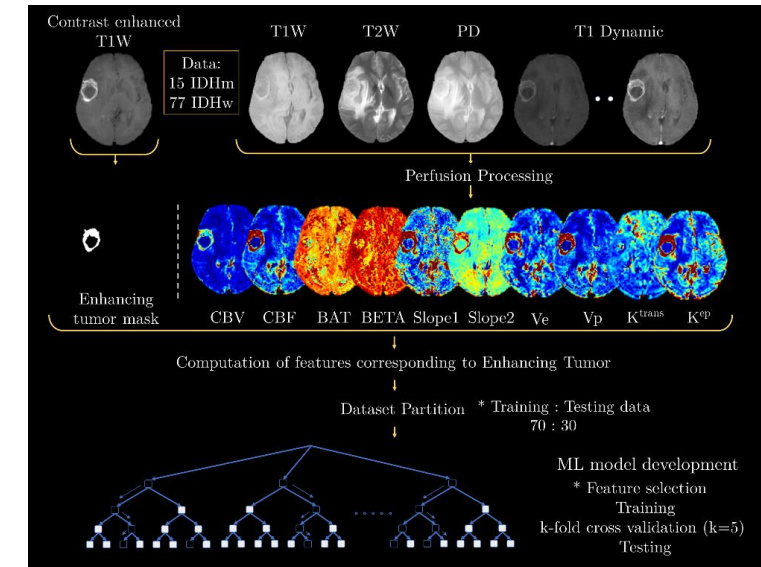


**Figure 1.** Flowchart shows the data processing pipeline, and the steps involved in model development.

		Predicted	
		IDH <sub>w</sub>	IDH <sub>m</sub>
Ground Truth	IDH <sub>w</sub>	21	4
	IDH <sub>m</sub>	0	3

**Figure 2.** Confusion matrix shows the predictions from the model on the test data.

# Prediction of Survival in Glioma Patient Using MRI-Derived Features, Clinical data, and Automated Machine Learning (AutoML) Methods

**Maninder Singh<sup>1</sup>, Sudhir Kumar Pathak<sup>2</sup>, B. V. Rathish Kumar<sup>3</sup>, Ranjeet Ranjan Jha<sup>4</sup>, Siddharth Singh<sup>1</sup>, Anit Parihar<sup>1</sup>, Chhitij Srivastava<sup>5</sup>, Bal Krishna Ojha<sup>5</sup>, Awadhesh Jaiswal<sup>6</sup>, Kuntal Kanti Das<sup>6</sup> and Durgesh Kumar Dwivedi<sup>1</sup>**

<sup>1</sup>Department of Radiodiagnosis, King George's Medical University, Lucknow, India, <sup>2</sup>Learning Research and Development Center, University of Pittsburgh, Pittsburgh, PA, United States, <sup>3</sup>Department of Mathematics and Statistics, Indian Institute of Technology, Kanpur, India, <sup>4</sup>Department of Mathematics, Indian Institute of Technology, Patna, India, <sup>5</sup>Department of Neurosurgery, King George's Medical University, Lucknow, India <sup>6</sup>Department of Neurosurgery, Sanjay Gandhi Postgraduate Institute of Medical Sciences, Lucknow, India

## Introduction

Gliomas, a diverse and complex group of primary brain tumors, present a significant clinical challenge due to their heterogeneity and profound impact on patient survival outcomes [1]. Generally, glioma has three typical regions: edema (ED), enhancing tumor (ET), and necrotic core (NC) (fig.1A). Accurate survival prediction is vital for informed clinical decision-making. Traditional machine learning (ML) approaches require manual algorithm selection and hyperparameter tuning, which can be time-consuming [2]. Instead of manually selecting and testing different machine learning algorithms, AutoML can automatically identify the best-performing models for the dataset. Hyperopt-sklearn (HSL), an automated machine learning (AutoML) method automatically search for the best model algorithms and their respective hyperparameters among inbuilt scikit-learn ML algorithms [2]. Our study aimed to utilize AutoML method for selection of regression algorithm and hyperparameter optimization process for the prediction of survival days of glioma patients.

## Methods

The radiomic features extracted from the UPENN-GBM dataset (T1GD sequence) [3] were pre-processed. Correlation analysis was performed (threshold = 0.15) to reduce redundancy and focus on the most informative features, narrowing down the feature set to 63. The curated dataset includes 176 patients with 63 radiomics features and clinical data (age, gender, IDH1 mutation and MGMT methylation status and survival days). The dataset was split into training and test sets in a 9:1 ratio. The workflow of model generation and evaluation is shown in Fig.1B. Correlation analysis and Kaplan Meier Survival analysis was performed to analyse the data and model outcomes. **Results**

### Results

Comparative studies of the proposed VAE-UNet were performed with state-of-the-art models like QSMNet, xQSM7, and 3D-UNet as in DeepQSM and the corresponding performance metrics were summarized in Table 1 and 2. A visual comparison of the proposed VAE-UNet with COSMOS is shown in Figure 1. Our experimental studies demonstrate that the VAE-UNet model efficiently balances accuracy and generalizability in QSM reconstruction

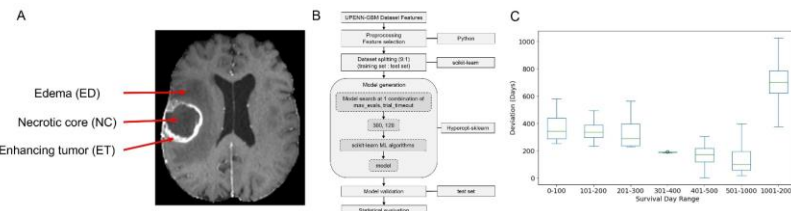


**Fig.1** (A) Three regions of glioma, edema (ED), enhancing tumor (ET), necrotic core (NC). (B) Workflow of study. (C) Statistical analysis of survival day groups showing performance of SGDRRegressor model in different ranges of survival days.

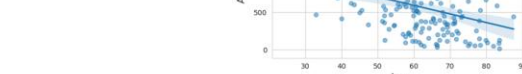


**Fig.2** Correlation of age with Survival days (Pearson Correlation: -0.296, P-value: 0.00023)

## Discussion

Our results demonstrated that the SGDR model showed adequate predictive accuracy within the 301-400 days, 401-500 days and 501-1000 days range, highlighting its potential in predicting mid-range survival for glioma patients. However, significant limitations emerged when attempting to generalize predictions to shorter and longer survival ranges, with the accuracy of the model substantially declining. Furthermore, feature importance identified age as a key parameter, along with other MRI-derived features, reinforcing its clinical

relevance in glioma prognosis. The association of IDH1 mutations and MGMT methylation showed better survival in glioma [4]. The negative correlation between age and survival days suggests that as age increases, survival days tend to decrease. The limited sample sizes across extreme survival groups contributed to performance variability and hindered the robustness of the model in these ranges. Glioma survival predictions were likely influenced by multifactorial and nonlinear interactions among variables, including tumor heterogeneity, patient demographics, and treatment responses [5]. Thus, more complex modeling techniques coupled with larger sample size could have better address the heterogeneity within the dataset.

## Conclusion

Our study highlights the potential of AutoML in glioma survival prediction, simplifying model development for clinicians but requires further validation for clinical deployment. Future work will focus on XGBoost, neural networks, and other algorithms, improved feature engineering, and balancing data to enhance predictive accuracy and reliability.

## Acknowledgements

Dr. D.K. Dwivedi and Prof. B.V. Rathish Kumar express their profound gratitude to the Indian Council of Medical Research (ICMR), New Delhi for their generous funding (Grant No. EM/Dev/IG/27/0337/2023).

Furthermore, Prof. B.V. Rathish Kumar (IITK, India) and Dr. S.K. Pathak (Pitt, USA) extend their heartfelt appreciation to SPARC for their funding support (Grant No. SPARC/2019-2020/P1622/SL). Additionally, Dr. D.K. Dwivedi sincerely acknowledges the financial support provided by UPCST (Grant No. CST/D-1381). Dr. D.K. Dwivedi also conveys sincere thanks to the Science and Engineering Research Board (now ANRF), New Delhi for their valuable funding support under Grant No. SUR/2022/001841).

## Reference

- [1] B. Spyridon, C. Sako, H. Akbari, M. Bilello, A. Sotiras, G. Shukla, J. D. Rudie et al., *Scientific data* 9, no. 1 (2022): 453.
- [2] H. F. Lücke J, Schmid t-Thieme L, KI - Künstliche Intelligenz 2015, 29 (4), 329-337
- [3] <https://www.cancerimagingarchive.net/collection/upenn-gbm/>
- [4] A. Pandith, I. Qasim, S.M. Baba, A. Koul, W. Zahoor, D. Afroze, A. Lateef et al., *Future Science OA* 7, no. 3 (2021): FSO663
- [5] J.R. Chandra, R. Mishra, P. Gandhi, et al., *Comput Biol Med*. 2021 Oct;137:104829

# Regional Cortical Thinning and Its Association with Cognitive Performance in Aging.

Mukesh Kumar<sup>1</sup>, Arman Deep Singh<sup>1</sup>, Swathi BH<sup>1</sup>, Bhargavi P<sup>1</sup>, Ashwini Godbole<sup>1</sup>, Subash Khushu<sup>1</sup>

The University of Trans-Disciplinary Health Sciences and Technology, Bengaluru, India

## Introduction

Aging is a continuous process with cortical thinning as a common consequence[1]. This study aimed to evaluate regional cortical thickness, volume and area differences associated with age in an Indian healthy population.

## Methods

76 healthy individuals categorized into a younger age group (G1), n=25, age 25-40 years; a middle-aged group (G2), n=24, age 41 to 55 years; and an older group (G3), n=27, age range 56-80 years. Participants underwent neuropsychological assessments and MRI scanning.

## Results

The elderly group had significantly reduced cortical thickness and volume in middle temporal, lateral occipital, whereas reduced cortical thickness in middle temporal, precuneus, superior temporal, lateral occipital, insula, posterior cingulate in elderly as compared to younger participants (Figure 1).

Age-related declines were also observed in auditory verbal learning, AVL memory, backward digit span, Digit Symbol Substitution Test in older as compared to younger groups. The reduced mean cortical thinning and total cortical volume correlated with age (Figure 2).

## Discussion

our study underscores the impact of aging on cortical thickness, volume and area revealing significant thinning in regions such as the posterior cingulate, precuneus, middle

temporal areas, and lateral orbitofrontal cortex, which correlates with decline cognitive performance. Along with aging, reduced cortical thickness and volume might reflect neuronal degeneration, with contributing factors including myelin loss, brain atrophy, and neuroinflammation, which tend to be more pronounced in older adults[2].

## Conclusion

These findings are important for early detection of cognitive decline in ageing population and the need for targeted intervention. .

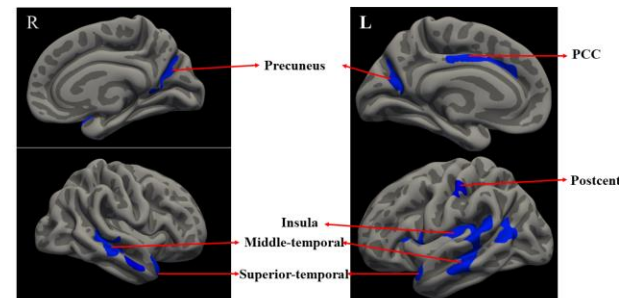


**Figure 1:** Significant cortical thickness (CTh) difference between young (G1) and elderly (G3) groups individuals

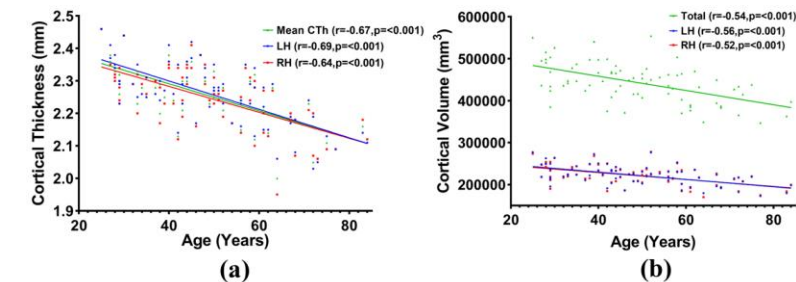


**Figure 2:** Correlation plot between Cortical thickness, volume and age (years) (a) left hemispheric (LH), right hemispheric (RH) and global cortical thickness (Mean CTh); and (b) left hemispheric (LH), right hemispheric (RH) and total cortical volume.

## Reference

H. Lemaitre et al., “Normal age-related brain morphometric changes: Nonuniformity across cortical thickness, surface area and gray matter volume?,” *Neurobiol. Aging*, vol. 33, no. 3, p. 617.e1-617.e9, 2012, doi: 10.1016/j.neurobiolaging.2010.07.013.

[2] M. de Chastelaine et al., “Cortical thickness, gray matter volume, and cognitive performance: a cross-sectional study of the moderating effects of age on their interrelationships,” *Cereb. Cortex N. Y. NY*, vol. 33, no. 10, pp. 6474–6485, Jan. 2023, doi: 10.1093/cercor/bhac518.

# Cerebrospinal Fluid Fraction (CSFF) as a Global Regularization for Brain Quantitative Susceptibility Mapping

Deepu Kurian<sup>1,2</sup>

Chandrasekharan Kesavadas, MD<sup>3</sup>

Joseph Suresh Paul, PhD<sup>1,2</sup>

<sup>1</sup> School of Electronic Systems and Automation, Kerala University of Digital Sciences Innovation and Technology, Kerala, India. <sup>2</sup> Indian Institute of Information Technology and Management – Kerala, India. <sup>3</sup> Department of Radiology, Sree Chitra Tirunal Institute, Kerala, India.

## Introduction

While the Quantitative Susceptibility Mapping (QSM) highly recommended for quantifying tissue magnetic susceptibility, it remains susceptible to contamination from cerebrospinal fluid (CSF), leading to erroneous susceptibility estimations, particularly in regions such as periventricular and sulcal areas. Although the (MEDI+0) algorithm [1], which employs an R\_2^\* map to segment ventricular CSF, substantially mitigates this issue, the reproducibility of the R2\* map under a fixed threshold remains limited when imaging parameters vary [2,3]. This study introduces a refined regularization framework that integrates cerebrospinal fluid fraction (CSFF) maps, to mitigate CSF contamination and improve the fidelity of QSM reconstructions. The primary objective of this framework is to improve the clinical reliability of QSM by incorporating global zero referencing, minimizing CSF contamination, and eliminating the smooth shading effect associated with partial CSF volume effects.

## Methods

The proposed method uses CSFF maps generated using multi-echo T\_2^\*-relaxometry. A two-compartment water model was fitted to the multi-echo gradient recalled echo (mGRE) signal to separate CSF from intra- and extracellular water, producing voxel-wise CSFF maps [4,5]. These maps were used to construct a comprehensive CSF mask, serving as an anatomical constraint to suppress CSF contamination, and to generate a binary weighting matrix that improves the QSM field-to-susceptibility inversion. In particular, the optimization framework integrates a novel regularization term informed by the global CSFF mask to promote spatial homogeneity in CSF regions, alongside a structural weighting matrix that incorporates gradients from both magnitude images and CSFF maps.

The susceptibility map  $\chi$  was estimated by minimizing the following cost function:

$$\operatorname{argmin}_{\chi} \left( \frac{1}{2} \| w(e^{if} - e^{i(d+\chi)}) \|_2^2 + \lambda_1 \| M_G \nabla \chi \|_1 + \lambda_1 \| CSFF_G \nabla \chi \|_1 + \lambda_2 \| M_{CSFF}(\chi - \chi_{CSFF}) \|_2^2 \right)$$

where  $f$  denotes the measured field map,  $d$  represents the dipole kernel, and  $W$  is a noise-weighting matrix. The first term ensures fidelity to the measured data, the second and third ensures reduced streaking artifacts that arise from the ill-posed nature of the dipole inversion problem utilizing the binary gradients masks from magnitude data  $M_G$  and the CSFF map  $[CSFF]_G$  where the gradient operator  $\nabla$  captures spatial variations in the susceptibility map  $\chi$ , and the fourth penalizes susceptibility variations within CSF-dominant regions using the CSF mask

$M\_CSFF$  generated from the CSFF map.

## Results

The proposed CSFF-regularization framework markedly improved susceptibility estimation by reducing CSF contamination, suppressing streaking artifacts and noise in periventricular and sulcal regions, and yielding anatomically consistent susceptibility maps. Figure 1 compares masks generated from CSFF and T\_2^\* maps, revealing that CSFF-based masks better capture CSF in the sulcal areas. Figure 2 illustrates QSM reconstructions from the MEDI+0 method and the proposed CSFF approach, demonstrating more homogeneous CSF regions and elimination of the smooth shading effect caused by partial CSF volume near sulcal boundaries. Quantitative analysis (Figure 2, Panel B) further indicates a lower mean ( $M = 0.0002$ ) and standard deviation ( $SD = 0.0238$ ) for QSM values in CSF-rich areas using the proposed method, compared with the MEDI method ( $M = -0.0076$ ;  $SD = 0.1121$ ), signifying enhanced homogeneity in the CSF regions.

## Discussion

Unlike traditional methods that rely on fixed ventricular CSF references or R2^\*-based masks, the CSFF-based approach offers a physiologically informed, voxel-wise representation of CSF distribution. This novel regularization strategy not only reduces susceptibility artifacts but also ensures anatomically consistent reconstructions, even in complex or artifact-prone regions.

By leveraging the high signal stability and specificity of the CSFF map, the method enhances susceptibility reconstruction fidelity while preserving structural details. This is particularly valuable for clinical applications, where precise susceptibility quantification is essential for tracking disease progression and evaluating therapeutic interventions.

With the growing interest of applying QSM for the longitudinal tracking of disease progression in various neurodegenerative conditions and aging—commonly associated with perivascular space dilation due to obstructed cerebrospinal fluid flow [5,6]—CSFF-informed QSM reconstructions are becoming increasingly important.

## Conclusion

The CSFF-based regularization framework represents a significant advancement in QSM methodology by directly addressing CSF contamination—a critical challenge in susceptibility mapping. By incorporating anatomically accurate CSFF maps into the inversion process, the proposed method delivers improved

accuracy, reliability, and clinical utility in susceptibility quantification. The framework's ability to suppress artifacts, enhance reproducibility, and improve diagnostic precision makes it a powerful tool for both research and clinical applications. Future research will focus on validating the method with clinical data sets emphasizing longitudinal and cross-sectional analysis.

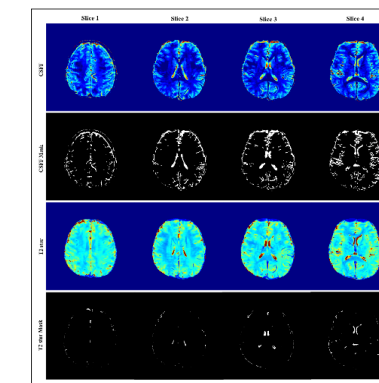


Figure 1: The rows indicate CSFF map, Mask from CSFF map, T\_2^\*-map and Mask from T\_2^\*-map respectively.

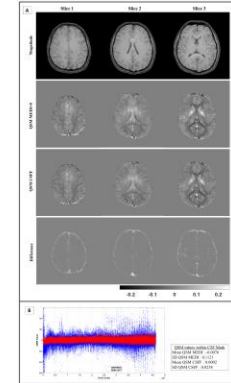


Figure 2: Panel A presents QSM reconstructions from the MEDI+0 method and the proposed CSFF approach. Panel B presents scatter plot of QSM values within CSF Mask.

## Reference

- [1] Z. Liu, P. Spincemaille, Y. Yao, Y. Zhang, and Y. Wang, "MEDI+0: Morphology enabled dipole inversion with automatic uniform cerebrospinal fluid zero reference for quantitative susceptibility mapping," *Magnetic Resonance in Medicine*, vol. 79, no. 5, pp. 2795–2803, May 2018, doi: 10.1002/mrm.26946.
- [2] Q. Qin, "A simple approach for three-dimensional mapping of baseline cerebrospinal fluid volume fraction," *Magn. Reson. Med.*, vol. 65, no. 2, pp. 385–391, Feb. 2011, doi: 10.1002/mrm.22705.
- [3] A. V. Dimov, T. D. Nguyen, P. Spincemaille, E. M. Sweeney, N. Zinger, I. Kovancikaya, B. H. Kopell, S. A. Gauthier, and Y. Wang, "Global cerebrospinal fluid as a zero-reference regularization for brain quantitative susceptibility mapping," *Journal of Neuroimaging*, vol. 32, no. 1, pp. 141–147, Jan. 2022, doi: 10.1111/jon.12923.
- [4] C. Pierpaoli and D. K. Jones, "Removing CSF contamination in brain DT-MRIs by using a two-compartment tensor model," in Proc. 8th Annu. Meeting Int. Soc. Magn. Reson. Med. (ISMRM), Denver, CO, USA, 2000, p. 841. [Online]. Available: [https://www.ncbi.nlm.nih.gov/sites/default/files/inline-files/removing\\_CSF\\_contamination.pdf](https://www.ncbi.nlm.nih.gov/sites/default/files/inline-files/removing_CSF_contamination.pdf)
- [5] Y. He et al., "Quantifying perivascular space in Alzheimer's disease by MRI relaxometry," *Alzheimer's & Dementia*, vol. -, early view, 2023, doi: 10.1002/alz.057721. [Online]. Available: <https://alz-journals.onlinelibrary.wiley.com/doi/full/10.1002/alz.057721>
- [6] L. Zhou, Y. Li, E. M. Sweeney, X. H. Wang, A. Kuceyeski, G. C. Chiang, J. Ivanidze, Y. Wang, S. A. Gauthier, M. J. de Leon, and T. D. Nguyen, "Association of brain tissue cerebrospinal fluid fraction with age in healthy cognitively normal adults," *Frontiers in Aging Neuroscience*, vol. 15, p. 1162001, Jun. 2023, doi: 10.3389/fnagi.2023.1162001.

# Ketamine and Electroconvulsive Therapy: Distinct Yet Partially Overlapping Mechanisms in Treatment of Depression

Ajay Sarawagi<sup>1,2</sup>

<sup>1</sup>CSIR-Centre for Cellular and Molecular Biology, Hyderabad, India, <sup>2</sup>Academy of Scientific and Innovative Research (AcSIR), Ghaziabad-2012002, India

## Introduction

Major depressive disorder is a debilitating mental health condition, characterized by persistent low mood, anhedonia, sleep disturbances, and suicidal ideation. Traditional antidepressants often suffer from low efficacy, delayed onset of results, and ineffectiveness in approximately 40% of depressed subjects. Ketamine and electroconvulsive therapy (ECT) are FDA-approved interventions for drug-resistant depression, offering rapid and highly effective therapeutic outcomes as compared to conventional antidepressants [1]. ECT involves the induction of a controlled seizure lasting a few seconds, followed by a post-ictal suppression phase characterized by reduced overall brain activity [2]. Ketamine, a non-competitive antagonist of N-methyl-D-aspartate (NMDA) receptors, induces anesthesia at higher doses [3], but exhibits rapid antidepressant effects at sub-anesthetic doses. However, the understanding of the impact of ECT and ketamine on the metabolic activity of excitatory, and inhibitory neurons and astrocytes is limited. Hence, the major aim of the study was to assess the impact of acute ECT and ketamine on neural circuitry.

## Methods

Two-month-old C57BL6 male mice in the ECT group received a single electroconvulsive shock under isoflurane anesthesia via corneal electrodes, while the sham group mice were anesthetized but had no electric shock [4]. The Ketamine group of mice was injected with (R,S)-ketamine (25 mg/kg, ip), while controls were injected with a normal saline solution. The impact of ECT and Ketamine administration on the metabolic activity of neurons and astrocytes was evaluated at different time points by conducting ex-vivo <sup>1</sup>H-[<sup>13</sup>C]-NMR spectroscopy in conjunction with intravenous [<sup>1,6-13C2</sup>]glucose or [<sup>2-13C</sup>]acetate infusion, respectively (Fig. 1) [5]. The transcriptomics and quantitative phosphoproteomics were conducted to assess the effects of these interventions at the molecular level in the mouse brain.

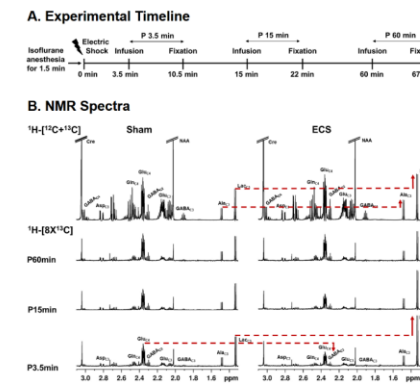


**Fig 1A.** Experimental timeline depicting mice were infused with [<sup>1,6-13C2</sup>]glucose after 3.5, 15 and 60 min of ECS, respectively. Brain Metabolism was arrested 7 min post infusion. B. Representative <sup>1</sup>H-[<sup>13</sup>C]-NMR spectra depicting total concentration of neurometabolites in top most panel, and <sup>13</sup>C labeled neurometabolites in the lower panel at different time points in Sham and ECS mice.

## Results

Sub-anesthetic ketamine administration led to a transient enhancement in cerebral glucose oxidation within 15 min of injection, and normalized within 25 min. A comparable surge in neurometabolic activity was observed during ECT-induced seizure (+64.3±15.3 %, p=0.005), while the astroglial activity remained unchanged. However, a drastic reduction in the oxidative metabolism in neurons (-43.3±3.0 %, p=0.0004) and astrocytes (-37.0±0.8 %, p=0.0003) occurred immediately after seizure termination, with a pronounced increase in non-oxidative glucose consumption (+112.8±9.8 %, p=0.0001). Interestingly, the neuronal and astroglial activity normalized within one hour after ECT. Phosphoproteomic analysis showed a very distinct set of differentially expressed phosphoproteins involved during ECT-induced seizure and after one hour of electroconvulsive shock. The transcriptomic analysis indicated a marginal overlap in the biological processes involved in the molecular mechanisms of acute ECT and ketamine interventions.

## Discussion

ECT and ketamine treatments are known to enhance synaptic plasticity,

neurogenesis, and synaptogenesis and reduce neuroinflammation [6, 7]. Ketamine-induced surge in the neurometabolic activity is in line with a previous study in rats highlighting a transient surge in glutamate release within PFC, which is responsible for the rapid antidepressant effects [8]. ECT was also found to enhance the metabolic activity of glutamatergic and GABAergic neurons during the seizure phase similar to ketamine's induced glutamate surge. However, the neurometabolic effects of ECT differ from ketamine in the post-ictal period, where neuronal and astroglial metabolic activity gets drastically reduced. Moreover, ECT seems to shift the brain ATP generation machinery to anaerobic glucose metabolism during the seizure and post-ictal suppression phase, reflecting an adaptive response of the brain to meet high energy demands or oxidative stress, potentially contributing to ECT's therapeutic effects. Interestingly, the effects of ketamine and ECT were normalized to their respective control, within 25 and 60 minutes of administration, respectively. The transcriptomic analysis further shows the distinction in the neuromodulatory effects of ECT and ketamine interventions in mouse brains.

## Conclusion

The assessment of metabolic activity of glutamatergic, GABAergic neurons, and astrocytes during acute ketamine administration, ECS-induced seizures, and post-ictal suppression phase provides valuable information about the potential mechanisms of ECT and ketamine and could inform the development of optimized treatment strategies for depression and minimize the immediate side effects associated with these interventions.

## Acknowledgment

CSIR-Health Care Theme FBR/MLP0150; DBT-Research fellowship DBT/2019/CCMB/1230

## Reference

- [1] Rhee et al, JAMA Psychiatry. 2022;79(12):1162; [2] Deng et al, Neuropsychopharmacol. 2024;49(1):150-162; [3] Moghaddam et al, J Neurosci. 1997;17(8):2921-2927; [4] Sarawagi et al, Neuroglia. 2024;5(3):306-322; [5] Mishra et al, J Neurochem. 2018;146(6):722-734; [6] Abe et al, J Neurochem. 2024; jnc.16054; [7] Krystal et al, Proc Natl Acad Sci USA. 2023;120(49):e2305772120; [8] Chowdhury et al, Mol Psychiatry. 2017;22(1):120-126.

# Swin UNETR-Based Deep Learning Framework for Automated Blood Vessel Segmentation in Brain Tumor DCE-MRI

Anshika Kesari<sup>1</sup>

Satyajit Maurya<sup>1</sup>

Mohammad Tufail Sheikh<sup>1</sup>

Rakesh Kumar Gupta<sup>2</sup>

Anup Singh<sup>1,3,4</sup>

<sup>1</sup>Centre for Biomedical Engineering, Indian Institute of Technology Delhi, New Delhi, India, <sup>2</sup>Department of Radiology, Fortis Memorial Research Institute, Gurugram, India, <sup>3</sup>Department of Biomedical Engineering, All India Institute of Medical Sciences, New Delhi, India, <sup>4</sup>Yardi School for Artificial Intelligence, Indian Institute of Technology Delhi, New Delhi, India

## Introduction

Brain tumor progression is closely linked to angiogenesis, where blood vessel density serves as a key indicator of tumor development and grade. Quantitative dynamic contrast enhanced-magnetic resonance imaging (DCE-MRI) has emerged as a valuable tool in brain tumor grading and monitoring treatment response. However, accurate quantification requires precise segmentation of large blood vessels (LBVs), as their presence can confound tumor assessment. Traditional manual and semi-manual approaches to LBV segmentation are time-consuming, subjective, and error-prone [1], [2]. The objective of this study was to develop and validate an automated deep learning approach using Swin UNETR architecture [3] for accurate LBV segmentation in brain tumor patients, addressing the critical need for efficient and reliable vessel segmentation in clinical practice.

## Methods

We conducted a retrospective study using MRI data of 142 glioma patients from FMRI, Gurugram, India. All imaging was performed on a 3T MRI system using a comprehensive protocol that included structural sequences (T1-weighted, T2-weighted, PD-weighted), DCE-MRI, and fluid-attenuated inversion recovery (FLAIR) imaging. Data processing was executed through an in-house developed MATLAB-2022a tool [4], incorporating essential pre-processing steps including skull-stripping, image registration, and noise filtering. Our quantitative DCE-MRI analysis pipeline integrated multiple analytical approaches: piecewise-linear model fitting for deriving alpha, beta, and slope parameters (Slope-1, Slope-2); first-pass analysis for cerebral blood volume (CBV) and cerebral blood flow (CBF) calculations; and generalized tracer-kinetic modeling to estimate volume transfer constant ( $K_{trans}$ ), plasma volume fraction ( $V_p$ ), and extravascular-extracellular-space volume fraction ( $V_e$ ). For segmenting the LBVs we implemented the Swin UNETR architecture, which combines the hierarchical feature extraction capabilities of Swin Transformers with the U-shaped encoder-decoder structure. The data was systematically divided into training (90), validation (17), and testing sets (35). The Swin UNETR model was trained using an Adam optimizer with a batch size of 16 to 200 epochs and the ground truth was generated using pre-defined segmentation protocols [5], with manual refinements by expert radiologists. To evaluate model generalizability and ensure robust validation, we included diverse brain tumor types, including 10 lymphoma and 10 metastasis patients. Whole tumor region was segmented using an in-house deep learning based tool on FLAIR images [6], with manual refinement applied when necessary to ensure accurate delineation. Statistical analysis included calculation of Dice similarity coefficients for segmentation accuracy, and t-tests for comparing quantitative parameters between tumoral regions with and without LBVs using both ground truth and predicted masks along with the comparison between generated ground truth and predicted mask itself as shown in flow diagram (Figure-1).

## Results

The Swin UNETR model demonstrated exceptional performance in LBV segmentation

across all datasets (Figure-2). The model achieved Dice scores of 0.979 and 0.973 on training and validation sets, respectively. Test set performance showed robust generalizability, with Dice scores ranging from 0.929 to 0.982 across different tumor types (Table-1). Quantitative analysis revealed significant differences ( $p<0.05$ ) in DCE-MRI parameters between regions with and without LBVs. The benefit of vasculature segmentation was further validated through bar plots and box and whisker plots of 95th percentile (Figure-3) of multiple quantitative parameters except the Slope-2 as tumor and vasculature both show lower intensity. After LBV removal using both ground truth and predicted masks, the quantitative parameters in non-vascular tumoral regions showed statistical similarity ( $p>0.05$ ), confirming the reliability of proposed approach. **Discussion** The observed ghosting artifacts in MRI images were traced to inconsistencies in the spatial encoding caused by non-linear increments in phase encode (PE) gradient areas. These irregularities lead to redundant or identical k-space coverage at certain PE steps, contributing to artifacts in the phase encoding direction. Addressing this issue required analyzing waveform data and introducing corrections to linearize the increment of PE gradient areas.

## Discussion

The high performance of our Swin UNETR-based approach represents a significant advancement in automated LBV segmentation for brain tumor analysis. The model's robust performance across different tumor types demonstrates its potential for broad clinical application. Our results suggest that accurate vessel segmentation significantly impacts the quantification of tumor parameters, highlighting the importance of this pre-processing step in tumor assessment. The statistical similarity between parameters obtained using ground truth and predicted masks validates the clinical reliability of our automated approach. However, future work should also evaluate the potential of the proposed model in data from other types of brain tumors as well as post-surgery data, particularly for treatment response assessment.

## Conclusion

The proposed Swin UNETR-based approach provides an accurate and generalizable solution for LBV segmentation in brain tumor imaging. The demonstrated performance across diverse tumor types, coupled with its ability to maintain parameter accuracy, positions this tool as a valuable asset for improving tumor grading accuracy and treatment planning.

## Acknowledgement

Authors acknowledge funding support from SERB-DST project number: CRG/2019/005032. The authors thank Dr. Rana Patir and Dr. Sunita Ahlawat for clinical inputs and Mr. Rakesh Kumar for data handling.

## Reference

[1] Li X, et al. Cancer Imaging. 2015 Mar;15(1):3.

[2] Passat N, et al. J Magn Reson Imaging. 2005 Jun;21(6):715-725.

[3] Hatamizadeh A, et al. In: Lecture Notes in Computer Science. 2022; 12962 LNCS:272–284. [4] Sasi DS, et al. Magnetic Resonance Imaging. 2021 Nov;83:77–88.

[5] Kesari A, et al. NMR in Biomedicine. 2019;32(6).

[6] Maurya S, et al. International MICCAI Brainlesion Workshop 2022;12963 LNCS:31 2-323.

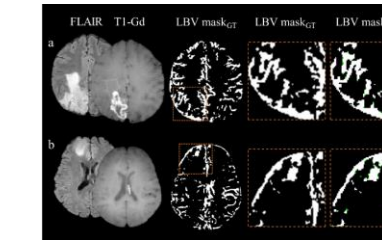


Figure-2: Conventional images of (a) Grade-4 and (b) Grade-2 patients and their respective large blood vessel (LBV) masks generated using ground truth (LBV maskGT) and Swin UNETR (LBV maskpred).

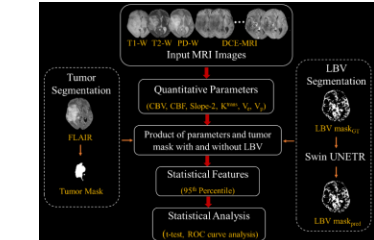


Figure-1: Methodology flow diagram.

Figure-2: Conventional images of (a) Grade-4 and (b) Grade-2 patients and their respective large blood vessel (LBV) masks generated using ground truth (LBV maskGT) and Swin UNETR (LBV maskpred). The comparison between both masks is shown in the LBV maskpred column, where white regions indicate similarity, green shows overestimated regions, and magenta shows underestimated regions

Testing Data Dice		
Glioma	Lymphoma	Metastasis
0.959±0.048	0.982±0.001	0.929±0.551

Table-1: Model training parameters and performance metrics of testing data.

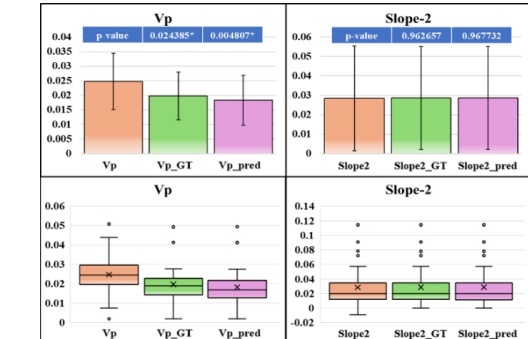


Figure-3: Box plots of mean and standard deviation and bar and whisker plot of 95th percentile of various quantitative parameters with and without vasculature (ground truth (GT) and predicted (pred)) showing statistical difference in each case. \* shows significant difference.

# Radiomics as an Alternative to T2\* value in Cardiac Iron Overload Staging: A Pilot Study Using Open Access Data.

Silva, KNS<sup>1</sup>, Hewadikaram, EHADK<sup>1</sup>, Rathnayaka, MB<sup>2\*</sup>

<sup>1</sup>Department of Electrical, Electronic and Telecommunication Engineering, General Sir John Kotelawala Defence University, Sri Lanka, <sup>2</sup> Department of Nuclear Science, University of Colombo, Sri Lanka

## Introduction

Thalassemia is a hereditary blood disorder that leads to severe anemia, requiring regular blood transfusions as a primary treatment.[1-3] However, repeated transfusions result in cardiac iron overload (CIO), a critical complication causing cardiomyopathy, arrhythmias, and heart failure, which is a leading cause of mortality in thalassemia major. Early detection of CIO is crucial but remains challenging due to the limitations of existing diagnostic methods like serum ferritin measurement, endomyocardial biopsy, and T2\*-weighted MRI, which face issues of invasiveness, cost and technical constraints. This study addresses these gaps by proposing a radiomics-based, noninvasive approach for CIO detection and staging, using high-dimensional quantitative imaging features and machine learning algorithms for accurate and early diagnosis, enabling better clinical outcomes.

## Methods

This study utilized the CHMMOTv1 [4] dataset comprising 124 thalassemia patients, focusing on T2\* and R2\* to classify CIO into Normal ( $T2^*>20$  ms), Moderate ( $20$  ms- $T2^*>10$  ms), and Severe ( $T2^*<10$  ms) categories. For the current study 42 subjects were randomly selected, covering all three stages. Regions of interest (ROIs) were segmented (Figure 1- (a) and (b)) from cardiac MRI images (TE/TR 3.2 ms/31.3 ms, matrix size = 128x116, slice thickness = 10 mm, FOV = 40x40 cm) using 3D Slicer software. Using the pyRadiomics Python library, a total of 856 radiomic features were extracted. These features encompass various categories, including first-order statistics, texture features, shape descriptors, and wavelet-transformed features. Feature selection techniques—Random Forest (RF), Recursive Feature Elimination (RFE), Lasso Regression, and Boruta—used to identify the top 10 most relevant features for classification. Machine learning models RF, support vector machine (SVM) and Extreme Gradient Boosting (XGB oost) were trained on these features. Class imbalance was addressed using the Synthetic Minority Oversampling Technique (SMOTE)[5]. Model performance was evaluated using accuracy, F1 score, and AUC-ROC, ensuring the identification of the best classifier for CIO detection.

## Results

Feature selection techniques, including RF, RFE, Lasso Regression, and Boruta, successfully identified the top 10 most relevant features. Among these, texture and shape features stood out as critical biomarkers for classification. The study demonstrated the effectiveness of radiomics features and machine learning model in classifying cardiac iron overload (CIO) severity levels in thalassemia patients. Among the tested models, XGBoost [6-8] achieved the best performance with an accuracy of 91%, an F1 score of 0.92, and an AUC-ROC of 1.00, (Figure 2 – (a) and (b)) showing superior capability in distinguishing Normal, Moderate, and Severe categories. RF performed reasonably well, with an accuracy of 73% and an F1 score of 0.74, but struggled with the Moderate class due to overlapping feature distributions. SVM displayed lower effectiveness.

## Discussion

The findings highlight the potential of radiomics and machine learning for non-invasive detection of CIO. XGBoost's ability to handle complex data interactions and high-dimensional datasets made it the preferred model for this application. The study also emphasized the significance of texture and shape features in capturing structural and textural alterations in cardiac tissues due to iron deposition. However, challenges such as the small dataset size and class imbalance impacted the differentiation of Moderate and Severe categories. Future efforts should focus on employing deep learning techniques, such as convolutional neural networks (CNNs), for automated feature extraction and integrating

radiomics features with clinical parameters like serum ferritin and T2\* relaxation times. These advancements could enhance model robustness, improve diagnostic accuracy, and support the development of a standardized multi-modal tool for early detection and personalized management of CIO in thalassemia patients.

## Conclusion

Our clustering-based analysis of Multiparametric-MRI demonstrates that high-intensity clusters of Ktrans, Ve, mean Ktrans and mean Kepl are statistically significant parameters for differentiating TP from PsP. Tumor volume difference between TP and PsP was near significant ( $p=0.07$ ), suggesting that TP is associated with more severe tumor profile. These findings support using DCE-MRI and clustering techniques as non-invasive tools for distinguishing TP from PsP. Future studies should validate these results with larger datasets and integrate more comprehensive multimodal imaging data.

## References

- [1] G. Bartoloni, F. Italia, G. Ferraro, T. Lombardo, C. Tamburino, and S. Cordaro, 'Histopathology of Thalassemic Heart Disease: An Endomyocardial Biopsy Study', *Cardiovascular Pathology*, vol. 6, no. 4, pp. 205–211, Jul. 1997, doi: 10.1016/S1054-8807(96)00136-6.
- [2] E. C. Chapchap et al., 'Alpha- and Beta-thalassemia: Rapid Evidence Review', *Am Fam Physician*, vol. 105, no. 3, pp. 272–280, Mar. 2022, doi: 10.1016/j.jafccm.2021.01.014.
- [3] H. L. Muncie and J. S. Campbell, 'Alpha and Beta Thalassemia', 2009. [Online]. Available: [www.aafp.org/afp](http://www.aafp.org/afp).
- [4] I. Abedi, M. Zamarian, H. Bolhasani, and M. Jalilian, 'CHMMOTv1 - cardiac and hepatic multi-echo (T2\*) MRI images and clinical dataset for iron overload on thalassemia patients', *BMC Res Notes*, vol. 16, no. 1, pp. 1–5, Dec. 2023, doi: 10.1186/S13104-023-06075-FIGURES/3.
- [5] R. Blagus and L. Lusa, 'SMOTE for high-dimensional class-imbalanced data', *BMC Bioinformatics*, vol. 14, no. 1, pp. 1–16, Mar. 2013, doi: 10.1186/1471-2105-14-106FIGURES/7.
- [6] A. Ogundeye and Q. G. Wang, 'XGBoost Model for Chronic Kidney Disease Diagnosis', *IEEE/ACM Trans Comput Biol Bioinform*, vol. 17, no. 6, pp. 2131–2140, Nov. 2020, doi: 10.1109/TCBB.2019.2911071.
- [7] D. Nielsen, 'Tree Boosting With XGBoost Why Does XGBoost Win "Every" Machine Learning Competition?'.
- [8] T. Chen and C. Guestrin, 'XGBoost: A scalable tree boosting system', *Proceedings of the ACM SIGKDD International Conference on Knowledge Discovery and Data Mining*, vol. 13–17-August-2016, pp. 785–794, Aug. 2016

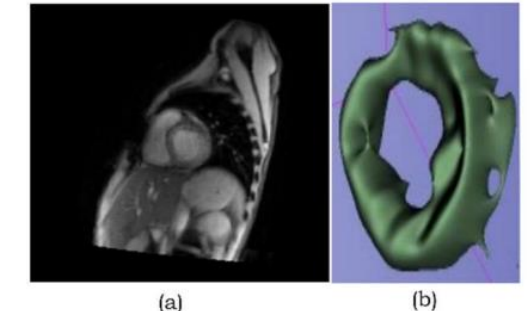


Figure 1- (a) cardiac MRI image from the database, (b) segmented myocardium

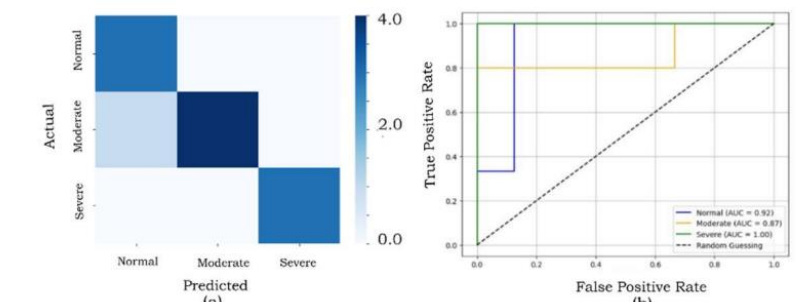


Figure 2 - (a) Confusion matrix for XGBoost classifier, (b) ROC AUC curve for XGBoost classifier

# MR VOLUMETRY, MORPHOLOGY AND MR ELASTOGRAPHY ASSESSMENT OF PANCREATIC TEXTURE IN TYPE 2 DIABETES MELLITUS

**Dr Anjali Chandoliya**

Third Year PG Junior Resident, Department of Diagnostic and Interventional Radiology, AIIMS Jodhpur

## Abstract

This study evaluates the potential of MRI in assessing pancreatic changes and predicting microangiopathy in Type 2 Diabetes Mellitus (T2DM). A prospective observational study of 125 T2DM patients was conducted to analyze pancreatic morphology, volume, fat fraction, and elasticity, and their correlation with diabetic nephropathy, neuropathy, and retinopathy. Pancreatic fat fraction and elastography were significantly associated with diabetic retinopathy ( $p = 0.041, 0.054$ ), while maximum pancreatic width was a key parameter for distinguishing microangiopathy ( $p = 0.020$ ). This comprehensive approach, combining MRI parameters with clinical and biochemical markers, enhances diagnostic accuracy for diabetic complications and supports better management strategies.

## Introduction

Type 2 Diabetes Mellitus is a chronic disorder characterized by significant microvascular complications that impair quality of life. Traditional diagnostic tools offer limited insight into pancreatic changes associated with these complications. MRI provides a non-invasive method for structural and functional evaluation, which this study leverages to explore its diagnostic role in microangiopathy.

## Methods

A prospective single-center study recruited 125 T2DM patients. Pancreatic MRI parameters, including morphology, volume, fat fraction, elastography, and ADC values, were assessed using a 3T MRI scanner. Statistical analyses identified correlations between these parameters and diabetic microangiopathy.

## Results

Significant differences in pancreatic MRI parameters were observed between patients with and without microangiopathy. Pancreatic fat fraction and elastography were notably higher in diabetic retinopathy cases ( $p = 0.041, 0.054$ ). Maximum width at the pancreatic body showed potential in predicting microangiopathy ( $p = 0.020$ ). ROC analysis indicated moderate discriminatory power of these parameters.

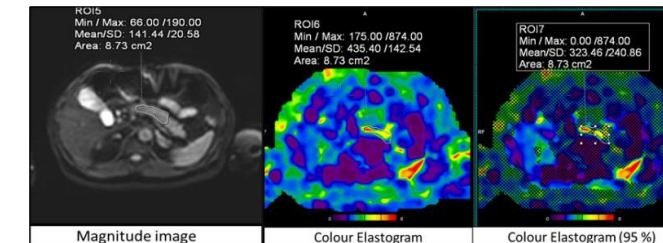


**Fig. 1.** 55 years old male with Type 2 Diabetes Mellitus with microangiopathy (diabetic nephropathy)

MR Elastogram shows pancreatic stiffness drawn within the free hand region of interest as - 3.2kPa.

## Discussion

MRI-based assessments offer a dual advantage of structural and functional evaluation, enabling early detection of complications. Pancreatic fat fraction and elastography emerged as critical predictors for retinopathy, while pancreatic width correlated with overall microangiopathy. These findings underscore the diagnostic value of MRI in T2DM management.

## Conclusion

MRI provides a reliable, non-invasive modality for assessing pancreatic changes in T2DM, aiding in the prediction of microangiopathy. Incorporating MRI findings with clinical markers enhances the ability to identify and manage diabetic complications effectively.

# MR Defecography as a Diagnostic Tool for Pelvic Floor Dysfunction in Chronic Constipation: Correlation with Manometry

**Dr Pratiksha Verma**

Second Year PG Junior Resident, Department of Diagnostic and Interventional Radiology, AIIMS Jodhpur

## Abstract

This study investigates the role of MR Defecography, an MRI-based technique, in diagnosing pelvic floor dysfunction (PFD) in patients with chronic constipation, and its correlation with anal manometry (ARM). A cross-sectional analysis of 41 patients was conducted, where MR defecography, ARM, were performed. The results showed that 65.9% of patients were diagnosed with PFD by ARM. MR defecography correlated with ARM findings, especially in Types 1 and 3 PFD, and detected structural anomalies in patients with normal ARM and balloon expulsion tests. The integration of MR defecography with ARM provides a comprehensive approach, improving diagnostic accuracy by combining functional and structural evaluations. This dual diagnostic methodology supports more targeted clinical decision-making, enhancing the management of chronic constipation.

## Introduction

Chronic constipation is a complex clinical problem, often hiding subtle functional and structural disruptions in pelvic floor dynamics. While traditional methods like anal manometry (ARM) and balloon expulsion tests assess functionality, MR defecography provides a cutting-edge, non-invasive visualization of structural abnormalities.

This study evaluates the findings of Magnetic Resonance (MR) Defecography in patients with chronic constipation and analyzes its correlation with anorectal manometry (ARM) parameters and the balloon expulsion test, aiming to improve diagnostic accuracy for pelvic floor dysfunction (PFD).

## Methods

This cross-sectional, single-center study included 41 patients with chronic constipation who underwent MR defecography. Anorectal Manometry (ARM) and balloon expulsion tests were conducted prior to MR imaging. MR defecography findings were correlated with anal and rectal pressures to classify PFD types based on The London Classification. The study also evaluated structural anomalies in cases with normal ARM results

## Results

Out of 41 patients, 27 (65.9%) were diagnosed with PFD on ARM. Type 1 PFD was observed in 12 patients (44.4%), Type 2 in 3 (11.1%), Type 3 in 11 (40.7%), and Type 4 in 1 patient. MR defecography findings were positive for PFD in

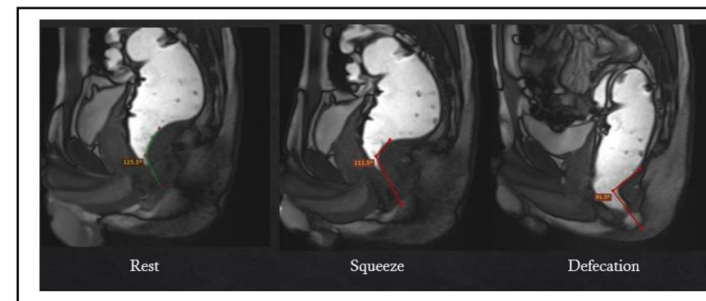


**Fig. 1.** 23y/m having chronic constipation. Anorectal manometry shows normal findings. MR Defecography during different maneuvers shows paradoxical decrease in anorectal angle during straining and defecation with prominent impression of puborectalis muscle.

7, 3, and 8 patients in Types 1, 2, and 3, respectively. Structural anomalies were identified in the remaining cases. Type 1 PFD patients (58.3%) demonstrated a paradoxical decrease in the anorectal angle on MR Defecography, while Type 3 PFD patients (72.7%) exhibited non-opening of the anorectal angle, findings consistent with ARM classification. Among the 14 patients without PFD on ARM, 12 had normal balloon expulsion tests, but MR Defecography revealed structural anomalies. The study showed excellent inter-observer agreement

## Discussion

The integration of MR Defecography and anal manometry provides a comprehensive diagnostic approach, offering novel insights into the interplay between structure and function in PFDs. Unlike standalone techniques, this combined method enhances diagnostic precision, particularly in complex cases such as mixed incontinence or obstructed defecation syndrome. Comparison with existing literature highlights the added value of MR Defecography in clinical decision-making and treatment planning.

## Conclusion

MR Defecography correlates with the London classification of different types of PFD on anal manometry. In addition, it rules out structural anomalies in patients with normal ARM.

# Associating Necrotic Patterns with IDH1(R132H) Mutation in Glioblastomas: A Radiomic Textural Analysis of Preoperative MRI

Ajavindu CN

Vaishnavi Ravi

Phaneendra K Yalavarthy

Department of Computational and Data Sciences, Indian Institute of Science, Bangalore- 560012 India e-mail: [yalavarthy@iisc.ac.in](mailto:yalavarthy@iisc.ac.in)

## Introduction

Glioblastomas are aggressive primary brain tumors with a median survival of 12–15 months despite surgery. IDH1 mutations significantly improve survival to approximately 31 months, highlighting the clinical importance of presurgical identification. Although definitive IDH1 testing relies on operative specimens due to low imaging specificity, radiomics offers a non-invasive alternative by extracting quantitative image features that characterize tissue heterogeneity, morphology, and texture. Various studies in the literature elaborate the link between these imaging features to molecular profiles. In this study, we evaluate the utility of texture features like GLCM and GLDM for IDH1 prediction using a simple linear SVM classifier ensuring performance gains are tied directly to raw texture information without added complexity from advanced methods. It also demonstrates the potential of these features to reflect necrosis patterns influenced by IDH1 mutations.

## Methods

The datasets required for this study are collected from The Cancer Imaging Archive (TCIA). The preliminary training, validation and test are performed on the UPENN-GBM dataset, and external evaluations on the BRATS-TCGA-GBM dataset. In both datasets, there are MRI scans of biopsy-confirmed glioblastomas with genome sequencing of the IDH1 gene, identifying both wild-type cases and R132H mutants whose age and the methylation status are matched. The important steps in the methodology are tumor segmentation, feature extraction, and model building. Tumor segmentation is performed using a BraTS pre-trained volumetric segmentation model from the MONAI framework. For the feature extraction step, we used Pyradiomics library to extract texture-related features - Gray Level Co-occurrence Matrix (GLCM), a 24x1 vector and Gray Level Dependence Matrix (GLDM), a 14x1 vector. For predicting the IDH1 status using these extracted features, a Support Vector Classifier (SVC) with a linear kernel is employed and evaluated using stratified 3-fold cross validation. To address the class imbalance, the Synthetic Minority Oversampling Technique (SMOTE) is applied to the training folds within a pipeline to prevent data leakage. Statistical significance was assessed using the binomial test and Fisher's method.

## Results

Only T1-weighted and FLAIR MR sequences are used for extracting GLCM, GLDM features and for subsequent classification tasks. The SVC is trained on the UPENN-GBM dataset and tested on both UPENN-GBM and BRATS-TCGA-GBM datasets. The classification accuracies on Unmethylated subsets under the influence of SMOTE is shown in the plot below.

## Discussion

This study explores how GLCM and GLDM features reflect mutation-driven necrosis patterns in T1-weighted and FLAIR sequences. Age was identified as a major confounder, prompting age-matched samples. MGMT promoter methylation, another necrosis driver, was addressed by incorporating its heterogeneity in both wild-type and mutant groups to isolate IDH1-related patterns. T1 outperformed FLAIR, capturing hypercellularity and necrotic boundaries more effectively. GLCM excelled in characterizing extensive necrosis through global patterns, while GLDM highlighted localized heterogeneity in subtle necrotic regions. SMOTE enhanced classification in unmethylated groups possibly by acting as a regularizer but showed reduced performance in methylated subgroups due to increased feature variability. Overlapping necrotic patterns in methylated samples complicated classification compared to groups with unmethylated MGMT. External datasets introduced challenges, including limited sample sizes and inconsistent imaging parameters. These findings emphasize the need for larger, standardized datasets to improve generalization and better distinguish IDH1-driven necrosis patterns.

## Conclusion

Our work employed a simple linear SVM classifier to identify the true necrotic reflection of IDH1mutation via GLCM/GLDM features. Radiomics textural analysis can effectively identify mutations that accelerate necrosis. However, when multiple genetic alterations produce

similar necrotic patterns, isolating the specific gene responsible becomes challenging. A simple classifier-linear SVM, was used in this study to highlight the evident textural differences between tumor genotypes, particularly in a necrosis based model like ours. Standardizing imaging parameters remains critical for developing more robust and generalizable studies. Standardized imaging protocols and larger datasets are essential for enhancing model robustness and generalizability.

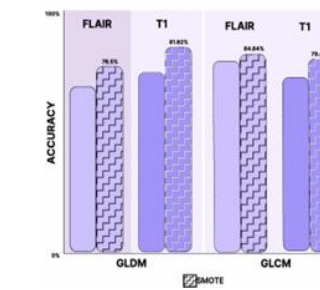


Fig.1 Accuracy bar plot

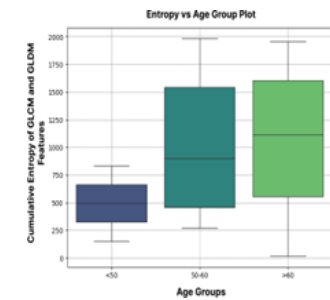


Fig.2 Entropy boxplot

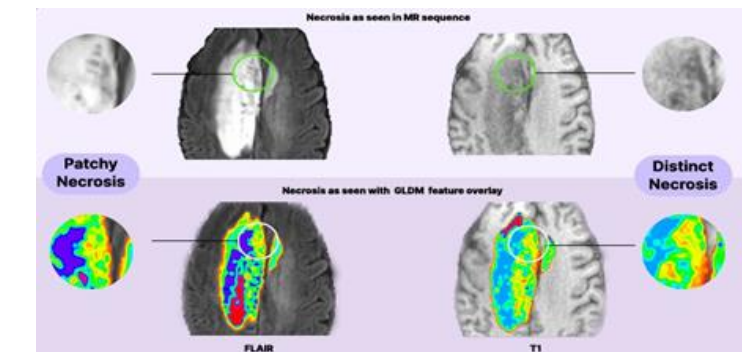


Fig.3 GLCM&GLDM necrosis feature comparisons

# Signal to RF interference Optimal Virtual Channel Estimation for RF Interference Removal

Sreevani Antharjanam.M.V    Harsh Kumar Agarwal    Nitin Jain    Rajagopalan Sundaresan    Ramesh Venkatesan

(GE HealthCare, Bangalore, India)

## Introduction

MR systems detect weak electromagnetic signal emitted by target anatomy when placed in a strong magnetic field[1]. External electromagnetic interference can degrade image quality. Narrowband RF interference manifests as zipper artifacts in MR images. Increased utility of MRI in clinical workflow has led to the democratization of MRI where in-value MRI systems like low-field MRI systems and mobile MRI systems[2] with derated hardware and novel use-case environments have led to the appearance of RF interference in the MRI. The lower signal levels at low-field MRI systems further leads to an increase in vulnerability to noise and artifacts[3,4].

Multi-channel receive in MRI has RF interference correlated across multiple channels and is utilized to remove the artifacts due to RF interference[3-6]. Additional sensors/coils placed away from anatomy are typically utilized to estimate and remove the RF interference from imaging coils in an iterative[4] or machine learning[3] or sparse low-rank[6] framework. However, these techniques rely on additional sensors/coil which may limit the application. Receive channels used for imaging-based RF interference removal[7] have been proposed however it can adversely affect the imaging signal. In this abstract novel formulation of the beamforming technique[7-9] is presented to generate virtual channels by optimizing the signal-to-RF interference ratio to improve artifact removal and overall image quality.

## Methods

**Virtual Channel Estimation:** The k-space signal received at ith channel,  $c_i$  can be modeled as,  $c_i(k) = s_i(k) + n_i(k) + r_i(k)$ , for  $i=1,2,\dots,N_c$ , where  $N_c$  is the number of channels.  $s_i$ ,  $n_i$  and  $r_i$  are signal, noise, and RF interference, respectively at ithchannel. Virtual channels can be used to suppress the RF interference while maintaining the image quality since the spatial variation of the desired signal across the channels is smooth and is captured in channel/coil sensitivity matrix while the spatial variation of the RF interference is dependent on the Fourier spectrum of the RF interference. Imaging signal source is closer to the receiver channels compared to the RF interference source. These different spatial variations can be utilized in beamforming framework to derive a set of virtual channels which can effectively steer the acquired signals and separate the interference from the desired data. The signal to interference in a virtual channel  $i$  with channel combination weights  $w_i$  is given by[6-8],

$$SIR_i = \frac{w_i^H R_S w_i}{w_i^H R_Z w_i}$$

where  $RS=E(SSH)$  is the inter-channel signal correlation and  $RZ=E(RRH)$  is the inter-channel RF-interference correlation matrices. The channel combination weights to generate virtual channels in order of SIR can be generated using generalized eigen decomposition[10].

**Data Acquisition:** Four volunteers were imaged at research 0.5T low-field MRI system using a 14-channel research head-and-neck coil with informed consent in an IRB approved study. The derated hardware permitted the RF interference from the MR equipment room into the magnet room. Thereby, manifesting as zipper artifact in the MR images.

## Results

RF interference is stationary in the above setup. Therefore, virtual channels are estimated using the channel/coil sensitivity matrix (for RS) and noise data (for RZ) acquired prior to the imaging data acquisition as shown in Figure 1. The area around the zipper spectral peak in noise data is used for the estimation of RZ. The usage of coil sensitivity and noise data helps in reducing the computational complexity during image reconstruction. However, if the RF interference changes between the noise data and imaging data or over the imaging data acquisition then this would lead to poor interference suppression.

Figure 2 shows qualitative comparison of the proposed virtual channel-based method to other virtual-channel-based methods. Channel compression[11] and noise whitening[12] based methods are not able to remove the RF interference leaving residual zipper artifacts in the image. Noise-whitening method was additionally modified to consider the RF interference in the noise data similar to the proposed technique removed the zipper artifacts at the expense of image quality. The proposed method is able to simultaneously remove artifact and retain imaging signal.

## Conclusion

Zipper-artifact due to RF interference suppression is presented by projecting the data into a subspace that allows better separation between the zipper artifact and the desired signal. Initial results demonstrate that our approach outperforms other virtual coil techniques by effectively eliminating artifacts while preserving the underlying data. Further assessment at other field strengths and imaging contrast is warranted.

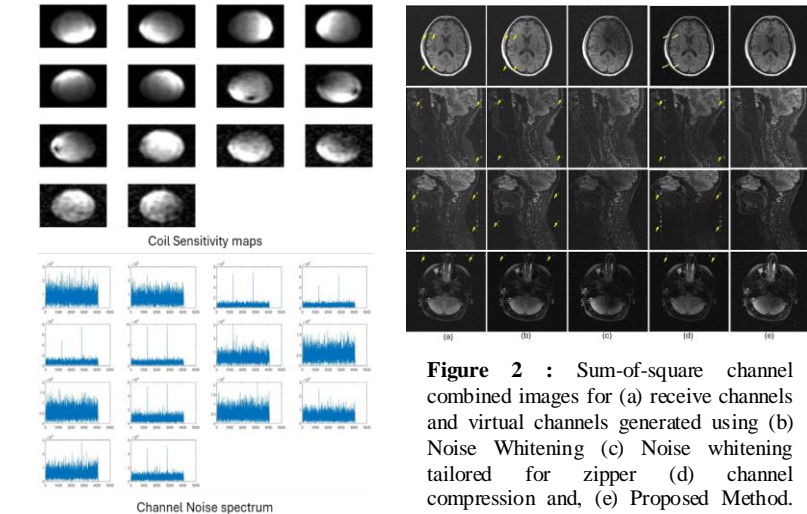


**Figure 1:** Coil sensitivity maps and spectrum of noise over 14 channels of HNU coil. Peaks in the noise spectra corresponds to the RF interference.

## Reference

- [1] Brown et.al., Magnetic resonance imaging: physical principles and sequence design. 2014.
- [2] Prabhat et.al., Methodology for low-field, portable magnetic resonance neuroimaging at the bedside. Frontiers in Neurology. 2021.
- [3] Zhao et.al. , Robust EMF elimination for RF shielding-free MRI through deep learning direct MR signal prediction. MRM. 2024;92(1).
- [4] Srinivas et.al. External dynamic interference estimation and removal (EDITER) for low field MRI. MRM. 2022;87(2).
- [5] Bian, W. A Review of Electromagnetic Elimination Methods for low-field portable MRI scanner. arXiv preprint 2024: arXiv:2406.17804.
- [6] Jin, K. H., Um, J. Y., Lee, D., Lee, J., et. al. MRI artifact correction using sparse+ low-rank decomposition of annihilating filter-based hankel matrix. Magnetic resonance in medicine. 2017;78(1), 327-340.
- [7] Agarwal, HK, et.al RF Interference Removal in Multi-Channel Receive coil, ISMRM 2023; 4260
- [8] Kim et.al Region-optimized virtual (ROVir) coils: Localization on and/or suppression of spatial regions using sensor-domain beamforming. MRM, 2021;86(1).
- [9] Monzingo, R. A., & Miller, T. W. Introduction to adaptive arrays. Scitech publishing 2004.
- [10] Parlett, B. N. The symmetric eigenvalue problem. Society for Industrial and Applied Mathematics 1998.
- [11] Buehrer et.al. Array compression for MRI with large coil arrays. MRM 2007, 57(6).
- [12] Roemer et.al, The NMR phased array. MRM, 1990;16(2).

# Role of in-vivo MR Spectroscopy and serum neuronal biomarkers to assess, characterize and monitor patients with Traumatic Brain Injury

Sujitra S<sup>1</sup>, Susheel K. Joseph<sup>2</sup>, Sarada Subramanian<sup>2</sup>, Dinesh K. Deelchand<sup>3</sup>, Dhaval Shukla<sup>4</sup>, Dwarakanath Srinivas<sup>4</sup>, Sriganesh Kamat<sup>5</sup>, Sandhya Mangalore<sup>1</sup>, Jitender Saini<sup>1</sup>, Anita Mahadevan<sup>6</sup>, Shantala Hegde<sup>7</sup>, and Manoj Kumar<sup>1</sup>

<sup>1</sup>Neuroimaging and Interventional Radiology, <sup>2</sup>Neurochemistry, <sup>4</sup>Neurosurgery, <sup>5</sup>Neuroanaesthesia, <sup>6</sup>Neuropathology, and <sup>7</sup>Clinical Psychology, National Institute of Mental Health and Neurosciences, Bengaluru, India. <sup>3</sup>Radiology, University of Minnesota, Minneapolis, MN, United States.

## Introduction

Traumatic brain injury (TBI) is an acquired disruption usually results from a violent blow or jolt to the head from the external force leading altered brain structural and functional integration. In-vivo <sup>1</sup>H magnetic resonance spectroscopy (MRS) provides a non-invasive method to measure neurochemical changes in brain for early and accurate characterization of any pathology, and also probe to assess therapeutic efficacy of the treatment. This study aims to compare the differences in serum biomarkers and neurometabolites alteration between TBI patients and healthy control using in vivo MRS. We also examine correlations between serum biomarkers [Neurofilament Light (NFL) and Glial Fibrillary Acidic Protein (GFAP)] and MRS derived metabolites between TBI patients and control.

## Methods

TBI patients (n=7) and age/gender matched healthy controls (n=6) with MRS derived neurometabolites and neuronal markers NFL and GFAP quantified from blood serum samples were included in the study. The neuronal marker levels were estimated by Simoa Neurology 2-Plex advantage kit and signal was detected by Simoa HD-X analyzer. The concentration of the target in the serum samples was interpolated from calibration curve. Single-voxel MEGA-PRESS data was acquired from anterior cingulate cortex (ACC) on 3.0T clinical MRI scanner (VIDA, Siemens Healthineers, Germany). Structural anatomical images were acquired using a T1-MPPRAGE to place spectral voxel. MRS data was acquired using a MEGA-PRESS edited pulse involving the collection of two interleaved datasets that differ in their treatment of the GABA spin, and MEGA-editing was achieved with 20-ms Gaussian editing pulses applied at 1.9 ppm and 7.5 ppm in an interleaved fashion<sup>1,2,,</sup>, and following acquisition parameters: were used: TR/TE=2260/68ms, Flip-angle =90°, voxel-size=30x30x30mm, number of averages=128. VAPOR technique<sup>3</sup> for water suppression, interleaved OVS modules to remove unwanted coherences and minimize signal outside the VOI. An unsuppressed water spectrum was acquired as a water reference for eddy current correction and water scaling for absolute neurometabolites quantification. MRSpa<sup>4</sup> and LC-Model<sup>5,6</sup> were used for postprocessing and neurometabolites quantification of MRS data. Spectra was frequency, phase and eddy current corrected. The edited and edit-off spectra was analysed and metabolites were quantified using LC-model using a simulated basis set. GABA and Glutamate from edit-on and metabolites like NAA, MI, Glx, Cr were analysed from edit-off spectra (Fig. 1 b-e).

## Results

Mann-Whitney U test was conducted for NFL and GFAP revealed significant differences between the two groups ( $p$  value=0.003) (Fig 2). Independent sample t-test for metabolite ratios revealed significant differences in NAA/CR+ levels between the two groups ( $p$  =0.007) (Fig 2). Spearman's rho correlations revealed both NFL ( $\rho$ =-0.635,  $p$ =0.020) and GFAP( $\rho$ =-0.599,  $p$  =0.031) showed negative correlation with NAA/CR+ while Nf-L ( $\rho$  = 0.768,  $p$  =0 .002) and GFAP ( $\rho$ =0.768,  $p$ =0.002) showing strong significant association(table 1). Metabolites including GABA, Glutamate, Cr, Glx, MI did not show a statistically significant difference between groups.

## Discussion

GFAP's positive correlation with NFL and negative association with NAA/CR+ reflects astrocytic activation concurrent with neuronal compromise, supporting its role as a glial injury marker<sup>7,8</sup>. NFL's negative association with NAA/CR+ aligns with previous studies linking elevated NFL to axonal damage and neuronal loss in TBI<sup>9,10</sup>. Non-significant findings for other metabolites such as Myoinositol, GABA and Glu could be due to the small sample size, which limits statistical power. To the best of our knowledge, this is the first study to look for relationship between MRS derived metabolites and brain neuronal biomarkers. This study provides unique perspective of exploring potential relationship between neurometabolites and biomarkers in understanding the underlying mechanism of neurochemical alteration at acute stage of evolving brain injury in mTBI.

## Conclusion

Our findings support the utility of NFL and GFAP as accessible, non-invasive tools for monitoring TBI pathology and highlight the potential of combined imaging and biomarker framework could aid in developing treatment strategies and progs

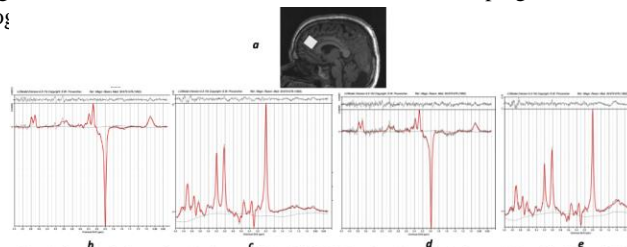


Figure 1: a demonstrates the placement of spectral voxel on a sagittal T1 weighted MPRAGE image. Spectra from anterior cingulate cortex (ACC) overlaid with LC model fit. b and d demonstrates an representative edit-ON from TBI subject and control. c e demonstrates an representative edit-OFF from TBI subject and control.

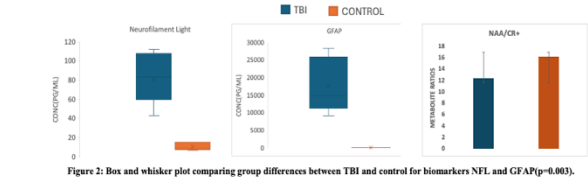


Figure 2: Box and whisker plot comparing group differences between TBI and control for biomarkers NFL and GFAP( $p$ =0.003). Bar graph showing NAA/Cr+ ratios between TBI and healthy control( $p$ =0.007)

	NFL(pg/ml)	Correlation Coefficient	NFL(pg/ml)	GFAP(pg/ml)	NAA/Cr+
Spearman's rho			1.000	.768**	-.635*
				.002	.020
				13	13
				13	13
				.002	.031
				13	13
				13	13
				.020	.031
				13	13

\*\*. Correlation is significant at the 0.01 level (2-tailed).

\*. Correlation is significant at the 0.05 level (2-tailed).

Table1: Spearman's correlations showing NFL( $p$ =0.02) and GFAP( $p$ =0.031) showing negative correlation with NAA/Cr+.

## Reference

- Deelchand, D. K., et al. (2021). NMR in Biomedicine, 34(5), e4199.
- Branzoli, F., et al. (2019). Magn Reson Med, 82, 1259–65.
- Tkác, I., et al. (1999). Magn Reson Med, 41, 649–56.
- MRspa: Magnetic Resonance signal processing and analysis. (<https://www.cmr.umn.edu/downloads/mrspa>).
- Provencher, S. W. (2001). NMR Biomed, 14, 260–4.
- Provencher, S. W. (1993). Magn Reson Med, 30, 672–9.
- Moffett, J. R., et al. (2007). Progress in Neurobiology, 81(2), 89–131.
- Biberthaler, P., et al. (2021). Neurotrauma Reports, 2(1), 617–625.
- Meier, S., et al. (2023). JAMA Neurology, 80(3), 287–297.
- Joyce, J. M., et al. (2022). Journal of Neurotrauma, 39(21–22), 1455–1476.

# Radiomic-Based Investigation of a Potential Link Between Precuneus and Fusiform Gyrus with Alzheimer's Disease

Ishsirjan Kaur Chandok<sup>1</sup>, Simran Sharma<sup>1</sup>, Kavita Kundal<sup>1</sup>, Neeraj Kumar<sup>1, 2\*</sup>, Rahul Kumar<sup>1\*</sup>

<sup>1</sup>Department of Biotechnology, Indian Institute of Technology Hyderabad, Kandi, Telangana 502284, India <sup>2</sup>Department of Liberal Arts, Indian Institute of Technology Hyderabad, Kandi, Telangana 502284, India

## Introduction

Alzheimer's disease (AD) is one of the most prevalent neurodegenerative disorders, with progressive cognitive decline and memory loss as its hallmark features. AD is characterized by extensive brain atrophy, particularly in memory, cognition, and emotional regulation regions. While much attention has been given to hippocampal degeneration, the precuneus and fusiform gyrus are emerging as regions of interest in the study of AD. The precuneus is involved in self-reflective processes, spatial cognition, and episodic memory, while the fusiform gyrus is critical for visual processing, particularly face recognition. Despite their known functions and vulnerability in AD, the specific links between these brain regions and the pathophysiology of Alzheimer's disease remain understudied. This study aims to perform a comprehensive radiomic-based analysis to investigate the connection between AD pathology and the precuneus and fusiform gyrus using MRI-based radiomic features, to enhance early detection and progression prediction in AD.

## Methods

The study utilized T1-weighted MRI scans from the Alzheimer's Disease Neuroimaging Initiative (ADNI) database. A total of 99 Alzheimer's Disease (AD) participants, 149 mild cognitive impairment (MCI) patients, and 134 cognitively normal (CN) participants were included, with scans collected at four distinct time points: baseline (0 months), 6 months, 12 months, and 24 months. Using the MRI data, we extracted 9 radiomic features related to the fusiform and precuneus brain regions, then comparing both right and left hemisphere, totaling of 36 features. Statistical analysis was performed using the Mann-Whitney U test, followed by the Benjamini-Hochberg correction to adjust for multiple comparisons. This approach allowed us to identify significant differences in two imaging features, gray matter volume (GMV) and cortical thickness (CT) between the AD, MCI, and CN groups, specifically in the precuneus and fusiform gyrus. Additionally, machine learning models were applied to classify participants into AD, MCI, and CN groups based on the extracted features, as well as predict the classification between the groups and progression of AD over time.

## Results

In terms of classification performance, the Stacking model that combined Random Forest (RF) and XGBoost, achieved accuracy around 95% for classifying for CN vs AD. Random Forest (RF) model achieved an impressive 96% accuracy in

distinguishing AD vs MCI participants. Other models, including Support Vector Machines (SVM) and logistic regression, were also evaluated, but they performed less effectively compared to the stacking model. For progression prediction, we developed a model to assess the likelihood of cognitive decline from AD patients for a period of 24 months, achieving a 77% accuracy. This model showed potential for early identification of individuals at high risk of progressing to AD, emphasizing the clinical relevance of radiomic features in predicting disease trajectory. The statistical analysis confirmed significant differences in GMV and CT between AD patients and both MCI and CN participants, with the greatest atrophy observed at the 24-month time point, suggesting that the precuneus and fusiform gyrus undergo progressive structural changes in AD.

## Discussion

The results of this study provide strong evidence that radiomic features in the precuneus and fusiform gyrus are significantly associated with Alzheimer's pathology. The analysis demonstrates that structural degeneration in these regions can be detected early and used as biomarkers for both diagnosis and progression prediction. The ensemble-based Stacking model, which combined the strengths of Random Forest and XGBoost, outperformed traditional machine learning models in terms of classification accuracy, underscoring the importance of using robust algorithms for neuroimaging-based diagnostics. Our findings are consistent with previous literature suggesting that precuneus atrophy plays a crucial role in AD pathogenesis, but we also extend the current understanding by highlighting the involvement of the fusiform gyrus in the disease. Furthermore, the 77% accuracy achieved in the progression prediction model suggests that radiomic analysis of brain regions, such as the precuneus and fusiform gyrus, holds potential for early intervention strategies by identifying at-risk individuals.

In comparison with existing studies, our work contributes novel insights into the role of the precuneus and fusiform gyrus in Alzheimer's disease and underscores the utility of radiomic analysis combined with machine learning models for improving the accuracy and reliability of AD diagnosis. In our previous study, we identified the fusiform gyrus and precuneus as potential imaging biomarkers. Building on these findings, we aim to validate these biomarkers with a larger dataset and investigate their role in disease progression [1]. For this purpose, ADNI has been a key resource for studies have investigating degeneration in the context of AD [2], but few have simultaneously considered the role of the fusiform gyrus,

which is often linked to visual and cognitive processing. Our findings align with studies that suggest that fusiform gyrus degeneration is associated with worsening cognitive impairment and visual recognition deficits in AD [3]. Additionally, our use of machine learning methods to analyze radiomic features expands on prior efforts in AI-based neuroimaging research, which have demonstrated high classification accuracy for AD detection [4], we moving forward aim to extend our study to the genomic data and present a more holistic picture of fusiform and precuneus being potential links for Alzheimer's disease [5].

## Conclusion

Our study highlights the importance of the precuneus and fusiform gyrus as key regions in the pathology of Alzheimer's disease. We demonstrate that radiomic-based analysis using MRI-derived features, combined with ensemble machine learning models, can achieve high accuracy for both AD classification and progression prediction. This approach paves the way for early diagnosis and personalized treatment strategies in AD. Future research should focus on incorporating multi-modal imaging data (e.g., PET, diffusion MRI) and exploring deep learning techniques to further enhance the predictive performance and clinical utility of radiomic models. Moreover, longitudinal studies extending beyond the 24-month period are needed to better understand long-term disease progression and refine our predictive models for more accurate and timely clinical applications.

## Reference

- [1] S. Sharma, K. Kundal, I. K. Chandok, N. Kumar, and R. Kumar, "Radiomic-based investigation of a potential link between precuneus and fusiform gyrus with Alzheimer's disease," *medRxiv*, vol. 2024, pp. 2024-05, 2024.
- [2] Alzheimer's Disease Neuroimaging Initiative (ADNI), "ADNI Data Collection and Processing," 2024.
- [3] J. Smith et al., "Structural MRI Findings in Alzheimer's Disease," *IEEE Trans. Med. Imaging*, vol. 42, no. 3, pp. 278-290, 2023.
- [4] R. Brown et al., "AI-Based Neuroimaging for AD Classification," *J. Neurobiol.*, vol. 65, no. 4, pp. 678-689, 2022.
- [5] B. Lee et al., "Genome-wide association study of quantitative biomarkers identifies a novel locus for Alzheimer's disease at 12p12.1," *BMC Genomics*, vol. 23, no. 1, p. 85, 2022.

# Differential Effect of Nicotine on Neural Metabolic Activity in Mice

Prajakta Pramod Biyani<sup>1,2, #</sup>, Ajay Sarawagi<sup>1,2, \$</sup> and Anant Bahadur Patel<sup>1,2, \*</sup>

<sup>1</sup>NMR Microimaging and Spectroscopy, CSIR-Centre for Cellular and Molecular Biology, Habsiguda, Uppal Road, Hyderabad 500007, India; <sup>2</sup>Academy of Scientific and Innovative Research, Ghaziabad 201002, India

## Introduction

Addiction is a neuropsychiatric disorder characterized by continued drug use despite its harmful consequences [1]. Tobacco is the second most psychoactive drug used worldwide, with the major constituent nicotine, being addictive. Acute nicotine increases extracellular dopamine levels in the nucleus accumbens [2], affecting glucose utilization in rat brain [3]. However, the effect of nicotine on glutamatergic, GABAergic, and astrocytic metabolic activity is not very clear. This study evaluated the impact of acute nicotine on the metabolic activity of glutamatergic, GABAergic neurons and astrocytes at various doses in the mice brain.

## Methods

Two-month-old male C57BL/6 mice were divided into two sets. The first set was used to understand the impact of nicotine (0.0125, 0.025, 0.25, 1.0 mg/kg and shams) on neuronal metabolic activity. The second set was used to study the astrocytic metabolic activity with nicotine (0.025 and 2.0 mg/kg). After 15 min of subcutaneous nicotine administration, mice were infused with [1,6-<sup>13</sup>C]glucose/[2-<sup>13</sup>C]acetate using a bolus variable infusion schedule, and at 7/10 min, respectively, the brain metabolism was arrested using focused beam microwave irradiation [4]. The <sup>13</sup>C labeling of brain amino acids was measured in tissue extracts. The cerebral metabolic rates of glucose oxidation (CMRGlc) and astrocytic rate of acetate oxidation (CMRAc(ox)) were determined from the <sup>13</sup>C label trapped into amino acids [5]. The statistical significance of the impact of nicotine on neurometabolic measures was assessed by one way ANOVA.

## Results

There was a significant effect of nicotine on the <sup>13</sup>C labeling of metabolites. A significant effect of nicotine on CMRGlc(Glu) [ $F(4,28)=11.31$ ,  $p_{adj}<0.0001$ ], CMRGlc(GABA) [ $F(4,28)=7.1$ ,  $p_{adj}=0.0004$ ], and CMRGlc(Total) [ $F(4,28)=11.09$ ,  $p_{adj}<0.0001$ ] was found in prefrontal cortex (PFC). Post hoc analysis showed that CMRGlc(Glu) ( $0.662\pm0.055 \mu\text{mol/g/min}$ ) increased significantly ( $p_{adj}=0.0100$ ) with nicotine (0.025 mg/kg) when compared with sham mice ( $0.561\pm0.047 \mu\text{mol/g/min}$ ) in the PFC (Fig. 1), and nicotine (0.0125 mg/kg) increased CMRGlc(Glu) in the bring it to hippocampus. In contrast, nicotine (1.0 mg/kg) decreased CMRGlc(Glu) and CMRGlc(GABA) in PFC, cerebral cortex, and hippocampus. Additionally, nicotine (2.0 mg/kg) significantly ( $p_{adj}<0.0001$ ) reduced CMRAc(Ox) in the PFC, cerebral cortex, and hippocampus

when compared with control mice (Fig. 1).

## Discussion

<sup>13</sup>C Label accumulated into Glu<sub>C4</sub> and GABA<sub>C2</sub> from [1,6-<sup>13</sup>C]<sup>2</sup>glucose [6] provides an excitation and inhibition balance in the brain. The post hoc analysis indicated a significant increase in the ratio Glu<sub>C4</sub>/GABA<sub>C2</sub> for nicotine (0.025 and 1.0 mg/kg), suggesting increased excitability of PFC neurons with nicotine. As neurotransmitter cycling flux is stoichiometrically coupled with neuronal glucose oxidation [7], the findings suggest heightened excitatory activity at a lower dose of nicotine (0.025 mg/kg) and decreased excitatory and inhibitory neurotransmission with a higher dose of nicotine (1.0 mg/kg). However, the reduction in inhibitory synaptic activity with nicotine (1 mg/kg) is more than the excitatory, thus leading to higher excitability of neurons.

## Conclusion

Nicotine perturbs the excitatory and inhibitory balance in PFC through a gain in glutamatergic activity at a lower dose, and a differential suppression in GABAergic and glutamatergic function at the higher dose. The PFC excitability was increased at both lower and higher doses of nicotine, suggesting a role in the reinforcement of nicotine use.

## Acknowledgements

This study was supported by funding from CSIR-CCMB. PPB acknowledges fellowship from CSIR.

## References

- [1] Zou Z, et al (2017) *Advan Exp Med Biol*;
- [2] Pontieri FE, et al (1996) *Nature*;
- [3] London ED, et al (1988) *J Neurosci*.
- [4] Soni ND, et al (2021) *J Cereb Blood Flow Metab*.
- [5] Mishra PK, et al (2018) *J Neurochem*.
- [6] Caldwell and Rothman DL (2021) *Front Neurol*.
- [7] Sibson NR, et al (1998) *Proc Natl Acad Sci USA*.

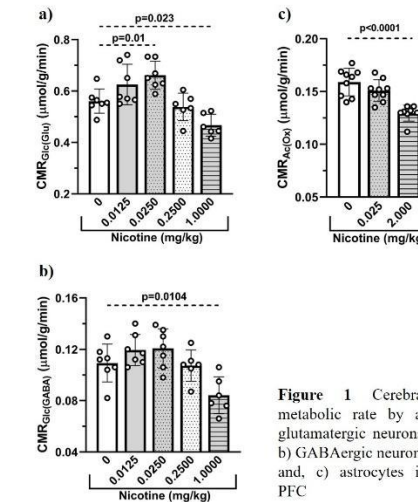


Figure 1 Cerebral metabolic rate by a) glutamatergic neurons, b) GABAergic neurons and, c) astrocytes in PFC

# Understanding Alzheimer's disease progression in 5xFAD Females using $^1\text{H}$ -[ $^{13}\text{C}$ ]-NMR spectroscopy

Akila Ramesh<sup>1,2, #</sup>, Sayeema<sup>2, \$</sup> and Anant Bahadur Patel<sup>1,2, \*</sup>

<sup>1</sup>CSIR-Centre for Cellular and Molecular Biology, Habsiguda, Uppal Road, Hyderabad 500007, India; <sup>2</sup>Academy of Scientific and Innovative Research, Ghaziabad 201002, India

## Introduction

Alzheimer's disease (AD) is a neurodegenerative disorder, and the most common form of dementia in older adults. It is characterized by the presence of amyloid beta (A $\beta$ ) plaques and neurofibrillary tangles with associated symptoms like loss of memory, progressive cognitive impairment, and behavioral changes. Epidemiological studies suggest that two-thirds of American AD subjects are women.<sup>2</sup> However, it is not clear whether the higher prevalence in women is due to longer life expectancy or increased susceptibility to AD. This study evaluates the memory, neurometabolism, and amyloid burden in young and old females using a 5xFAD mouse model of AD.

## Methods

All animal experiments were performed under protocols approved by the Institutional Animal Ethics Committee of CSIR-CCMB. 5xFAD Female mice of 6 and 12 months of age were used for the study. Memory was assessed using Y-Maze and Morris Water Maze (MWM) tests. For metabolic analysis, the mice were anesthetized with urethane (1.5 g/kg, intraperitoneal), and administered intravenously with either [1,6- $^{13}\text{C}_2$ ]glucose for 10 min or [2- $^{13}\text{C}$ ]acetate for 15 min using a bolus rate infusion protocol. Blood was collected from the retro-orbital sinus, and mice were euthanized by a focused beam microwave irradiation (3kW, 1.2s). The neurometabolites were extracted from the cerebral cortex and hippocampus.  $^1\text{H}$ -[ $^{13}\text{C}$ ]-NMR spectroscopy was performed to measure the concentrations of  $^{13}\text{C}$  labeled neurometabolites. The cerebral metabolic rates of glucose (CMRGlc(Ox)) and acetate (CMRAce(Ox)) oxidation were calculated from the  $^{13}\text{C}$  label trapped into amino acids. The A $\beta$ -plaque load in the cerebral cortex and hippocampus was assessed by immunohistochemistry.

## Results

There was no significant difference in the spontaneous alternation in 5xFAD females at 6 and 12 months of age in Y-maze. In MWM, 12-month-old 5xFAD (84.5 $\pm$ 12.2 s, p<0.0001) showed poor learning until the last day of training when compared to age-matched Wild type (WT) (41.1 $\pm$ 25.4 s). The escape latency of 5xFAD mice at 6 months (37.9 $\pm$ 31.7 s) was not different from WT (46.3 $\pm$ 3 s). However, at 12 months, 5xFAD mice (84.0 $\pm$ 13.9 s) took significantly (p<0.0001) longer time than controls (41.4 $\pm$ 28.3 s), indicating memory impairment. The 5xFAD female mice at 6 months exhibited a heavy A $\beta$  plaque load that further increased at 12 months. There was a significant decrease in the NAA levels (5xFAD: 5.6 $\pm$ 0.4  $\mu\text{mol/g}$ ; WT: 6.6 $\pm$ 0.3  $\mu\text{mol/g}$ ,

p=0.041) and increase in myo-inositol level (8.4 $\pm$ 0.8 vs 6.5 $\pm$ 0.6  $\mu\text{mol/g}$ , p<0.0001) at 12 months. The  $^{13}\text{C}$  labeling of GluC4(5xFAD: 1.3 $\pm$ 0.3  $\mu\text{mol/g}$ ; WT: 1.7 $\pm$ 0.6  $\mu\text{mol/g}$ , p=0.005) and GABA C2 (0.14 $\pm$ 0.3 vs. 0.17 $\pm$ 0.2  $\mu\text{mol/g}$ , p=0.025) was also significantly reduced (Fig. 1). There was no significant difference in CMRGlc(Glu) and CMRGlc(GABA) at 6 months in the cerebral cortex and hippocampus in female 5xFAD mice. The cerebral metabolic rate of glucose oxidation in glutamatergic neurons (CMRGlc(Glu)) was decreased in the cerebral cortex (5xFAD: 0.146 $\pm$ 0.035  $\mu\text{mol/g/min}$ ; WT: 0.193 $\pm$ 0.033  $\mu\text{mol/g/min}$ , p=0.011) and hippocampus (0.126 $\pm$ 0.023 vs 0.180 $\pm$ 0.020  $\mu\text{mol/g/min}$ , p=0.0002) of 12-month-old 5xFAD females (Fig. 2). Similarly, in GABAergic neurons, CMRGlc(GABA) was significantly reduced in the cerebral cortex (0.033 $\pm$ 0.008 vs 0.041 $\pm$ 0.008  $\mu\text{mol/g/min}$ , p=0.048) and hippocampus (0.035 $\pm$ 0.006 vs 0.049 $\pm$ 0.007  $\mu\text{mol/g/min}$ , p=0.0007). CMRAce(Ox) was not significantly different in the cerebral cortex (0.136 $\pm$ 0.017 vs 0.129 $\pm$ 0.009  $\mu\text{mol/g/min}$ , p=0.376) and hippocampus (0.143 $\pm$ 0.011 vs 0.140 $\pm$ 0.008  $\mu\text{mol/g/min}$ , p=0.562).

## Discussion

The cognitive function of 5xFAD female mice was intact till 6 months of age but was impaired at 12 months. The neurometabolite homeostasis was unperturbed at 6 months of age. At 12 months, 5xFAD mice showed reduced NAA levels, suggesting decreased neuronal viability and increased myo-inositol points towards increased glial activity or population. However, unperturbed CMRAce(Ox) suggests no change in the astrogliosis activity in 12-month 5xFAD females. Despite having amyloid plaques, there was no change in memory and cerebral glucose metabolism, suggesting intact synaptic activity in 6-month-old 5xFAD female mice.

## Conclusion

At younger ages, female 5xFAD mice do not exhibit any AD phenotype. However, there was deterioration in cognition and neurometabolism in age-matched 5xFAD males (data not shown). At older ages, females exhibited impairment in memory and neurometabolism, which was very similar to that seen in males. The presentation of AD only at older ages in females suggests a protective mechanism in play at younger age.

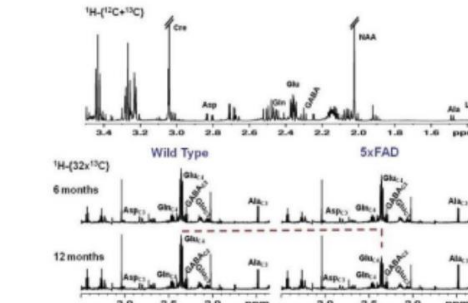
## Acknowledgements

This study was supported by the Council of Scientific and Industrial Research (CSIR-CCMB: NCP/MLP0139).

## References

- [1] WHO (2017) Global action plan on the public health response to dementia 2017–2025.
- [2] Alzheimer's Association (2017) Alzheimers Dement 13:325–373.
- [3] Holcomb et al (1998) Nat Med 4:97–100.
- [4] Morris R (1981) Learning and Motivation 12:239–260.
- [5] Tiwari et al (2013) J Cereb Blood Flow Metab, 33:1523–1531.
- [6] De Graaf et al (2003) Magn Reson Medicine, 49:37–46.

Fig. 1  $^1\text{H}$ -[ $^{13}\text{C}$ ]-NMR spectra of cortical tissue extracts of 6 and 12-month-old 5xFAD females infused with [1,6- $^{13}\text{C}_2$ ]glucose.



The spectrum at the top represents the total level of metabolites ( $^1\text{H}$ -[ $^{13}\text{C}$ ]). Spectra at the lower panels show  $^{13}\text{C}$  labeling of amino acids from [1, 6- $^{13}\text{C}_2$ ]glucose.

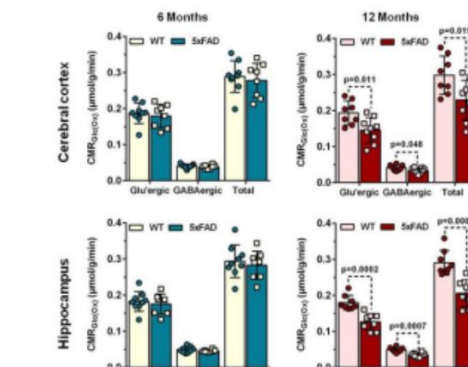


Fig. 2 Cerebral metabolic rates of glucose oxidation CMRGlc(Ox) of 6 and 12-month-old female WT and 5xFAD mice in the cerebral cortex and hippocampus.

# Prognosticating Epilepsy by Artificial Intelligence Based Brain Volumetric Analysis

Prof. (Dr.) Rajul Rastogi

Department of Radiodiagnosis, Teerthanker Mahaveer Medical College and Research Center, Moradabad, Uttar Pradesh

## Introduction

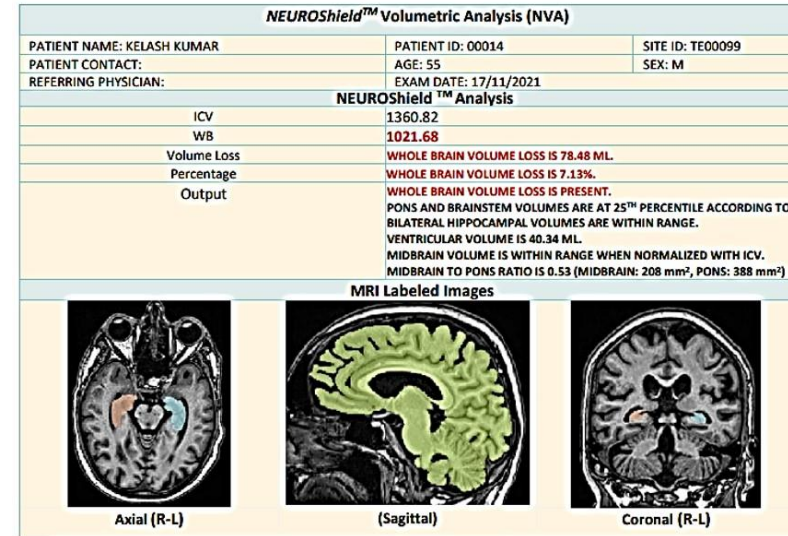
Epilepsy is a neurological disorder associated with high morbidity and psychosocial impact. Evidence exists in Medical Literature suggesting neuronal loss or neurodegenerative phenomenon in patients with Epilepsy. However, this may be visually apparent late in the disease when other manifestations may occur. Hence, we planned a pilot study where we utilised Artificial Intelligence (AI) based volumetric assessment of brain patients suffering with epilepsy to establish its relationship with brain atrophy, hence predicting prognosis.

## Methods

One hundred patients with epilepsy and 100 age & sex matched subjects underwent MRI brain with subsequent brain volumetric analysis using AI based tool. Patients with seizures due to organic causes were excluded from the study.

## Results

The age range of patients was 30-50years with equal number of males & females. At least 55 out of 100 patients revealed some degree of reduced brain volume compared to controls.



- Whole Brain volume (WBV) in *controls* was as follows:
  - Males: 1200-1300mL
  - Females: 1100-1200mL
- Whole Brain volume (WBV) in *cases* was as follows:
  - Males: 1150-1225mL
  - Females: 1000-1075mL

## Conclusion

Epilepsy is associated with brain atrophy and neurodegenerative process, hence serial artificial intelligence based volumetric brain analysis should be part of the routine imaging protocol for Epilepsy by MRI Brain for its early detection and instituting aggressive management & psycho-counselling. As brain atrophy is a long-term complication of epilepsy which often escapes visual detection in early stage, AI based volumetric brain analysis may not only aid in better management but may also be used to evaluate the effect of drugs retarding or halting the progression of brain atrophy objectively.

# Regional Comparison of DCE-MRI based Pharmacokinetic Model Fitting Accuracy in Glioblastoma

Subhanon Bera<sup>1,2</sup>, Sourav Basak<sup>1</sup>, Sankar Narayan Misra<sup>1,2</sup>, Gabriela W Kostrzanowska<sup>3</sup>, Archith Rajan<sup>4</sup>, Sanjeev Chawla<sup>4</sup>, Harish Poptani<sup>3</sup>, Sourav Bhaduri<sup>1,2</sup>

<sup>1</sup>Institute for Advancing Intelligence, TCG Centres for Research and Education in Science and Technology, Kolkata, India, <sup>2</sup>Academy of Scientific and Innovative Research (AcSIR), Ghaziabad, India, <sup>3</sup>Centre for Preclinical Imaging, University of Liverpool, Liverpool, UK, <sup>4</sup>Department of Radiology, Perelman School of Medicine, University of Pennsylvania, Philadelphia, USA.

## Introduction

Glioblastoma (GBM) is a highly aggressive brain tumor with limited survival rates despite extensive treatment [1]. Pharmacokinetic (PK) modeling of dynamic contrast-enhanced MRI (DCE-MRI) provides information about tumor vascularity and perfusion [2],[3],[4]. However, selecting an optimal PK model remains challenging due to variations in complexity and fit across tumor regions. This study aims to apply a parsimonious model selection approach using the Akaike Information Criterion (AIC)[5],[6] on five PK models to identify the model that best balances fit and simplicity. After segmenting tumor regions using the automated nnUNet algorithm [7],[8], the models were evaluated across these regions to optimize parameter estimation in DCE-MRI.

## Methods

This retrospective study included MRI datasets from 56 GBM patients acquired using a 3T Tim Trio MR scanner at the University of Pennsylvania and shared with TCG CREST (data sharing ID: RIST76150). All data usage and analyses were conducted in accordance with ethical guidelines and with approval from the relevant institutional review boards at both institutions. Tumors were segmented into enhancing, non-enhancing, and edema regions using the automated nnU-Net algorithm [7],[8]. DCE-MRI data from each segmented region were fitted to five pharmacokinetic (PK) models: Non-linear Tofts, Extended Tofts, Shutter-Speed, Two Compartment Exchange (2CXM), and Three-Site Two-Exchange (3S2X). Each model estimated parameters, including the volume transfer constant (Ktrans), extracellular volume fraction (Ve), and reverse reflux rate constant (Kep) [9],[10],[11],[12]. Additional parameters were generated depending on the model: plasma volume fraction (Vp) from the Extended Tofts, 2CXM, and 3S2X models; water molecule half-life inside cells (ti) from the Shutter-Speed and 3S2X models.

Following PK model fitting at each voxel, an R<sup>2</sup> map was generated (Fig. 1), and the Akaike Information Criterion (AIC) & R-squared(R<sup>2</sup>) values were calculated [6][13]. The model with the lowest AIC was selected for each voxel, indicating the best fit. A parsimonious model was formed by aggregating the selected best-fit models across the dataset. Finally, mean AIC and R<sup>2</sup> values were calculated for each model and the parsimonious model within each region (enhancing, non-enhancing, and edema) for each patient.

### Akaike Information Criterion (AIC):

$$AIC = N \cdot \ln \left( \sum_{i=1}^N (y_i - C_t(i))^2 \right) + \frac{2 \cdot p \cdot (p+1)}{N-p-1}$$

where: N - number of observations, y<sub>i</sub> - observation at time i, C<sub>t</sub>(i) - associated fitted value at time i, and p - number of parameters in the model

## Results

Parsimonious Model Selection from PK Models with Parameters Ktrans, Ve, and Kep: All

PK models containing Ktrans, Ve, and Kep are compared within the enhancing region of the tumor (Fig.1). The Parsimonious Model provided a superior performance to individual models in the enhancing region. Among the five models, the Extended Tofts and 2CXM models showed the lowest mean AIC and highest mean R-squared value (Fig. 2a and b). A similar trend was observed in the non-enhancing (Fig. 3a and b) and edema regions as well.

### Parsimonious Model Selection from PK Models with Parameters Vp:

Only the Extended Tofts, 2CXM, and 3S2X models, which include the parameter Vp, were compared in the enhancing region (Fig. 2c and d). The Parsimonious Model surpassed the performance of individual models in the enhancing region. Among the three models, the Extended Tofts and 2CXM had the lowest mean AIC and highest mean R-squared value (Fig. 2c and d). This trend was similarly noted in the non-enhancing (Fig.3c and d) and edema regions .

Parsimonious Model Selection from PK Models with Parameters ti: Only the Shutter-Speed and 3S2X models, including the ti parameter, were compared in the enhancing region (Fig. 2e and f). The Parsimonious Model surpassed the performance of individual models. Shutter-Speed had the lowest mean AIC and highest mean R-squared value among the two models (Fig. 2e and f). This trend was also observed in the non-enhancing (Fig. 3e and f) and edema regions .

The results indicate that AIC-based parsimonious model selection can effectively optimize PK model performance across distinct tumor regions. The Parsimonious Model consistently achieved superior performance, showing optimal results not only in the enhancing region but also excelling in the non-enhancing and edema regions.

## Discussion

GFAP's positive correlation with NFL and negative association with NAA/CR+ reflects astrocytic activation concurrent with neuronal compromise, supporting its role as a glial injury marker [7,8]. NFL's negative association with NAA/CR+ aligns with previous studies linking elevated NFL to axonal damage and neuronal loss in TBI[9,10]. Non-significant findings for other metabolites such as Myoinositol, GABA and Glu could be due to the small sample size, which limits statistical power. To the best of our knowledge, this is the first study to look for relationship between MRS derived metabolites and brain neuronal biomarkers. This study provides unique perspective of exploring potential relationship between neurometabolites and biomarkers in understanding the underlying mechanism of neurochemical alteration at acute stage of evolving brain injury in mTBI.

## Conclusion

Our findings support the utility of NFL and GFAP as accessible, non-invasive tools for monitoring TBI pathology and highlight the potential of combined imaging and biomarker

framework could aid in developing treatment strategies and prognosticate clinical outcomes.

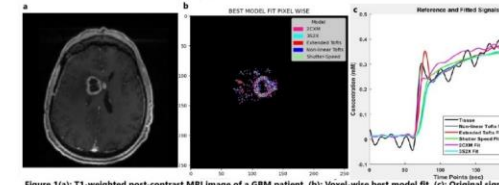


Figure 1(a): T1-weighted post-contrast MRI image of a GBM patient. (b): Voxel-wise best model fit. (c): Original signal with five fitted PK curves in a specific voxel, displaying R<sup>2</sup> for each model.

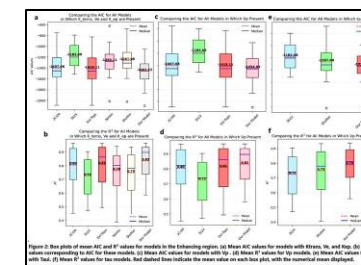


Figure 2: Box plots of mean AIC and R<sup>2</sup> values for models in the Enhancing region. (a) Mean AIC values for models with Ktrans, Ve, and Kep. (b) Mean R<sup>2</sup> values for the same models. (c) Comparing the AIC for All Models in Which Vp is Present. (d) Comparing the R<sup>2</sup> for All Models in Which Vp is Present. (e) Comparing the AIC for All Models in Which Ve and Kep are Present. (f) Comparing the R<sup>2</sup> for All Models in Which Ve and Kep are Present.

Reference

- [1] Stupp, R., Mason, W. P., van den Bent, M. J., et al. (2005). "Radiotherapy plus concomitant and adjuvant temozolomide for glioblastoma." *New England Journal of Medicine*, 352(10), 987-996.
- [2] Tofts, P. S., & Kermode, A. G. (1991). "Measurement of the blood-brain barrier permeability and leakage space using dynamic MR imaging. I. Fundamental concepts." *Magnetic Resonance in Medicine*, 17(2), 357- 367.
- [3] Bauer, S., Wiest, R., Nolte, L. P., & Reyes, M. (2013). "A survey of MRI-based medical image analysis for brain tumor studies." *Physics in Medicine & Biology*, 58(13), R97-R129.
- [4] Li, X., & Vaidya, V. (2011). "Quantification of tumor microcirculation using DCE-MRI: A review of the principles, techniques, and clinical applications." *Journal of Clinical Imaging Science*, 1(1), 32.
- [5] Burnham, K. P., & Anderson, D. R. (2004). *Model Selection and Multimodel Inference: A Practical Information-Theoretic Approach* (2nd ed.).
- [6] Fusco, R., Sansone, M., Maffei, S., Raiano, N. and Petrillo, A., 2012. Dynamic contrast-enhanced MRI in breast cancer: A comparison between distributed and compartmental tracer kinetic models. *Journal of Biomedical Graphics and Computing*, 2(2), p.28.
- [7] Isensee, F., Jaeger, P. F., Full, P. M., Vollmuth, P., & Maier-Hein, K. H. (2021). "nnU-Net: a self-configuring method for deep learning-based biomedical image segmentation." *Nature Methods*, 18(2), 203-211.
- [8] Isensee, F., Kickingenberger, P., Wick, B., Bendszus, M., & Maier-Hein, K. H. (2019). "No New-Net." *Proceedings of the International MICCAI Brainlesion Workshop*, 234–244.
- [9] Tofts, P. S., Kermode, A. G. (1991). "Measurement of the blood-brain barrier permeability and leakage space using dynamic MR imaging. I. Fundamental concepts." *Magnetic Resonance in Medicine*, 17(2), 357- 367.
- [10] Tofts, P. S. (1997). "Modeling tracer kinetics in dynamic Gd-DTPA MR imaging." *Journal of Magnetic Resonance Imaging*, 7(1), 91-101.
- [11] Yankelev, T. E., Rooney, W. D., Li, X., & Springer, C. S. (2003). "Dynamic contrast enhanced MRI in oncology: Theory, data acquisition, analysis, and examples." *Current Medical Imaging Reviews*, 3(2), 91-107.
- [12] Brix, G., et al. (1997). "Pharmacokinetic modeling of tissue microcirculation using T1-weighted dynamic contrast-enhanced MRI." *Magnetic Resonance in Medicine*, 52(3), 420-429.
- [13] Motulsky, H. J., & Ransnas, L. A. (1987). "Fitting curves to data using nonlinear regression: A practical and nonmathematical review." *FASEB Journal*, 1(5), 365-374.

# Probabilistic Modeling for Quantitative Susceptibility Mapping: A VAE U-Net Approach

Aaqilah A J<sup>1</sup>, Sunil Kumar<sup>2</sup>, C Kesavadas<sup>2</sup>, Raji Susan Mathew<sup>1</sup>

<sup>1</sup>School of Data Science, Indian Institute of Science Education and Research, Thiruvananthapuram, India.

<sup>2</sup> Department of Imaging Sciences and Interventional Radiology, Sree Chitra Tirunal Institute for Medical Sciences and Technology, Thiruvananthapuram, India.

## Introduction

Quantitative susceptibility mapping (QSM) is an MRI-based technique for quantifying magnetic susceptibility in tissues, offering precise measurement of spatial variations in susceptibility. This capability enables a wide range of applications, including tissue differentiation based on magnetic properties such as iron and calcium content. Traditional QSM reconstruction methods, including thresholded k-space division<sup>1</sup>, and calculation of susceptibility through multiple orientation sampling (COSMOS)<sup>2</sup>, are computationally intensive and often limited by the ill-posed nature of the dipole inversion problem. Recent advancements in deep learning have introduced opportunities to overcome these limitations. Data-driven models like DeepQSM<sup>3</sup> and QSMNet<sup>4</sup> have demonstrated improved reconstruction accuracy and robustness.

## Methods

This study presents a Variational Autoencoder (VAE) U-Net architecture for robust QSM reconstruction that utilizes a probabilistic framework enabling superior generalization to unseen datasets, outperforming state-of-the-art models even in limited data settings. By incorporating UNet-like skip connections across the encoders and decoders of VAE, the model better captures features at multiple scales and retains the fine anatomical details that could otherwise have been lost. The model was trained using input local fields paired with COSMOS ground truth, with a physics-informed loss function combining reconstruction loss quantified using mean squared error (MSE), KL divergence, and dipole loss. Reconstruction Loss :  $\text{Loss}_{\text{recon}} = \text{MSE}(\chi_{\text{recon}}, \chi)$

$$\text{KL Divergence Loss : } \text{Loss}_{\text{kl}} = \frac{1}{2} \sum (1 + \log \sigma^2 - \mu^2 - \sigma^2)$$

$$\text{Dipole Loss : } \text{Loss}_{\text{dipole}} = \|F^{-1}D\chi_{\text{recon}} - \delta\|_2$$

$$\text{Total Loss : } \text{Loss}_{\text{total}} = \|\lambda\|_{\text{recon}} \|\text{Loss}\|_{\text{recon}} + \lambda_{\text{kl}} \|\text{Loss}\|_{\text{kl}} + \lambda_{\text{dipole}} \|\text{Loss}\|_{\text{dipole}}$$

where  $\chi$  denotes susceptibility,  $\sigma$  and  $\mu$  represents variance and mean respectively,  $F$  is the Fourier transform operator,  $D$  is the dipole kernel and  $\delta$  is the local field, and  $\lambda$  denotes the weight of each loss term. The training was performed in both sufficient as well as limited data settings using the dataset shared by Yoon et al.<sup>4</sup>. The trained model was validated on the same dataset as well as on another benchmark dataset<sup>5</sup>. The model was assessed using structural similarity index measure (SSIM), peak signal to noise ratio (PSNR), normalized mean squared error (NMSE), and high frequency error norm (HFEN)<sup>6</sup> to quantify structural fidelity, noise reduction, and preservation of high-frequency details.

## Results

Comparative studies of the proposed VAE-UNet were performed with state-of-the-art models like QSMNet, xQSM<sup>7</sup>, and 3D-UNet as in DeepQSM and the corresponding performance metrics were summarized in Table 1 and 2. A visual comparison of the

proposed VAE-UNet with COSMOS is shown in Figure 1. Our experimental studies demonstrate that the VAE-UNet model efficiently balances accuracy and generalizability in QSM reconstruction.

**Table 1:** Quantitative metrics (mean  $\pm$  std) of the reconstructed susceptibility maps from the model trained with maximum data and evaluated on unseen data

Model	SSIM [↑]	PSNR(dB) [↑]	NMSE(%) [↓]	HFEN(%) [↓]
QSMNet	0.928 $\pm$ 0.01	32.98 $\pm$ 1.72	61.78 $\pm$ 3.32	56.43 $\pm$ 4.49
xQSM	0.928 $\pm$ 0.01	33.10 $\pm$ 1.83	61.68 $\pm$ 3.34	57.54 $\pm$ 4.50
3D-UNet	0.928 $\pm$ 0.01	33.07 $\pm$ 1.75	61.64 $\pm$ 3.28	57.27 $\pm$ 4.49
VAE-U-Net	0.931 $\pm$ 0.01	33.01 $\pm$ 1.69	60.04 $\pm$ 3.41	55.48 $\pm$ 4.38

**Table 2:** Quantitative metrics (mean  $\pm$  std) of the reconstructed susceptibility maps from the model trained with limited data and evaluated on unseen data

Model	SSIM [↑]	PSNR(dB) [↑]	NMSE (%) [↓]	HFEN(%) [↓]
QSMNet	0.920 $\pm$ 0.01	33.07 $\pm$ 1.77	65.27 $\pm$ 3.14	60.93 $\pm$ 4.28
xQSM	0.919 $\pm$ 0.01	32.98 $\pm$ 1.69	65.52 $\pm$ 3.10	61.37 $\pm$ 4.10
3D-UNet	0.920 $\pm$ 0.01	33.01 $\pm$ 1.72	65.43 $\pm$ 2.86	61.76 $\pm$ 3.87
VAE-U-Net	0.926 $\pm$ 0.01	33.12 $\pm$ 1.86	63.46 $\pm$ 3.05	58.46 $\pm$ 3.99

## Discussion

Unlike deterministic models like QSMNet or xQSM, our VAE-UNet incorporates a probabilistic framework via the latent space. Probabilistic modeling approaches, such as variational inference, are largely unexplored in QSM reconstruction. This study underscores their capability to capture uncertainty and complex latent representations, paving the way for further development. Our model exhibits superior generalizability which is critical for deployment in diverse clinical and research contexts where acquisition protocols vary.

## Conclusion

Our study shows that probabilistic modeling using VAE-UNet is a promising direction for

QSM reconstruction. The model achieves accurate, robust, and generalizable reconstructions by effectively leveraging the probabilistic framework and incorporating physics-based constraints. Accurate susceptibility mapping can improve the diagnosis and monitoring of neurodegenerative diseases (e.g., multiple sclerosis, Parkinson's, and Alzheimer's) and conditions like stroke. The model's robustness under sparse data conditions makes it particularly suitable for real-world clinical applications where high-quality data are often scarce. Generalizability across datasets highlights its potential for use in multi-center studies, reducing variability across imaging protocols.

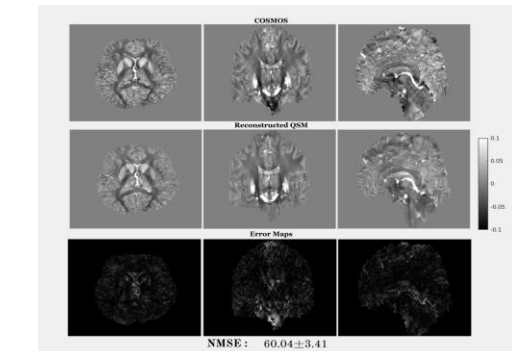


**Figure 1:** A comparison between COSMOS maps, reconstructed QSM (axial view) and difference images (with respect to COSMOS) of the sample test volume on unseen data when trained with maximum data. The NMSE (%) of the test volumes with respect to COSMOS are given.

## Reference

- [1] K. Shmueli et al. "Magnetic susceptibility mapping of brain tissue in vivo using MRI phase data". MRM 62.6 (2009), pp. 1510–1522
- [2] Tian Liu et al. "Calculation of susceptibility through multiple orientation sampling (COSMOS): a method for conditioning the inverse problem from measured magnetic field map to susceptibility source image in MRI". MRM 61.1 (2009), pp. 196–204.
- [3] S. Bollmann et al., "Deep QSM - using deep learning to solve the dipole inversion for quantitative susceptibility mapping," NeuroImage, vol. 195, pp. 373–383, Mar. 2019.
- [4] J. Yoon et al., "Quantitative Susceptibility Mapping using Deep Neural Network: QSMNet," arXiv.org, 2018.
- [5] K.-W. Lai, M. Aggarwal, van Zijl, X. Li, and J. Sulam, "Learned Proximal Networks for Quantitative Susceptibility Mapping," arXiv.org, 2020. <https://arxiv.org/abs/2008.05024>.
- [6] C. Milovic et al., "The 2016 QSM Challenge: Lessons learned and considerations for a future challenge design," MRM, vol. 84, no. 3, pp. 1624–1637, Feb. 2020.
- [7] Y. Gao et al., "xQSM: quantitative susceptibility mapping with octave convolutional and noise-regularized neural networks," NMR in Biomedicine, vol. 34, no. 3, Dec. 2020.

# Performance Comparison of 3T MRI Surface Coils Using Flexible Stranded Wire and Single Copper Wire

Niraj Yadav<sup>1,2</sup>, Lena Nohava<sup>1,2</sup>, Elmar Laistler<sup>1,2</sup>

<sup>1</sup> High Field MR Center, Center for Medical Physics and Biomedical Engineering, Medical University of Vienna, Vienna, Austria

<sup>2</sup> Christian Doppler Laboratory for Patient-Centered Breast Imaging, Medical University of Vienna, Vienna, Austria

## Introduction

Flexible RF coils are at the forefront of MRI research, offering enhanced patient comfort and adaptability to various anatomical regions [1]. Recent studies have explored innovative designs to improve coil flexibility [2,3]. This study examines a flexible 9 cm MRI surface coil loop constructed with stranded wires, comparing its performance to a conventional rigid single wire coil of identical dimensions. The aim of this work is to explore the potential of stranded wire designs in advancing flexible MRI coil technology.

## Methods

Two 9 cm diameter receive coils (Figure 1) were fabricated to compare SNR, impedance matching, active detuning, and Q-factors [4,5,6]. Both coils were optimized for operation at a Larmor frequency of 123.2 MHz (3T Siemens Healthineers scanners, Erlangen, Germany). The rigid coil was constructed using copper wire ( $d = 1 \text{ mm}$ ) with enameled coating, while the flexible coil utilized silver coated copper stranded wires with PTFE insulation (22 AWG RS Pro 841-7392). For the bench and MR tests a saline container phantom filled with 5 g/L NaCl and doped with Gadolinium-based contrast agent as shown in Figure 2 was employed. Unloaded and loaded Q values were measured at the Larmor frequency using a double-loop probe, with the coils connected to their interfacing networks (see Fig. 1) and  $50 \Omega$  terminated. The interfacing circuits included fuses, active and passive decoupling circuits as shown in the schematic in Figure 3. Coaxial cables connecting the coils to the scanner were equipped with floating cable traps [7]. MR imaging tests consisted of a GRE pulse sequence with parameters set to a TE of 10 ms, TR of 300 ms, slice thickness of 3 mm, resolution of  $1 \times 1 \text{ mm}^2$ , matrix size of  $256 \times 256$ , and a bandwidth of 33.28 kHz. To evaluate B1+ distortion, a Saturated Turbo Flash B1 mapping sequence was utilized.

## Results

The unloaded Q of the flexible coil and the standard coil were 36 and 31, respectively. Similarly, the loaded Q was 17 for both the flexible coil and the standard coil, resulting in Q ratios of 2.1 and 1.8, respectively. The measured return losses were -18 dB for the flexible coil and -22 dB for the standard coil. Similarly, the active decoupling isolation were -17 dB for the flexible coil and -21 dB for the standard coil. As presented in Figure 4, the measured SNR values in a 2D circular ROI were 560 and 552 for the flexible and the standard coil, respectively. B1+ distortion shown in Figure 5 was measured using the scanner's body coil with and without the receive coil present on the phantom. Results show 3% B1+ difference for the flexible coil and 9% for the standard coil, indicating good decoupling from the body coil in both cases.

## Discussion

The findings indicate that the flexible coil made from stranded wire performs similarly to the standard rigid copper wire coil and can therefore be used for applications where flexibility of the coil conductor is beneficial, in particular, where strong intersubject variability of the targeted anatomy is expected. Future work will focus on optimizing interfacing elements to minimize losses and miniaturize the interfacing electronics, with subsequent *in vivo* testing planned to validate the performance improvements.

## Conclusion

This study highlights that 9 cm flexible stranded wire receive coils offer no performance disadvantages compared to standard copper conductor coils at 3T. These findings suggest that stranded wire coils are a promising option for flexible MRI surface coils.

## Reference

- Darnell D, Truong TK, Song AW. Recent Advances in Radio-Frequency Coil Technologies: Flexible, Wireless, and Integrated Coil Arrays. *J Magn Reson Imaging*. 2022.
- Nohava L, et al. Flexible Multi-Turn Multi-Gap Coaxial RF Coils: Design Concept and Implementation for Magnetic Resonance Imaging at 3 and 7 Tesla. *IEEE Trans Med Imaging*. 2021.
- Obermann Michael MSc; Nohava Lena PhD; et al. Panoramic Magnetic Resonance Imaging of the Breast With a Wearable Coil Vest. *Investigative Radiology* 58(11); p 799-810, 2023.
- Kumar, A., Edelstein, W. A. & Bottomley, P. A. Noise figure limits for circular loop MR coils. *Magn. Reson. Med.* 61, 1201–1209, 2009.
- Mispelter J, Lupu M, Briguet A, et al., NMR Probeheads for Biophysical And Biomedical Experiments. Imperial College Press, 2006.
- Roemer, P. B., Edelstein, W. A., Hayes, C. E., Souza, S. P. & Mueller, O. M. The NMR Phased Array. *Magn. Reson. Med.* 16, 192–225, 1990.
- Seeger, D.A., Jevtic, J. and Menon, A., Floating shield current suppression trap. *Concepts Magn. Reson.*, 21B: 26-31, 2004.

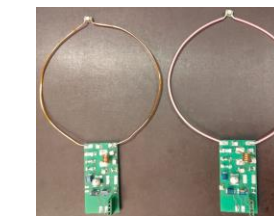


**Fig. 1:** Standard rigid copper wire coil (left) and flexible stranded wire coil (right) and their interfacing networks.



**Fig. 2:** Measurement setup using the flexible coil on the container phantom with a size of  $18.5 \times 14.5 \times 25.2 \text{ cm}^3$ .

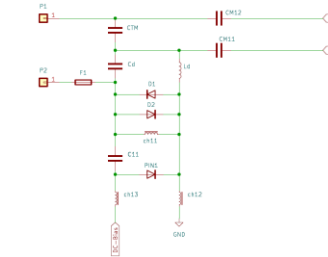


**Fig. 3:** Schematic of the interface board consisting of the coil ports (P1 and P2), a fuse (F1), tuning and matching capacitors (CTM, CM1, CM2), detuning elements (Cd and Ld), crossed diodes (D1, D2), a PIN diode (PIN1), RF chokes (ch11, ch12, ch13), and a DC block capacitor (C11).

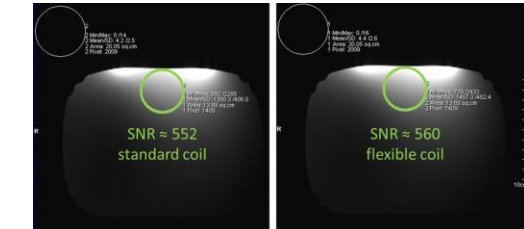


**Fig. 4:** SNR comparison on a container phantom. The axial slice and the coils are positioned at the phantom's center.

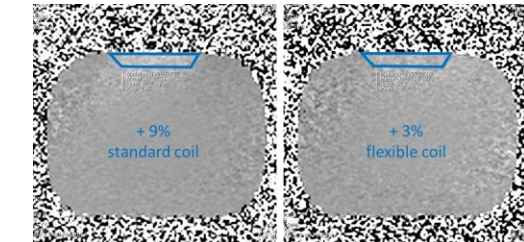


**Fig. 5:** B1+ change with and without the receive respective coil placed on the container phantom. The slice and the coils are positioned at the phantom's center. The pixel intensity ranges from 0 (white) to 4095 (black), a value of 2048 corresponds to 0% change.

# Performance Evaluation of Indigenous MRI System: Insights from ACR Phantom Validation

**Laxmi Salagare, Mahadev Dipnaik, Tejashree Jadhav, Sanket Gothankar, Rahul Roy Chowdhury, Dharmesh Verma, Tapas Bhuiya, Rajesh Harsh**

Scientist, Medical System Divison, SAMEER, Mumbai, India

## Introduction

Alzheimer's disease (AD) is a progressive neurodegenerative disorder characterized by cognitive decline and memory impairment, affecting millions worldwide. Early detection is crucial for implementing effective interventions that can slow disease progression. Recent advancements in neuroimaging, particularly multi-parametric magnetic resonance imaging (MRI), have provided detailed insights into brain structure and function, offering potential biomarkers for early AD detection. However, the high dimensionality and complexity of neuroimaging data present significant challenges in analysis and interpretation. To address these challenges, machine learning techniques, including Radial Basis Function Neural Networks (RBFNN), have been explored for their ability to model complex, nonlinear relationships in data. This study aims to integrate advanced neuroimaging biomarkers with hybrid metaheuristic algorithms and RBFNN to enhance the accuracy and efficiency of early AD detection.

## Methods

**Data Acquisition:** We utilized publicly available datasets from the Alzheimer's Disease Neuroimaging Initiative (ADNI), comprising structural and functional MRI scans of healthy controls, individuals with mild cognitive impairment (MCI), and AD patients. Pre-processing steps included normalization to standardize image intensities, segmentation to isolate regions of interest, and extraction of features such as cortical thickness, volumetric measurements, and diffusion tensor imaging metrics.

**Feature Selection:** Given the high dimensionality of the extracted features, we employed a hybrid feature selection approach combining Exponential Mutated Swarm Optimization (EMSO) and Harris Hawk Optimization (HHO). EMSO is effective in exploring the search space to identify global optima, while HHO provides robust mechanisms for exploiting promising solutions. This combination leverages the strengths of both algorithms to identify the most informative features for distinguishing between healthy, MCI, and AD subjects.

**Surrogate Modelling with RBFNN:** The selected features served as inputs to an RBFNN, which is well-suited for modelling nonlinear relationships due to its universal approximation capabilities. The RBFNN parameters, including the number of neurons and the spread parameter, were optimized using the hybrid EMSO-HHO algorithm to enhance predictive performance.

**Model Evaluation:** We assessed the model's performance using metrics such as accuracy, sensitivity, specificity, and the area under the receiver operating characteristic curve (AUC). A 10-fold cross-validation strategy was implemented to ensure the robustness and generalizability of the results.

## Results

The hybrid EMSO-HHO algorithm effectively reduced the feature set, identifying key neuroimaging biomarkers associated with early-stage AD. The optimized RBFNN model achieved high accuracy, better sensitivity, specificity and AUC. These results indicate a significant improvement over traditional feature selection methods and standard neural network models.

## Discussion

Our findings underscore the potential of integrating advanced neuroimaging biomarkers with hybrid metaheuristic algorithms and RBFNN for early AD detection. The hybrid feature selection method effectively addresses the challenges of high-dimensional data, while the RBFNN provides a powerful tool for modelling complex relationships inherent in neuroimaging data. This approach aligns with recent studies that have explored machine learning frameworks for early MRI-based AD diagnosis, highlighting the importance of combining multiple modalities and advanced algorithms to improve diagnostic accuracy. For instance, Zhang and Shen proposed a multi-modal multi-task learning framework that jointly predicts multiple regression and classification variables in AD, demonstrating the efficacy of combining different data sources and learning tasks. Our study builds upon this foundation by incorporating a hybrid feature selection method and RBFNN, offering a

novel approach to early AD detection.

Furthermore, the use of hybrid metaheuristic algorithms for feature selection addresses the limitations of traditional methods, which may struggle with the high dimensionality and complex interactions present in neuroimaging data. By leveraging the exploration capabilities of EMSO and the exploitation strengths of HHO, our approach effectively identifies the most informative features, enhancing the performance of the subsequent RBFNN model.

## Conclusion

This research demonstrates that combining advanced neuroimaging biomarkers with hybrid metaheuristic algorithms and RBFNN significantly enhances the early detection of Alzheimer's disease. The methodology not only improves predictive accuracy but also ensures computational efficiency and reproducibility. These advancements hold substantial clinical relevance, offering a robust tool for early AD diagnosis, potentially leading to better patient outcomes and more effective intervention strategies. Future work will focus on validating the model with larger, multi-centre datasets and exploring its applicability to other neurodegenerative disorders.

# Role of Artificial Intelligence in Prognosticating Neurodegenerative Diseases

Prof. (Dr.) Rajul Rastogi

Department of Radiodiagnosis, Teerthanker Mahaveer Medical College and Research Center, Moradabad, Uttar Pradesh

## Introduction

Neurodegenerative disorders is a group of debilitating and progressive neurological diseases like Alzheimer's disease, Parkinson's disease, etc. The diagnosis is often based on clinical criteria following exclusion of organic disorder. These diseases are associated with neuronal loss evident in form of grey and white matter volume reduction which is visually apparent on brain MRI late in the disease. Hence, we conducted pilot study to assess the volumetric alterations in brain on MRI using Artificial Intelligence (AI) based tools.

## Methods

Twenty patients with clinical neurodegenerative disease and 20 age & sex matched controls underwent MRI brain with subsequent volumetric analysis using AI based tool.

## Results

Age range of patients was 40-50years with only males in our study group. All the patients revealed variable but diffuse volumetric loss of grey and white matter on AI based volumetric analysis of

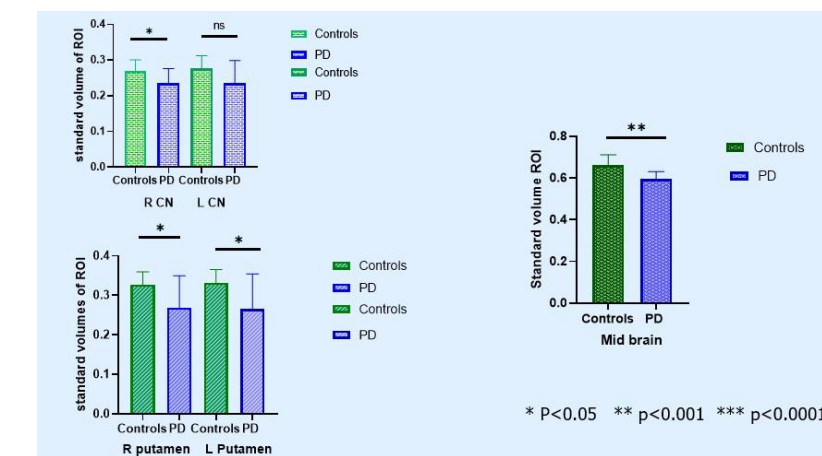
brain compared to controls which was apparent visually in only 6 out of 20 patients.

## Conclusion

Artificial Intelligence Based Volumetric Brain Analysis on MRI in neurodegenerative disease can objectively identify neurodegeneration early in the course of disease allowing time for institution of aggressive medical treatment and psycho-counselling. It helps in detecting volume loss of grey & white matter before it becomes visually apparent, also allowing objective assessment of the various drugs in their role of retarding or cessation of the progression of neurodegenerative disease.

	Parkinson's Disease Mean ± SD	Controls Mean ± SD	P value
Right Caudate nucleus	0.24 ± 0.04	0.27 ± 0.03	0.053
Left Caudate nucleus	0.24 ± 0.06	0.28 ± 0.04	0.093
Right Putamen	0.27 ± 0.08	0.33 ± 0.03	0.049
Left Putamen	0.27 ± 0.09	0.33 ± 0.30	0.040
Mid Brain	0.60 ± 0.04	0.66 ± 0.05	0.001

study groups	Healthy Controls (n = 10)	Parkinson's Disease (n = 10)	p value
<b>Characteristics</b>			
Age (Mean ± SD)	51.8 ± 10.0	59.8 ± 6.0	0.064
Sex M:F	1:1	3:2	0.653



\* P<0.05 \*\* p<0.001 \*\*\* p<0.0001

# Brain Structural Changes Caused by Severe Subjective Tinnitus: A Comprehensive Analysis of Cortical Morphometry and Neuroplasticity

Himanshu Raj Pandey<sup>1,2</sup>

Amit Keshri<sup>3</sup>

Neeraj Sinha<sup>1,2</sup>

Uttam Kumar<sup>1,2\*</sup>

<sup>1</sup>Centre of Biomedical Research (CBMR), Sanjay Gandhi Post Institute of Medical Sciences Campus, Raebareli Road, Lucknow, 226014, India. <sup>2</sup>Academy of Scientific and Innovative Research (AcSIR), Ghaziabad, Uttar Pradesh, 201002, India. <sup>3</sup>Sanjay Gandhi Postgraduate Institute of Medical Sciences, Lucknow (India). \*Corresponding Author E-mail: dr.uttam.kumar@gmail.com

## Introduction

Subjective tinnitus is the perception of sound that occurs without an external auditory source, often known as a sound hallucination. Tinnitus affects 14.4% of adults and the elderly worldwide. [1,2] Subjective tinnitus, experienced by most tinnitus sufferers, is an internal auditory condition without a physical sound source. Its exact causes are complex and not entirely known, involving potential neuroplastic changes in the auditory pathway. While there is no definitive cure yet, treatments like sound therapy and cognitive-behavioral therapy offer symptom relief for many. Ongoing research is promising and aims to uncover more effective treatments. Severity of tinnitus associated with changes in the gray matter in auditory cortex, amygdala and parahippocampal regions and other non-auditory regions.

In this study we find out how severe tinnitus patients brain structure changes as compared to non-severe tinnitus patients which caused the worsen effects to suffers.

## Methods

In this study we included 58 subjective tinnitus patients. In this patients group comprised 36 males and 22 females, with an average age of  $39.07 \pm 13.95$  years we divided two subgroups severe sufferers (35), and non-severe sufferers (23) based of their respective THI (Tinnitus handicap Inventory) scores. All the Patients has been recruited from SGPGI, Lucknow. All patients have informed written consent of the study and shown no pathology related to ear or brain.

T1 MRI data was acquired using a 3 T Siemens MRI scanner at the CBMR with the following parameters: 192 slices; TR of 1900 ms; TE of 2.44 ms; flip angle of 12°; slice thickness of 1.00 mm; matrix dimension 224x256; and isotropic voxels at 1 mm<sup>3</sup> resolution. Surface-based morphometric analyses and cortical estimation were performed using the Computational Anatomy Toolbox (CAT12, and SPM12). [3]

Fractal Dimension (FD): Measures the complexity of brain folding by analyzing surface area resolution and geometric patterns. Gyration: Quantifies the degree of cortical folding by comparing the surface area of

gyri and sulci to the brain's outer surface. Sulcus Depth: Assesses the depth of the brain's sulci, indicating the degree of cortical folding and complexity. Cortical Thickness: Measures the thickness of the cerebral cortex, reflecting structural and functional aspects of the brain.

## Results

**Fractal Dimension:** In the left hemisphere, fractal dimension (FD) analysis revealed increased FD in the medial orbitofrontal cortex and the banks of the superior temporal sulcus (bankssts), while decreased FD was observed in the superior parietal region. In the right hemisphere, increased FD was identified in the pars triangularis and temporal pole, whereas decreased FD was noted in the precentral, paracentral, bankssts, and transverse temporal regions.

**Gyration:** In the left hemisphere, increased gyration was observed in the insula, while decreased gyration was noted in the pars opercularis, isthmus cingulate, and frontal pole. In the right hemisphere, increased gyration was found in the precentral and postcentral regions.

**Sulcus Depth:** In the left hemisphere, increased sulcal depth was observed in the middle temporal and rostral anterior cingulate regions. Decreased sulcal depth was noted in the cuneus region.

**Thickness:** In the left hemisphere, increased cortical thickness was observed in the lateral occipital, transverse temporal, lingual, and cuneus regions. In the right hemisphere, increased cortical thickness was identified in the pericalcarine, lateral occipital, and cuneus regions. Decreased cortical thickness was noted in the parahippocampal region.

## Discussion

In conclusion, this study found significant structural brain variations between severe and non-severe tinnitus patients, including changes in fractal dimension (FD), gyration, sulcus depth, and cortical thickness in both hemispheres. The **frontal pole**, with decreased gyration, indicates disruptions in cognitive and emotional regulation, whereas the **medial orbitofrontal cortex**, with increased FD, represents abnormalities in emotional processing related to tinnitus severity. The **temporal pole** has increased FD, which is associated with auditory and emotional processing, whereas decreased FD in the **superior parietal** suggests impaired sensory integration and spatial processing related to tinnitus. In

the **insula**, increased gyration implies changes in sensory and emotional processing, whereas decreased gyration in the **cingulate** indicates disruptions in emotional regulation and cognitive control. Structural changes in the **paracentral** and **precentral** gyri, defined by decreased FD and cortical thickness, point to potential tinnitus-related motor and sensory processing impairments. Increased cortical thickness in the **lateral occipital, lingual, and cuneus** regions indicates changes in visual processing and integration, whereas increased thickness in the pericalcarine region indicates alterations in both visual and sensory processing. [4] These findings indicate that severe tinnitus causes large neuroplastic changes in the brain, particularly in areas associated to auditory processing and emotional regulation, are possible indicators of tinnitus severity and could be used as biomarkers to assess its impact.

## Conclusion

This study provides understanding on the neurological foundations of tinnitus, which could help guide the development of more specific and effective therapies.

## References

1. Jarach, Carlotta M., et al. "Global prevalence and incidence of tinnitus: A systematic review and meta-analysis." JAMA neurology (2022)
2. Pandey, Himanshu R., et al. "Using ALE coordinate-based meta-analysis to observe resting-state brain abnormalities in subjective tinnitus." Brain Imaging and Behavior (2024): 1-14.
3. Gaser, Christian, et al. "CAT: a computational anatomy toolbox for the analysis of structural MRI data." Gigascience 13 (2024): giae049.
4. Pandey, Himanshu R., et al. "Neuroanatomical correlates of subjective tinnitus: insights from advanced cortical morphology analysis." Cerebral Cortex 34.11 (2024): bhae432.

# Improving the sensitivity in imaging of Central Lymphatics: Optimized MR Lymphangiography using relaxation properties of Chyle

Monica Gunasingh<sup>1,2</sup>

Natesan Chidambaranathan<sup>3</sup>

Jaladhar Neelavall<sup>1</sup>

Narayana Krishana Rolla<sup>4</sup>

1 Biomedical Engineering, Indian Institute of Technology, Hyderabad, India, 2 Philips India Limited, Chennai, India, 3 Department of Radiology, Apollo Hospitals, Chennai, India, 4 Philips India Limited, Bangalore, India

## Introduction

Lymphangiography plays a vital role in the diagnosis and management of various clinical areas by mapping the lymphatic anatomy. [1,2] Limitations of conventional methods such as X-ray or CT Lymphangiography and Lymphoscintigraphy include the use of ionizing radiation and poor spatial resolution and invasive nature. In addition to the risk of intra-lymphatic inflammatory reaction with the use of ethiodized oil, the procedure is time-consuming and invasive. Moreover, iodinated contrast agent reduces the feasibility in patients with renal impairment. [3-6] Non-contrast MRI on the other hand, has superior soft tissue resolution and can be advantageous in delineating the complex and variable anatomy of the lymphatics without the need for intervention. The thoracic duct is the largest lymphatic vessel in the body, and highly variable in anatomy, and differs in composition differs from the peripheral and intestinal lymphatic vessels. [7] To improve the sensitivity in visualization of the central lymphatics, the relaxation properties of Chyle, an enriched lymph, originating from the small intestine were measures and the sequence parameters were optimized. Preliminary results from this work are presented here.

## Methods

Informed consent was obtained from the participants in the study, and the local institutional review board approved the study as part of a larger ongoing research study. The Chyle sample was obtained from one patient with a history of Chylothorax and underwent ultrasound-guided aspiration. The fluid was collected in a container and subjected to MR relaxometric measurements within 2 hrs. of sample collection. The sample was stored in a refrigerator at 4°C and measurements were repeated after 24 hrs. The sample was allowed to thaw for 45 minutes before subjecting it to relaxometric measurements. T1 and T2 values of Chyle showed that a longer TE was possible, which provided sufficient signal from Chyle in the lymphatic ducts while significantly suppressing the signal from the background tissue. This, in turn, helped in conspicuous visualization of the central lymphatics.

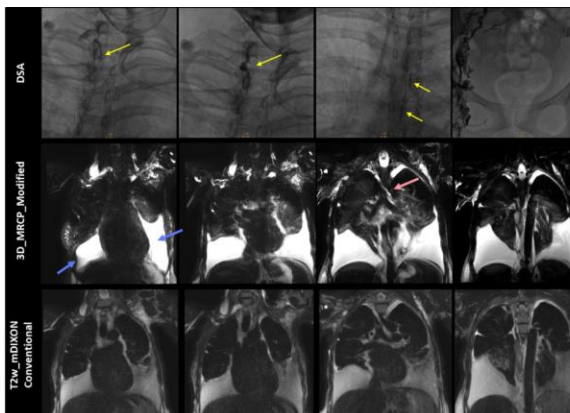
## Results

Figure 2 shows the photograph of the Chyle sample collected. The sample had slight contamination from blood during the aspiration, which gave it a pink coloration. T1 and T2 of the Chyle was measured to be 2814.6/- 79.4 ms and 1181.2/- 137.5 ms respectively (see Figure-2) and it was consistent between the two timepoints of measurement. Based on these values, the 3D MRCP sequence was modified as follows, keeping in mind the need to balance the contrast-SNR-scan time (Figure 3): TE was increased from 400 ms to 600 ms, TR from 978 to 2500 ms and TSE factor of 185. Any further increase in TE resulted in an increase in scan time. The FOV was increased to cover the extent of the thoracic duct, and

the overlapping slices allowed for mapping the continuity of the vessel. Higher in-plane resolution allowed for multi-planar reformation in orthogonal orientation, without loss in duct conspicuity. Qualitative evaluation of the curved MIP in the patient and the volunteers showed that the optimized sequence consistently provided better visualization (vs. conventional technique) of the lymphatic vessels in the thoracic region in all cases. Figure 3 shows the curved MIP of the thoracic region in the conventional and the optimized sequence (MRCP\_modified) from two volunteers. Figure 4 shows the images from the patient with chylothorax. Lymphatic vessels imaged using fluoroscopy in the thoracic region show their tortuosity and their small calibre. These vessels are completely missed in the conventional T2 mDIXON images. On the other hand, the lymphatic vessels could be clearly seen in the optimized sequence (MRCP\_modified). While this work presents preliminary results from an improved lymphangiography sequence, further, systematic study may be warranted to explore room for further optimization.

## Conclusion

In this work, we measured the T1 and T2 properties of chyle which enabled optimization of an existing 3D technique for improved visualization of central lymphatics. T1 and T2 values of Chyle showed that a longer TE was possible, which provided sufficient signal from Chyle in the lymphatic ducts while significantly suppressing the signal from the background tissue. This, in turn, helped in conspicuous visualization of the central lymphatics.



**Figure 4:** Chyle leak in a 43-year-old woman with chylous pleural effusion. Thoracic duct on a fluoroscopic image shows abnormal contrast agent flow (yellow arrows). On the modified Lymphangiogram protocol, the severity of the chylous pleural effusion is better appreciated (Blue arrows) and mapping of the thoracic duct (pink arrow) is better seen on the modified MRI sequence.

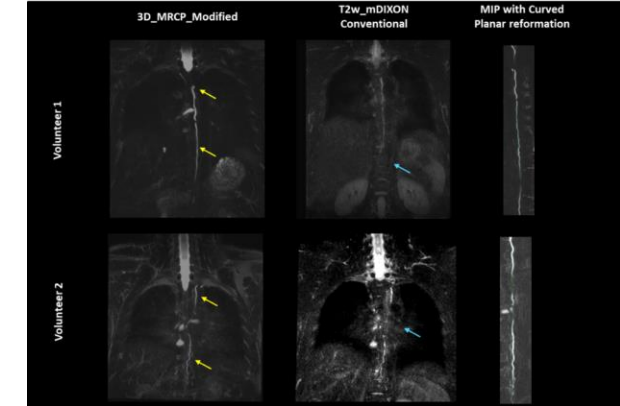


**Figure 5:** Shows representative images from two Volunteers of the 3D\_MRCP\_Modified sequence, Conventional T2w\_mDIXON sequence and the Maximum Intensity Projection with Curved Planar Reformation of the thoracic duct. The duct conspicuity and extent are well appreciated on the modified protocol in comparison to the conventional sequences (Yellow arrows). Moreover, artifacts arising from the mediastinal structures and poor background suppression obscures the thoracic duct in the conventional protocol (Blue arrow).

## References

- Lee, E., Bikò, D. M., Sherk, W., Masch, W. R., Ladino-Torres, M., & Agarwal, P. P. (2022). Understanding Lymphatic Anatomy and Abnormalities at Imaging. *RadioGraphics*, 42(2), 487–505. <https://doi.org/10.1148/rgr210104>
- Pamarthi, V., Pabon-Ramos, W. M., Mamell, V., & Hurwitz, L. M. (2017). MRI of the Central Lymphatic System. *Topics in Magnetic Resonance Imaging*, 26(4), 175–180. <https://doi.org/10.1097/rmr.0000000000000130>
- Monfore, N., Downing, T., Sanogo, M. L., Kokabi, N., Khaja, M. S., Majdalany, B. S., Association for Radiologic & Imaging Nursing, & Elsevier Inc. (2020). Lymphatic imaging techniques. In *Journal of Radiology Nursing* [Journal-article]. <https://doi.org/10.1016/j.jradnu.2019.07.010>
- Polomska, A. K., Proulx, S. T., ETH Zürich, & University of Bern. (2020). Imaging technology of the lymphatic system. In *Advanced Drug Delivery Reviews* (Vol. 170, pp. 294–311) [Journal-article]. <https://doi.org/10.1016/j.addr.2020.08.013>
- Jørgensen, M. G., Hermann, A. P., Madsen, A. R., Christensen, S., & Sørensen, J. A. (2021). Indocyanine green lymphangiography is superior to clinical staging in breast cancer-related lymphedema. *Scientific Reports*, 11(1). <https://doi.org/10.1038/s41598-021-00396-2>
- Schwartz, F. R., James, O., Kuo, P. H., Witte, M. H., Kowek, L. M., & Pabon-Ramos, W. M. (2020). Lymphatic Imaging: Current Noninvasive and Invasive Techniques. *Seminars in Interventional Radiology*, 37(03), 237–249. <https://doi.org/10.1055/s-0040-1713441>
- Negm, A. S., Collins, J. D., Bendel, E. C., Takahashi, E., Knavel Koepsel, E. M., Gehling, K. J., Burke, C. E., Barker, D. R., Stenzel, W. S., Bathke, A. M., Polites, S. F., Abejco, A. S., Morris, J. M., Favazza, C., Lu, A., François, C. J., Young, P., & Thompson, S. M. (2024). MR Lymphangiography in Lymphatic Disorders: Clinical Applications, Institutional Experience, and Practice Development. *RadioGraphics*, 44(2). <https://doi.org/10.1148/rgr230075>
- Notohamiprodjo, M., Weiss, M., Baumeister, R. G., Sommer, W. H., Helck, A., Crispin, A., Reiser, M. F., & Herrmann, K. A. (2012). MR Lymphangiography at 3.0 T: Correlation with Lymphoscintigraphy. *Radiology*, 264(1), 78–87. <https://doi.org/10.1148/radiol.12110229>
- Sanshan, H., & Miyazaki, M. (1999). Thoracic Duct: Visualization at Nonenhanced MR Lymphography—Initial Experience. In *Radiology* (Vol. 212, pp. 598–600).

# Integrating Tensor-Based Morphometry with Machine Learning for Diagnosis of SCA12

Dhruv Chandra Lohani<sup>1</sup>, Bharti Rana<sup>1\*</sup>, S Senthil Kumaran<sup>2</sup>, Achal Kumar Srivastava<sup>3</sup>, Snigdha Agrawal<sup>4</sup>, Pankaj

1 Department of Computer Science, University of Delhi, Delhi, India, 2 Department of NMR, All India Institute of Medical Sciences, New Delhi, India, 3 Department of Neurology, All India Institute of Medical Sciences, New Delhi, India, 4 School of Computer and Systems Science, Jawaharlal Nehru University, Delhi, India

## Introduction

Spinocerebellar ataxia type 12 (SCA12), degenerative neurological condition, prevalent in the North Indian population, is linked to CAG repeat expansions (>43 repeats) in the PPP2R2B gene, causing cerebello-cortical atrophy. It primarily appears as early-onset action tremors in the upper extremities, along with gait ataxia, speech disturbances, head tremors, and autonomic dysfunction [1]. Automatic diagnosis of SCA12 using MRI is limited and need attention of Machine Learning (ML) community. Thus, the aim of this study is to identify volumetric changes in brain structures in SCA12 subgroups by leveraging ML for the analysis of deformation fields extracted from structural MRI (sMRI) scans.

## Methods

With informed consent from subjects and ethical approval, MRI volumes 34 SCA12 and 34 Healthy controls (HC) age-balanced were acquired at AIIMS, New Delhi, using a 3T Philips Ingenia scanner with a 3D Turbo Field Echo sequence using parameters as mentioned in [2]. Jacobian determinants (JB) were obtained using segmentation pipeline as mentioned in [2]. It captures the local change in volume of each voxel. Using JB, the present work used Tensor-based morphometry (TBM) for identification of the atrophic regions that may help to differentiate SCA12 patient from HC. The JB volumes were co-registered and parcellated using two brain atlases (Automated Anatomical Labelling atlas 3 (AAL3) [3] and Neuromorphometrics [4]). Both atlases are designed to study whole brain regions. Co-registered JB volumes were used for TBM to identify clusters of localized shape variations and volumetric changes. We used both contrasts (SCA12 < HC using [-1 1] and SCA12 > HC using [1 -1]) to conduct TBM. Subsequently, the identified values of the voxels were utilized as features, which were then used to train ML-based classifiers, namely Logistic regression with L1 regularization (LR\_L1) [5] and Support Vector Machine (SVM) [6]. The performance of the classifiers was assessed through the leave-one-out cross-validation (LOOCV) approach. The hyper-parameters were tuned for both the classifiers and the best set of hyper-parameters were used.

## Results

Table 1 shows the classification results after classification for both the atlases. Table 1 demonstrates that LR\_L1 achieved 91.18% accuracy for classifying SCA12 from HC for SCA12 > HC contrast. The superior performance of LR\_L1 compared to SVM can be attributed to its ability to induce sparsity, effectively reducing the irrelevant features. Furthermore, to trace the regions of atrophy or growth, the weights of the LR\_L1 classifier were analysed, as these weights

correspond to the contributing voxels in classification. Figure 1 and Figure 2 shows the identified voxels after LR\_L1 classifier. A comparative analysis was conducted to evaluate the proposed approach against recent sMRI-based studies on ML detection of SCA12, establishing a performance benchmark. Table 2 summarizes performance metrics from related studies and the best results achieved by the proposed method, with data sourced from primary references.

Table 1. The classification results using TBM (in %) for AAL3 and Neuromorphometrics atlases.

Contrast	Classifier	AAL3 [3]						Neuromorphometrics [4]					
		Acc	Pre	Rec	Spec	F1	Acc	Pre	Rec	Spec	F1		
SCA12 < HC	LR_L1	83.82	92.59	73.53	94.12	81.97	86.76	93.1	79.41	94.12	85.71		
	SVM	83.82	87.1	79.41	88.24	83.08	83.82	87.1	79.41	88.24	83.08		
SCA12 > HC	LR_L1	83.82	92.59	73.53	94.12	81.97	91.18	96.67	85.29	97.06	90.63		
	SVM	82.35	82.35	82.35	82.35	82.35	82.35	80.56	85.29	79.41	82.86		

\*LR\_L1: Logistic Regression using L1-regularization. SVM: Linear Support Vector Machine, Acc: Accuracy, Pre: Precision, Rec: Recall, Spec: Specificity, F1: F1-score

## Discussion

The application of TBM enabled the detection of significant changes in JB volumes among SCA12 patients with 91.18% accuracy, which is better than the existing work except [2]. Further, it is observed that the atrophy in SCA12 is not only restricted to the cerebellum regions, but has affected the other brain regions also.

## Acknowledgements

The present work is part of the project “Differential diagnosis of SCA1, 2, 3, 6 and 12 using structural MRI and resting state MRI,” funded by IoE, University of Delhi, under Major Research Project (MRP) scheme and Project No: EMR/2017/002294, funded by Science and Engineering Research Board (SERB), New Delhi, India. This financial support is gratefully acknowledged by the authors.

Table 2. Comparison of the proposed approach with ML methods in the literature.

Author	Sample Size (SCA12, healthy)	Used Features	Accuracy
[7]	30, 30	Texture-based	85%
[8]	30, 30	Texture-based	90%
[2]	30, 30	3D Discrete Wavelet Transform	95%
Proposed Approach	34, 34	TBM	91.18%

## References

- [1] D. Kumar, A. K. Srivastava, M. Faruq, and V. R. Gundluru, ‘Spinocerebellar ataxia type 12: An update’, *Ann. Mov. Disord.*, vol. 2, no. 2, p. 48, Aug. 2019, doi: 10.4103/AOMD.AOMD\_5\_19.
- [2] S. Agrawal, R. K. Agrawal, S. S. Kumaran, B. Rana, and A. K. Srivastava, ‘Integration of graph network with kernel SVM and logistic regression for identification of biomarkers in SCA12 and its diagnosis’, *Cereb. Cortex*, vol. 34, no. 4, p. bhae132, Apr. 2024, doi: 10.1093/cercor/bhae132.
- [3] E. T. Rolls, C.-C. Huang, C.-P. Lin, J. Feng, and M. Joliot, ‘Automated anatomical labelling atlas 3’, *NeuroImage*, vol. 206, p. 116189, Feb. 2020, doi: 10.1016/j.neuroimage.2019.116189.
- [4] ‘Neuromorphometrics, Inc. | Building a Model of the Living Human Brain’. Accessed: Jan. 13, 2025. [Online]. Available: <https://www.neuromorphometrics.com/>
- [5] D. R. Cox, *Analysis of Binary Data*, 2nd ed. New York: Routledge, 2017. doi: 10.1201/9781315137391.
- [6] V. Vapnik, *The Nature of Statistical Learning Theory*. Springer Science & Business Media, 2013.
- [7] S. Agrawal, S. S. Kumaran, A. K. Srivastava, R. K. Agrawal, and M. K. Narang, ‘Study of 2D Feature Extraction Techniques for Classification of Spinocerebellar Ataxia Type 12 (SCA12)’, in *Studies in Health Technology and Informatics*, P. Otero, P. Scott, S. Z. Martin, and E. Huesing, Eds., IOS Press, 2022, doi: 10.5233/SIHT220162.
- [8] S. Agrawal, R. K. Agrawal, S. S. Kumaran, A. K. Srivastava, and M. K. Narang, ‘Fusion of 3D feature extraction techniques to enhance classification of spinocerebellar ataxia type 12’, *Int. J. Inf. Technol.*, vol. 16, no. 1, pp. 91–103, Jan. 2024, doi: 10.1007/s41870-023-01579-y.

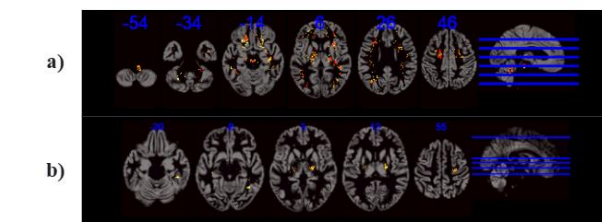


Fig 1. Identified regions after performing TBM while keeping SCA12<HC using co-registered JB volumes co-registered with a) AAL3 atlas and b) Neuromorphometrics atlas.

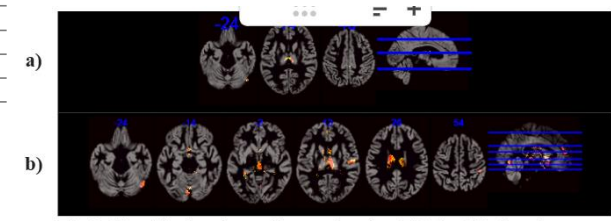


Fig 2. Identified regions after performing TBM while keeping SCA12>HC using co-registered JB volumes co-registered with a) AAL3 atlas and b) Neuromorphometrics atlas.

# Investigating neurometabolism in fast progressing ALS using Transgenic Mouse Model

Sohini Ghosh<sup>1,2</sup>

Anant Bahadur Patel<sup>1,3</sup>

<sup>1</sup> CSIR-Centre for Cellular and Molecular Biology, Hyderabad, India, <sup>2</sup> Academy of Scientific and Innovative Research (AcSIR), Ghaziabad-2012002, India

## Introduction

Amyotrophic lateral sclerosis (ALS) is a fatal and rapidly progressing neurodegenerative disorder that results from selective degeneration of upper and lower motor neurons in the brain stem and spinal cord [1]. It is characterized by alterations in cellular processes that include impaired proteostasis, accumulation of misfolded proteins, enhanced oxidative stress, and excitotoxicity. Currently, no definitive diagnostics or biomarker for ALS exists. Riluzole, the only FDA-approved treatment for ALS, extends the survival only by a few months. <sup>13</sup>C NMR spectroscopic measurements in rats and the human brain have established that the neurotransmitter cycling flux is stoichiometrically coupled with neuronal glucose oxidation, suggesting that neurotransmitter energy is supported by oxidative glucose metabolism [2]. The objective of the current study is to evaluate quantitatively the behavior and energetics of neurotransmitters in a transgenic mouse model of ALS.

## Methods

All the experimental procedures with mice were approved by the Animal Institutional Ethics Committee of CSIR-CCMB. SOD1G93A mice (4.5 months) were used in the study. The motor function in ALS mice was measured using a paw grip strength meter [3]. Briefly, the muscle strength of the forelimbs of mice was assessed by lowering the animals over the top of the grid, and pulling it back horizontally across the length of the grid. The maximum force exerted by the paw on the grid before release was recorded in the meter. Additionally, the motor coordination of mice was evaluated by the rotarod test [4]. The latency of mice to fall from the accelerating rotarod (4–40 rpm) for 300 s was monitored to measure motor coordination. Moreover, neurological scoring was performed to assess the severity of ALS by giving a score of 0–4. For neurometabolic measurements, mice were anesthetized using urethane (1.5 g/kg, intraperitoneal), and the lateral tail vein was cannulated. In order to determine the rate of neuronal glucose oxidation, [<sup>1,6-</sup><sup>13</sup>C<sub>2</sub>]glucose was administered via the tail vein as a bolus-variable rate infusion over 10 min [5]. The brain metabolism was arrested by freezing the mice in liq. N<sub>2</sub>. The neurometabolites were extracted from the frozen brain tissue [6]. The lyophilized brain extracts were dissolved in D<sub>2</sub>O for the <sup>1</sup>H-[<sup>13</sup>C]-NMR analysis at a 600 MHz spectrometer [5]. The concentrations and <sup>13</sup>C labeling of brain metabolites of the spinal cord and cerebral cortex were measured in <sup>1</sup>H-[<sup>13</sup>C]-NMR spectrum of tissue extracts. The cerebral metabolic rates were calculated from the <sup>13</sup>C labeling of cerebral metabolites from [<sup>1,6-</sup><sup>13</sup>C<sub>2</sub>]glucose [7].

## Results

There was a significant ( $p<0.0001$ ) reduction in the forelimb grip strength of SOD1G93A male mice ( $0.42\pm0.10$  N, n=10) when compared with WT control mice ( $1.13\pm0.19$  N, n=10) [Fig. 1A]. Additionally, the motor coordination assessed by rotarod indicates that the area under the curve for SOD1G93A male mice ( $9.6\pm8.3$  revolution, n= 8) is significantly lower ( $p=0.0003$ ) than controls ( $56.7\pm18.3$  revolution) [Fig. 1B]. Moreover, SOD1G93A male mice exhibited an increase in the neurological score ( $2.9\pm0.7$ , n=10) when compared with WT controls ( $0.0\pm0.0$ , n=10). Similar motor deficits were seen in female SOD1G93A mice. The typical <sup>1</sup>H-[<sup>13</sup>C]-NMR spectra showing concentration (top) and <sup>13</sup>C labeling of spinal cord extract is presented in Figure 2. There was a reduction in the levels of glutamate (SOD1G93A 7.2  $\mu$ mol/g; Control: 8.0  $\mu$ mol/g, p=0.02), GABA (1.1 vs 1.3  $\mu$ mol/g, p=0.001), aspartate (1.1 vs 1.3  $\mu$ mol/g, p=0.000), NAA (4.9 vs 6.3  $\mu$ mol/g, p=0.001), NAAG (1.0 vs 1.7  $\mu$ mol/g, p=0.000), alanine (0.25 vs 0.33  $\mu$ mol/g, p=0.005), while taurine (3.1 vs 2.5  $\mu$ mol/g, p=0.014) and inositol (14.8 vs 9.3  $\mu$ mol/g, p=0.001) levels were increased in the spinal cord of SOD1G93A mice [Fig. 2]. There was no significant perturbation in neurometabolite levels in the cerebral cortex of SOD1G93A mice. The neurometabolic analysis in the different brain regions of SOD1G93A mice is in progress..

## Discussion

Behavioral analysis indicated severe impairment in limb strength, motor coordination, and neurological score in female as well as in male mice, suggesting severe ALS phenotype in both genders of SOD1G93A mice. The neurometabolic homeostasis is severely perturbed in the spinal cord, with no significant changes in the cerebral cortex.

## Conclusion

The severe impairment in neurometabolite homeostasis in neuronal and astrocytic markers suggests impaired neural activity in the spinal cord. Early diagnosis of ALS by assessing the spinal cord-specific metabolites, including NAAG, will aid in the diagnosis of the disease and follow therapeutic progress during the course of intervention.

## Acknowledgment

This study was supported by funding from CSIR-CCMB.

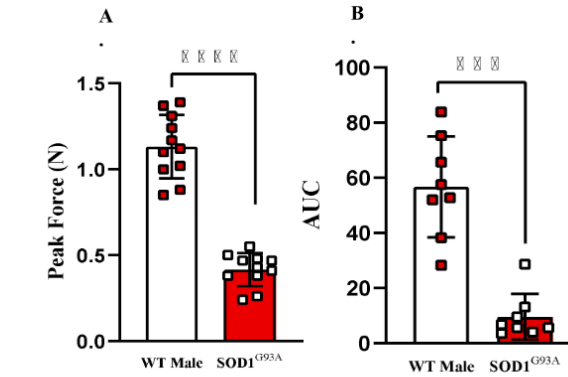


Fig. 1 Motor function, A. Grip Strength. B. Motor Coordination, \*\*\* p <0.005 and \*\*\*\*p<0.0001

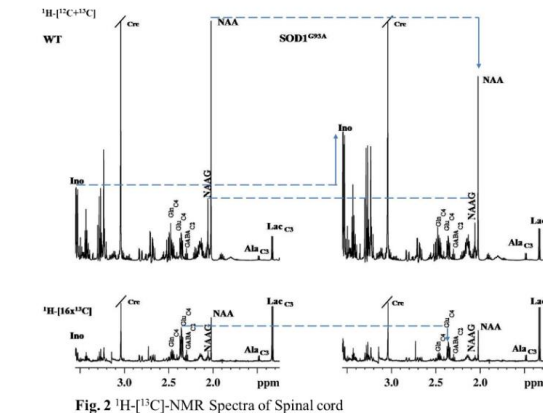


Fig. 2 <sup>1</sup>H-[<sup>13</sup>C]-NMR Spectra of Spinal cord

## Reference

- [1] Wood et al (2014) J Med Chem 57:6316;
- [2] Hyder et al (2006) J Cereb Blood Flow Metab 26:865;
- [3] Bagga et al (2013) J Neurochem 127(3):365;
- [4] Luh et al (2017) Nat Protoc 12:1451;
- [5] Tiwari et al (2013) J Cereb Blood Flow Metab 33:1523;
- [6] Patel et al (2001) Brain Res 919:207;
- [7] Mishra et al (2018) J Neurochem 146:722.

# Investigating Role of Corpus Callosum WM Integrity in Predicting Neurocognitive Outcomes in TBI Patients using Mediation Analysis: A DTI Study.

Manoj Kumar<sup>1</sup>, Sujitra S<sup>1</sup>, Dhaval Shukla<sup>2</sup>, Sandhya Mangalore<sup>1</sup>, Dwarakanath Srinivas<sup>2</sup>, Sriganesh Kamat<sup>3</sup>, Dinesh Kumar Deelchand<sup>4</sup>, Sarada Subramanian<sup>5</sup>, Anita Mahadevan<sup>6</sup>, and Jitender Saini<sup>1</sup>

<sup>1</sup>Neuroimaging and Interventional Radiology, <sup>2</sup>Neurosurgery, <sup>3</sup>Neuroanesthesia, <sup>5</sup>Neurochemistry, and <sup>6</sup>Neuropathology, National Institute of Mental Health and Neurosciences, Bengaluru, India. <sup>4</sup>Radiology, University of Minnesota, Minneapolis, MN, United States.

## Introduction

The corpus callosum (CC), the largest WM tract, plays a crucial role in interhemispheric communication and is often affected after traumatic insult, making it a focal point for understanding pathophysiological changes and WM damage can lead to cognitive deficits in TBI patients<sup>1</sup>. However, research suggests that damage isolated to CC may not fully account for cognitive impairments observed post-TBI. Instead, damage across a broader network of the WM tracts appears to be more predictive of cognitive outcomes, as cognitive functions rely on the coordinated integrity of multiple interconnected regions<sup>2,3</sup>. The study aims 1) to examine differences in neurocognitive test performance between healthy controls and individuals with mild-TBI. 2) to investigate the mediating role of WM integrity in relationship between interhemispheric involvement of the CC and cognitive scores from the individuals with TBI compared to healthy controls.

## Methods

TBI patients(n=13) and age/gender matched healthy controls (n=17) with DTI data and neurocognitive test scores were included in the study. MRI data was acquired on 3.0T clinical MRI scanner using 64 channel transmit-received head coil. DTI data was acquired with 64 diffusion directions. A multishell diffusion scheme was used, and the b-values were 0, 500 ,1000 and 2500 s/mm<sup>2</sup>. The in-plane resolution was 2.500 mm. The slice thickness was 2.50 mm.

**Neurocognitive assessment:** Visuospatial and verbal working memory were assessed using the Wechsler Memory Scale-Third Edition (WMS-III)<sup>4</sup> through the Spatial Span Forward and Backward tasks, where participants were required to remember and reproduce the order of blocks pointed at by the examiner, and the Digit Span Forward and Backward tasks, where participants recalled sequences of numbers in both original and reversed orders.

**DTI data analysis:** DTI preprocessing was conducted using FSL 6.0.7.9 (FMRIB Software Library). The eddy tool was used to correct for motion and eddy current distortions in the diffusion images. Eddy-corrected images were processed using a tensor fitting model to compute DTI maps i.e. FA, MD, AD and RD. TBSS was conducted on FA using 5000 randomizations to perform a general linear model (GLM) analysis. Statistical computations were performed on the output images, with a significance threshold set at  $p \leq 0.05$ . Region of interest (ROI) extraction was performed using the fslmeans command on the TBSS-derived FA image using the ROI masks generated using JHU ICBM-DTI-81 WM Atlas labels.

## Statistical analysis:

Independent sample t test was conducted to examine the differences in neurocognitive scores. The mediation role of neighbouring WM were examined, with the interhemispheric involvement of the CC as the predictor variable. The PROCESS macro (Model-7) using SPSS v30 was employed to assess the mediation effects, controlling for covariates such as sex and age.

## Results

Independent sample t test identified significant group differences ( $p < .001$ ) in cognitive scores(DST and SST) between two groups (Fig 1). Callosal FA significantly predicted neighbouring WM FA ( $\beta = 0.9589$ ,  $p = 0.0057$ ), and mediator positively affected cognitive scores ( $\beta = 194.1473$ ,  $p = 0.0216$ ).

Neighbouring WM FA significantly mediated the relationship between callosal FA and cognitive scores in both groups, with an effect of 146.9608 (95% CI: 31.8687 to 289.6033) in Group-1 (TBI patients) and 107.7625 (95% CI: 36.3414 to 233.6978) in Group-2 (heathy controls). However, callosal FA had a significant negative direct effect on cognitive scores ( $\beta = -116.8463$ ,  $p = 0.0178$ ) in TBI patients (Table-2).

## Conclusion

This analysis underscores the complex interplay between interhemispheric involvement for information processing and cognitive performance, particularly in TBI patients. These findings are indicating that increased FA during acute and subacute periods of TBI maybe due to a compensatory mechanism and compaction of axonal neurofilament resulting from traumatic insult<sup>5,6</sup> . Prior research has also highlighted that the WM microstructure, as reflected by FA values, plays a key role in supporting cognitive processes by facilitating efficient neural communication<sup>7,8</sup>. However, in clinical populations, such as TBI patients, structural changes in WM may involve compensatory or maladaptive responses, complicating the expected benefits of higher FA<sup>9,10</sup>. This preliminary study highlights the importance of considering WM metrics in understanding cognitive outcomes in clinical populations and suggests potential avenues for interventions targeting WM health to improve cognitive function in various neuropathological conditions.

## Reference

- [1] Chung et al., 2024, *American Journal of Neuroradiology*, 45(6), 788-794..
- [2] Newcombe et al., 2011, *PLoS One*, 6(5), e19214.
- [3] Shenton et al., 2012, *Brain Imaging and Behavior*, 6, 137-192.
- [4] Tulsky et al., 2003, *Clinical interpretation of the WAIS-III and WMS-III* (pp. 93–139). Academic Press.
- [5] Croall et al., 2014, *Neurology*, 83(6), 494-501.
- [6] Bazarian et al., 2007, *Journal of Neurotrauma*, 24(9), 1447-1459.
- [7] Fields, 2008, *Trends in Neurosciences*, 31(7), 361-370.
- [8] Penke et al., 2010, *Journal of Neuroscience*, 30(22), 7569-7574.
- [9] Kinnunen et al., 2011, *Brain*, 134(2), 449-463.
- [10] Palacios et al., 2012, *Neurology*, 78(12), 852-860.

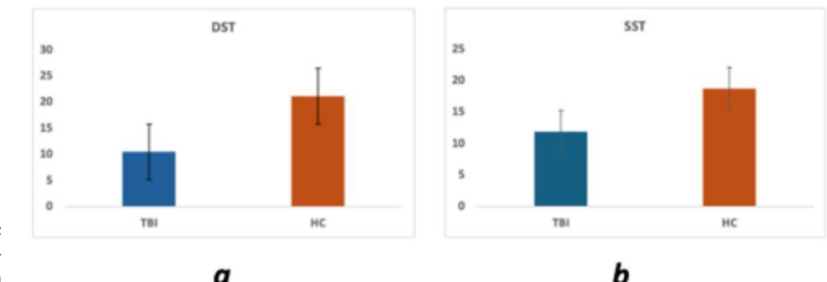


Figure 1 a and b bar graphs showing differences in neurocognitive scores(DST and SST) between TBI subjects and healthy controls. Independent sample t test revealed significant differences ( $p < .001$ )



# Ketamine and Electroconvulsive Therapy: Distinct Yet Partially Overlapping Mechanisms in Treatment of Depression

Ajay Sarawagi<sup>1,2</sup>

<sup>1</sup>CSIR-Centre for Cellular and Molecular Biology, Hyderabad, India, <sup>2</sup>Academy of Scientific and Innovative Research (AcSIR), Ghaziabad-2012002, India

## Introduction

Major depressive disorder is a debilitating mental health condition, characterized by persistent low mood, anhedonia, sleep disturbances, and suicidal ideation. Traditional antidepressants often suffer from low efficacy, delayed onset of results, and ineffectiveness in approximately 40% of depressed subjects. Ketamine and electroconvulsive therapy (ECT) are FDA-approved interventions for drug-resistant depression, offering rapid and highly effective therapeutic outcomes as compared to conventional antidepressants [1]. ECT involves the induction of a controlled seizure lasting a few seconds, followed by a post-ictal suppression phase characterized by reduced overall brain activity [2]. Ketamine, a non-competitive antagonist of N-methyl-D-aspartate (NMDA) receptors, induces anesthesia at higher doses [3], but exhibits rapid antidepressant effects at sub-anesthetic doses. However, the understanding of the impact of ECT and ketamine on the metabolic activity of excitatory, and inhibitory neurons and astrocytes is limited. Hence, the major aim of the study was to assess the impact of acute ECT and ketamine on neural circuitry.

## Methods

Two-month-old C57BL6 male mice in the ECT group received a single electroconvulsive shock under isoflurane anesthesia via corneal electrodes, while the sham group mice were anesthetized but had no electric shock [4]. The Ketamine group of mice was injected with (R,S)-ketamine (25 mg/kg, ip), while controls were injected with a normal saline solution. The impact of ECT and Ketamine administration on the metabolic activity of neurons and astrocytes was evaluated at different time points by conducting ex-vivo <sup>1</sup>H-[<sup>13</sup>C]-NMR spectroscopy in conjunction with intravenous [<sup>1,6-13C2</sup>]glucose or [<sup>2-13C</sup>]acetate infusion, respectively (Fig. 1) [5]. The transcriptomics and quantitative phosphoproteomics were conducted to assess the effects of these interventions at the molecular level in the mouse brain.

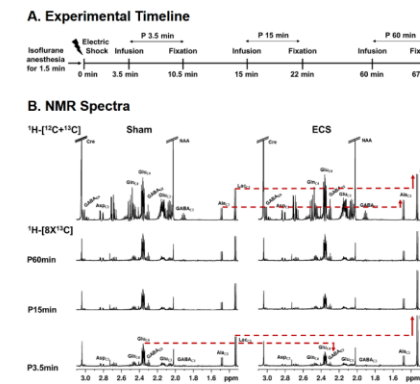


**Fig 1A.** Experimental timeline depicting mice were infused with [<sup>1,6-13C2</sup>]glucose after 3.5, 15 and 60 min of ECS, respectively. Brain Metabolism was arrested 7 min post infusion. B. Representative <sup>1</sup>H-[<sup>13</sup>C]-NMR spectra depicting total concentration of neurometabolites in top most panel, and <sup>13</sup>C labeled neurometabolites in the lower panel at different time points in Sham and ECS mice.

## Results

Sub-anesthetic ketamine administration led to a transient enhancement in cerebral glucose oxidation within 15 min of injection, and normalized within 25 min. A comparable surge in neurometabolic activity was observed during ECT-induced seizure (+64.3±15.3 %, p=0.005), while the astroglial activity remained unchanged. However, a drastic reduction in the oxidative metabolism in neurons (-43.3±3.0 %, p=0.0004) and astrocytes (-37.0±0.8 %, p=0.0003) occurred immediately after seizure termination, with a pronounced increase in non-oxidative glucose consumption (+112.8±9.8 %, p=0.0001). Interestingly, the neuronal and astroglial activity normalized within one hour after ECT. Phosphoproteomic analysis showed a very distinct set of differentially expressed phosphoproteins involved during ECT-induced seizure and after one hour of electroconvulsive shock. The transcriptomic analysis indicated a marginal overlap in the biological processes involved in the molecular mechanisms of acute ECT and ketamine interventions.

## Discussion

ECT and ketamine treatments are known to enhance synaptic plasticity,

neurogenesis, and synaptogenesis and reduce neuroinflammation [6, 7]. Ketamine-induced surge in the neurometabolic activity is in line with a previous study in rats highlighting a transient surge in glutamate release within PFC, which is responsible for the rapid antidepressant effects [8]. ECT was also found to enhance the metabolic activity of glutamatergic and GABAergic neurons during the seizure phase similar to ketamine's induced glutamate surge. However, the neurometabolic effects of ECT differ from ketamine in the post-ictal period, where neuronal and astroglial metabolic activity gets drastically reduced. Moreover, ECT seems to shift the brain ATP generation machinery to anaerobic glucose metabolism during the seizure and post-ictal suppression phase, reflecting an adaptive response of the brain to meet high energy demands or oxidative stress, potentially contributing to ECT's therapeutic effects. Interestingly, the effects of ketamine and ECT were normalized to their respective control, within 25 and 60 minutes of administration, respectively. The transcriptomic analysis further shows the distinction in the neuromodulatory effects of ECT and ketamine interventions in mouse brains.

## Conclusion

The assessment of metabolic activity of glutamatergic, GABAergic neurons, and astrocytes during acute ketamine administration, ECS-induced seizures, and post-ictal suppression phase provides valuable information about the potential mechanisms of ECT and ketamine and could inform the development of optimized treatment strategies for depression and minimize the immediate side effects associated with these interventions.

## Acknowledgment

CSIR-Health Care Theme FBR/MLP0150; DBT-Research fellowship DBT/2019/CCMB/1230

## Reference

- [1] Rhee et al, JAMA Psychiatry. 2022;79(12):1162; [2] Deng et al, Neuropsychopharmacol. 2024;49(1):150-162; [3] Moghaddam et al, J Neurosci. 1997;17(8):2921-2927; [4] Sarawagi et al, Neuroglia. 2024;5(3):306-322; [5] Mishra et al, J Neurochem. 2018;146(6):722-734; [6] Abe et al, J Neurochem. 2024; jnc.16054; [7] Krystal et al, Proc Natl Acad Sci USA. 2023;120(49):e2305772120; [8] Chowdhury et al, Mol Psychiatry. 2017;22(1):120-126.

# Knee Cartilage Evolution is Linked to Intra-Limb Baseline Hip Cartilage: A Longitudinal Compositional MRI Study

Rupsa Bhattacharjee, PhD<sup>1</sup>, Yurui Qian, PhD<sup>1</sup>, Misung Han, PhD<sup>1</sup>, Fei Jiang, PhD<sup>2</sup>, Richard B. Souza, PT, PhD<sup>1,3</sup>, Sharmila Majumdar, PhD<sup>1</sup>

1 Department of Radiology and Biomedical Imaging, University of California San Francisco, San Francisco, CA 2 Department of Epidemiology and Biostatistics, University of California San Francisco, San Francisco, CA, 3 Department of Physical Therapy and Rehabilitation Science, University of California San Francisco, San Francisco, CA

## Introduction

The polyarticular nature of osteoarthritis (OA) tends to manifest in more than one joint[1]. This is especially important in the hip and the knee, as these joints are connected by movement, bodily load bearing, and balancing. Almost 45% of lone hip OA patients have been shown to develop subsequent knee OA [2]. Therefore, from a therapeutic intervention perspective, it is crucial to identify the early effects of hip OA, specifically hip cartilage degradation, on the normal-appearing knee cartilage. Increased T1p values depict early microscopic degradations of cartilage suffering proteoglycan loss [3][4]. Recently, evidence of cross-sectional associations between hip femoral cartilage T1p and contralateral knee patellofemoral cartilage T1p was demonstrated in a cohort of none-to-moderate hip OA[5]. We hypothesize longitudinal changes in contralateral knee patellar cartilage proteoglycan composition might be associated with baseline hip femoral cartilage compositional behavior.

## Methods

Sixteen subjects with none-to-moderate radiographic hip OA (age:53.25±11.46 years, eight females, BMI: 23.93 ± 3.84 kg/m<sup>2</sup>) provided written consents for the IRB-approved ongoing prospective multi-joint study and underwent two MRI scanning sessions at a gap of one year. Both the MRI scans (bilateral hip and knee imaging; 32 hips and 32 knees) were performed (Table-1) in a 3.0T GE-Signa Premier scanner (GE Healthcare, Waukesha, WI). Exclusion in this study was defined as either of the hips having advanced stages of OA (Kellgren-Lawrence-score = 4) at the baseline visit. The algorithms (Figure-1) for mapping multi-echo images into T1p relaxation times, for the bilateral hip[6] and bilateral knee[7] have been previously validated. The fitted hip T1p maps underwent an atlas-based algorithmic approach[6][8]. The analysis yielded T1p of six hip femoral subregional (R2-R7) cartilages[8][6]. The subregions can be classified as R2 as posterior, R3 as posterior-superior, R4 as superior, R5 as anterior-superior, R6 as anterior, and R7 as anterior-inferior cartilage regions[9]. R1 and R8 are regions with no viable hip cartilage to assess. In the case of the knees, a deep learning (DL)-based approach was employed for automatically segmenting knee cartilages into patellar subregions, and extracting T1p values [5]. All image analyses were performed using an in-house program developed in MATLAB version R2021a (MathWorks, Natick, MA). Comparisons between baseline and follow-up knee patellar T1p values of each study participant were performed with repeated measures analysis-of-variance (ANOVA). Relative change in patellar T1p values ( $\Delta T1p$ -Patellar) across visits was determined by [(follow-up - baseline) / baseline]. Correlation between relative change in knee patellar cartilage subregion ( $\Delta T1p$ -Patellar) and baseline T1p values of intra-limb hip femoral subregional (R2-R7) cartilages were performed with a linear mixed effects model, which controls for age, gender, BMI, and properly corrects for multiple measurements from the same subject. 95% Confidence Intervals and p-values were computed using a Wald test. All statistical analyses have been performed using RStudio (R Core Team, 2022, version 12.0+353). The effect is considered significant if  $p \leq 0.05$ .

## Discussion

We observed a significant longitudinal increase in mean cartilage patellar T1p values from baseline scan to one-year follow-up (Figure-2). After adjusting for age, gender, BMI, and within-subject clustering,  $\Delta T1p$ -Patellar was significantly negatively associated with baseline T1p values of intra-limb posterior-superior hip femoral cartilage R3 (Table-2). The strengths of associations were noted in terms of beta estimates, 95% CIs, and p-values. In a previous study reporting baseline hip-knee T1p characteristics of this cohort, R3 (load-bearing posterior-superior subregions of hip femoral cartilage) was positively associated [5] with baseline knee patellar T1p. Balancing the bodily mechanical load in sync with compositional variations in load-bearing hip cartilage can lead to varied loading of the contralateral knee joint during movement. It might lead to altered gait patterns [15] and provide compensatory relief to the intra-limb patellar cartilage. This potential mechanism explains the negative associations between T1p values of hip femoral R3 vs. longitudinal changes ( $\Delta T1p$ ) in knee patellar subregions. The causality of the relationship cannot be directly inferred from the given data. Future mediation analyses with existing loading data in the cohort are solicited (including a higher number of subjects) to probe the extent to which these associations are systemically linked vs. mechanically propagated.

## Conclusion

In this study, we present one of the first exploratory results of the compositional correlations between longitudinal knee patellar cartilage vs. baseline intra-limb hip femoral cartilage. Relative changes in knee patellar T1p values were negatively associated with baseline T1p values of intra-limb hip femoral load-bearing posterior-superior cartilage subregion. These findings will eventually lead to a better understanding of the mechanical propagation of OA between these two joints and might be useful for the prevention of polyarticular OA development.

## Reference

- [1] "A treatise on rheumatic gout, or chronic rheumatic arthritis of all the joints / by Robert Adams.,," Wellcome Collection. Accessed: Mar. 27, 2023. [Online]. Available: <https://wellcomecollection.org/works/zdkdkp2s>
- [2] P. Dieppe, J. Cushnaghan, M. Tucker, S. Browning, and L. Shepstone, "The Bristol 'OA500' study': progression and impact of the disease after 8 years," *Osteoarthritis Cartilage*, vol. 8, no. 2, pp. 63–68, Mar. 2000, doi: 10.1053/joca.1999.0272.
- [3] M. C. Gallo et al., "T1p and T2 relaxation times are associated with progression of hip osteoarthritis," *Osteoarthritis Cartilage*, vol. 24, no. 8, pp. 1399–1407, Aug. 2016, doi: 10.1016/j.joca.2016.03.005.
- [4] A. J. Wheaton, G. R. Dodge, A. Borthakur, J. B. Kneeland, H. R. Schumacher, and R. Reddy, "Detection of changes in articular cartilage proteoglycan by T1rho) magnetic resonance imaging," *J. Orthop. Res. Off. Publ. Orthop. Res. Soc.*, vol. 23, no. 1, pp. 102–108, Jan. 2005, doi: 10.1016/j.orthres.2004.06.015.
- [5] R. Bhattacharjee et al., "Effects of T Characteristics of Load-Bearing Hip Cartilage on Bilateral Knee Patellar Cartilage Subregions: Subjects With None to Moderate Radiographic Hip Osteoarthritis," *J. Magn. Reson. Imaging*, vol. 60, no. 1, pp. 186–202, 2024, doi: 10.1002/jmri.29009.
- [6] M. C. Gallo et al., "T1p and T2 Relaxation Times are Associated with Progression of Hip Osteoarthritis," *Osteoarthr. Cartil. OARS Osteoarthr. Res. Soc.*, vol. 24, no. 8, pp. 1399–1407, Aug. 2016, doi: 10.1016/j.joca.2016.03.005.
- [7] V. Pedoia et al., "MRI and biomechanics multidimensional data analysis reveals R2-R1p as an early predictor of cartilage lesion progression in knee osteoarthritis," *J. Magn. Reson. Imaging*, vol. 47, no. 1, pp. 78–90, Jan. 2018, doi: 10.1002/jmri.25750.
- [8] K. E. Roach, R. B. Souza, S. Majumdar, and V. Pedoia, "Local Patterns in 2-Year T 1 p and T 2 Changes of

Hip Cartilage Are Related to Sex and Functional Data: A Prospective Evaluation on Hip Osteoarthritis Participants," *J. Magn. Reson. Imaging*, vol. 57, no. 4, pp. 1042–1053, Apr. 2023, doi: 10.1002/jmri.28347.

[9] K. Subburaj et al., "Regional variations in MR relaxation of hip joint cartilage in subjects with and without femoralacetabular impingement," *Magn. Reson. Imaging*, vol. 31, no. 7, pp. 1129–1136, Sep. 2013, doi: 10.1016/j.mri.2013.01.009.

[10] S. van Drongelen, S. Braun, F. Stief, and A. Meurer, "Comparison of Gait Symmetry and Joint Moments in Unilateral and Bilateral Hip Osteoarthritis Patients and Healthy Controls," *Front. Bioeng. Biotechnol.*, vol. 9, Nov. 2021, doi: 10.3389/fbioe.2021.756460.

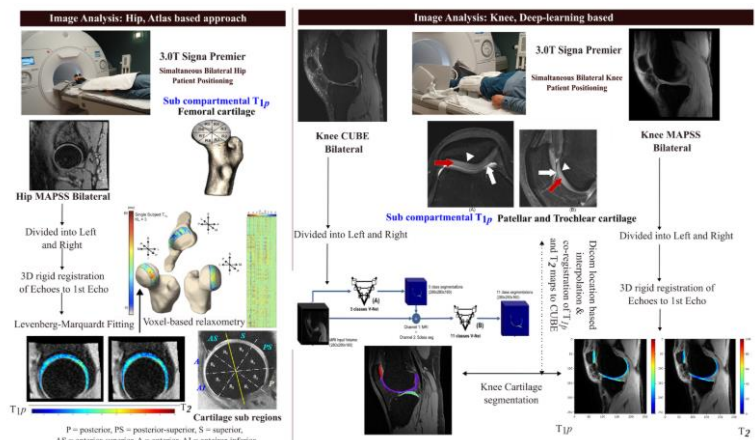


Figure 1: Schema of image processing methodology, segmentation, analysis, and evaluation

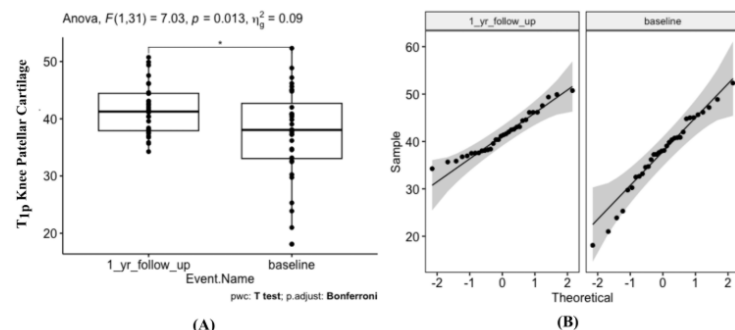


Figure 2: (A) Comparison of mean T<sub>1p</sub> values at baseline and 1-year follow-up, for bilateral knee patellar cartilages. Post-hoc analyses with a Bonferroni adjustment revealed that all the pairwise differences, between time points, were statistically significantly different ( $p \leq 0.05$ ). (B) Normality assumptions were met.

# Leveraging Deep Learning with Multimodal Data for Timely Interventions in Alzheimer's Disease

Dr. Venkateswarlu Gonuguntla

"Symbiosis Centre for Medical Image Analysis, Symbiosis International (Deemed University), Pune 412115, India

## Introduction

Early detection of Alzheimer's Disease (AD) is crucial for effective intervention but remains challenging despite advancements in biomarker identification. Structural neuroimaging via magnetic resonance imaging (MRI) provides anatomical insights, while magnetic resonance spectroscopy (MRS) allows noninvasive biochemical information, detecting early metabolic alterations even when structural MRI appears normal. Additionally, cerebrospinal fluid (CSF) biomarkers and electrophysiological measures from electroencephalography (EEG) contribute valuable physiological information. However, integrating these heterogeneous data sources for precise and timely intervention requires advanced computational techniques.

## Methods

This study leverages deep learning to integrate multimodal data for improved AD detection and intervention strategies. As illustrated in the blue-highlighted figure, which focuses on identifying key structural alterations in disease progression, we analyzed T1-weighted MRI scans from 200 subjects within the Alzheimer's Disease Neuroimaging Initiative (ADNI), categorized as cognitively normal (n=50), mild cognitive impairment (MCI, n=50), progressive MCI (PMCI, n=50), and AD (n=50). FreeSurfer software was used for image processing, extracting cortical thickness and volumetric features, which were statistically analyzed via a General Linear Model with Cluster Correction.

## Results

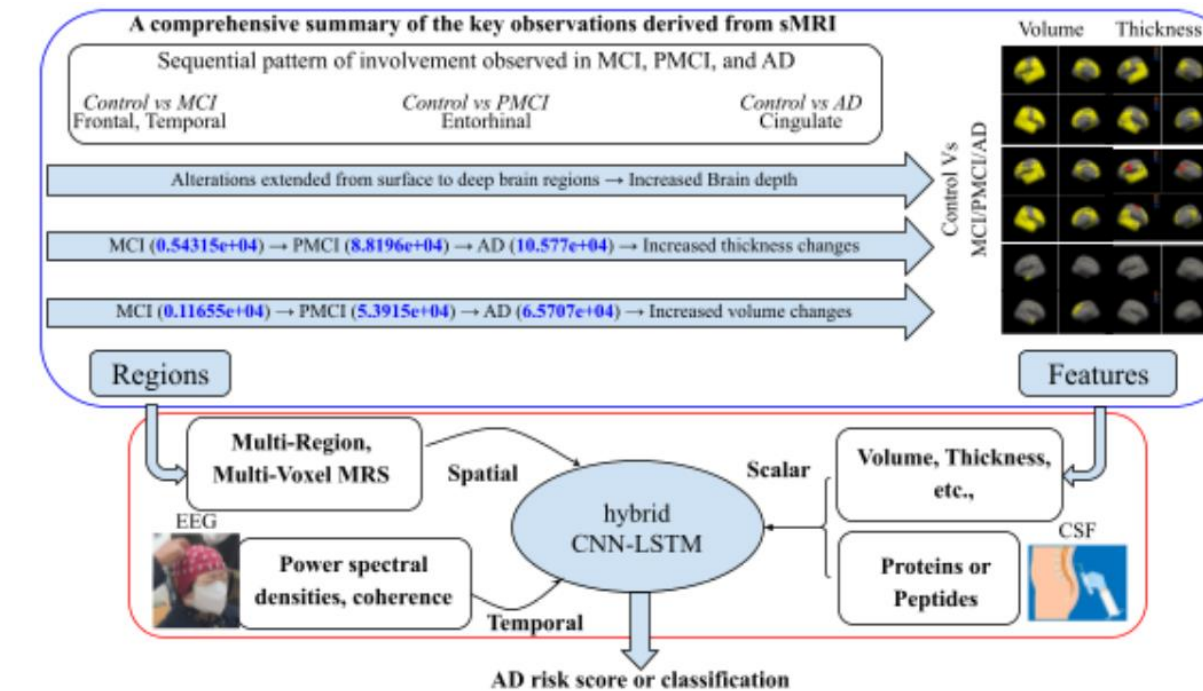
Findings revealed significant structural alterations in cortical thickness and volume, progressing from surface to deep brain regions, predominantly in the right hemisphere. Initial changes were observed in the middle and inferior temporal and superior frontal regions, with later-stage involvement of the isthmus cingulate and entorhinal cortex. Volume reductions extended from inferior temporal regions to the posterior cingulate, medial orbitofrontal, precuneus, precentral, and entorhinal regions. These results highlight the potential of structural MRI as a reliable biomarker for AD progression and mapping neurodegeneration. Additionally, it plays a crucial role in accurately computing the AD risk score and classification.

## Conclusion

Future research, as illustrated in the red-highlighted figure, will integrate MRS-derived metabolite information from structural MRI-informed regions, whole-brain EEG data, and CSF biomarkers to develop a robust deep learning framework. A hybrid Convolutional Neural Network-Long Short-Term Memory (CNN-LSTM) model will be explored for multimodal fusion, incorporating clinical history for enhanced prediction accuracy. This approach aims to refine early diagnostic strategies and improve personalized interventions for AD patients.

## Acknowledgements

We acknowledge the Department of Science and Technology, Government of India, for the technical and financial support provided under the DST-PURSE Program, Grant No. SR/PURSE/2023/181 (G) - TPN - 88132."



# MRI-Based Radiomics and ML Approach to Classify Various Renal Cell Carcinoma subtypes

**Siddhant Gupta<sup>1</sup>, Sanjoy Sureka<sup>2</sup>, Arpan Yadav, B. V. Rathish Kumar, Sudhir Kumar Pathak, Ranjeet Ranjan Jha, Anit Parihar, Saurabh Kumar, Manoj Kumar Deo, Apul Goel, Manoj Kumar, Durgesh Kumar Dwivedi<sup>1</sup>**

<sup>1</sup>Department of Radiodiagnosis, King George's Medical University, Lucknow, India, <sup>2</sup>Deaprtmetn of Urology, Sanjay Gandhi Post Graduate Institute of Medical Science, Lucknow, India ,Department of Mathematics and Statistics, Indian Institute of Technology, Kanpur, India, Learning Research and Development Center,University of Pittsburgh, Pittsburgh, PA, United States, Department of Mathematics, Indian Institute of Technology, Patna, India, Department of Neurosurgery, King George's Medical University, Lucknow, India.

## Introduction

Renal Cell Carcinoma (RCC) is the most common form of kidney cancer, comprising distinct subtypes such as Clear Cell RCC (ccRCC), Papillary RCC (pRCC), and Chromophobe RCC (chRCC), each exhibiting unique biological behavior and prognosis. These subtypes differ in biological behavior and prognosis [1]. Accurate classification of RCC subtypes is crucial for personalized treatment and improved patient outcomes.

## Methods

MRI data of RCC subtypes total of 66 patients obtained from The Cancer Imaging Archive TCIA were analyzed, focusing on tumor segmentation from the center slices of T2-weighted images using 3D Slicer. Radiomic features, including First Order Statistics, Shape-Based features, GLCM, GLRLM, GLSJM, and NGTDM, were extracted using Pyradiomics and saved in CSV format. The data was split into 80:20 training and testing subsets. 120 features were extracted per patient extracted PCA was applied to reduce over 100 features to the top 10 for subtype classification. Four machine learning models (Logistic Regression, SVM, Random Forest, and Gradient Boosting) were evaluated using Accuracy, F1-Score, ROC-AUC, and confusion matrices.

## Results

Among the 120 radiomics features extracted using Pyradiomics, PCA reduced 100+ radiomic features to 10 key predictors, including original\_fristorder\_Maximum,original\_glcg\_JointEnergy, and original\_glszm\_LargeAreaEmphasis. Among the machine learning models evaluated, Random Forest achieved the highest performance with 88.24% accuracy and an ROC-AUC of 0.88 (**Table 1, Figure 3**), outperforming Gradient Boosting, Logistic Regression, and Support Vector Machine (SVM) in distinguishing ccRCC from non-ccRCC. Key bio were original\_fristorder\_Mean,original\_glcg\_SumAverage, and original\_ngtmd\_Coarseness.

## Discussion

We previously demonstrated the use of MRI based radiomic features to predict high-grade histology (aggressive tumors) and tumor necrosis in ccRCC [2]. This study demonstrates the feasibility of classifying RCC subtypes using T2-weighted MRI radiomic features. Pyradiomics and machine learning identified key imaging biomarkers, while PCA reduced complexity and highlighted

predictive features. Although the results align with existing literature on GLCM and GLSJM, limited data for rarer subtypes remains a challenge. Future work will focus on expanding datasets and refining algorithms.

## Conclusion

Our study demonstrated the feasibility of using MRI-based radiomics and machine learning for non-invasive RCC subtype classification. Identified biomarkers hold promise for advancing diagnostic precision. Further research will enhance model accuracy and broaden clinical applicability.

## Acknowledgements

Dr. D.K. Dwivedi and Prof. B.V. Rathish Kumar express their profound gratitude to the Indian Council of Medical Research (ICMR), New Delhi for their generous funding (Grant No. EM/Dev/IG/27/0337/2023). Furthermore, Prof. B.V. Rathish Kumar (IITK, India) and Dr. S.K. Pathak (Pitt, USA) extend their heartfelt appreciation to SPARC for their funding support (Grant No. SPARC/2019-2020/P1622/SL). Additionally, Dr. D.K. Dwivedi sincerely acknowledges the financial support provided by UPCST (Grant No. CST/D-1381). Dr. D.K. Dwivedi also conveys sincere thanks to the Science and Engineering Research Board (now ANRF), New Delhi for their valuable funding support under Grant No. SUR/2022/001841)

## Reference

- [1] V. F. Muglia, A Prando. Radiol Bras, 48 (2015), 166. <https://doi.org/10.1590/0100-3984.2013.192>.
- [2] Dwivedi DK, Xi Y, Kapur P, Madhuranthakam AJ, Lewis MA, Udayakumar D, Rasmussen R, Yuan Q, Bagrodia A, Margulis V, Fulkerson M, Brugarolas J, Cadeddu JA, Pedrosa I, Proc. 23rd Annu. Meet. ISMRM (2021) 12-21.e1

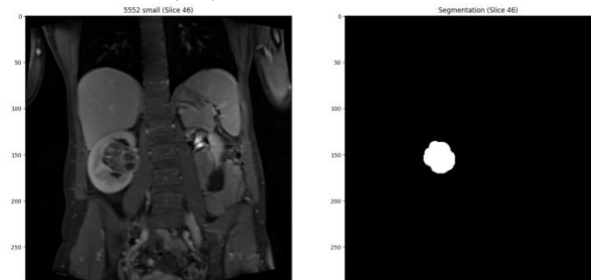


**Fig. 1** MRI Slice with Segmentation Mask: A center slice from a T2-weighted MRI of a renal tumor. The raw MRI image (left) and its segmentation mask (right) highlight the tumor region, used to extract radiomics features for RCC subtype classification

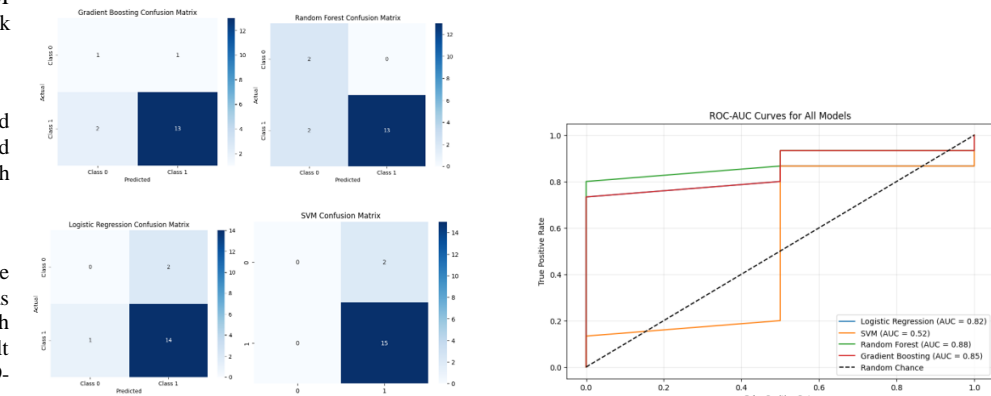


**Fig. 2** Confusion Matrices of Classifiers: Confusion matrices for Logistic Regression, SVM, Random Forest, and Gradient Boosting classifiers. Diagonal values indicate correct classifications, while off-diagonal values represent misclassifications, highlighting the performance of each model.

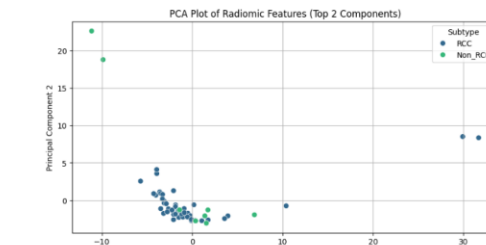


**Fig. 3** ROC-AUC curves comparing classifier's performance: Random Forest (AUC = 0.88) and Gradient Boosting (AUC = 0.85) show the highest AUC values, indicating superior performance over Logistic Regression (AUC = 0.82) and SVM (AUC = 0.52).

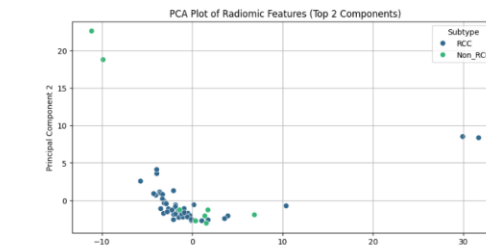


**Fig. 4** The PCA (Principal Component Analysis) plot visualizes the distribution of extracted radiomic features after dimensionality reduction to two principal components. It segregates data points based on tumor subtypes (e.g., RCC vs. Non-RCC). The clustering of points indicates patterns in the feature space that machine learning models exploit for classification. The variance explained by the components supports the effectiveness of feature selection in distinguishing between the two subtypes.

## MRTC: An extensible platform for real-time MR therapy applications.

Shashank Hegde<sup>1</sup>, Mahesh Kammar<sup>1</sup>, Prasanna Kumar<sup>1</sup>, Sunita Behera<sup>1</sup>, Ranjith P<sup>1</sup>, Manivannan Jayapalan<sup>1</sup>

<sup>1</sup> Philips Healthcare, PIC, Bangalore, India.

### Introduction

MRI guided interventional procedures are becoming increasingly common across many cardiology, neurology and oncology applications. In all of these applications, the external treatment device interacts with the MR system during the treatment. Although many treatment devices have been integrated with the MRI system through dedicated interfaces over the past decades, their spread has been limited due to cumbersome setup procedures and a lack of standardization. We report here an extensible platform for external medical devices to connect to the MR scanner. Using this interface between a Philips MR and Insightec High Intensity Focused Ultrasound (HIFU) system, an MR guided Focused Ultrasound (MRgFUS) treatment is performed.

### Methods

The Philips MR system interacts with the external HIFU system through a dedicated MR Therapy Control (MRTC) interface for end-to-end treatment workflow (Fig.1a). MRTC uses Google Protobufs to serialize messages that are exchanged via IPC TCP/IP. There are messages to exchange system configuration, read ExamCards, create or select an exam, select a scan protocol, start, pause, resume and stop a scan, receive images and change the orientation during scanning. Inherent safety checks are built into the interface via a token system to prevent unauthorized use. 1D MR tracking techniques are developed for the localization of e.g. a HIFU transducer or intravascular active catheter. Multi-Echo gradient-echo MR sequences are optimized for temperature monitoring. A dedicated Insightec head-coil with an integrated tracking coil and MR imaging coils is used to perform the MRgFUS treatment (Fig. 1b).

### Results

During the MRgFUS treatment, images are transferred in real-time via the MRTC interface. Based on the multi-echo phase images, temperature is continually monitored during the treatment. Volunteer and patient scans with the entire system setup has been demonstrated (Fig. 1c). End-to-end workflow including planning, tracking and precise targeting of thermal energy has been performed. Following the volunteer trials, the system has been deployed in a multi-center clinical trial involving patients.

### Discussion

The MRTC interface permits multiple interactions between the MR and external systems allowing for an end-to-end clinical workflow that can be controlled from the external interface. The interface is easily extensible, allowing multiple other external systems like MR-electrophysiology interventions to utilize the same platform. For MRgFUS, using the MRTC platform, interaction between the MR system and external HIFU system was established. The system has recently obtained FDA approval and commercial deployment is in progress [1].

### Conclusion

The MRTC interface has been successfully implemented in a wide range of therapeutic applications and is ready to support new treatments. Further standardization of MR interfaces over vendors is desirable.

### Reference

[1] <https://insightec.com/news/fda-approval-exablate-neuro/>

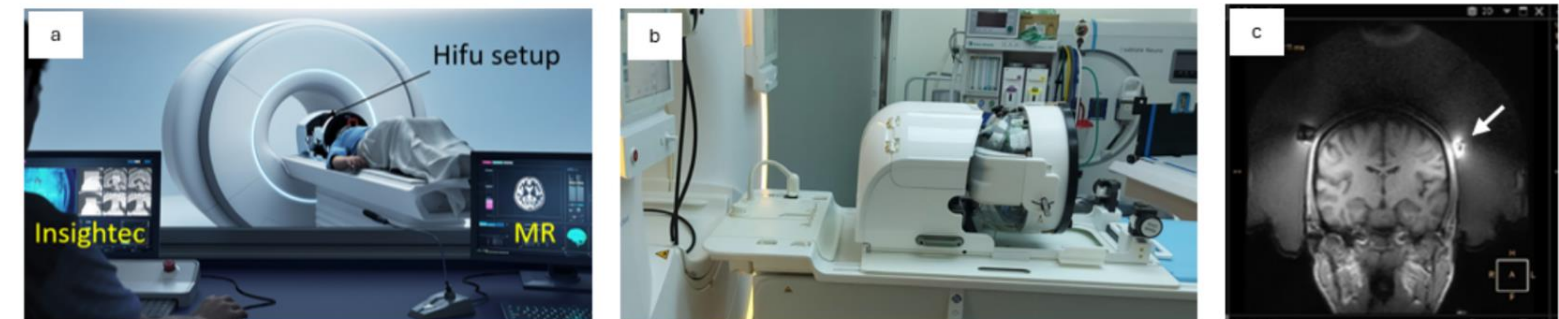


**Fig. 1** (a) MR guided HIFU setup with the Insightec and Philips systems connected via the MRTC interface. (b) Insightec helmet coil with the integrated tracking and imaging coils. (c) Volunteer scan showing the tracking coil (arrow) and surrounding water bath for temperature control

# Multi-class analysis of Dementia based on geometric variations in amygdala and hypothalamus regions

**Monisha A, Shrimathi M, Kuruvavarshni R S K, Alagumalairajan A R and Dr. Kavitha G**

Department of Biomedical Engineering, College of Engineering Guindy, Anna University

## Introduction

Dementia is a neurodegenerative disorder characterized by progressive cognitive decline, which manifests in various stages, including Early Mild Cognitive Impairment (EMCI), Mild Cognitive Impairment (MCI), Late Mild Cognitive Impairment (LMCI), and Alzheimer's Disease (AD). This study aims to analyze the substages of dementia by examining structural variations in the brain, with a focus on the decline in the amygdala [1] and hypothalamus [2]. Structural MR images were sourced from the ADNI database. The dataset used in this study comprises of 185 AD, 202 EMCI, 200 MCI, 180 LMCI, and 205 Control Normal (CN) subjects. To preprocess and segment the amygdala (Fig.1a) and hypothalamus (Fig.1b), FreeSurfer [3] software was employed. The segmentation process involved multiple preprocessing steps, including motion correction, intensity normalization, and non-uniform intensity correction, ensuring that the MRI scans were free from artifacts and signal inconsistencies. Skull stripping was performed to remove non-brain tissues, followed by an automated parcellation process to identify and label subcortical structures. FreeSurfer utilizes an atlas-based approach with probabilistic models refined by manual annotations, ensuring accurate segmentation of the amygdala and hypothalamus. The quality of segmentation was carefully inspected, and manual corrections were applied to improve precision. Geometric features [4] such as volume, surface area, extent, equivalent diameter, and solidity were

extracted to quantify structural variations in the amygdala and hypothalamus across different dementia stages. A one-way ANOVA revealed significant differences in structural attributes of the amygdala and hypothalamus across dementia stages. In the amygdala, equivalent diameter and volume were the most significant features, while in the hypothalamus, equivalent diameter emerged as the strongest marker, followed by volume and surface area. These findings highlight equivalent diameter and volume as key biomarkers for studying the progression of dementia-like disorders.

## Reference

- [1] L. Al-Ani, A. Tao, J. Dyke, G. Chiang, and M. Ishii, "Amygdala atrophy as an early manifestation of Alzheimer's Disease (S39.005)", *Neurology*, vol. 100, no. 17, April 2023.
- [2] A., Myslinski, Z., Pan, Y., Iadecola, C., Dyke, J., Chiang, G., & Ishii, M., "Hypothalamic atrophy in Alzheimer's Disease (1819)", *Neurology*, vol. 96, no. 15, April 2021.
- [3] B. Fischl, "FreeSurfer", *NeuroImage*, vol. 62, no. 2, pp. 774–781, January 2012.
- [4] A. Ali, J. F. A. Ronickom, and R. Swaminathan, "Assessment of structural variations in Fornix of MCI and AD using MR images and geometrical features", *Journal of Medical and Biological Engineering*, vol. 44, no. 4, pp. 548–555, July 2024.

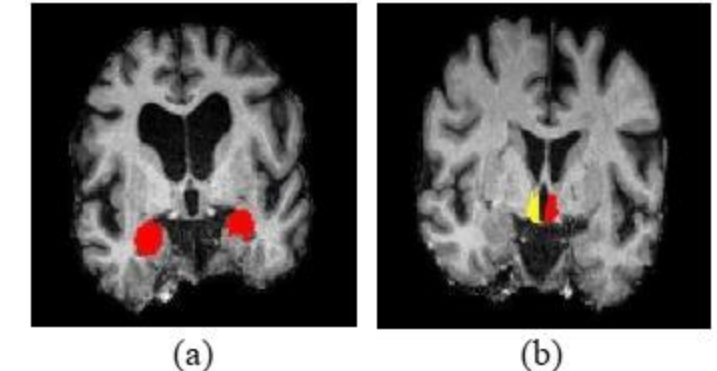


**Fig.1 – (a)** Segmented amygdala and **(b)** hypothalamus regions, superimposed on the pre-processed structural MR image

FEATURES	AD Mean±SD	LMCI Mean±SD	MCI Mean±SD	EMCI Mean±SD	CN Mean±SD	ANOVA p-value
VOLUME	0.382 ± 0.168	0.455 ± 0.18	0.517 ± 0.164	0.549 ± 0.159	0.56 ± 0.145	4.66e-32
SURFACE AREA	0.421 ± 0.152	0.472 ± 0.153	0.507 ± 0.141	0.542 ± 0.132	0.544 ± 0.127	1.39e-21
SOLIDITY	0.582 ± 0.197	0.626 ± 0.194	0.704 ± 0.137	0.679 ± 0.138	0.727 ± 0.099	1.25e-23
EXTENT	0.4 ± 0.170	0.425 ± 0.158	0.481 ± 0.129	0.482 ± 0.135	0.508 ± 0.109	1.11e-16
EQUIVALENT DIAMETER	0.494 ± 0.173	0.566 ± 0.174	0.626 ± 0.155	0.656 ± 0.146	0.668 ± 0.127	1.34e-33

**Table.1**-Characterization and statistical significance of the amygdala region features

considered in the study across five classes

# Multiparametric MRI Based Radiomics Features Extraction for Prediction of Brain Invasion in Meningiomas

Sanskriti Srivastava<sup>1</sup>, Rakesh Kumar Gupta<sup>2</sup>, Anup Singh<sup>1,3</sup>

<sup>1</sup>Centre for Biomedical Engineering, Indian Institute of Technology Delhi, India, <sup>2</sup>Fortis Memorial Research Institute, Gurugram, India, <sup>3</sup>Department of Biomedical Engineering, All India Institute of Medical Sciences, Delhi, India

## Introduction

Meningiomas are the most common brain tumors in adults, which account for 37% [1] of all intracranial brain tumors. According to the WHO 2021 classification of the central nervous system of brain tumors, brain invasion is a stand-alone criterion for atypical (grade 2) meningiomas. [2] The standard diagnosis of brain invasion is a histopathological examination; the histopathological definition of brain invasion is infiltration of meningiomas tumor cells in the brain parenchyma without separating the connective tissue layer.[3] This method requires extensive brain tissue sampling at the tumor-brain interface during surgical resection. In some studies, it has been shown that MRI-based imaging features correlate with brain invasion. These features are tumor location, tumor shape, peritumoral edema, cerebrospinal fluid (CSF) cleft, distribution of arachnoid layers, etc. [4],[5] Radiomic analysis is a reasonable image-processing tool that helps quantify high-dimensional tumor features that cannot be seen from necked eyes, such as texture, small intensity change, and the edge between the tumor-brain interface, which is essential for predicting brain invasion. Also, it is a non-invasive method for quantifying tumor heterogeneity. In this study, we proposed a machine learning-based model for predicting brain invasion in meningiomas using MR images (T1CE and FLAIR) and radiomic features.

## Methods

In this retrospective study, we collected preoperative T1CE and FLAIR MR sequences from the online repository of The Cancer Imaging Archive and a local hospital. 65 patients with histopathological confirmed meningiomas, 32 with brain invasion, and 33 without brain invasion. The proposed pipeline is shown in Figure 1. The preprocessing involves 3D registration of T1CE and FLAIR using the Python library SimpleITK, followed by manual segmentation of tumor core from T1CE and peritumoral edema from FLAIR. The ground truth segmentation is performed on an open-source software 3D slicer, and the ground truth is further varied by experienced radiologists. From the segmented mask, we extracted 214 radiomic features from the Python library pyradiomics. Next, feature selection is performed by finding the importance of features by random forest; we selected 41 features for model training. Top 5 features are shown in Figure 2. These features are fed to machine learning classification models (XGBoost Classifier and Random Forest classifier) to predict meningioma brain invasion. The model's performance was evaluated using various metrics such as accuracy, F1 score, recall, and precision.

## Results

Overall, the XGBoost classifier achieves the highest accuracy, with 85% on multicentric test data. The performance parameters of the models are shown in Table 1. The computed accuracies for the XGBoost and random forest classifiers are 0.85 and 0.80; computed F1 scores are 0.85 and 0.80, respectively; computed recalls are 0.82 and 0.81, respectively; computed precisions are 0.86 and 0.81, respectively.

## Discussion

In this study, we extracted radiomic features of the tumor core and peritumoral edema to predict brain invasion in meningiomas using a machine-learning classifier model. The preoperative prediction of brain invasion will help in surgical planning and adjuvant therapy. Hence, this approach is a non-invasive and rapid method for predicting brain invasion in meningiomas without histopathological examination. Also, the model performance is tested on multicentric data. However, further studies should be carried out to validate the results on large datasets from different hospitals and evaluate the generalizability of the proposed approach.

## Conclusion

Brain invasion can be predicted using radiomic features extracted from the tumor core and peritumoral edema, which is a simple and feasible approach to predict brain invasion without histopathological examination.

Model	Accuracy	Recall	F1-Score	Precision
XGBoost classifier	0.85	0.82	0.85	0.86
Random forest	0.80	0.81	0.80	0.81

Table 1: Performance parameters of classification models for prediction of brain invasion in meningiomas.

## Reference

- [1] Y. W. Park et al., Eur Radiol, doi: 10.1007/s00330-018-5830-3.
- [2] M. L. P. Nasrallah et al., Springer. doi: 10.1007/s11060-022-04228-9.
- [3] A. Perry et al., Free Neuropathol, doi: 10.17879/freeneuropathology-2021-3276.
- [4] K. J. Lee et al., Surg Neurol, doi: 10.1016/j.surneu.2007.03.027.
- [5] K. J. Lee et al., Surg Neurol, doi: 10.1016/j.surneu.2007.03.027.

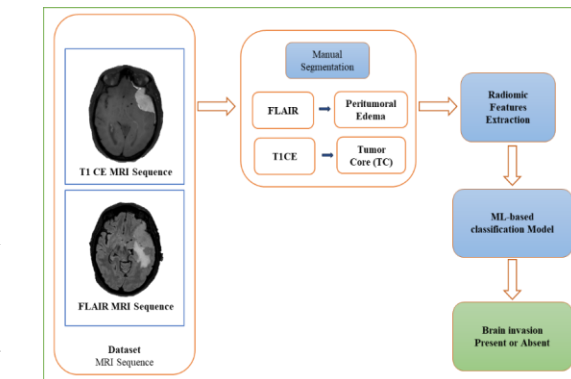


Figure 1: Framework for the proposed methodology

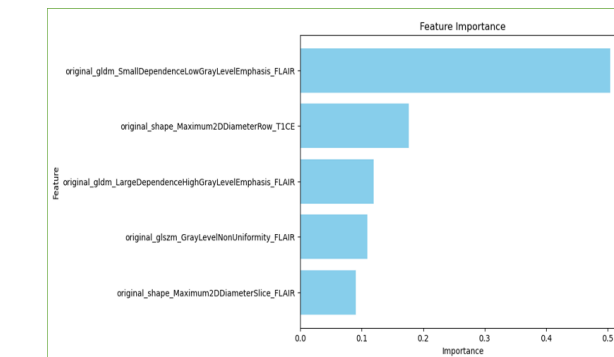


Figure 2: Feature importance for the prediction of brain invasion

# Neurometabolic Analysis using $^2\text{H}$ and $^1\text{H}$ NMR Spectroscopy

Akila Ramesh<sup>1,2\*</sup> and Anant Bahadur Patel<sup>1,2</sup>

<sup>1</sup>CSIR-Centre for Cellular and Molecular Biology(CCMB), Habsiguda, Uppal Road, Hyderabad, India; <sup>2</sup>Academy of Scientific and Innovative Research, Ghaziabad, India

## Introduction

$^{13}\text{C}$  Labeled substrates, in combination with NMR spectroscopy, are used to study neurometabolism. The lower sensitivity of  $^{13}\text{C}$  NMR is resolved to some extent by  $^1\text{H}$ - $[^{13}\text{C}]$ -NMR spectroscopy.  $^2\text{H}$ -NMR, in combination with a  $^2\text{H}$  tracer, has been an efficient approach for metabolic measurement.<sup>1,2</sup> In this study, we have compared the measurements of  $^2\text{H}$ -labeled amino acids using  $^2\text{H}$  (direct) and  $^1\text{H}$  (indirect)NMR spectroscopy.

## Methods

All animal experiments were performed under protocols approved by the Institutional Animal Ethics Committee of CCMB. Four weeks old SD ( $n=16$ ) rats were used in the study. Rats were anesthetized with urethane (1.5 g/kg, intraperitoneal), and infused with [6,6'- $^2\text{H}$ ]glucose for 10, 20, 40, and 90 min using a bolus variable infusion rate.<sup>3</sup> Blood was withdrawn from the retro-orbital sinus, and brain metabolism was arrested by a focused beam microwave irradiation (3kW, 1.8s). Metabolites were extracted from the rat cerebral cortex using ethanol-extraction protocol.<sup>4</sup> The lyophilized extracts were dissolved in a phosphate buffer (50 mM) prepared in  $\text{D}_2\text{O}$  (1%),  $\text{H}_2\text{O}$  (99%) containing TSP (0.25 mM). The  $^2\text{H}$  NMR spectroscopy of cortical extract was obtained with a zg2h pulse program using a triple resonance probe with the following parameters: repetition time, 0.6 s; spectral width, 1197 Hz; and number of averages: 16384 in the block of 16 with 1024 scans for each block.  $^1\text{H}$ - $[^{13}\text{C}]$ -NMR spectroscopy was performed to measure the concentrations of  $^2\text{H}$  labeled neurometabolites using an indirect a

## Results

The  $^2\text{H}$  NMR spectra of the cerebral cortex prepared after [6, 6'- $^2\text{H}$ ]glucose infusion for different time points are shown in Figure 1. The  $^2\text{H}$  resonances of lactate, glutamate, and glucose are seen at 10 min. Additionally, labeling of aspartate and glutamine is seen at later time points ( $\geq 20$  min). The concentrations of  $^2\text{H}$ -labeled metabolites obtained from the  $^2\text{H}$  spectra are shown in Figure 2A. The  $^1\text{H}$  resonances of  $\text{Glu}_{\text{C}3}$  were used to estimate the total concentration of glutamate. The level of [4- $^2\text{H}$ ]Glu was indirectly estimated by subtracting the  $^1\text{H}$ - $\text{Glu}_{\text{C}4}$ measured glutamate concentration from the total. The loss/dilution of  $^2\text{H}$  label in [4- $^2\text{H}$ ]Glu level was corrected by multiplying it with a factor of 1.33. The [4- $^2\text{H}$ ]Glu concentrations measured using  $^1\text{H}$  and  $^2\text{H}$  NMR at various time points of infusion were in good agreement (Fig. 2B).

## Discussions

The loss/dilution of label ( $^{13}\text{C}$  and  $^2\text{H}$ ) occurs at different stages of metabolism like glycolysis or tricarboxylic acid cycle (TCA) cycle. In case of  $^{13}\text{C}$ -glucose, label is lost as  $\text{CO}_2$  in TCA cycle only. However, there is differential dilution/loss of  $^2\text{H}$  from the glycolytic and TCA cycle intermediates in case of [6, 6'- $^2\text{H}$ ]glucose. The detailed analyses in the fractionated extract prepared after 90 min [6,6'- $^2\text{H}$ ]glucose infusion showed no signal of [2- $^2\text{H}$ ]Asp (~3.90 ppm), [2- $^2\text{H}$ ]Glu (~3.76 ppm), and [3- $^2\text{H}$ ]Glu(~2.09 ppm) suggesting complete loss/dilution of  $^2\text{H}$  from the TCA cycle intermediates beyond oxaloacetate. As a result  $^1\text{H}$ - $\text{Glu}_{\text{C}3}$  resonance was used for the estimation of the total glutamate pool, and the concentration measured using  $^1\text{H}$ - $\text{Glu}_{\text{C}4}$ resonance was subtracted from the total for the indirect estimation of [4- $^2\text{H}$ ]Glu.

## Conclusion

The close resemblance of  $^2\text{H}$  levels estimated using  $^2\text{H}$  and  $^1\text{H}$  NMR spectroscopy indicates that  $^2\text{H}$  labeling can be efficiently measured using  $^1\text{H}$ -NMR spectroscopy for neurometabolic measurement. This approach promises the least experimental time and higher sensitivity without any additional requirement of hardware and can provide valuable insights into the neurometabolic status of various neurological diseases.

## Acknowledgments

This study was supported by the Council of Scientific and Industrial Research (CSIR-CCMB).

## References

- de Graaf et al. (2021) ACS Chem Neurosci 12(1):234.
- Rich LJ et al. (2020) Nat Biomed Eng 4(3):335.
- Fitzpatrick et al (1990) J Cereb Blood Flow Metab, 10(2):170
- Patel et al (2001) Brain Res 919:207.

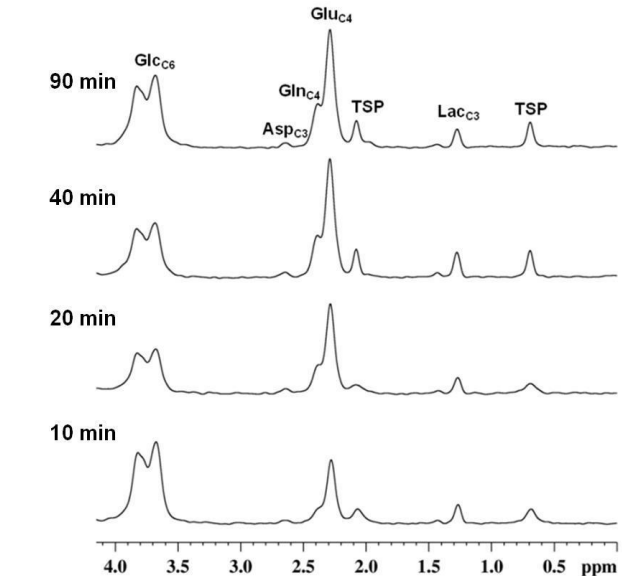


Figure 1:  $^2\text{H}$  NMR spectra of cortical extracts from SD rats infused with [6,6'- $^2\text{H}$ ]glucose for various time pints.

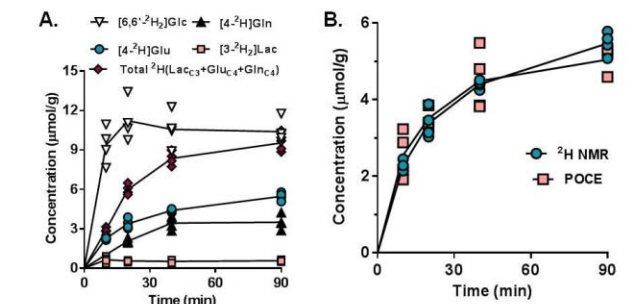


Figure 2:  $^2\text{H}$  NMR spectra of cortical extracts from SD rats infused with [6,6'- $^2\text{H}$ ]glucose for various time pints.

# Novel Approach for Integrating Magnetic Resonance for Design of Artificial Electro Magnetic Heart using Machine Learning

Pradyumna Yambar

## Introduction

The artificial electromagnetic heart (AEH) is an emerging innovation in cardiac therapy. But the major problem is to design an AEH that could accurately mimic the natural heart's electromagnetic properties. This paper aims to integrate the MRI data with the techniques of machine learning (ML) to design an AEH which is highly efficient and physiologically accurate. The main intention was to improve current AEH designs by optimizing simulations of electromagnetic fields and heart dynamics utilizing more advanced computational methods.

## Methods

The study used high-resolution MRI data from the human subject to model the electromagnetic properties of the heart. A novel machine learning framework was developed to process and analyze the MRI data, enabling the generation of precise electromagnetic field maps. The ML model incorporated convolutional neural networks (CNNs) for image segmentation and recurrent neural networks (RNNs) for temporal dynamics prediction. The designed AEH prototype was evaluated using computational fluid dynamics (CFD) simulations and bench testing under physiological conditions. The performance indices determined here were electromagnetic field intensity, energy efficiency, and hemodynamic compatibility.

## Results

The ML-based method was evaluated to achieve 95% accuracy in segmenting MRI data and electromagnetic field distribution predictions. Energy efficiency was improved by 30% when compared with available models for the AEH prototype. According to CFD, hemodynamic performance was optimal without significant turbulence and minimal pressure drops. The bench tests

validated that electromagnetic fields can indeed be kept constant by AEH under a number of physiological states. Some representative figures and plots are given: electromagnetic field map, comparison energy efficiency, and hemodynamic performance.

## Discussion

The fusion of MRI with ML is one big step ahead of AEH. The current investigation clearly demonstrated how ML may offer a good source of enhancement towards precision and the efficiency of an AEH. The proposed design has better precision in modeling an electromagnetic field in comparison to any conventional method applied, and predictive accuracy of dynamics in the heart. The study is in recent literature on applying ML in biomedical engineering but progresses the state of the art forward by addressing specifically the challenges toward AEH design. The approach is novel and integrates MRI data, ML algorithms, and simulation of the electromagnetic field to yield a physiologically accurate model of AEH.

## Conclusion

This work illustrates the feasibility of applying machine learning for designing an artificial electromagnetic heart with superior performance and physiological accuracy. The proposed approach is highly relevant in a clinical setting and provides a promising alternative for end-stage heart failure patients. The bottom line is that next-generation artificial organs may be revolutionized by combining advanced computational methods like ML with medical imaging data. Future work will include *in vivo* testing and long-term performance evaluation of the AEH prototype.

## Reference

- [1] J. Zhang, Y. Wang, and L. Li, "Machine Learning in Medical Imaging: A Review of Recent Advances and Future Directions," *IEEE Transactions on Biomedical Engineering*, vol. 67, no. 5, pp. 1344–1359, May 2020, doi: 10.1109/TBME.2019.2945701.
- [2] A. Gupta, S. Patel, and R. Kumar, "Artificial Intelligence in Cardiovascular Imaging: Applications and Challenges," *IEEE Journal of Biomedical and Health Informatics*, vol. 25, no. 7, pp. 2532–2545, Jul. 2021, doi: 10.1109/JBHI.2020.3048999.
- [3] M. Smith, K. Johnson, and P. Brown, "Magnetic Resonance Imaging for Cardiac Electrophysiology: Techniques and Applications," *IEEE Transactions on Medical Imaging*, vol. 39, no. 12, pp. 3875–3888, Dec. 2020, doi: 10.1109/TMI.2020.2996789.
- [4] R. Lee, T. Nguyen, and H. Chen, "Design and Optimization of Artificial Hearts Using Computational Fluid Dynamics and Machine Learning," *IEEE Transactions on Biomedical Circuits and Systems*, vol. 14, no. 3, pp. 512–525, Jun. 2020, doi: 10.1109/TBCAS.2020.2974567.
- [5] S. Kumar, A. Sharma, and V. Singh, "Integration of Machine Learning and Magnetic Resonance Imaging for Biomedical Device Design," *IEEE Reviews in Biomedical Engineering*, vol. 13, pp. 245–260, 2020, doi: 10.1109/RBME.2019.2957758

# On An Analytic Approach to Designing Gradient Waveforms for Isotropic Diffusion-Weighted Imaging

Hariraj M.S, Rizvi S.M., Neelavalli J.

Department of Biomedical Engineering, Indian Institute of Technology Hyderabad.

## Introduction

Trace-weighted or isotropic diffusion-weighted imaging (DWI) is one of the most widely used contrast mechanisms in clinical magnetic resonance imaging (MRI). By providing insights into tissue microstructure abnormalities associated with conditions such as cancer, stroke, and traumatic injury, it has become an indispensable tool in diagnostic imaging. Traditionally, generating an isotropic DWI image requires at least three separate acquisitions with diffusion weighting applied along the x, y, and z axes, followed by their combination. This approach is time-consuming and can significantly prolong scan times, particularly in motion-sensitive applications such as fetal MRI, making the data acquisition prone to motion artifacts. An alternative approach to obtaining an isotropically weighted DWI image involves ensuring that the cross-terms of the diffusion tensor vanish while the diagonal elements remain equal [1,2]. This concept was first demonstrated by Mori et al. [1], who employed a bipolar gradient waveform, while Wang et al. [2] explored an alternative approach using oscillating gradient waveforms. Both methods have contributed to the development of isotropic diffusion encoding (IDE), a term that has gained increasing recognition in recent literature. However, the bipolar gradient waveform approach suffers from challenges such as long echo times (TE) and eddy current distortions, whereas continuous gradient waveforms have shown greater efficiency in addressing these limitations. Existing methods for designing gradient waveforms that satisfy isotropic diffusion weighting conditions primarily rely on numerical optimization [1,2]. In this work, we present an analytical approach to deriving gradient waveform shapes that achieve isotropic diffusion weighting using two distinct methods: one based on utilizing a continuous sinusoidal basis and the other a linear combination of Walsh basis functions with varying indices.

## Methods

For designing Gx, Gy and Gz gradients for isotropic diffusion weighting, the following conditions must be satisfied:

$$\int_0^T G_x(t) \cdot dt = \int_0^T G_y(t) \cdot dt = \int_0^T G_z(t) \cdot dt = 0 \quad \dots \text{Eq. 1}$$

$$\int_0^T \left( \int_0^t y \cdot G_x(t) \cdot dt' \right)^2 \cdot dt = \int_0^T \left( \int_0^t y \cdot G_y(t) \cdot dt' \right)^2 \cdot dt = \int_0^T \left( \int_0^t y \cdot G_z(t) \cdot dt' \right)^2 \cdot dt = 0 \quad \dots \text{Eq. 2}$$

$$\int_0^T \left( \int_0^t y \cdot G_x(t) \cdot dt' \right) \cdot \left( \int_0^t y \cdot G_y(t) \cdot dt' \right) \cdot dt' = 0; \int_0^T \left( \int_0^t y \cdot G_y(t) \cdot dt' \right) \cdot \left( \int_0^t y \cdot G_z(t) \cdot dt' \right) \cdot dt' = 0; \int_0^T \left( \int_0^t y \cdot G_z(t) \cdot dt' \right) \cdot \left( \int_0^t y \cdot G_x(t) \cdot dt' \right) \cdot dt' = 0 \quad \dots \text{Eq. 3}$$

where diffusion is occurring over the time interval [0,T]. If the gradient waveform shapes for each axis are expanded in terms of a basis function decomposition, such as a Fourier series or a Walsh series, the problem reduces to determining the coefficients that satisfy the required isotropic diffusion weighting conditions. For the Fourier series representation, this takes the form:

$$G(t) = \sum_{k=0}^N a_k \cdot \cos \cos(k \cdot \omega_o t) + b_k \cdot \sin \sin(k \cdot \omega_o t)$$

Here,  $\omega_o = 2\pi/T$  to ensure that Eq.1 is satisfied. A similar approach can be applied to Walsh basis expansion, where the gradient waveform is expressed as a linear combination of Walsh functions with appropriate coefficients.

In this method, the problem is simplified to finding  $2N$  unknown coefficients for each gradient axis, where  $N$  and  $m$ , both positive integers, define the number and type of harmonic components in a gradient waveform. The equations are 2nd order polynomials in terms of Fourier series coefficients, solvable using Grobner basis decomposition. System hardware conditions like maximum gradient amplitude or maximum slew rate per axis can further refine the solution. After determining Fourier Coefficients for a harmonic configuration, gradient waveform shapes can be defined for the desired b-value (i.e., diffusion weighting measured in sec/mm<sup>2</sup>), with  $T$  as a free or fixed parameter to determine the maximum b-value achievable for that configuration. This applies to continuous sinusoidal waveforms. A similar approach can be applied to Walsh functions.

## Results

### Continuous sinusoidal waveform

Several families of solutions exist based on the number of harmonics used per gradient axis. A simple choice is assigning the  $m^{th}$ ,  $(m+1)^{th}$  and  $(m+2)^{th}$  harmonics along, say Gx, Gy, Gz directions, respectively. ‘m’ is a positive integer.

$$G_x(t) = (m \cdot \omega_o t)$$

$$G_y(t) = a \cdot ((m+1) \cdot \cos \cos((m+1) \cdot \omega_o t))$$

$$G_z(t) = a \cdot ((m+2) \cos \cos \theta \cdot \cos \cos((m+2) \cdot \omega_o t) + \frac{(m+2)}{\sqrt{3}} \cdot \sin \sin \theta \cdot \sin \sin((m+2) \cdot \omega_o t))$$

This combination can be permuted among the x, y, and z directions without loss of generality. Here,  $a$  is the gradient amplitude scaling factor,  $m$  is a positive integer, and  $\theta$  is an independent parameter. Regardless of the value of  $m$ , this solution results in a b-value of  $\frac{y^2 T^2 a^2}{8\pi^2}$

Another solution is having the first harmonic terms in two gradient axes and the first and the second harmonic terms in the third gradient axis.

$$G_x(t) = ((m \cdot \omega_o t) + \sin \sin(m \cdot \omega_o t)) / f$$

$$G_y(t) = ((m \cdot \omega_o t) + \sin \sin(m \cdot \omega_o t)) / f$$

$$G_z(t) = (((m \cdot \omega_o t) + \sin \sin(m \cdot \omega_o t)) +$$

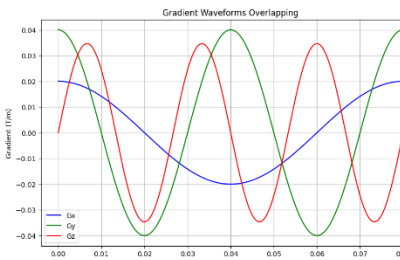
$$((m+1) \cdot \omega_o t) + \sin \sin((m+1) \cdot \omega_o t)) / f$$

Without loss of generality, if we assume  $a_{1x} = 1$ , and  $a_{1y} = a$ , The remaining fourier coefficients are determined as:

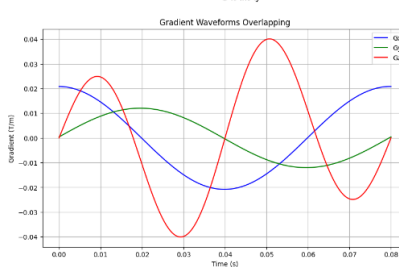
$$b_{1x} = -\frac{a}{\sqrt{3}}; \quad b_{1y} = \frac{1}{\sqrt{3}}; \quad a_{1z} = 0; \quad b_{1z} = -\frac{1}{6} \left( \frac{m+1}{m} \right) \cdot \sqrt{\frac{3(a^2+1)}{5}} \sin \sin \theta;$$

$$a_{2z} = \left( \frac{m+1}{m} \right) \cdot \sqrt{a^2 + 1} \cos \cos \theta; \quad b_{2z} = \frac{1}{2} \left( \frac{m+1}{m} \right) \cdot \sqrt{\frac{3(a^2+1)}{5}} \sin \sin \theta;$$

Here,  $\theta$  and  $f$  are independent free parameters, with  $f$  serving as a scaling factor to ensure the maximum gradient strength remains within realistic limits. Interestingly, the b-value for this family of solutions is dependent on the value of  $m$  as well as of  $a$  and  $f$ :  $\frac{y^2 T^2 (a^2+1)}{8 \cdot \pi^2 \cdot m^2 \cdot f^2}$ .



Parameter values:  $T = 80$  ms,  $a = 20$  mT/m,  
 $m = 1, f = 1$ , Max Gx = 20.0 mT/m,  
Max Gy = 40.0 mT/m, Max Gz = 34.6 mT/m



Parameter values:  $T = 80$  ms,  $a = 20$  mT/m,  
 $m = 1, f = 48$ , Max Gx = 20.83 mT/m, Max Gy = 12.03 mT/m, Max Gz = 40.10 mT/m

## Walsh basis functions

Similarly, Walsh functions can be written,

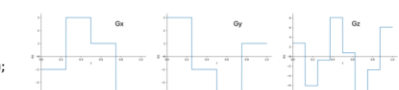
$$G_x = a_x \cdot wal(1, t) + b_x \cdot wal(2, t);$$

$$G_y = a_y \cdot wal(1, t) + b_y \cdot wal(2, t);$$

$$G_z = a_z \cdot wal(1, t) + b_z \cdot wal(2, t) + a_{2z} \cdot wal(4, t) + b_{2z} \cdot wal(5, t);$$

$$ax = 1; ay = 1; az = a;$$

$$bx = -2; by = 2; bz = 0; az = -a \cdot \frac{8}{3}; bz = \sqrt{32 - a^2 \cdot \frac{112}{9}}$$



with the resultant gradient waveforms also shown above. The b-value achievable in Walsh basis function  $\frac{y^2 T^2 a^2}{6}$ .

## Reference

- [1] Mori, S., & van Zijl, P. C. M. Diffusion Weighting by the Trace of the Diffusion Tensor within a Single Scan. *Magn Reson Med* 1995; 33:41-52.
- [2] Wong EC, Cox RW, Song AW: Optimized isotropic diffusion weighting. *Magn Reson Med* 1995; 34:139–143.
- [3] Avram AV, Sarlis JE, Bassar PJ: Measuring non-parametric distributions of intravoxel mean diffusivities using a clinical MRI scanner. *NeuroImage* 2019; 185:255–262.
- [4] Sjöland J, Szczepankiewicz F, Nilsson M, Topgaard D, Westin C-F, Knutsson H: Constrained optimization of gradient waveforms for generalized diffusion encoding. *J Magn Reson* 2015; 261:157–168.
- [5] Cheng, D.K. (1979). Theory and Applications of Generalized Walsh Functions in Digital Systems.